Lateral Features of Amphipathic Structures: Theory and Simulations

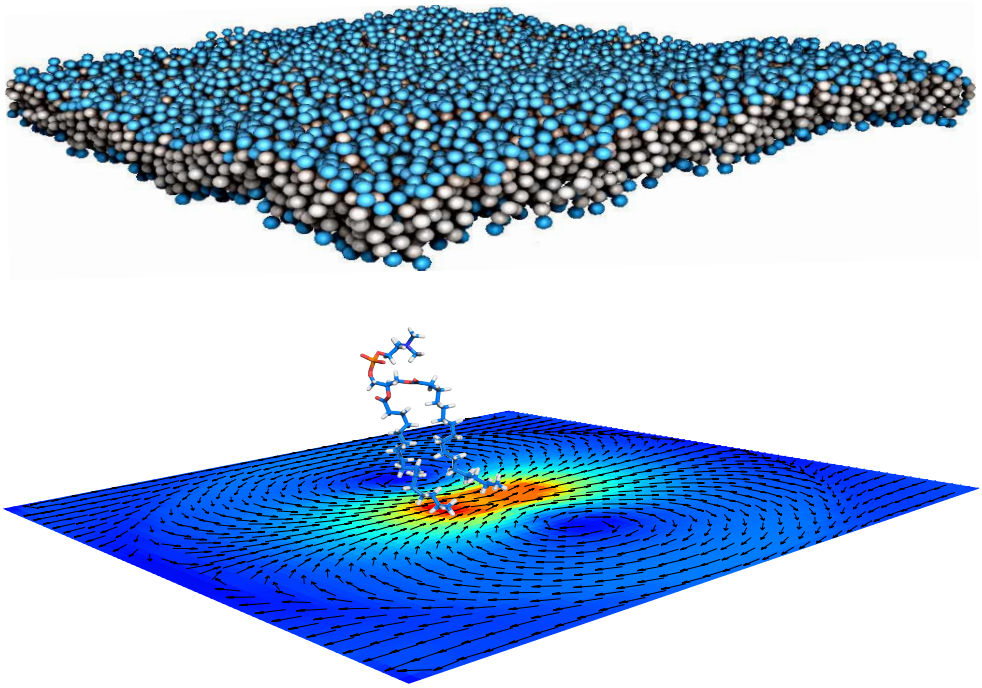

Sergio Panzuela Pérez

A dissertation submitted for the Degree of

Doctor of Philosophy

Universidad Autónoma de Madrid
Department of Theoretical Condensed Matter Physics

Supervised by:

Enrique Velasco Caravaca
Luis Mederos Martín

Madrid, February 6, 2019.

Contents

List of Acronyms

This is a list of the acronyms used in the text (in alphabetical order).

au	arbitrary units.
BD	Brownian Dynamics.
BDHI	Brownian Dynamics with Hydrodynamics Interactions.
DFT	Density Functional Theory.
DDFT	Dynamic Density Functional Theory.
DPPC	Dipalmitoylphosphatidylcholine.
FDDFT-HI	Fluctuating Dynamic Density Functional Theory with Hydrodynamic Interactions.
FENE	Finitely Extensible Non-linear Elastic.
FHD	Fluctuation Hydrodynamics.
FWHM	Full Width at Half Mean.
GPU	Graphics Processor Unit.
LJ	Lennard-Jones.
MD	Molecular Dynamics.
MSD	Mean Squared Displacement.
PBC	Periodic Boundary Conditions.
PME	Particle Mesh Ewald.
POPC	Palmitoyloleoylphoshatidylcholine.
Q2D	Quasi-Two-Dimensional.
RF	Reaction Field.
RPY	Rotne-Prager-Yamakawa.
WCA	Weeks-Chandler-Andersen.

Abstract

English

This thesis is devoted to the theoretical and computational study of the lateral features of different amphipathic complexes of the pulmonary surfactant system. Experimental and theoretical studies have indicated the existence of condensed lipid domains that coexist with an expanded lipid domain in monolayers, membranes and vesicles. It is thought these condensed domains are stable and crucial for the modulation of dynamic and thermodynamic properties, although this is a highly controversial issue. Other sorts of domains, this time of a few lipid molecules and in fluid membranes, present collective properties that have not yet been clarified. Specifically, experiments have characterised the short-time diffusion of lipids as streamflow. Consistently, computer simulations have shown that lipids unexpectedly tend to move coherently at short times, forming very interesting patterns of collective motion.

In the first part of this thesis, we tackle questions regarding the stabilisation of condensed domains. Particularly, we characterise the structural properties of lipids and (expanded and condensed) domains in lipid monolayers that are placed in a vapour-water interface. Due to the great dependence of the properties of lipids and domains on the atomistic details, we perform molecular dynamics simulations of state-of-the-art force fields (CHARMM36+OPC). As a peculiarity of this study, we distinguish between lipids that belong to condensed and expanded domains. On the one hand, our analyses unveil that condensed domains tend to be elongated/rectangular. Furthermore, these analyses show that condensed domains exhibit a high dipolar order, which emerges from the high (parallel) alignment of acyl chains of lipids, with a relative orientation to the interface of the expanded and condensed domains $\sim 10°$. These results suggest the existence of an anisotropic line tension at the boundary of condensed domains. On the other hand, analyses on the orientation and hydration of the most representative chemical groups of lipids (head and tail) may point out deficiencies in the force field with regard to the properties of the head

group of lipids.

In the second part of this thesis, we consider general questions regarding the collective dynamics of lipids in fluid membranes. We develop a theoretical framework that allows addressing the collective dynamics of generic quasi-two-dimensional systems (particles/molecules confined in a liquid-liquid interface). Previously, as an introduction to the extraordinary phenomenology of quasi-two-dimensional systems, we start with the development of a preliminary theory, and the analysis of the ideal scenarios. This theory shows anomalous (divergent) collective diffusion coefficients as well as non-negligible (in some cases quasi-giant) fluctuations. The results are confirmed by means of very fast fluctuating hydrodynamics simulations in the Brownian regime. To study systems similar to membranes lipids, we relax ideal constrains, so that we develop an alternative formalism for the quasi-two-dimensional theory for the diffusion. In addition to ratifying previous results, we show new features and explore the limits of this new formalism. At the end of this thesis, we apply the quasi-two-dimensional theory to the diffusion to membrane lipids. To contrast the results, we perform fluctuating hydrodynamics simulations as well as molecular dynamics simulations, and we use different models of a membrane lipid (MARTINI and Cooke-Deserno). Our results validate the quasi-two-dimensional theory for the diffusion at short-times *i.e.* the collective diffusion coefficient of lipids diverge. By contrast, this theory is violated at long-times. Finally, partial results suggest a casual relationship between the quasi-two-dimensional hydrodynamics and the coherent motion of lipids at short-times.

Español

Esta tesis está dedicada al estudio teórico y computacional de las características laterales de diferentes complejos anfifáticos que componen el sistema surfactante pulmonar. Estudios experimentales y teóricos han señalado la existencia de dominios lipídicos condensados que coexisten con un dominio lipídico expandido en monocapas, membranas y vesículas. Se piensa que estos dominios condensados son estables y cruciales para la modulación de propiedades dinámicas y termodinámicas, aunque este asunto se encuentra rodeado de un alto grado de controversia. Otros tipos de dominios, en este caso del tamaño de pocas moléculas lipídicas y en membranas fluidas, presentan propiedades colectivas no clarificadas aún. En particular, experimentos han caracterizado la difusión de los lípidos a cortos tiempos como la de un flujo de corriente. Por otro lado, simulaciones por ordenador han mostrado que los lípidos tienden a moverse coherentemente a cortos tiempos, formando interesantes patrones de movimientos colectivos.

En la primera parte de esta tesis, tratamos preguntas relacionadas con la estabilización de dominios condensados. En concreto, caracterizamos las propiedades estructurales de lípidos y dominios (expandidos y condensados) en monocapas lipídicas que se encuentran en una interfaz agua-vapor. Debido a la gran dependencia de las propiedades de los lípidos y dominios de los detalles atomísticos, realizamos simulaciones de dinámica molecular de los modelos computacionales más avanzados (CHARMM36+OPC). Como particularidad de este estudio, hacemos una distinción entre los lípidos que pertenecen a dominios condensados y expandidos. Nuestros análisis revelan que los dominios condensandos tienden a ser elongados/rectangulares. Además, estos análisis demuestran que los dominios condensados presentan un gran orden dipolar, el cual subyace de la gran alineación (paralela) de las cadenas acílicas de los lípidos con una orientación relativa a la interfaz entre los dominios condensados y expandidos $\sim 10^{\circ}$. Estos resultados sugieren la existencia de una tensión de línea anisotrópicas en la frontera del los dominios condensados. Por otra parte, análisis sobre la orientación e hidratación de los grupos químicos más representativos de los lípidos (cabeza y cola), podrían indicar alguna deficiencia del modelo computacional usado en cuanto a las propiedades del grupo cabeza de los lípidos.

En la segunda parte de esta tesis, tratamos de entender cuestiones generales de la dinámica colectiva de los lípidos en membranas fluidas. Para ello, desarrollamos todo un marco teórico que permite abordar la dinámica colectiva de sistemas casi dos dimensionales genéricos (partículas/moléculas confinadas en una interfaz líquido-líquido). Previamente, como introducción a la extraordinaria fenomenología de los sistemas casi dos dimension-

ales, comenzamos con el desarrollo de una teoría preliminar y el análisis de sus casos más ideales. Esta teoría demuestra la presencia de un coeficiente de difusión colectivo anómalo (divergente) así como fluctuaciones considerables (en algunos casos casi gigantes). Los resultados son constatados mediante simulaciones ultra rápidas de hidrodinámica fluctuante en el régimen Browniano. Para el estudio de un escenario más aproximado al que sería el de una membrana, relajamos las condiciones de idealidad, por lo que desarrollamos una teoría casi dos dimensional de la difusión con un formalismo alternativo al anterior. Además de ratificar los resultados previos, mostramos nuevos resultados y exploramos los límites de este nuevo formalismo. A final de esta tesis, aplicamos la teoría casi dos dimensional de la difusión a membranas lipídicas. Para contrastar los resultados en membranas, realizamos simulaciones tanto de hidrodinámica fluctuante como de dinámica molecular, y usamos distintos modelos de membranas lipídicas (MARTINI y Cooke-Deserno). Nuestros resultados revelan la validez de la teoría casi dos dimensional de la difusión a cortos tiempos *i.e.* el coeficiente de difusión colectivo de los lípidos diverge. En cambio, a largos tiempos esta teoría es violada. Finalmente, resultados parciales sugieren una relación de causalidad entre la hidrodinámica casi dos dimensional y el movimiento coherente de los lípidos a cortos tiempos.

1

General introduction

Every great magic trick consists of three parts or acts. The first part is called "The Pledge". The magician shows you something ordinary: a deck of cards, a bird or a man. He shows you this object. Perhaps he asks you to inspect it to see if it is indeed real, unaltered, normal. But of course... it probably isn't. The second act is called "The Turn". The magician takes the ordinary something and makes it do something extraordinary. Now you're looking for the secret... but you won't find it, because of course you're not really looking. You don't really want to know. You want to be fooled. But you wouldn't clap yet. Because making something disappear isn't enough; you have to bring it back. That's why every magic trick has a third act, the hardest part, the part we call "The Prestige".

— **Christopher Priest**, *The Prestige,* 2006.

Nowadays it is widely accepted that *lipid membranes* are lipid-protein complexes that enclose and separate cells from their environment, and that they regulate the traffic of substances that come in and out of the cells, however, it took no less than 175 years to get a clear picture of a lipid membrane [1]. To understand the genesis of the discussion we have to take ourselves back in time to the middle 19th century, when primitive foundations of "membranes" appeared for the first time. At the time, studies encouraged by the precursor of *The Cell Theory* (a botanist, Matthias Jacob Schleiden, and a physiologist, Theodor Schwann, both German in origin) on animal and vegetal cells suggested for the first time

the existence of a cell boundary. Being that cell boundary (also called cell wall[1]), formed by the most external and hardened part of the cells, responsible for separating the cells from their environment. But the lack of experimental techniques and data as well as theoretical relevance did not help in its acknowledgement.

In the second half of 19th century, early *osmosis* studies already acknowledged that changes in the volume of cells were strongly associated with the movement of water molecules across the cell border. However, results obtained from osmosis studies in precipitation membranes were hardly to be extrapolated to those of cell membranes. So it was not until after Nernst's hypothesis for the *permeability* of a membrane [2] and posterior observation by Overton of the permeability of a membrane over 500 different substances [3] that it could be concluded that there exists a cell membrane at the cell boundary, distinct from the cell wall, and whose molecular composition consists, probably, of cholesterol and *phospholipid* molecules.

At the beginning of the early 20th century the concept of cell membrane was already strongly supported by three main research lines: Overton's permeability studies, microinjections experiments and electrophysiology experiments. Nevertheless, the greatest milestone was yet to come. In 1925 Gorter and Grendel proved that, certainly, lipids are the main component of cell membranes [4]. For this, they proved that the area covered by synthesised globe blood lipids on a *Langmuir monolayer* is equal to the cell membrane area assuming that the cell membranes are composed of two lipid layers [4], *i.e.* lipids are distributed into two monolayers with their acyl chains confronted (for visual representation see Fig. 1.1). Which results surprising bearing in mind that very little was known at the time about the *amphipathic* character of lipid molecules. Unfortunately, neither the cell membrane structure nor its thickness would become accessible until the development of electron microscopy techniques (two decades later).

By the 1930s, two main discoveries in the field of cytology propitiated the creation of a new cell membrane model, *The Paucimolecular Model*; Since the 19th century there were overwhelming proofs that cell membranes (lipid membranes from now on) were also constituted of proteins [5, 6], although little was known about their functionality. So, when posterior studies established cell membranes reduces the surface tension of oil-water interfaces, it was thought that proteins were the main culprit's in this feature of cell membranes. Thus, the Paucimolecular model proposed a particular structure for cell membranes based on the positions of proteins. Within this view, proteins have to be on the outer levels of a cell membrane so that they can efficiently decrease the surface tension at the interface.

[1]Note that at the time there was no way to distinguish between cell membrane and cell wall.

However, soon after, it was reasoned the structures depicted by the Paucimolecular models had to be dismissed.

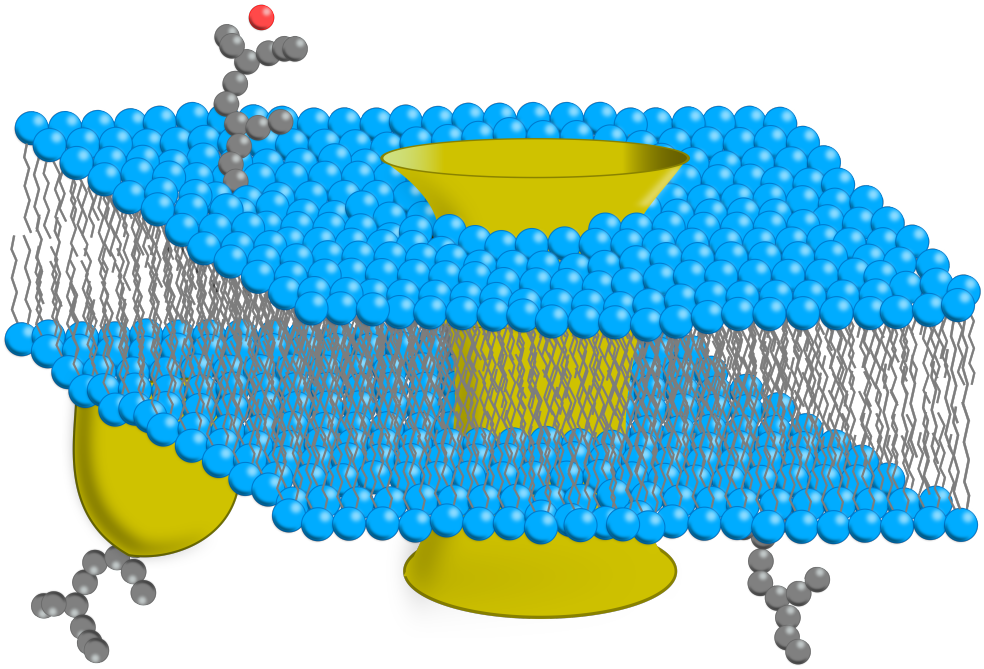

Figure 1.1: Schematic cross section of the fluid mosaic model. Lipids are depicted in blue (polar group) and grey (acyl chains), proteins in yellow and glicoproteins in grey.

A few years later, Singer and Nicolson proposed as an alternative to the Paucimolecular model what it is regarded as today's modern foundations of a cell membrane in a model known as *The Fluid Mosaic Model* [7]. This model was supported by a great number of studies, of which we highlight permeability, conformational and transport studies[8–13] among others. It states that: (1) in presence of polar aqueous media, lipids self-organise into bilayers, which are the optimal structure (from the thermodynamic point of view) to minimize *hydrophobic* and *hydrophilic* interactions. Consequently, acyl chains of lipids of different monolayers are confronted. (2) Cell membranes are composed of three main types of molecules: lipids, proteins and oligosaccharides. (3) While phospholipids provide a matrix to settle proteins and oligosaccharides, these two last characterise the functionality of the cell membrane. (4) In physiological conditions, the natural state of a cell membrane is fluid rather than crystalline. (5) Because of the specialisation of the monolayers of the cell membrane (inner and outer monolayers), both monolayers are different from each other regarding their concentrations of lipids, proteins and oligosaccharides. Hence cell membranes are asymmetric.

Finally, the fluid mosaic model deprecated the Paucimolecular model by the end of the

20th century, and is considered nowadays among the accepted principles in the field of cytology. And such is the merit of Singer and Nicolson that since the foundation of the fluid mosaic model it has only been necessary to make slight adjustments.

1.1 Pulmonary Surfactant

Beyond the cell membrane and the fluid mosaic model there are other sorts of amphipathic structures that are also thermodynamically favourable and which fulfil, roughly, the main assumptions of the fluid mosaic model. For instance, it is very well known that, during the digestion process, fats (lipids) are emulsified by bile acids in the small intestine to form the so-called *micelles*. These emulsions consist of lipid molecules distributed spherically, with their polar group in contact with their external environment and keeping acyl chains away from it, in such a way that lipase aids the processing (breaking down of lipids into glycerol plus fatty acids) and transport of lipids very efficiently. So, in this respect, micelles are the optimal structures. Other examples of amphipathic structures (apart from lipid micelles and bilayers) are lipid *vesicles* and *monolayers*, which we might find in diverse biological scenarios; Golgi's apparatus, lysosomes, small and large intestine, neuron synapse and so on. Notice though that the presence of one of the named structures (we depict them in Fig. 1.2) in a particular system does not necessary exclude its coexistence with other amphipathic structures, and for it, the perfect example is the pulmonary surfactant, or lung surfactant, system.

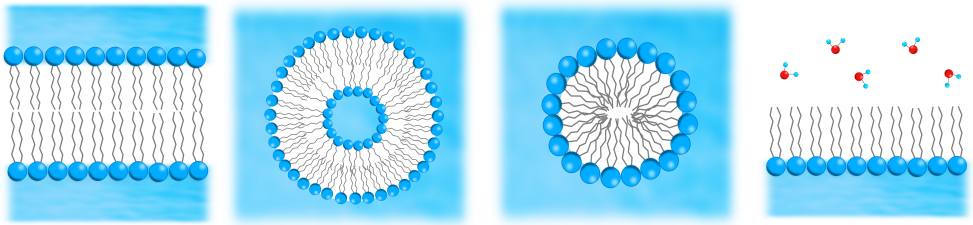

Figure 1.2: Cross section sketch of lipid structures. From left to right: lipid membrane, vesicle, micelle and monolayer.

The pulmonary surfactant system, just like a cell membrane, is a lipid-protein complex, segregated by the type II pneumocyte of the alveoli epithelium at the air-liquid interface of the alveolus boundary, and assembled into an elaborate network of lipid monolayers, bilayers, multilayers and vesicles (for a visual representation, see Fig. 1.3) [14]. Regarding

its composition, around 80% of the pulmonary surfactant is made of lipids, of which half of them are dipalmitoylphosphatidylcholine (DPPC), 5-10% represents neutral lipids (mainly cholesterol), and proteins contribute the last 8-10% [14]. Among its main features, we underscore its transcendence for defensive and tenso-active purposes.

Before the skin, the pulmonary surfactant is the largest surface contact that air-breathing vertebrates have with their surrounding [15], in such a way it optimises gas exchanges during the breathing process. It is therefore the pulmonary surfactant that accounts for specialised proteins that combat external threats, such as viruses, fungi, bacteria and parasites as well as allergens (pollens) and pollutants (dust and other nanoparticles) [16].

To understand the strategic positioning of the pulmonary surfactant we have to invoke its tenso-active features. And inevitably, talking about tenso-active features of the pulmonary surfactant is inherently associated with talking about DPPC, which is the most predominant and efficient tenso-active molecule of the pulmonary surfactant epithelium [14]. This is because the chemical composition of DPPC allows to dramatically reduce the surface tension of air-liquid interfaces when these molecules assemble in the form of a monolayer at the aforementioned interface. Thus, because of this property of DPPC monolayers, the pulmonary surfactant is also supposed to reduce the surface tension of air-liquid interfaces, which facilitates the gas exchanges during the breathing cycle.

However, the high melting temperature of DPPC monolayers (314 K) gives rise to poor fluidity properties [14] at physiological temperature (≈ 310 K), which is very inconvenient since fluidity is of vital relevance for the proper functioning of the pulmonary surfactant [14]. By contrast, a Palmitoyloleoylphoshatidylcholine (POPC) lipid, unlike a DPPC lipid, presents a *cis* bond in one of its acyl chains, and a much lower melting temperature (270 K). However, because of its low compressibility, POPC monolayers tend to exhibit poor tenso-active qualities. Therefore it is clearly not an easy task, not to say impossible, to find proper pulmonary surfactants (*in vitro*) from a single lipid specie. Neither does it become simpler when one uses different DPPC+POPC mixtures in which the melting temperature is below the physiological temperature while keeping reasonable tenso-active and fluidity properties [15]. Likewise DPPC+cholesterol mixtures have also been proposed as possible models of pulmonary surfactant taking advantage of the interesting properties of cholesterol [17–20] *e.g.* above the melting temperature of lipids cholesterol tends to order the acyl chains of lipids, leading to a decrease of the fluidity, whereas it tends to disorder the acyl chains of lipids leading to an increase of the fluidity otherwise [21, 22]. Although these models have failed too.

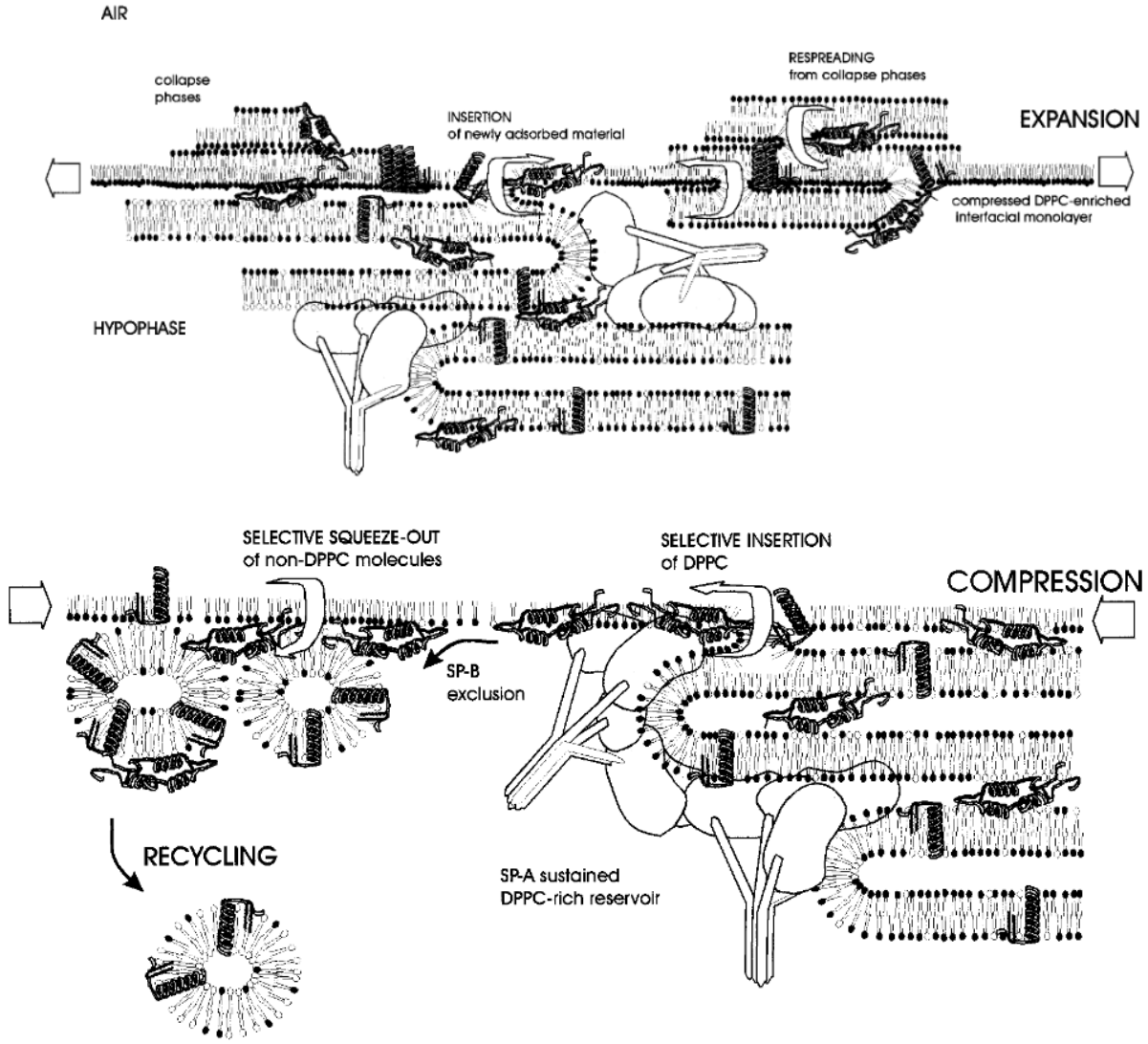

Figure 1.3: Schematic representation of the pulmonary surfactant system. Top and bottom figures represent a pulmonary surfactant film subjected to expansion and compression in analogy to the successive expansions and compressions of alveoli undergone during the breathing process. Lipids are represented by white and black head groups plus two acyl chains and proteins are represented by helices and tree structures. Figure taken from J. Pérez-Gil *et al.* [15].

Indeed, the pulmonary surfactant is more complicated than a DPPC+POPC or DPPC+ cholesterol mixtures [14]. And a proof of it is its extraordinary and unexpected surfactant capabilities: high compressed native pulmonary surfactant monolayers reduce the surface tension of air-liquid interfaces to values similar to those of pure DPPC monolayers. However, many of the lipids present in the pulmonary surfactant composition have a single or double *cis* bond in their acyl chains, so in theory the pulmonary surfactant was never

expected to be that good as a tenso-active agent. Thus, in an effort to reconcile theory and experiment, the so-called squeeze-out or collapse[2] hypothesis [24, 25] proposes that high packing fractions (and consequently low surface tensions) can be achieved in compressed pulmonary surfactant monolayers by the selective dispatch of low-compressible lipids to the hypophase (aquous phase). In this way the pulmonary surfactant not only yields low surface tension values (up to $\approx 1\ mN/m$) at the air-liquid interface but also allows for the rapid disposal of lipids (when required) "stored" in the hypophase. For this last process, the pulmonary surfactant creates the so-called surfactant associates, which consist of lipid bilayers, multilayers and vesicles that are linked to the air-liquid interface by means of specialised proteins (see Fig. 1.3).

1.1.1 Surfactant Proteins

Proteins, as much as lipids, are essential parts of the pulmonary surfactant system, participating in every biological process given in it (transportation, signalling, fusion, scaffolding, defence, etc.). Such is their relevance that the number of works on this topic have increased notably in the last few decades.

Surfactant proteins make up about 8-10% of the pulmonary surfactant system, and are mostly localized at the interfacial monolayer as well as the surfactant associates (Fig. 1.3). According to their structure, properties and functionality, surfactant proteins are typically bound together into two groups, each of them composed by a pair of proteins: Surfactant protein A and D, (SP-A and SP-D), and surfactant protein B and C, (SP-B and SP-C) [15, 26].

SP-A and SP-D belong to the family of collectins, form large size oligomers of hydrophilic character and their main functionality is as antibodies[3] [15, 26, 27]. These proteins have been demonstrated to be barely relevant for tenso-activity purposes [28], although it is not discarded, SP-A may promote aggregation of the surfactant associates to the interfacial monolayer as well as lateral organisation of lipids [15, 26, 27].

[2] As it is very well clarified in Ref. [14] we have to distinguish between the two meanings of the word "collapse" used in the literature. On the one hand this term is employed when referring to the irreversible breakdown of lipid monolayers that are undergone under extreme high lateral compressions. On the other hand, it stands for a reversible mechanism by which, at moderate to high compressions, lipid monolayers fold to form lipid bilayers or multilayers [23]. During this thesis we will use collapse to refer to the folding of a monolayer to form a bilayer, unless we explicitly mention the breakdown of the lipid monolayer.

[3] SPs-A and SPs-D are able to bind to the surface of a wide variety of pathogen agents contributing to their elimination.

SP-B and SP-C, in contrast to SP-A and SP-D, exhibit an amphipathic character and are fundamental for the main tenso-activity tasks in the pulmonary surfactant system [15, 27]. Hence, SPs-B induces membrane-membrane, membrane-monolayer, vesicle-monolayer and vesicle-vesicle fusion, so they are crucial for the aggregation of the surfactant associates to the interfacial monolayer [29–32]. SPs-C, unlike other surfactant proteins, are the most characteristic surfactant proteins of mammalian animals, and present a very specialised function for bilayer-monolayer and bilayer-bilayer stabilisation. Consequently SPs-C are assumed to be the main agents in the pulmonary surfactant system responsible for aiding bidirectional transfer of lipids between the surfactant associates and the interfacial monolayers [33, 34]. Preferably, SP-B and SP-C are found in disordered regions of the surfactant associates, although their configuration within different surfactant associates is not yet totally: For instance, it is known SPs-C adopt a transmembrane configuration in bilayers and that they expose its C-terminal when placed on thin films [27, 35], while SPs-B configurations are more elusive. This last fact is because the high hydrophobicity of SPs-B hinders their synthesis (without denaturalising them), and therefore their characterisation (secondary, tertiary, and quaternary structures) [27, 36].

Therefore, it is clear that the proper operation of the pulmonary surfactant (interfacial monolayer collapse, surfactant associate stabilisation, reversible transfer of lipids between the surfactant associates the interfacial monolayer, etc.) depends strongly on the surfactant proteins. And as evidence for it, *in vivo* and *in vitro* experiments show that the deficiency of SPs-B and/or SPs-C are associated with different respiratory pathologies, which may even become lethal in case of a complete lack of SPs-B [37–41].

1.1.2 Mechanical Functioning of the Pulmonary Surfactant

Mechanics in the pulmonary surfactant system is a vitally important subject of enquiry as it is directly involved in the breathing process all along. Any malfunction in it may result in severe problems, or even worse, may cause the death [42]. For instance, the pulmonary surfactant system matures over the last few weeks of gestation ($\sim 35^{th}$ week of gestation) [16], so babies who are born prematurely will lack full lung capacities. These babies may hardly be able to breath without any mechanical assistance, and may suffer from chronic respiratory diseases [16].

In spite of the many efforts made to understand mechanics involved in the breathing cycle, little is known about it yet. So far, it is believed that over inspiration and expiration

cycles the number and size of alveoli change, but not simultaneously [14]. Consequently, two connected spherical alveolus, of radii r and r', are submitted to a pressure difference $\Delta p = p_1 - p_2$, where p_1 and p_2 are the pressure inside of each alveolus. In the ideal approximation, alveoli are assumed to be spherical, and thus the pressure inside of them is given by the *Young-Laplace* equation

$$\Delta p = \frac{2\gamma}{r}. \tag{1.1}$$

As a result, small alveoli tend to collapse into big alveoli. And if nothing stop this process, the collapse of small alveoli would continue successively, leading to a sort of chain reaction. At the end, only one alveolus would remain, completing the collapse of the lungs. In practice, however, this is not the physiological situation, and alveoli remain stable.

At this time, most of the authors agree that the pressure difference between alveoli is counteracted by an enrichment of high compressible surfactants at the air-liquid interface of the alveoli, for which the pulmonary surfactant squeezes-out low compressible lipids [43]. In this way, the surface tension γ in the alveoli boundary is decreased, so that the pressures inside small alveoli is also reduced (via Eq. (1.1)), and the pressure difference is equilibrated. An alternative and less accepted theory suggests that the pressure difference between alveoli is balanced via the so-called recruitment mechanism [44]. Thus the stabilisation of alveoli actually comes from small cavities, also called "daughter alveoli", inside the alveoli, or "mother alveoli", which releases high pressures and/or overpressures.

1.2 Lateral Organisation in Surfactant Films

Nowadays, *in vitro* experiments in surfactant films are able to imitate quasi-perfectly the tenso-activity of the pulmonary surfactant system at physiological conditions. Consequently, this makes it possible to address pertinent inquiries with reference to the *in situ* response of the pulmonary surfactant system during the successive compression-expansion that is undergone during the breathing process. For instance, Langmuir-Wilhelmy experiments can characterise the tenso-activity capability of a surfactant film in an air-liquid interface [45]. To do so, a controlled amount of surfactants are deposited on an air-water interface of area A, which is controlled by a mobile piston at one side, and by a fixed point

(Wilhelmy plate) at the other side. Then, using the Wilhelmy equation,

$$\gamma = \frac{f}{l\cos(\theta)}, \tag{1.2}$$

the surface tension γ of the air-liquid interface plus the surfactant films is obtained from the wetting forces f on the Wilhelmy plate, the length of the Wilhelmy plate l, and the contact angle θ between and the plate and the water. Thus, the surface pressure $\pi = \gamma_0 - \gamma$, is defined as the surface tension of the interface without the surfactant film[4] (γ_0) minus the surface tension γ. Therefore, in this way the surface pressure, or equivalently, the surface tension can be very easily controlled versus the area A. Albeit, some inconveniences may arise when using compression-expansion rates similar to those of the pulmonary surfactant system ($\sim 15-20$ cycles per minute); it is known that high rates induce uncontrolled leaks of surfactants (lipids) into the aqueous hypophase, which yields non reliable measurements.

Alternatively, air bubble experiments also characterise the tenso-activity capability of a surfactant film in an air-liquid interface while trying to minimise geometrical differences with the native pulmonary surfactant system. For this, an air bubble is immersed in a water chamber and is forced to change its radius, either directly (using a capillary to change the air pressure) [46] or indirectly (changing the hydrodynamic pressure of water) [47, 48]. Then the surface tension is measured from the radius of curvature of the bubble and the pressure difference inside and outside of the bubble by using the Young-Laplace Eq. (1.1), or its modification to allow for gravity and buoyancy forces [47, 48]. Thus, these techniques overcome leakage problems (in particular, techniques [47, 48]) and yield very efficient compression-expansion rates.

Based on these techniques, experiments in compression of surfactant films under isothermal ($T = 298\ K$) compression rates (typically used 20 cm^2/min) show a progressive reduction of the surface tension of an air-liquid interface by the presence of DPPC films, up to surface tensions $\approx 1\ mN/m$ [49–52]. At that stage, DPPC molecules are in their minimum area per lipid ($\approx 0.5\ nm^2$), presenting $\sim 100\%$ of their acyl chains in a *tilted* configuration. So further compressions lead to the collapse (breakdown) of the surfactant film [49–52]. Consequently, notice from Fig. 1.4 that the derivative of the surface tension isotherm of a DPPC monolayer during compression-expansion, or any surfactant film in general, is not the same at all areas per lipid [49–52], meaning that the surface tension reduction depends strongly on the concentration of surfactant molecules. Hence, it is not strange that surfactant films in expanded (LE) and condensed (LC) liquid state may present different

[4] For air-water interfaces at room temperature $\gamma_0 = 70$ mN/m.

surface tension derivatives, except when $LC - LE$ liquid coexistence, then the surface tension derivative must be null (according to the thermodynamic definition of coexistence). Notwithstanding this fact, at regions of $LC - LE$ liquid coexistence the surface tension derivative is different from zero [49–52], which seems to suggest that all surface tensions reported so far in the literature have been calculated for monolayers in a non-equilibrium state.

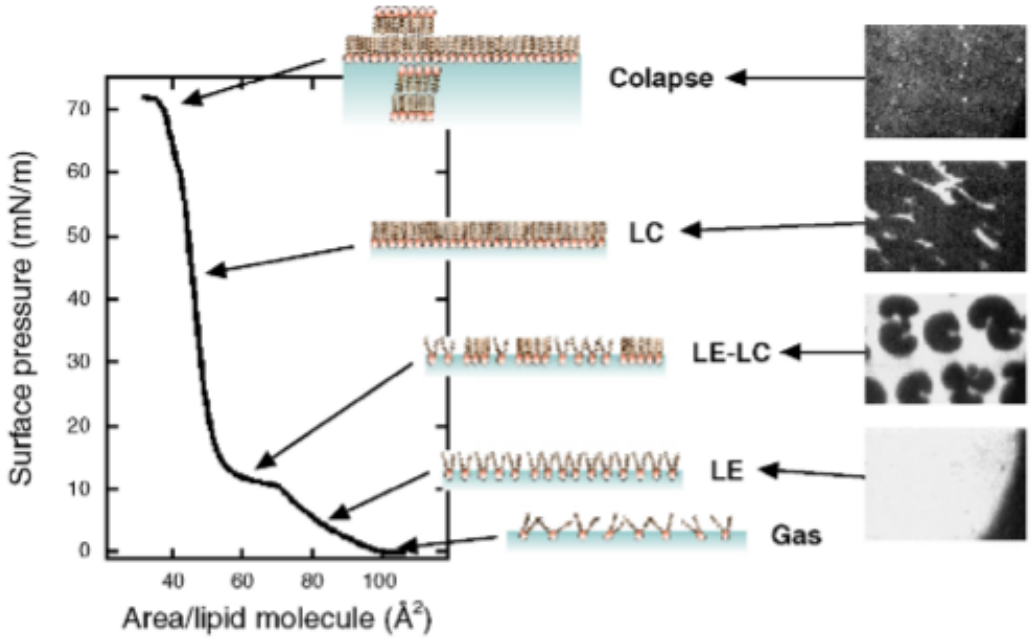

Figure 1.4: Surface pressure-area per lipid isotherm of a DPPC monolayer at 297 K. Figure taken from Ref. [51].

A further very interesting topic concerns the aspect of the LC and LE phases, where the multiple LC domains are heterogeneously distributed within the LE phase, and whose size, morphology (see Fig. 1.5) and number depend on the available area per lipid [50, 53–57]. These lateral heterogeneities resemble similar patterns found in a wide range of systems [58–61], where it has been postulated these patterns are thermodynamically stables and modulate the behaviour of the system under study [58]. Thereby, lateral heterogeneities of surfactant films have been proposed to be thermodynamically stables [62], and necessary to modulate the main properties of pure lipid monoalyers [51], bilayers [63] and simplified models of pulmonary surfactant [14]; diffusion coefficient, bending rigidity, permeability and lateral arrangement [14, 64]. But the truth is that at the present there is not a clear view of this phenomenon, thus we believe that fundamental questions like, "*Are LC domains really thermodynamically stable or do they coalesce instead?*" should be revisited.

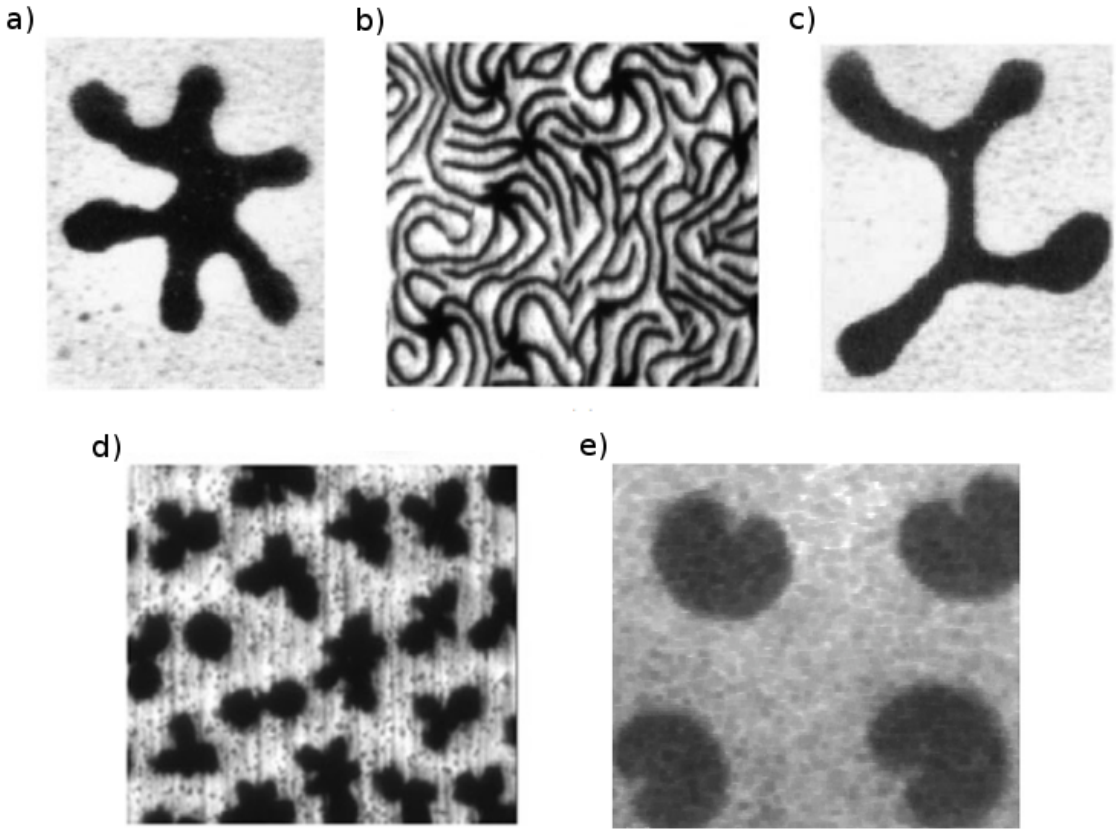

Figure 1.5: Typical domain morphologies found in different surfactant films: images in panels a) and c) are obtained from Ref. [65], b) and d) from Ref. [62] and e) from Ref. [66].

1.3 Dynamics within Surfactant Membranes

The respreading of squeezed-out lipids and proteins on film expansion from the surfactant reservoirs (mainly membranes) has widely been investigated in experiments [14]. Their dynamic properties are found to depend on composition, orientation of the lipids and presence of macromolecules [67, 68]. Theoretically, one of the most recognised contributions in dynamics within lipid membranes dates from 1975. In pioneer works, the physicists Saffman and Delbrück provided a theoretical foundation for predicting the dynamics of transmembrane proteins [69]. In the Saffman-Delbrück modelling, a transmembrane protein is considered as a cylinder of radius a and height h. This protein is inserted in an infinite lipid membrane, which spans the $x-y$ plane, confined between the planes $z = 0$ and $z = -h$, and immersed in a 3D solvent (see Fig. 1.6).

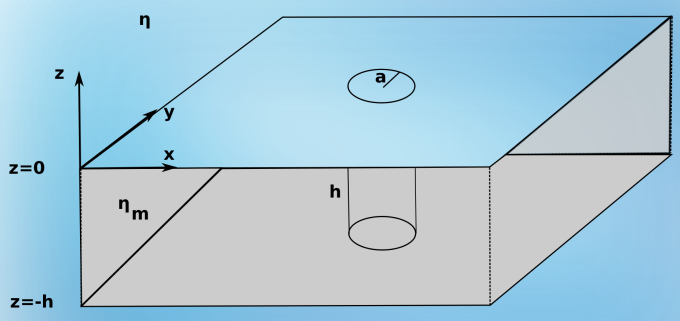

Figure 1.6: Saffman and Delbrück modelling of a transmembrane protein of radius a and height h in a lipid membrane of width h. A lipid membrane is considered a continuum medium with dynamic viscosity η_m (in surface poise $sP \equiv$ P· m) that is surrounded by a continuum solvent with dynamic viscosity η.

Within this approach, a lipid membrane is considered as a continuous fluid with characteristic dynamic viscosity η_m, which is much larger than the solvent dynamic viscosity η, *i.e.* $\eta_m \gg \eta$. In the Stokes flow approximation, Saffman and Delbrück found that the (long-time) self-diffusion coefficient of a transmembrane protein is given by

$$D \approx \frac{k_B T}{4\pi\eta_m h}\left[\ln\left(2L_{SD}/a\right) - 0.577\right], \tag{1.3}$$

with $k_B T$ representing the thermal energy, $L_{SD} = \frac{\eta_m}{2\eta}$ the Saffman-Delbück characteristic length scale and $a \ll L_{SD}$. Using typical values for $\eta_m \approx 0.1-10\times10^{-6}$ $P{\cdot}cm$ [70, 71] and the viscosity of water at 298 K ($\eta \approx 1$ cP) one finds $L_{SD} \approx 0.1-10$ μm, so that the applicability of Eq. (1.3) for transmembrane proteins ($a \approx 1-10$ nm) is ensured. Recently, computer simulations have demonstrated the validity of the Saffman-Delbück theory for membrane proteins [72]. Interestingly, even though the Saffman-Delbück theory was originally developed for transmembrane proteins, computer simulations have also shown the validity of

the Saffman-Delbück theory on lipids [73, 74]. This has been proved by the estimation of the self-diffusion coefficient of lipids in periodic systems. In addition, experiments have validated the Saffman-Delbück theory for nanometric to nearly micrometric lipid domains [70, 71], while smaller domains are much more controversial in this respect. Experiments in bilayers have proved a non-lineal dependence of the self-diffusion coefficient of lipids on the inverse of the bilayer width, $1/h$ [75].

At short times, the dynamic properties of membrane lipids are even more intriguing. Specifically, studies have discovered that the self-diffusion coefficient of lipids surprisingly differs at short-times from long-times by two orders of magnitude; empirical techniques such as quasi-elastic neutron scattering, nuclear magnetic resonance and electron spin resonance have predicted a short-time self-diffusion coefficient of lipids $D_0 \approx 10^{-6}\ cm^2/s$ [76, 77], whereas fluorescence recovery after photobleaching has predicted a long-time self-diffusion coefficient $D_s^{(l)} \approx 10^{-8}\ cm^2/s$ [76–79]. Theoretical and experimental investigations have linked the discrepancies between these two values with the presence of fast and coherent (collective) motion of lipids at short-times [80–85]. Some indications suggest the collective motion of lipids at short-times may be encouraged by the intrinsic hydrodynamics of membranes [80, 84, 85], even though how it takes place precisely and under which circumstances is still puzzling.

1.4 Outline

During this thesis we address fundamental questions regarding the lateral features of different amphipathic structures, questions closely linked to the pulmonary surfactant system. In chapter 2 we introduce the theoretical basis of this thesis and we present our contributions in the rest of the chapters. We divide the latter chapters into two parts: these correspond to chapter 3 and chapters 4-6.

In the first part of this thesis (chapter 3) we analyse the structural properties of surfactant films. In particular, we study the properties of lipids as well as the properties of expanded and condensed liquid domains of a DPPC monolayer in a vapour-water interface. For this study we perform state-of-the-art simulations. To analyse these lipids and domains, we present a new and accurate methodology. Finally, results are directly contrasted with experiments.

In the second part of this thesis we analyse the dynamics of confined particle systems in a liquid-liquid interface as well as the dynamics of membrane lipids, emphasising lipids and their collective dynamics. We start in chapter 4 with an extensive introduction to the

extraordinary phenomenology surrounding the dynamics of confined particle systems in liquid-liquid interfaces. To this purpose, we use a preliminary and idealised theory (non-interacting particles and strict confinements). Additionally, we develop an ultra fast algorithm to validate this theory. Then, in chapter 5 we relax ideal constraints as far as possible (interacting particles and soft confinements). For the study of this new scenario, we develop an alternative theory, and we verify it against simulations. Another advantage of this new theory is its compatibility with studies of the collective dynamics of lipids. In chapter 6 we study the collective dynamics of membrane lipids. In this study we perform simulations of lipid membranes using different models of lipids and different simulation techniques. Numerical results on the collective dynamics of lipids are compared to the theory developed in chapter 5 and available data on experiments and simulations.

Towards the end, in chapter 7, we summarise and discuss all the results produced by the research leading to this thesis. In the same way, we discuss the remaining open questions and their possible implications. Eventually, we speculate about future research that may emerge from this thesis.

Bibliography

[1] J. Lombard, *Once upon a time the cell membranes: 175?years of cell boundary research*, Biology Direct **9**, 32 (2014).

[2] N. W., *Ein osmotischer versuch*, International journal of research in physical chemistry and chemical physics **6U**, 37 (1890).

[3] E. Overton, *The probable origin and physiological significance of cellular osmotic properties*, Papers on biological membrane structure pp. 45–52 (1968).

[4] E. Gorter and F. Grendel, *On bimolecular layers of lipoids on the chromocytes of the blood*, J. Exp. Med. **41**, 439 (1925).

[5] W. D. Halliburton and W. M. Friend, *The stromata of the red corpuscles*, J. Physiol. **10**, 532 (1889).

[6] E. Jorpes, *The protein component of the erythrocyte membrane or stroma*, Biochem. J. **26**, 1488 (1932).

[7] S. J. Singer and G. L. Nicolson, *The fluid mosaic model of the structure of cell membranes*, Science **175**, 720 (1972).

[8] R. S. Bar, D. W. Deamer, and D. G. Cornwell, *Surface area of human erythrocyte lipids: Reinvestigation of experiments on plasma membrane*, Science **153**, 1010 (1966).

[9] H. H. Ussing, *Transport of ions across cellular membranes*, Physiological reviews **29**, 127 (1949).

[10] A. Bangham, M. Standish, and J. Watkins, *Diffusion of univalent ions across the lamellae of swollen phospholipids*, Journal of Molecular Biology **13**, 238 (1965).

[11] J. Lenard and S. J. Singer, *Protein conformation in cell membrane preparations as studied by optical rotatory dispersion and circular dichroism*, Proceedings of the National Academy of Sciences **56**, 1828 (1966).

[12] D. Branton, *Fracture faces of frozen membranes*, Proceedings of the National Academy of Sciences **55**, 1048 (1966).

[13] J. D. Robertson, *New observations on the ultrastructure of the membranes of frog peripheral nerve fibers*, J. Biophys. Biochem. Cytol. **3**, 1043 (1957).

[14] E. Parra and J. Pérez-Gil, *Composition, structure and mechanical properties define performance of pulmonary surfactant membranes and films*, Chemistry and Physics of Lipids **185**, 153 (2015).

[15] J. Pérez-Gil and K. M. Keough, *Interfacial properties of surfactant proteins*, Biochimica et Biophysica Acta (BBA) - Molecular Basis of Disease **1408**, 203 (1998).

[16] J. Pérez Gil, *El sistema surfactante pulmonar*, Investigación y Ciencia: Edición Española de Scientific American pp. 38–45 (2010).

[17] T. Xiang and B. Anderson, *Phase structures of binary lipid bilayers as revealed by permeability of small molecules*, Biochimica et biophysica acta **1370**, 64—76 (1998).

[18] R. W. Evans, *Aggregates of saturated phospholipids at the air-water interface*, Chemistry and Physics of Lipids **78**, 163 (1995).

[19] H. J. Risselada and S. J. Marrink, *The molecular face of lipid rafts in model membranes*, Proceedings of the National Academy of Sciences **105**, 17367 (2008).

[20] G. W. Feigenson, *Phase diagrams and lipid domains in multicomponent lipid bilayer mixtures*, Biochimica et Biophysica Acta (BBA) - Biomembranes **1788**, 47 (2009).

[21] L. Bagatolli and P. B. Sunil Kumar, *Phase behavior of multicomponent membranes:*

Experimental and computational techniques, Soft Matter **5**, 3234 (2009).

[22] Y. Zhang, A. Lervik, J. Seddon, and F. Bresme, *A coarse-grained molecular dynamics investigation of the phase behavior of dppc/cholesterol mixtures*, Chemistry and Physics of Lipids **185**, 88 (2015).

[23] S. Baoukina, L. Monticelli, H. J. Risselada, S. J. Marrink, and D. P. Tieleman, *The molecular mechanism of lipid monolayer collapse*, Proceedings of the National Academy of Sciences **105**, 10803 (2008).

[24] J. A. Clements, *Functions of the alveolar lining*, American Review of Respiratory Disease **115**, 67 (1977).

[25] J. Watkins, *The surface properties of pure phospholipids in relation to those of lung extracts*, Biochimica et Biophysica Acta (BBA) - Lipids and Lipid Metabolism **152**, 293 (1968).

[26] J. Johansson and T. Curstedt, *Molecular structures and interactions of pulmonary surfactant components*, European Journal of Biochemistry **244**, 675 (2004).

[27] J. Johansson and T. Curstedt, *Molecular structures and interactions of pulmonary surfactant components*, European Journal of Biochemistry **244**, 675 (1997).

[28] T. R. Korfhagen, A. M. LeVine, and J. A. Whitsett, *Surfactant protein a (sp-a) gene targeted mice*, Biochimica et Biophysica Acta (BBA) - Molecular Basis of Disease **1408**, 296 (1998).

[29] A. Cruz, C. Casals, K. M. W. Keough, and J. Pérez-Gil, *Different modes of interaction of pulmonary surfactant protein sp-b in phosphatidylcholine bilayers*, Biochemical Journal **327**, 133 (1997).

[30] A. Cruz, L.-A. Worthman, A. G. Serrano, C. Casals, K. M. W. Keough, and J. Pérez-Gil, *Microstructure and dynamic surface properties of surfactant protein sp-b/dipalmitoylphosphatidylcholine interfacial films spread from lipid-protein bilayers*, European Biophysics Journal **29**, 204 (2000).

[31] S. Baoukina and D. P. Tieleman, *Direct simulation of protein-mediated vesicle fusion: Lung surfactant protein b*, Biophysical Journal **99**, 2134 (2010).

[32] S. Baoukina and D. Tieleman, *Lung surfactant protein sp-b promotes formation of bilayer reservoirs from monolayer and lipid transfer between the interface and subphase*, Biophysical Journal **100**, 1678 (2011).

[33] M. Ross, S. Krol, A. Janshoff, and H.-J. Galla, *Kinetics of phospholipid insertion into monolayers containing the lung surfactant proteins sp-b or sp-c*, European Biophysics Journal **31**, 52 (2002)

[34] L. A. Creuwels, E. H. Boer, R. A. Demel, L. M. van Golde, and H. P. Haagsman, *Neutralization of the positive charges of surfactant protein c. effects on structure and function*, Journal of Biological Chemistry **270**, 16225 (1995).

[35] A. Gericke, C. Flach, and R. Mendelsohn, *Structure and orientation of lung surfactant sp-c and l-alpha-dipalmitoylphosphatidylcholine in aqueous monolayers*, Biophysical Journal **73**, 492 (1997).

[36] B. Olmeda, B. García-Álvarez, and J. Pérez-Gil, *Structure–function correlations of pulmonary surfactant protein sp-b and the saposin-like family of proteins*, European Biophysics Journal **42**, 209 (2013).

[37] S. E. Wert, J. A. Whitsett, and L. M. Nogee, *Genetic disorders of surfactant dysfunction*, Pediatric and Developmental Pathology **12**, 253 (2009).

[38] J. C. Clark, S. E. Wert, C. J. Bachurski, M. T. Stahlman, B. R. Stripp, T. E. Weaver, and J. A. Whitsett, *Targeted disruption of the surfactant protein b gene disrupts surfactant homeostasis, causing respiratory failure in newborn mice*, Proceedings of the National Academy of Sciences **92**, 7794 (1995).

[39] K. R. Melton, L. L. Nesslein, M. Ikegami, J. W. Tichelaar, J. C. Clark, J. A. Whitsett, and T. E. Weaver, *Sp-b deficiency causes respiratory failure in adult mice*, American Journal of Physiology-Lung Cellular and Molecular Physiology **285**, L543 (2003).

[40] S. W. Glasser, A. P. Senft, J. A. Whitsett, M. D. Maxfield, G. F. Ross, T. R. Richardson, D. R. Prows, Y. Xu, and T. R. Korfhagen, *Macrophage dysfunction and susceptibility to pulmonary pseudomonas aeruginosa infection in surfactant protein c-deficient mice*, J. Immunol. **181**, 621 (2008).

[41] W. E. Lawson, V. V. Polosukhin, G. T. Stathopoulos, O. Zoia, W. Han, K. B. Lane, B. Li, E. F. Donnelly, G. E. Holburn, K. G. Lewis, et al., *Increased and prolonged pulmonary fibrosis in surfactant protein c-deficient mice following intratracheal bleomycin*, The American Journal of Pathology **167**, 1267 (2005).

[42] S. Han and R. K. Mallampalli, *The role of surfactant in lung disease and host defense against pulmonary infections*, Ann. Am. Thorac. Soc. **12**, 765 (2015).

[43] J. Perez-Gil and T. E. Weaver, *Pulmonary surfactant pathophysiology: Current models and open questions*, Physiology **25**, 132 (2010).

[44] E. Namati, J. Thiesse, J. de Ryk, and G. McLennan, *Alveolar dynamics during respiration*, American Journal of Respiratory Cell and Molecular Biology **38**, 572 (2008).

[45] J. A. Clements, *Surface tension of lung extracts*, Proceedings of the Society for Experimental Biology and Medicine **95**, 170 (1957).

[46] G. Enhorning, *Pulsating bubble technique for evaluating pulmonary surfactant*, Journal of Applied Physiology **43**, 198 (1977).

[47] G. Putz, J. Goerke, S. Schurch, and J. A. Clements, *Evaluation of pressure-driven captive bubble surfactometer*, Journal of Applied Physiology **76**, 1417 (1994).

[48] S. Schurch, H. Bachofen, J. Goerke, and F. Possmayer, *A captive bubble method reproduces the in situ behavior of lung surfactant monolayers*, Journal of Applied Physiology **67**, 2389 (1989).

[49] B. Piknova, W. R. Schief, V. Vogel, B. M. Discher, and S. B. Hall, *Discrepancy between phase behavior of lung surfactant phospholipids and the classical model of surfactant function*, Biophysical Journal **81**, 2172 (2001).

[50] J. Pérez-Gil, K. Nag, S. Taneva, and K. Keough, *Pulmonary surfactant protein sp-c causes packing rearrangements of dipalmitoylphosphatidylcholine in spread monolayers*, Biophysical Journal **63**, 197 (1992).

[51] R. Wüstneck, J. Perez-Gil, N. Wüstneck, A. Cruz, V. Fainerman, and U. Pison, *Interfacial properties of pulmonary surfactant layers*, Advances in Colloid and Interface Science **117**, 33 (2005).

[52] Y. Y. Zuo, E. Keating, L. Zhao, S. M. Tadayyon, R. A. Veldhuizen, N. O. Petersen, and F. Possmayer, *Atomic force microscopy studies of functional and dysfunctional pulmonary surfactant films. i. micro- and nanostructures of functional pulmonary surfactant films and the effect of sp-a*, Biophysical Journal **94**, 3549 (2008).

[53] K. Ekelund, E. Sparr, J. Engblom, H. Wennerström, and S. Engström, *An afm study of lipid monolayers. 1. pressure-induced phase behavior of single and mixed fatty acids*, Langmuir **15**, 6946 (1999).

[54] E. Sparr, K. Ekelund, J. Engblom, S. Engström, and H. Wennerström, *An afm study of lipid monolayers. 2. effect of cholesterol on fatty acids*, Langmuir **15**, 6950 (1999).

[55] C. W. McConlogue and T. K. Vanderlick, *A close look at domain formation in dppc monolayers*, Langmuir **13**, 7158 (1997).

[56] P. Dhar, E. Eck, J. N. Israelachvili, D. W. Lee, Y. Min, A. Ramachandran, A. J. Waring, and J. A. Zasadzinski, *Lipid-protein interactions alter line tensions and domain size distributions in lung surfactant monolayers*, Biophys. J. **102**, 56 (2012).

[57] A. K. Sachan and J. A. Zasadzinski, *Interfacial curvature effects on the monolayer morphology and dynamics of a clinical lung surfactant*, Proceedings of the National Academy of Sciences **115**, E134 (2018).

[58] M. Seul and D. Andelman, *Domain shapes and patterns: The phenomenology of modulated phases*, Science **267**, 476 (1995).

[59] Q. Ouyang and H. L. Swinney, *Transition from a uniform state to hexagonal and striped turing patterns*, Nature **352**, 610 EP , (1991).

[60] R. Huebener, *Dynamics of magnetic flux structures in superconductors*, Physics Reports **13**, 143 (1974).

[61] E. Bodenschatz, J. R. de Bruyn, G. Ahlers, and D. S. Cannell, *Transitions between patterns in thermal convection*, Phys. Rev. Lett. **67**, 3078 (1991)

[62] F. Campelo, A. Cruz, J. Pérez-Gil, L. Vázquez, and A. Hernández-Machado, *Phase-field model for the morphology of monolayer lipid domains*, The European Physical Journal E **35**, 49 (2012).

[63] M. R. Nussio, N. H. Voelcker, M. J. Sykes, S. J. P. McInnes, C. T. Gibson, R. D. Lowe, J. O. Miners, and J. G. Shapter, *Lateral heterogeneities in supported bilayers from pure and mixed phosphatidylethanolamine demonstrating hydrogen bonding capacity*, Biointerphases **3**, 96 (2008).

[64] J. Pérez-Gil, *Structure of pulmonary surfactant membranes and films: The role of proteins and lipid–protein interactions*, Biochimica et Biophysica Acta (BBA) - Biomembranes **1778**, 1676 (2008).

[65] K. Y. C. Lee and H. M. McConnell, *Quantized symmetry of liquid monolayer domains*, The Journal of Physical Chemistry **97**, 9532 (1993).

[66] K. Klopfer and T. Vanderlick, *Isotherms of dipalmitoylphosphatidylcholine (dppc) monolayers: Features revealed and features obscured*, Journal of Colloid and Interface Science **182**, 220 (1996).

[67] C. Alonso, A. Waring, and J. A. Zasadzinski, *Keeping lung surfactant where it belongs: Protein regulation of two-dimensional viscosity*, https://doi.org/10.1529/biophysj.104.052092 Biophysical Journal **89**, 266 (2005).

[68] R. Wüstneck, J. Perez-Gil, N. Wüstneck, A. Cruz, V. Fainerman, and U. Pison, *Interfacial properties of pulmonary surfactant layers*, http://www.sciencedirect.com/science/article/pii/S0001868605000801 Advances in Colloid and Interface Science **117**, 33 (2005).

[69] P. G. Saffman and M. Delbrück, *Brownian motion in biological membranes*, Proceedings of the National Academy of Sciences **72**, 3111 (1975).

[70] E. P. Petrov and P. Schwille, *Translational diffusion in lipid membranes beyond the saffman-delbrück approximation*, Biophysical Journal **94**, L41 (2008).

[71] P. Cicuta, S. L. Keller, and S. L. Veatch, *Diffusion of liquid domains in lipid bilayer membranes*, The Journal of Physical Chemistry B **111**, 3328 (2007).

[72] B. A. Camley, M. G. Lerner, R. W. Pastor, and F. L. H. Brown, *Strong influence of periodic boundary conditions on lateral diffusion in lipid bilayer membranes*, The Journal of Chemical Physics **143**, 243113 (2015).

[73] M. Vögele, J. Köfinger, and G. Hummer, *Hydrodynamics of diffusion in lipid membrane simulations*, Phys. Rev. Lett. **120**, 268104 (2018).

[74] M. Vögele and G. Hummer, *Divergent diffusion coefficients in simulations of fluids and lipid membranes*, The Journal of Physical Chemistry B **120**, 8722 (2016).

[75] W. L. Vaz and H. Dieter, *Experimental evidence against the applicability of the saffman-delbrück model to the translational diffusion of lipids in phosphatidylcholine bilayer membranes*, FEBS Letters **152**, 287 (1983).

[76] J.-F. Tocanne, L. Dupou-Cézanne, and A. Lopez, *Lateral diffusion of lipids in model and natural membranes*, Progress in Lipid Research **33**, 203 (1994).

[77] W. Vaz and P. Almeida, *Microscopic versus macroscopic diffusion in one-component fluid phase lipid bilayer membranes*, Biophysical Journal **60**, 1553 (1991).

[78] K. Jacobson, *Lateral diffusion in membranes*, Cell Motility **3**, 367 (1983).

[79] P. F. F. Almeida, W. L. C. Vaz, and T. E. Thompson, *Lateral diffusion in the liquid phases of dimyristoylphosphatidylcholine/cholesterol lipid bilayers: a free volume analysis*,

Biochemistry **31**, 6739 (1992).

[80] G. S. Ayton and G. A. Voth, *Mesoscopic lateral diffusion in lipid bilayers*, Biophysical Journal **87**, 3299 (2004).

[81] M. C. Rheinstädter, J. Das, E. J. Flenner, B. Brüning, T. Seydel, and I. Kosztin, *Motional coherence in fluid phospholipid membranes*, Phys. Rev. Lett. **101**, 248106 (2008).

[82] C. L. Armstrong, M. Trapp, J. Peters, T. Seydel, and M. C. Rheinstadter, *Short range ballistic motion in fluid lipid bilayers studied by quasi-elastic neutron scattering*, Soft Matter **7**, 8358 (2011).

[83] S. Busch, C. Smuda, L. C. Pardo, and T. Unruh, *Molecular mechanism of long-range diffusion in phospholipid membranes studied by quasielastic neutron scattering*, Journal of the American Chemical Society **132**, 3232 (2010).

[84] E. Falck, T. Róg, M. Karttunen, and I. Vattulainen, *Lateral diffusion in lipid membranes through collective flows*, Journal of the American Chemical Society **130**, 44 (2008).

[85] T. Apajalahti, P. Niemelä, P. N. Govindan, M. S. Miettinen, E. Salonen, S.-J. Marrink, and I. Vattulainen, *Concerted diffusion of lipids in raft-like membranes*, Faraday Discuss. **144**, 411 (2010).

2

Theoretical Background, Computational Techniques and Force Fields

The main purpose of this chapter is to introduce the theoretical basis and the computational techniques we will use all through this thesis. To begin with, we will introduce the *Molecular Dynamics* (MD) technique, and we will continue with the *Brownian Dynamics* (BD) technique. After that, we will present the basics of the classical *Density Functional Theory* (DFT), and its natural extension to account for time-dependent systems, the *Dynamic Density Functional Theory* (DDFT), to finally reach to our real interest, the *Fluctuating Dynamic Density Functional Theory with Hydrodynamic Interactions* (FDDFT-HI). Additionally, we will briefly introduce the inertial coupling method to efficiently solve the dynamics of particles embedded in Newtonian fluids. Last, but not least, we will present the different models of lipids that we will make use of during this thesis.

2.1 Molecular Dynamics

Molecular Dynamics is a standard method for predicting the macroscopic properties and the time dependent behaviour of complex molecular systems. In the most common version, it consists in solving numerically Newton's equations for the position $\boldsymbol{q}$ of N particles

$$m_i \frac{d^2 \boldsymbol{q}_i}{dt^2} = \boldsymbol{F}_i \left(\boldsymbol{q}_1, \boldsymbol{q}_2 \cdots \boldsymbol{q}_N \right), \qquad i = 1 \ldots N, \tag{2.1}$$

given a total force on the i-th particle $\boldsymbol{F}_i = -\frac{\partial V(\boldsymbol{q}_1, \boldsymbol{q}_2 \cdots \boldsymbol{q}_N)}{\partial \boldsymbol{q}_i}$, with $V\left(\boldsymbol{q}_1, \boldsymbol{q}_2 \cdots \boldsymbol{q}_N \right)$ the potential energy of the system. Often, the potential energy is divided into four terms of the type

$$\begin{aligned} V\left(\boldsymbol{q}_1, \boldsymbol{q}_2 \cdots \boldsymbol{q}_N \right) = & \sum_{\text{bonds}} k_{\text{b}} (b - b_0)^2 + \sum_{\text{bends}} k_\theta (\theta - \theta_0)^2 + \sum_{\text{dihedrals}} k_\phi \left(1 + \cos(n\phi + \delta)\right) \\ & + \sum_{i,j} \left\{ \epsilon_{ij} \left[\left(\frac{\sigma_{ij}}{r_{ij}} \right)^{12} - \left(\frac{\sigma_{ij}}{r_{ij}} \right)^{6} \right] + \frac{q_{e_i} q_{e_j}}{4\pi\epsilon_0 \epsilon r_{ij}} \right\}, \end{aligned} \tag{2.2}$$

with the three first terms representing intramolecular interactions that are related to the bonds b, the valence angles θ and the dihedral angles ϕ (with multiplicity n and phase shift δ) of molecules, and with the parameters k_b, k_θ and k_ϕ the respective force constants. The latter term in Eq. (2.2) represents the nonbonded interactions, typically Lennard-Jones (LJ) and Coulomb types (with parameters interpreted in their usual meaning). The advantage of the MD technique is that it does not needed any assumptions regarding the mechanism/process to be investigated, *i.e.* one only requires the details about the set of parameters $\{b_0, \theta_0, n, \delta, \sigma_{ij}, \epsilon_{ij}, \epsilon, q_{e_i}, q_{e_j}, k_b, k_\theta, k_\phi\}$, or *force field*, of a molecular system. Thus, results obtained from simulations allow for the direct comparison with experiments.

A standard method for the integration of Eq. (2.1) is the finite difference method. It consist in approximating the equation of motion of a particle by its temporal discretisation, which can be solved recursively in each time step. Nevertheless, because of the wide range of time scales involved in MD (from particle collisions to diffusion of macromolecules), the time step is needed to be small (to accommodate all time scales), which hinders the approach of the long-time regime in large systems.

From the theoretical point of view, it is pointless to perform double precision calculations with the aim of evaluating the exact trajectories of the particles; any infinitesimal change in the trajectory of a particle with respect to the real trajectory (the one we would have if we had infinite numerical precision) results in a trajectory that exponentially separates

from the real one over time (due to molecular chaos). In fact, more important than the actual motion is the statistical *ensemble*[1] and the momentum conservation, which are the key to guarantee the correct thermodynamics and dynamics of the system. Hence, too little accuracy is not recommended either. Consequently, the success of a good MD algorithm is intimately related to the integration of the Eq. (2.1), which depends on a delicate balance between computer efficiency and accuracy.

Two examples of the most common, reliable and accurate integration algorithms are leap-frog and velocity-Verlet. Both algorithms are second order (in terms of finite-difference methods), reversible (invariant under time reversal) as well as symplectic[2], but with the subtle difference that, while in the velocity-Verlet algorithm both positions and velocities are given at the same time-step, in the leap-frog algorithm they are not, *i.e.* velocities $\boldsymbol{v}$ and positions $\boldsymbol{q}$ are given at times $t - \frac{\Delta t}{2}$ and t,

$$\boldsymbol{v}_i\left(t + \frac{\Delta t}{2}\right) = \boldsymbol{v}_i\left(t - \frac{\Delta t}{2}\right) + \boldsymbol{F}_i\left(t\right)\frac{\Delta t}{m}, \tag{2.3a}$$

$$\boldsymbol{q}_i\left(t + \Delta t\right) = \boldsymbol{q}_i\left(t\right) + \boldsymbol{v}_i\left(t + \frac{\Delta t}{2}\right)\Delta t. \tag{2.3b}$$

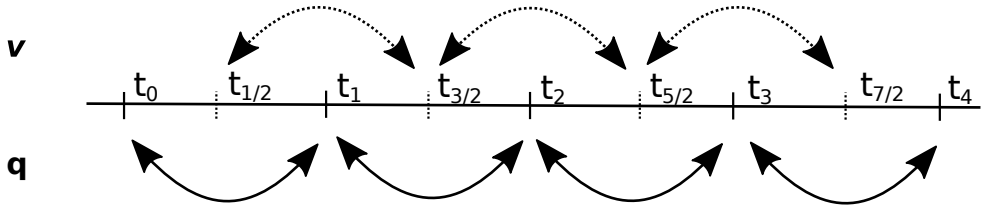

Figure 2.1: Representation of a leap-frog step.

The principal disadvantage of leap-frog integration algorithms is more than obvious (*e.g.* potential and kinetic energies are not defined at the same time-step), although they are more efficient than velocity-Verlet integration algorithms.

Usually, when performing MD simulations, one also needs the use of temperature and/or pressure control (thermostat and barostat respectively) in order to reproduce specific conditions [1–5]. To this end, the so-called Berendsen thermostat and Berendsen barostat are the most efficient; they relax a system from state A of pressure and temperature to a target

[1]The ensembles NVE, NPT, NVT and so forth are meant for simulations in which specific parameters are fixed. These can be: the number of particles N, volume V, pressure P, temperature T and so on.
[2]Symplectic implies that the algorithm conserves the energy, or more correctly, the Hamiltonian.

state B exponentially over the time [2]. However, we should be aware these types of thermostats and barostats do not reproduce the correct statistical ensemble *i.e.* they are only used for equilibration purposes. Conversely, to measure the equilibrium properties we must use thermostats and barostats that guarantee the correct statistical ensemble *e.g.* Nosé-Hoover thermostat and Parrinello-Rahman barostat [1, 3–5]. Notice though that some of these techniques do not preserve either local momentum or total momentum, leading to a wrong dynamical description [1, 3, 4].

2.2 Brownian Dynamics

Brownian Dynamics enable the description of the long-time regime of molecular systems (inertial terms are neglected), thus overcoming one of the most serious issues in MD simulations. It applies as far as there exists a clear time-scale separation; systems in which there exist slow dynamic processes compared to other (irrelevant) dynamic processes *e.g.* the diffusion of pollen grains compared to the equilibration of the velocity of the pollen grains by multiple collisions with their surroundings [6]. Alluding to the rapidly varying properties of fast processes, one can describe the dynamics of particles by means of a *Stochastic Differential Equation* of the form [7], this is

$$\gamma \frac{d\boldsymbol{q}_i}{dt} = \boldsymbol{F}_i\left(\boldsymbol{q}_1, \boldsymbol{q}_2 \cdots \boldsymbol{q}_N\right) + \boldsymbol{\xi}_i, \qquad i = 1 \ldots N. \tag{2.4}$$

From the physical perspective, we should understand the term $\boldsymbol{\xi}_i$ as a random variable that arises from the stochastic nature of the collisions among Brownian particles and solvent particles, while γ is a friction that Brownian particles experience due to the fact they are immersed in a solvent, and $\boldsymbol{F}_i$ is the total force on the i-th particle. Then, the stochastic term in Eq. (2.4) is required to satisfy the following properties

$$\left\langle \boldsymbol{\xi}_i\left(t\right)\right\rangle = \mathbf{0}, \tag{2.5a}$$

$$\left\langle \boldsymbol{\xi}_i\left(t\right)\boldsymbol{\xi}_j\left(t'\right)\right\rangle = 2\gamma k_B T \boldsymbol{\delta}_{ij}\boldsymbol{\delta}(t-t'). \tag{2.5b}$$

with k_B Boltzmann's constant, T the temperature, δ_{ij} the Kronecker delta and $\delta(t-t')$ the Dirac delta. Equation (2.5a) is justified under the pretext of the random nature of the variable $\boldsymbol{\xi}_i$ (collisions), while its correlation (Eq. (2.5b)) is imposed in order to ensure the correct equilibrium distribution (*fluctuation-dissipation* theorem [8]).

Using the Ito calculus one arrives at the particle position

$$\boldsymbol{q}_i\left(t+\Delta t\right)=\boldsymbol{q}_i\left(t\right)+\frac{\Delta t}{\gamma}\boldsymbol{F}_i(t)+\sqrt{2k_BT\frac{\Delta t}{\gamma}}\hat{\boldsymbol{\xi}}_i,\qquad i=1\ldots N, \tag{2.6}$$

where we have renormalised the noise term $\boldsymbol{\xi}_i$ *i.e.* $\hat{\boldsymbol{\xi}}_i$ has mean $\mu=0$ and variance $\sigma=1$.

Even though in BD simulations neither local momentum nor total momentum are conserved (due to the stochastic nature of the Brownian motion), we emphasise that this kind of methods yield thermodynamic properties that are consistent with the thermodynamic properties obtained by means of MD simulations. As an interesting note, we would like to remark that the kinetic temperature T is ill-defined if one tries to calculate it from the average velocity ($\boldsymbol{v}=\frac{\boldsymbol{q}_i(t+\Delta t)-\boldsymbol{q}_i(t)}{\Delta t}$), *i.e.* if we consider (just for the sake of clarity) the case of ideal particles ($\boldsymbol{F}_i=0$), from Eq. (2.6) we can derive that the average velocity $\boldsymbol{v}\propto\Delta t^{-1/2}$. This means that the average velocity of the particles depends on the time step Δt, and so does the kinetic energy, and consequently the temperature. Notwithstanding the peculiar behaviour of this limit notice that in truth the equilibrium temperature of the system is well defined by construction (see Eq. (2.5b)).

2.3 Density Functional Theory

In the classical sense, DFT is a suitable tool to describe thermodynamic magnitudes as well as structural properties of inhomogeneous fluids that are unreachable or roughly described by means of MD simulations *e.g.* free energy, surface tension and so on. Unlike MD techniques, all thermodynamic properties can be calculated from first principles *i.e.* from a thermodynamic energy, so that the control of relevant variables under study becomes much more intuitive. The key to DFT lies in the existence of a density distribution $\rho\left(\boldsymbol{r}\right)$ that unequivocally minimises the grand potential [9, 10] at a given external potential v_{ext} *i.e.* the external potential is also a functional of the density,

$$\Omega[\rho(\boldsymbol{r})]=F[\rho(\boldsymbol{r})]+\int\rho(\boldsymbol{r})\left(v_{\text{ext}}(\boldsymbol{r})-\mu\right)d\boldsymbol{r}, \tag{2.7}$$

where Ω stands for nothing more than the Legendre transformation of the Helmholtz free energy F ($F=U-TS$, with U the internal energy, T the temperature and S the entropy) with respect to the variables $-\mu N$, where μ stands for the chemical potential and N for

its conjugate variable (number of particles). Mathematically, it reads

$$\left.\frac{\delta\Omega\left[\rho\right]}{\delta\rho}\right|_{\rho=\rho_0} = 0, \tag{2.8a}$$

$$\Omega\left[\rho_0\right] = \Omega_0 \leq \Omega, \tag{2.8b}$$

where ρ_0 is the equilibrium density. Conveniently, one can always (without loss of generality) split up the total free energy into two contributions; one contribution coming from the ideal gas and another contribution that takes into account the intermolecular interactions (excess contribution), $F = F_{\text{id}} + F_{\text{exc}}$. While the ideal gas contribution of the free energy (F_{id}) and its functional derivative are always known exactly,

$$\beta F_{\text{id}}\left[\rho\right] = \int \rho\left(\boldsymbol{r}\right)\left[\ln\left(\Lambda^3\rho\left(\boldsymbol{r}\right)\right) - 1\right] d\boldsymbol{r}, \tag{2.9a}$$

$$\frac{\delta F_{\text{id}}}{\delta\rho\left(\boldsymbol{r}\right)} = \frac{1}{\beta}\ln\left[\Lambda^3\rho\left(\boldsymbol{r}\right)\right], \tag{2.9b}$$

with $\beta^{-1} \equiv k_B T$ the thermal energy and Λ the Broglie wavelength, the excess contribution and its functional derivative are analytically known only in a few cases [11]. Thus, the key for the success of DFT models depends on the distinct approximations made [12]. A standard way to proceed is to approximate the excess functional contribution F_{exc} taking advantage of the density functional relations

$$c^{(1)}\left(\boldsymbol{r}\right) = -\beta\frac{\delta F_{\text{exc}}\left[\rho\right]}{\delta\rho\left(\boldsymbol{r}\right)}, \tag{2.10-1}$$

$$\vdots$$

$$c^{(n)}\left(\boldsymbol{r}_1\cdots\boldsymbol{r}_n\right) = -\beta\frac{\delta c^{(n-1)}\left(\boldsymbol{r}_1\cdots\boldsymbol{r}_{n-1}\right)}{\delta\rho\left(\boldsymbol{r}_n\right)} = -\beta\frac{\delta^n F_{\text{exc}}\left[\rho\right]}{\delta\rho\left(\boldsymbol{r}_1\right)\cdots\delta\rho\left(\boldsymbol{r}_n\right)}. \tag{2.10-n}$$

Eventually, using Eqs. (2.10-1) (2.9b) and (2.8a), $\rho_0(\boldsymbol{r})$ can be obtained

$$\rho_0(\boldsymbol{r}) = \Lambda^{-3}\exp\left[-\beta\left(v_{\text{ext}} - \mu\right) + c^{(1)}\left(\boldsymbol{r}\right)\right], \tag{2.11}$$

although, it is more practical to approximate ρ_0 from the numerical minimisation of the excess contribution of the functional.

2.3.1 Dynamic Density Functional Theory

In this section we present the DDFT extension to the classical density functional theory for studying the relaxation dynamics of systems. The starting point is the microscopic density

$$\hat{\rho}(\boldsymbol{r},t) = \sum_{i=1}^{N} \delta\left[\boldsymbol{q}_i(t) - \boldsymbol{r}\right], \tag{2.12}$$

which is given by a sum of delta functions with these last centred at the position of particles. Then, one of the novelties is that the particles are assumed to be Brownian, so their dynamics are governed by Eqs. (2.4), (2.5a) and (2.5b). In doing so, the time evolution of Eq. (2.12) becomes stochastic.

Applying the Ito calculus to the microscopic density one obtains the following stochastic differential equation for its evolution

$$\begin{aligned}\frac{\partial\hat{\rho}(\boldsymbol{r},t)}{\partial t} = \nabla\cdot\Big[&\nabla\hat{\rho}(\boldsymbol{r},t) + \hat{\rho}(\boldsymbol{r},t)\,\nabla V_{\text{ext}}(\boldsymbol{r}) \\ &+ \hat{\rho}(\boldsymbol{r},t)\int \hat{\rho}(\boldsymbol{r}',t)\,\nabla V_{\text{int}}(\boldsymbol{r}-\boldsymbol{r}')\,d\boldsymbol{r}' \\ &+ \sqrt{\hat{\rho}(\boldsymbol{r},t)}\xi(\boldsymbol{r},t)\Big],\end{aligned} \tag{2.13}$$

with V_{int} and V_{ext} an intermolecular potential and an external potential respectively to which Brownian particles are subjected, $\sqrt{\hat{\rho}(\boldsymbol{r},t)}\xi(\boldsymbol{r},t)$ a multiplicative noise (depending on the position) and where we have taken natural units *i.e.* $\gamma = 1$ and temperature $T = 1$ [13]. Although mathematically the multiplicative noise term in Eq. (2.13) does not make a complete sense (and neither does Eq. (2.13)) [14], we know the (macroscopic) density that emerges from averaging over the random noise realisations, $\rho(\boldsymbol{r},t) \equiv \langle\hat{\rho}(\boldsymbol{r},t)\rangle$, provides a density evolution equation that makes perfect sense

$$\begin{aligned}\frac{\partial\rho(\boldsymbol{r},t)}{\partial t} = \nabla\cdot\Big[&\nabla\hat{\rho}(\boldsymbol{r},t) + \hat{\rho}(\boldsymbol{r},t)\,\nabla V_{\text{ext}}(\boldsymbol{r}) \\ &+ \int \langle\rho(\boldsymbol{r},t)\,\rho(\boldsymbol{r}',t)\rangle\,\nabla V_{\text{int}}(\boldsymbol{r}-\boldsymbol{r}')\,d\boldsymbol{r}'\Big].\end{aligned} \tag{2.14}$$

Notice that Eq. (2.14), as it is written, is nothing more than a continuity equation for the average density, in which the sources of density current are of entropic (first term), external (second term) and molecular (third term) origin. Thus, as one would expect, Eq. (2.14) reduces the Fick's second law when the external and the molecular forces vanish

(ideal particles),

$$\frac{\partial \rho(\boldsymbol{r},t)}{\partial t} = \nabla^2 \rho(\boldsymbol{r},t)\,. \tag{2.15}$$

Generally speaking, Eq. (2.14) is not closed since, in order to calculate the average density $\rho(\boldsymbol{r},t)$, we need its second moment $\rho^{(2)} = \langle \rho(\boldsymbol{r},t)\,\rho(\boldsymbol{r}',t)\rangle$. Although it is tempting to take the ideal gas approximation $\rho^{(2)} \approx \rho(\boldsymbol{r},t)\,\rho(\boldsymbol{r}',t)$ in order to close Eq. (2.14), in practice, this approach leads to a pathological behaviour of the density [13]. In contrast, a standard route that works reasonably well consists in: (1) assuming that the system is locally in equilibrium and (2) to truncating the Bogoliubov–Born–Green–Kirkwood–Yvon (BBGKY) chain at the n-th level and calculating $\rho^{(2)}$ from the n-th density moment approach $\rho^{(n)} \approx \rho(\boldsymbol{r}_1,t)\,\rho(\boldsymbol{r}_1,t)\ldots\rho(\boldsymbol{r}_{n-1},t)$.

Hence, to guarantee the use of these approximations one can always look for an external and unique potential $u(\boldsymbol{r})$ in such a way that it forces the system to be temporally in equilibrium [13]. In this way, and after some manipulation, one can find the following relations

$$\nabla\rho(\boldsymbol{r},t) + \rho(\boldsymbol{r},t)\,\nabla V_{\text{ext}}(\boldsymbol{r}) = \rho(\boldsymbol{r},t)\,\nabla\frac{\delta F_{\text{id}}[\rho(\boldsymbol{r}',t)]}{\delta\rho(\boldsymbol{r},t)}, \tag{2.16a}$$

$$\int \langle\rho(\boldsymbol{r},t)\,\rho(\boldsymbol{r}',t)\rangle\,\nabla V_{\text{int}}(\boldsymbol{r}-\boldsymbol{r}')\,d\boldsymbol{r}' = \rho(\boldsymbol{r},t)\,\nabla\frac{\delta F_{\text{exc}}[\rho(\boldsymbol{r},t)]}{\delta\rho(\boldsymbol{r},t)}, \tag{2.16b}$$

which finally lead to rewriting Eq. (2.14) into a more compact expression

$$\frac{\partial \rho(\boldsymbol{r},t)}{\partial t} = \nabla\cdot\left[\rho(\boldsymbol{r},t)\,\nabla\frac{\delta F[\rho(\boldsymbol{r},t)]}{\delta\rho(\boldsymbol{r},t)}\right]. \tag{2.17}$$

Again, Eq. (2.17) has the form of a continuity equation, $\frac{\partial\rho}{\partial t} + \nabla\cdot\boldsymbol{j} = 0$, but very interestingly, the density current in here is given by the density times the gradient of the functional derivative of the free energy with respect to the density,

$$\boldsymbol{j}(\boldsymbol{r},t) = -\rho(\boldsymbol{r},t)\,\nabla\frac{\delta F[\rho(\boldsymbol{r},t)]}{\delta\rho(\boldsymbol{r},t)}, \tag{2.18}$$

connecting so the DDFT and the DFT formalisms.

2.3.2 Fluctuating Dynamic Density Functional Theory with Hydrodynamic Interactions

The classical DDFT can be further extended to account for hydrodynamic interactions and *fluctuations*, whose result is known as the FDDFT-HI. The main idea behind this theory is analogous to that of the classical DDFT. This is to formulate an evolution equation for the macroscopic density that depends on the functional derivative of the free energy with respect to the density, but also including hydrodynamic interactions. To achieve this, in a way analogous to previous section, the starting point is the microscopic density (2.12), bearing in mind that the particles are now correlated. To be specific, let us consider a collection of N (correlated) particles that interact via a conservative forces $F_i = -\nabla_{\boldsymbol{q}_i} V(\boldsymbol{Q})$ ($\boldsymbol{Q} = \{\boldsymbol{q}_1, \cdots, \boldsymbol{q}_N\}$ stands for the set of the positions of the particles).

Then, the Ito equation associated with the *Fokker-Planck* equation for the probability density $P(\boldsymbol{Q}, t) = \nabla_{\boldsymbol{Q}} \cdot \{\boldsymbol{\mathcal{M}} [(\nabla_{\boldsymbol{Q}} V) P + (k_B T) \nabla_{\boldsymbol{Q}} P]\}$ of correlated Brownian particles is

$$d\boldsymbol{q}_i = -\boldsymbol{\mathcal{M}} (\nabla_{\boldsymbol{q}_i} V) dt + (2k_B T \boldsymbol{\mathcal{M}})^{1/2} \hat{\boldsymbol{\xi}}_i dt + k_B T (\nabla_{\boldsymbol{q}_i} \cdot \boldsymbol{\mathcal{M}}) dt, \quad i = 1 \dots N, \tag{2.19}$$

where $\hat{\boldsymbol{\xi}}_i$ is an additive white noise whose mean $\mu = 0$ and variance $\sigma = 1$, $k_B T$ is the thermal energy, and $\boldsymbol{\mathcal{M}}$ is the mobility tensor, which is symmetric positive semi-definite and translationally-invariant,

$$\boldsymbol{\mathcal{M}} (\boldsymbol{q}_i, \boldsymbol{q}_j) = \boldsymbol{\mathcal{M}} (\boldsymbol{r} = \boldsymbol{q}_i - \boldsymbol{q}_j) = f(r) \boldsymbol{I} + g(r) \frac{\boldsymbol{r} \otimes \boldsymbol{r}}{r^2}, \tag{2.20}$$

with $f(r)$ and $g(r)$ functions that depend on the type of mobility, and $\otimes$ the dyadic product. In this way, we also introduce the self-diffusion coefficient as $\boldsymbol{D}_s (\boldsymbol{r}) = (k_B T) \boldsymbol{\mathcal{M}} (\boldsymbol{q}_i, \boldsymbol{q}_i) = D_s \boldsymbol{I}$, $\boldsymbol{I}$ being the identity matrix. Then, comparing Eq. (2.19) with Eq. (2.6) we notice the presence of the extra term $k_B T (\nabla_{\boldsymbol{q}_i} \cdot \boldsymbol{\mathcal{M}}) dt$, which is necessary for the time-reversibility of the associated Fokker-Planck equation. Nevertheless, for standard fluids this term usually vanishes (incompressible fluids), and in the ideal approximation, Eq. (2.19) leads to a macroscopic density that is described by the familiar Fickean diffusion equation [14, 15].

Applying the Ito calculus to the microscopic density the following advection-diffusion

equation for the microscopic density can be found [14, 15],

$$\begin{aligned}\frac{\partial\hat{\rho}(\boldsymbol{r},t)}{\partial t} =& -\nabla\cdot(\boldsymbol{\omega}(\boldsymbol{r},t)\,\hat{\rho}(\boldsymbol{r},t)) + \nabla\cdot(D_s(\boldsymbol{r})\,\nabla\hat{\rho}(\boldsymbol{r},t) + \nabla\cdot D_s(\boldsymbol{r})\,\hat{\rho}(\boldsymbol{r},t))\\ &+(k_BT)\,\nabla\cdot\left(\hat{\rho}(\boldsymbol{r},t)\int\boldsymbol{\mathcal{M}}(\boldsymbol{r}-\boldsymbol{r}')\,\nabla'\hat{\rho}(\boldsymbol{r}',t)\,d\boldsymbol{r}'\right)\\ &+\nabla\cdot\left(\hat{\rho}(\boldsymbol{r},t)\int\boldsymbol{\mathcal{M}}(\boldsymbol{r}-\boldsymbol{r}')\,\nabla' V_{\text{ext}}(\boldsymbol{r}')\,\hat{\rho}(\boldsymbol{r}',t)\,d\boldsymbol{r}'\right)\\ &+\nabla\cdot\left(\hat{\rho}(\boldsymbol{r},t)\int\boldsymbol{\mathcal{M}}(\boldsymbol{r}-\boldsymbol{r}')\,\nabla' V_{\text{int}}(\boldsymbol{r}',\boldsymbol{r}'')\,\hat{\rho}(\boldsymbol{r}',t)\,\hat{\rho}(\boldsymbol{r}'',t)\,d\boldsymbol{r}'d\boldsymbol{r}''\right)\end{aligned} \tag{2.21}$$

where V_{int} and V_{ext} are an intermolecular and an external potential respectively and $\boldsymbol{\omega}(\boldsymbol{r},t)$ is a random velocity field which emerges from the thermal fluctuations of the fluid velocity field. This random velocity field is white in time and has a spatial variance $\langle\boldsymbol{\omega}(\boldsymbol{r},t)\otimes\boldsymbol{\omega}(\boldsymbol{r},t')\rangle = 2k_BT\boldsymbol{\mathcal{M}}(\boldsymbol{q}_i,\boldsymbol{q}_j)\,\delta_{tt'}$.

Following the same reasoning as in the previous section, the average of the microscopic density over the noise realisations and the first members of the BBGKY hierarchy [14, 16] give rise to the macroscopic density time-evolution equation

$$\begin{aligned}\frac{\partial\rho(\boldsymbol{r},t)}{\partial t} =& \nabla\cdot(D_s(\boldsymbol{r})\,\nabla\rho(\boldsymbol{r},t)) + (k_BT)\,\nabla\cdot\left(\int\boldsymbol{\mathcal{M}}(\boldsymbol{r}-\boldsymbol{r}')\,\nabla'\rho^{(2)}(\boldsymbol{r},\boldsymbol{r}',t)\,d\boldsymbol{r}'\right)\\ &+\nabla\cdot\left((k_BT)^{-1}D_s(\boldsymbol{r})\,\nabla V_{\text{ext}}(\boldsymbol{r})\,\rho(\boldsymbol{r},t) + \int\boldsymbol{\mathcal{M}}(\boldsymbol{r}-\boldsymbol{r}')\,\nabla' V_{\text{ext}}(\boldsymbol{r}')\,\rho^{(2)}(\boldsymbol{r},\boldsymbol{r}',t)\,d\boldsymbol{r}'\right)\\ &+\nabla\cdot\left(\int\left[(k_BT)^{-1}D_s(\boldsymbol{r})\,\nabla V_{\text{int}}(\boldsymbol{r},\boldsymbol{r}') + \boldsymbol{\mathcal{M}}(\boldsymbol{r}-\boldsymbol{r}')\,\nabla' V_{\text{int}}(\boldsymbol{r},\boldsymbol{r}')\right]\rho^{(2)}(\boldsymbol{r},\boldsymbol{r}',t)\,d\boldsymbol{r}'\right)\\ &+\nabla\cdot\left(\int\boldsymbol{\mathcal{M}}(\boldsymbol{r}-\boldsymbol{r}')\,\rho^{(3)}(\boldsymbol{r},\boldsymbol{r}',\boldsymbol{r}'',t)\,\nabla' V_{\text{int}}(\boldsymbol{r}',\boldsymbol{r}'')\,d\boldsymbol{r}'d\boldsymbol{r}''\right),\end{aligned} \tag{2.22}$$

and eventually, Eq. (2.22) can be expressed in terms of the functional derivative of the free energy with respect to the density [14, 16],

$$\begin{aligned}\frac{\partial\rho(\boldsymbol{r},t)}{\partial t} =& (k_BT)^{-1}\nabla\cdot\left[D_s(\boldsymbol{r})\,\rho(\boldsymbol{r},t)\,\nabla\frac{\delta F[\rho(\boldsymbol{r},t)]}{\delta\rho(\boldsymbol{r},t)}\right]\\ &+\nabla\cdot\left[\int\boldsymbol{\mathcal{M}}(\boldsymbol{r}-\boldsymbol{r}')\,\rho^{(2)}(\boldsymbol{r},\boldsymbol{r}',t)\,\nabla'\frac{\delta F[\rho(\boldsymbol{r},t)]}{\delta\rho(\boldsymbol{r},t)}d\boldsymbol{r}'\right].\end{aligned} \tag{2.23}$$

Therefore, Eq. (2.23) yields a continuity equation with two sources of density current

$$\boldsymbol{j}_1(\boldsymbol{r},t) = -(k_B T)^{-1} D_s(\boldsymbol{r})\,\rho(\boldsymbol{r},t)\,\nabla\frac{\delta F[\rho(\boldsymbol{r},t)]}{\delta\rho(\boldsymbol{r},t)}, \tag{2.24a}$$

$$\boldsymbol{j}_2(\boldsymbol{r},t) = -\int \boldsymbol{\mathcal{M}}(\boldsymbol{r}-\boldsymbol{r}')\,\rho^{(2)}(\boldsymbol{r},\boldsymbol{r}',t)\,\nabla'\frac{\delta F[\rho(\boldsymbol{r},t)]}{\delta\rho(\boldsymbol{r},t)}d\boldsymbol{r}', \tag{2.24b}$$

one similar to the density current obtained in the DDFT formalism ($\boldsymbol{j}_1$), and another one originated from the hydrodynamic correlations ($\boldsymbol{j}_2$).

2.4 Inertial Coupling Method

From the numerical point of view, solvents can be grouped into two main categories regarding their degree of resolution: explicit and implicit solvents, and our interest in this section lies principally in the latter kind. Due to obvious reasons, the main advantage of this type of solvents is that they considerably reduce considerable the number of degrees of freedom of the system, which results in much more efficient simulations of particles in a fluid (saving up to 90% of the computational time compared to explicit solvents). Among other computational techniques [17–19], Eulerian-Lagrangian methods [20–23], also known as inertial coupling methods, solve the dynamics of solvent particles very efficiently by describing the solvent by means of the Navier-Stokes equations (continuum description), together with the dynamics of particles, which are described by Newton's or Hamilton's equations (discrete description). During this section, we will follow the inertial coupling method proposed for the graphics processor units (GPU) open-source solver FLUAM, which has been developed in our group [23–26].

The first set of equations, the Navier-Stokes equations, consist of two coupled non-linear partial differential equations, which correspond respectively to the mass and momentum conservation equations of the solvent

$$\frac{D}{Dt}\rho = -\rho\nabla\cdot\boldsymbol{u}, \tag{2.25a}$$

$$\rho\frac{D}{Dt}\boldsymbol{u} = -\nabla p + \nabla\cdot\boldsymbol{\sigma} + \rho\boldsymbol{F}_f, \tag{2.25b}$$

with $\frac{D}{Dt} \equiv \partial_t + \boldsymbol{u}\cdot\nabla$ the convective derivative operator, $\boldsymbol{u}$ the velocity field of the solvent, p the static or mechanical pressure, $\boldsymbol{\sigma} = \zeta(\nabla\cdot\boldsymbol{u})\boldsymbol{I} + \eta\left(\nabla\boldsymbol{u} + (\nabla\boldsymbol{u})^T - \frac{2}{3}(\nabla\cdot\boldsymbol{u})\boldsymbol{I}\right) + \boldsymbol{\xi}$ the stress tensor, $\boldsymbol{\xi}$ a stochastic flux that is originated by the thermal agitation and that fulfils

the fluctuation-dissipation balance [27–30], and $\boldsymbol{F}_f$ an external force that is exerted on the solvent *e.g.* gravity.

Then, (solute) particles are coupled to the solvent by making use of the immersed boundary method [20, 21], which is based on the followings trademark properties: first, the solvent dynamics are coupled to the particle dynamics by means of a Lagrange multiplier. Second, assuming that the particles are spheres of radius a, and that the solvent fills all the simulation domain (this is done for numerical stability reasons [20, 21]), the velocity of the solvent $\boldsymbol{u}$ in regions located inside a particle is forced to be equal to the velocity of the particles $\boldsymbol{v}$ (no-slip condition)

$$\boldsymbol{u}(\boldsymbol{r},t) = \boldsymbol{v}(t), \qquad \|\boldsymbol{r} - \boldsymbol{q}(t)\| \leq a. \tag{2.26}$$

By doing so, the density flux of solvent over the surface of the particle is null, $(\boldsymbol{v} - \boldsymbol{u}(a))\cdot\boldsymbol{n} = 0$ (density inside the particle is always constant), which allows one to interpret the solvent that is inside of the particle as a simple rescaling of the mass m of the particle

$$m = m_e + m_f, \tag{2.27}$$

where the mass m_e is defined as the excess mass with respect to the solvent mass m_f. Thus, a particle in a fluid is neutrally buoyant if $m_e = 0$, while $m_e < 0$ or $m_e > 0$ makes the particle float or sink respectively. Third, to transfer information between particles and solvent, the averaging operator $\boldsymbol{J}$ converts Eulerian (fluid) variables into Lagrangian (particle) variables and the spreading operator $\boldsymbol{S}$ converts Lagrangian (particle) variables into Eulerian (fluid) variables *e.g.* these operators apply to the solvent velocity field $\boldsymbol{u}$ and the particle velocities $\boldsymbol{v}$,

$$\boldsymbol{J}\boldsymbol{u}(\boldsymbol{r},t) = \int \delta_h(\boldsymbol{q}-\boldsymbol{r})\,\boldsymbol{u}(\boldsymbol{r},t)\,d\boldsymbol{r}, \tag{2.28a}$$

$$\boldsymbol{S}\boldsymbol{v} = \delta_h(\boldsymbol{q}-\boldsymbol{r})\,\boldsymbol{v}, \tag{2.28b}$$

and transform them into a point velocity $\boldsymbol{J}\boldsymbol{u}(\boldsymbol{r},t)$ and velocity field $\boldsymbol{S}\boldsymbol{v}$ respectively by means of the normalised weight function $\delta_h(\boldsymbol{q}-\boldsymbol{r})$ (in units of inverse of volume $\mathcal{V}^{-1}$ and integral equal to unity) [21, 22, 25]. At this point, it is also important to mention that

these operators are required to satisfy

$$\frac{d\boldsymbol{J}\boldsymbol{u}}{dt} = \boldsymbol{J}\left[\partial_t \boldsymbol{u} + \nabla\cdot(\boldsymbol{v}\boldsymbol{u})\right], \tag{2.29a}$$

$$\mathcal{V} = (\boldsymbol{J}\boldsymbol{S})^{-1} = \left(\int \delta_h^2(\boldsymbol{q}-\boldsymbol{r})\, d\boldsymbol{r}\right)^{-1}, \tag{2.29b}$$

in order to guarantee the fluctuation-dissipation theorem [22, 25]. Fourth and last, Newton's second law for particles immersed in an implicit solvent is given as

$$m_e \frac{d\boldsymbol{v}}{dt} \approx \boldsymbol{\lambda} + \boldsymbol{F}, \tag{2.30}$$

where $\boldsymbol{F}$ stands for the interparticle forces and/or external forces that act on a particle and $\boldsymbol{\lambda} = \mathcal{V}\boldsymbol{J}\boldsymbol{f}$ is a Lagrange multiplier that represents the force exerted by the solvent on a particle, with $\boldsymbol{f}$ a density force exerted by the particle on the solvent, $\boldsymbol{f} = \boldsymbol{S}\boldsymbol{\lambda}$, thus ensuring Newton's third law *i.e.* the force exerted by a particle on the solvent is of the same modulus and in the opposite direction as the force exerted by the solvent on a particle. Consequently, the equations of motion of the implicit solvent and the particles are given by a set of four coupled non-linear partial differential equations

$$\partial_t \rho + \nabla\cdot(\rho\boldsymbol{u}) = 0, \tag{2.31a}$$

$$\partial_t(\rho\boldsymbol{u}) + \nabla\cdot(\rho\boldsymbol{u}\boldsymbol{u}) = -\nabla p + \nabla\cdot\boldsymbol{\sigma} + \rho\boldsymbol{F}_f - \boldsymbol{S}\boldsymbol{\lambda}, \tag{2.31b}$$

$$m_e\frac{d\boldsymbol{v}}{dt} = \boldsymbol{F} + \boldsymbol{\lambda}, \tag{2.31c}$$

$$\frac{d\boldsymbol{q}}{dt} = \boldsymbol{v} = \boldsymbol{J}\boldsymbol{u}. \tag{2.31d}$$

2.5 Molecular Models of Lipids

The fast development of GPUs[3] has encouraged the adaptation of standard MD algorithms to GPU ones to increase the efficiency of simulations [31]. Nevertheless, we are still far from managing detailed (atomistic) MD simulations of large and complex biological systems, *e.g.*

[3] In the past, the development of GPUs was fostered by computer gaming. Today, the progress in GPU efficiency is motivated by scientific computation, artificial intelligence and cryptocurrency mining.

simulations of a cell ($\approx 10^{-4}\ m$) from the dynamics of atoms ($\approx 10^{-14}\ s$) to the dynamics of large structures ($\approx 10^{-6}\ s$) [32–36]. Thus, in practice, what one does is to focus on specific time and length-scales where the phenomenon of interest takes place. As we already know, one could perform BD simulations to study the long-time behaviour of systems. Moreover, molecular models of systems under study (lipid membranes and monolayers in this thesis) may be approximated with less resolved models, while preserving the physics of interest (see in Fig. 2.2 the representation of a lipid according to different models). In essence, these *coarse-grained* approaches [37] try to integrate/remove specific non-relevant degrees of freedom so that simulations can be sped up. For instance, we already presented in Sect. 2.4 a case of coarse-grained model by describing solvent particles in the continuum limit. Evidently, these models come at a cost on accuracy *e.g.* in Sect. 2.4 we lost information about the solvent structure, albeit by gaining the advantages of the resulting coarse-grained models (faster simulations of larger systems).

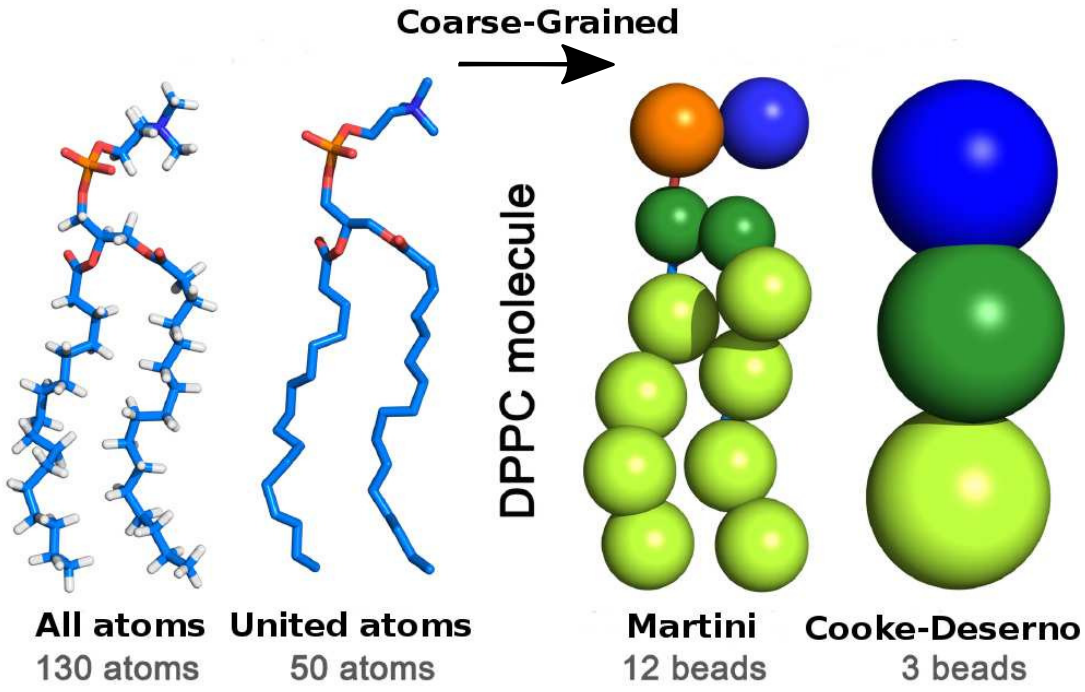

Figure 2.2: Schematic representation of a DPPC lipid within different models (figure taken from Ref. [38]). From left to right: all atoms, united atoms, MARTINI and Cooke-Deserno model. The level of resolution of DPPC decreases following the arrow.

2.5.1 Atomistic Model: CHARMM36+OPC

Computer simulations have demonstrated that the atomistic model CHARMM36 of a lipid [39, 40] forecasts lipid membrane properties such as thickness, head group area, Deuterium order parameter and form factors that are in quantitative agreement with the empirical values [40]. To achieve such degree of accuracy the CHARMM36 force field is obtained from first-principle calculations. Namely, the CHARMM36 force field is based on quantum mechanics calculations of lipids in vacuum and in realistic environments using very well known methods: Hartree-Fock and second order Møller–Plesset perturbation theory [41, 42]. The results from these methods are compared with quantum mechanics data. Then, the force field of lipids is obtained by adjusting the quantum mechanics potential energy to (2.2). Eventually, thermodynamic characterisations of lipids obtained by means of MD simulations of the resulting force fields are compared with the thermodynamic data and used as feedback for further quantum mechanics parametrisations (if needed). Although the CHARMM36 force field is meant to be used with the TIP3P model of water molecules, very recently, the combination of the atomistic force field CHARMM36 [39, 40] with a much more accurate model of water molecules (average relative error about 0.76% with the same computational cost as the TIP4P water model), the four-point OPC model of water [43], has showed to reproduce nearly quantitatively the features of DPPC and POPC lipid monolayers at an air-water interface [44].

The parametrisation of the four-point OPC model follows a non-orthodox methodology: in contrast to other atomistic models of water molecules *e.g.* TIPs or SPCE model, the water geometry is not imposed, or tightly imposed. This is, the OPC model seeks for the solution of the geometrical water equations (relative positions of the atoms and their charges) that best reproduces six key bulk properties of water: static dielectric constant, self diffusion coefficient, heat of vaporisation, density, position and height of the first peak in the Oxygen-Oxygen pair distribution function [43].

2.5.2 MARTINI Model

Coarse-grained models can still provide precise features of lipid structures while improving the statistical sampling. In this respect, the MARTINI model of a lipid has been shown to be the most efficient and reliable one [45–48]. On average, MARTINI parametrises four "heavy" atoms into one MARTINI atom (or bead) with an effective mass of 72 u, *e.g.* four water molecules are MARTINIsed into one bead, with Oxygen considered as a heavy atom in this example. Thanks to this 4:1 mapping philosophy, MARTINI achieves an average

speed-up of about 5-10 times with respect to atomistic models.

Another key to the success of MARTINI is the simplicity of its force field, *i.e.* the MARTINI force field only considers four main types of interacting families: Polar (P), non-polar (N), apolar (C) and Charged (Q). Regarding their parametrisation, the MARTINI force field, in contrast to other force fields, focuses only on reproducing accurate thermodynamic data of the hydration, vaporisation and partition free energy, and structural details of a set of organic systems.

Table 2.1: MARTINI interaction energies used for the LJ potential in kJ/mol. We enumerate the beads of a DPPC MARTINI lipid from its polar head to its acyl chains; 1-Q_0, 2-Q_a, 3-N_a, 4-N_a and [5-12]-C. The bead P corresponds to water molecules.

	P	Na	C	Q_0	Q_a
P	5.0	4.0	2.0	5.6	5.6
Na	4.0	4.0	2.7	4.0	4.0
C	2.0	2.7	3.5	2.0	2.0
Q0	5.6	4.0	2.0	3.5	4.5
Qa	5.6	4.0	2.0	4.5	5.0

In MARTINI, a DPPC lipid is represented by 12 beads, each one of radius $\sigma = 0.47\ nm$ (see Fig. 2.2), with a total mass of 864 u. The interactions among the beads of the lipids consists in LJ and Coulomb like interactions[4] (summarised in table 2.1). To be specific, both the LJ and the Coulomb potentials are truncated and smoothly shifted to set equal to zero the force at the cut-off distance; the Coulomb interactions are softly modified from distance $r = 0$ to $1.2\ nm$ while LJ interactions are only modified from distance $r = 0.9$ to $1.2\ nm$. In addition, lipids exhibit intramolecular bonded interactions in order to preserve their molecular geometry: harmonic interactions are introduced to represent chemically bonded atoms

$$V_{\text{bond}} = \frac{1}{2} k_b (r - r_b)^2, \tag{2.32}$$

with $r_b = \sigma$ the equilibrium distance and $k_b = 1250\ kJ\ mol^{-1}\ nm^{-1}$ the stiffness of the bonds. Harmonic interactions of cosine type are introduced to represent the bend of the

[4] In the MARTINI force field, only the groups Q_α, $\alpha = [0, a]$ contains electrostatic interactions. The relative dielectric constant is usually fixed to $\varepsilon_r = 15$.

acyl chains of lipids

$$V_{\text{bend}} = \frac{1}{2} k_\theta \left[\cos(\theta) - \cos(\theta_0)\right]^2, \tag{2.33}$$

with θ_0 the equilibrium angle and k_θ the stiffness of the chains. The parameters θ_0 and k_θ may vary depending on the sort of lipid; for acyl chains in a *trans* configuration $\theta_0 = 180$ and $k_\theta = 45\ kJ/mol$ while for acyl chains in a *cis* configuration $\theta_0 = 120$ and $k_\theta = 45\ kJ/mol$. On the other hand, saturated acyl chains are fixed with $\theta_0 = 180$ and $k_\theta = 25\ kJ/mol$.

2.5.3 Cooke-Deserno Model

A minimal model of a lipid that is able to spontaneously self-assemble into lipid bilayers and predicts reasonably accurate bilayer properties [49–53] has been introduced by Cooke *et al.* [53]. Since this model does not require explicit water molecules to stabilise amphipathic structures, it becomes a serious candidate when performing BD and BD with hydrodynamic interactions simulations.

In the Cooke-Deserno model, a lipid is just described with three beads (see Fig 2.2): one bead for the polar group (H) and two beads for the acyl chains (T). The interactions among beads consist in a Weeks-Chandler-Andersen (WCA) potential, which is a LJ potential that is truncated and shifted at its minimum

$$V_{WCA} = \begin{cases} 4\epsilon\left[\left(\frac{\sigma}{r}\right)^{12} - \left(\frac{\sigma}{r}\right)^{6} + \frac{1}{4}\right], & r \le r_c \\ 0, & r > r_c \end{cases} \tag{2.34}$$

with r the distance between two beads, $r_c = 2^{1/6}\sigma$ the cut-off of the WCA potential, σ the diameter of a bead and ϵ the energy (strength) of the potential. Additionally, T-T beads interact via a "long-ranged" cohesive potential

$$V_{attr} = \begin{cases} -\epsilon, & r < r_c \\ -\epsilon \cos^2\left(\frac{\pi(r - r_c)}{2w_c}\right), & r_c \le r_c \le r_c + w_c \\ 0, & r > r_c + w_c \end{cases} \tag{2.35}$$

with w_c the long-range scope of the cohesive potential (2.35) (see Fig. 2.3).

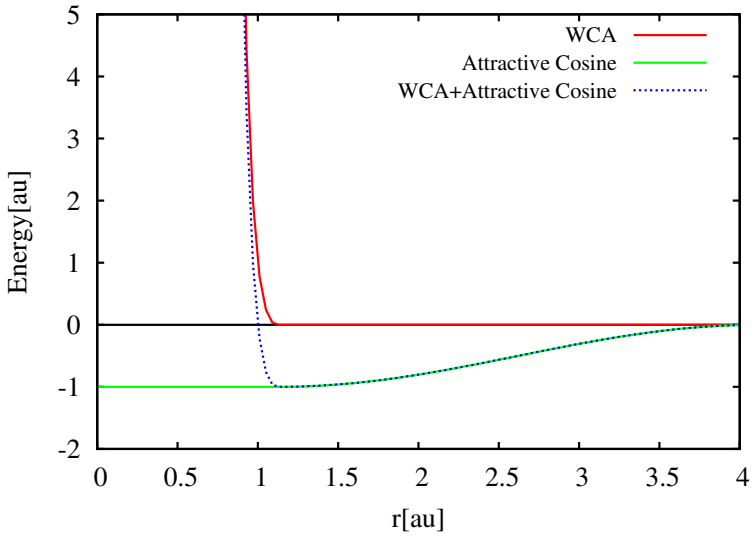

Figure 2.3: Potential energy due to the WCA potential (2.34), the square attractive cosine potential (2.35) and their sum (blue line). The diameter of a bead $\sigma = 1.0$, the energy $\epsilon = 1.0$ and the long-range cut-off $w_c = 3.0$, in arbitrary units (au).

These three beads are jointed together by means of bonds: finitely extensible non-linear elastic (FENE) bonds between neighbour beads (H-T and T-T)

$$V_{\text{bond}} = -\frac{1}{2} k_b r_\infty^2 \ln\left[1 - \left(\frac{r}{r_\infty}\right)^2\right], \tag{2.36}$$

and harmonic bonds between the edges of a lipid (H-T)

$$V_{\text{bend}} = \frac{1}{2} k_\theta \left(r - 4\sigma\right)^2, \tag{2.37}$$

with $k_b = 30\epsilon/\sigma^2$ and $k_\theta = 10\epsilon/\sigma^2$ the force constant of the bonds and $r_\infty = 1.5\sigma$ the divergence length of the FENE bond.

According to authors in Ref. [53] the long-range attractive term in Eq. (2.35) has been discovered to be key to stabilise lipid membranes and vesicles, and claimed to emerge from solvent-mediated interactions. Hence, as it is shown in Fig. 2.4, depending on the temperature and the long-range character of the potential (2.35) the Cooke-Deserno force field leads to stable lipid bilayers in both fluid and gel phases.

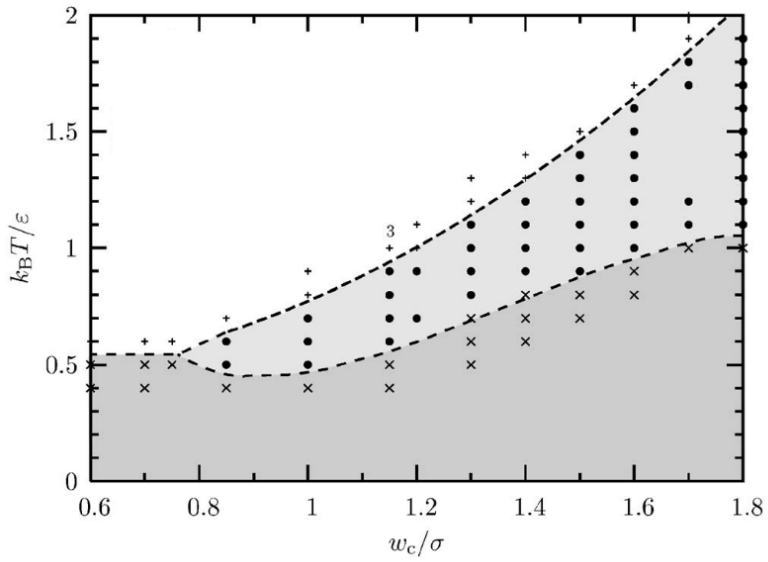

Figure 2.4: Phase diagram of a Cooke-Deserno lipid bilayer at zero lateral tension as a function of the ratio k_BT/ϵ and w_c/σ (figure taken from Ref. [53]): × denotes bilayers in a gel phase, • denotes bilayers in a fluid phase and + denotes unstable bilayers. Dashed lines represent an approximation to the regions of phase transition.

Bibliography

[1] H. C. Andersen, *Molecular dynamics simulations at constant pressure and/or temperature*, The Journal of Chemical Physics **72**, 2384 (1980).

[2] H. J. C. Berendsen, J. P. M. Postma, W. F. van Gunsteren, A. DiNola, and J. R. Haak, *Molecular dynamics with coupling to an external bath*, The Journal of Chemical Physics **81**, 3684 (1984).

[3] D. J. Evans and B. L. Holian, *The Nose–Hoover thermostat*, The Journal of Chemical Physics **83**, 4069 (1985).

[4] M. Parrinello and A. Rahman, *Crystal structure and pair potentials: A molecular-dynamics study*, Phys. Rev. Lett. **45**, 1196 (1980).

[5] P. Español, *Dissipative Particle Dynamics* (Springer Netherlands, 2005), pp. 2503–2512.

[6] C. Gardiner, *Stochastic Methods: A Handbook for the Natural and Social Sciences*, Springer Series in Synergetics (Springer, 2009).

[7] P. Langevin, C. R. Math. **146**, 530 (1908).

[8] R. Kubo, *The fluctuation-dissipation theorem*, Reports on Progress in Physics **29**, 255 (1966).

[9] J. K. Percus and G. Stell, *The Equilibrium Theory of Classical Fluids* (WA Benjamin, New York, 1964).

[10] C. Ebner, W. F. Saam, and D. Stroud, *Density-functional theory of simple classical fluids. i. surfaces*, Phys. Rev. A **14**, 2264 (1976).

[11] J. K. Percus, *Equilibrium state of a classical fluid of hard rods in an external field*, Journal of Statistical Physics **15**, 505 (1976).

[12] Á. Mulero, *Theory and Simulation of Hard-Sphere Fluids and Related Systems*, vol. 753 (Springer, 2008).

[13] U. M. B. Marconi and P. Tarazona, *Dynamic density functional theory of fluids*, The Journal of Chemical Physics **110**, 8032 (1999).

[14] A. Donev and E. Vanden-Eijnden, *Dynamic density functional theory with hydrodynamic interactions and fluctuations*, The Journal of Chemical Physics **140**, 234115 (2014).

[15] A. Donev, T. G. Fai, and E. Vanden-Eijnden, *A reversible mesoscopic model of diffusion in liquids: from giant fluctuations to fick's law*, Journal of Statistical Mechanics: Theory and Experiment **2014**, P04004 (2014).

[16] M. Rex and H. Löwen, *Dynamical density functional theory for colloidal dispersions including hydrodynamic interactions*, The European Physical Journal E **28**, 139 (2009).

[17] R. A. Gingold and J. J. Monaghan, *Smoothed particle hydrodynamics: theory and application to non-spherical stars*, Monthly Notices of the Royal Astronomical Society **181**, 375 (1977).

[18] C.-J. Hsu, *Numerical heat transfer and fluid flow*, Nuclear Science and Engineering **78**, 196 (1981).

[19] B. Dünweg and A. J. C. Ladd (Springer, Berlin, Heidelberg, 2009), chap. Lattice Boltzmann Simulations of Soft Matter Systems, pp. 89–166.

[20] C. S. Peskin, *The immersed boundary method*, Acta Numerica **11**, 479–517 (2002).

[21] P. J. Atzberger, P. R. Kramer, and C. S. Peskin, *A stochastic immersed boundary method for fluid-structure dynamics at microscopic length scales*, Journal of Computational Physics

224, 1255 (2007).

[22] P. J. Atzberger, *Stochastic eulerian lagrangian methods for fluid-structure interactions with thermal fluctuations*, Journal of Computational Physics **230**, 2821 (2011).

[23] F. BalboaUsabiaga, J. Bell, R. Delgado-Buscalioni, A. Donev, T. Fai, B. Griffith, and C. Peskin, *Staggered schemes for fluctuating hydrodynamics*, Multiscale Modeling & Simulation **10**, 1369 (2012).

[24] S. Delong, F. B. Usabiaga, R. Delgado-Buscalioni, B. E. Griffith, and A. Donev, *Brownian dynamics without green's functions*, The Journal of Chemical Physics **140**, 134110 (2014).

[25] F. B. Usabiaga, R. Delgado-Buscalioni, B. E. Griffith, and A. Donev, *Inertial coupling method for particles in an incompressible fluctuating fluid*, Computer Methods in Applied Mechanics and Engineering **269**, 139 (2014).

[26] FLUAM, *fluid and matter*.

[27] L. Landau and E. Lifshitz, *Fluid Mechanics* (Pergamon Press, Oxford, England, 1959).

[28] A. Donev, E. Vanden-Eijnden, A. Garcia, and J. Bell, *On the accuracy of finite-volume schemes for fluctuating hydrodynamics*, Commun. Appl. Math. Comput. Sci. **5**, 149 (2010).

[29] P. J. Atzberger, *Spatially adaptive stochastic numerical methods for intrinsic fluctuations in reaction–diffusion systems*, Journal of Computational Physics **229**, 3474 (2010).

[30] J. M. O. de Zárate and J. V. Sengers, *Hydrodynamic Fluctuations in Fluids and Fluid Mixtures* (Elsevier, Amsterdam, 2006).

[31] NVIDIA, *data center*.

[32] I. Yu, T. Mori, T. Ando, R. Harada, J. Jung, Y. Sugita, and M. Feig, *Biomolecular interactions modulate macromolecular structure and dynamics in atomistic model of a bacterial cytoplasm*, eLife **5**, e19274 (2016).

[33] G. Zhao, J. R. Perilla, E. L. Yufenyuy, X. Meng, B. Chen, J. Ning, J. Ahn, A. M. Gronenborn, K. Schulten, C. Aiken, et al., *Mature hiv-1 capsid structure by cryo-electron microscopy and all-atom molecular dynamics*, Nature **497**, 643 EP (2013).

[34] W. Eckhardt and A. Heinecke, *Supermuc boosts the largest molecular dynamics simulation by 4x in number of particles*, Innovatives Supercomputing in Deutschland **11**, 19 (2013).

[35] J. Gumbart, L. G. Trabuco, E. Schreiner, E. Villa, and K. Schulten, *Regulation of the*

protein-conducting channel by a bound ribosome, Structure **17**, 1453 (2009).

[36] J. R. Perilla, B. C. Goh, C. K. Cassidy, B. Liu, R. C. Bernardi, T. Rudack, H. Yu, Z. Wu, and K. Schulten, *Molecular dynamics simulations of large macromolecular complexes*, Curr Opin Struct Biol **31**, 64 (2015).

[37] P. Español, *Statistical Mechanics of Coarse-Graining* (Springer Berlin Heidelberg, Berlin, Heidelberg, 2004), pp. 69–115.

[38] K. Pluhackova and R. A. Böckmann, *Biomembranes in atomistic and coarse-grained simulations*, Journal of Physics: Condensed Matter **27**, 323103 (2015).

[39] J. Huang and A. D. MacKerell Jr, *Charmm36 all-atom additive protein force field: Validation based on comparison to nmr data*, Journal of Computational Chemistry **34**, 2135 (2013).

[40] J. B. Klauda, R. M. Venable, J. A. Freites, J. W. O'Connor, D. J. Tobias, C. Mondragon-Ramirez, I. Vorobyov, A. D. MacKerell, and R. W. Pastor, *Update of the charmm all-atom additive force field for lipids: Validation on six lipid types*, The Journal of Physical Chemistry B **114**, 7830 (2010).

[41] B. R. Brooks, R. E. Bruccoleri, B. D. Olafson, D. J. States, S. Swaminathan, and M. Karplus, *Charmm: A program for macromolecular energy, minimization, and dynamics calculations*, Journal of Computational Chemistry **4**, 187 (1983).

[42] B. R. Brooks, C. L. Brooks III, A. D. Mackerell Jr., L. Nilsson, R. J. Petrella, B. Roux, Y. Won, G. Archontis, C. Bartels, S. Boresch, et al., *Charmm: The biomolecular simulation program*, Journal of Computational Chemistry **30**, 1545 (2009).

[43] S. Izadi, R. Anandakrishnan, and A. V. Onufriev, *Building water models: A different approach*, The Journal of Physical Chemistry Letters **5**, 3863 (2014).

[44] M. Javanainen, A. Lamberg, L. Cwiklik, I. Vattulainen, and O. H. S. Ollila, *Atomistic model for nearly quantitative simulations of langmuir monolayers*, Langmuir **34**, 2565 (2018).

[45] S. J. Marrink, A. H. de Vries, and A. E. Mark, *Coarse grained model for semiquantitative lipid simulations*, The Journal of Physical Chemistry B **108**, 750 (2004).

[46] S. J. Marrink, H. J. Risselada, S. Yefimov, D. P. Tieleman, and A. H. de Vries, *The martini force field: coarse grained model for biomolecular simulations*, The Journal of Physical Chemistry B **111**, 7812 (2007).

[47] S. Baoukina, L. Monticelli, H. J. Risselada, S. J. Marrink, and D. P. Tieleman, *The molecular mechanism of lipid monolayer collapse*, Proceedings of the National Academy of Sciences **105**, 10803 (2008).

[48] W. D. Bennett and D. P. Tieleman, *Computer simulations of lipid membrane domains*, Biochimica et Biophysica Acta (BBA) - Biomembranes **1828**, 1765 (2013).

[49] V. A. Harmandaris and M. Deserno, *A novel method for measuring the bending rigidity of model lipid membranes by simulating tethers*, The Journal of Chemical Physics **125**, 204905 (2006).

[50] J. M. Gardner, M. Deserno, and C. F. Abrams, *Effect of intrinsic curvature and edge tension on the stability of binary mixed-membrane three-junctions*, The Journal of Chemical Physics **145**, 074901 (2016).

[51] B. J. Reynwar, G. Illya, V. A. Harmandaris, M. M. Müller, K. Kremer, and M. Deserno, *Aggregation and vesiculation of membrane proteins by curvature-mediated interactions*, Nature **447**, 461 EP (2007).

[52] M. Hu, J. J. Briguglio, and M. Deserno, *Determining the gaussian curvature modulus of lipid membranes in simulations*, Biophysical Journal **102**, 1403 (2012).

[53] I. R. Cooke and M. Deserno, *Solvent-free model for self-assembling fluid bilayer membranes: Stabilization of the fluid phase based on broad attractive tail potentials*, The Journal of Chemical Physics **123**, 224710 (2005).

Part I.

Lateral Properties of Lipid Monolayers

3

Phase Coexistence of Condensed and Expanded Liquids

In the first part of the thesis we will examine the structural properties of lipid monolayers at air-water interfaces. More precisely, we will study the case of DPPC monolayers in which condensed (LC) and expanded (LE) liquid domains coexist, being this inquiry very important to understand the proper functioning of the pulmonary surfactant system [1]. Thus, we devote this chapter to an atomistic MD simulation of DPPC monolayers that aims at answering general questions regarding the properties of these domains [1–5].

So far, all models that have been proposed to explain the reasons why multiple LC domains seem to coexist without reaching full thermodynamic separation [1–3] (as would be expected from typical first order transition [3, 6–9]) invoke a classical theory of competing interactions [10]. Within this theory, line tension (the cost in creating boundaries between two 2D regions) and long-range dipolar repulsive interactions are the only key ingredients to stabilise domains of extremely diverse sizes and appearances [10]. Electric dipolar interactions between lipids (mostly encouraged by the choline group located at lipid heads) that belong to a LC domain, together with the line tension λ, have been proved

to (qualitatively) predict the shape aspect/morphology of LC domains of several *in vitro* monolayer setups [3, 9, 11]. The electric dipolar moment of lipids is assumed to be oriented parallel to the normal axis of the monolayer (in this way dipolar interactions are purely repulsive) and, at the same time, the line tension is taken to be isotropic (independent of the orientation of lipids relative to the $LC - LE$ boundary) [3, 9, 11].

On the contrary, there exist studies, both theoretical and experimental, that contradict the stabilisation of LC domains. For instance, Monte Carlo simulations of a 2D lattice model of lipid monolayers [12] were the first to conclude that the formation and growth of domains are subject to very slow relaxation times, even if lipids do not interact via long-range forces. This means that it is likely that LC domains may look stable during their relaxation stage *i.e.* they are metastable. This fact was also noted experimentally in studies in which LC domains changed in number and morphology when perturbed via an external stimulus [13]. Further evidence of this view is the unusual behaviour of the surface pressure-area per lipid isotherms in the region of $LC - LE$ coexistence. By definition, regions of phase coexistence are characterised by horizontal isotherms (lever rule). However, all experimental studies show deviations from the lever rule in $LC - LE$ coexistence regions, which strongly suggest that LC domains may not be in thermodynamic equilibrium [6, 12, 14–16].

Moreover, most of the studies that predict the stabilisation of LC domains [3, 9, 11] do not deal with some fundamental issues, or their results are incomplete [17]. First of all, both simulations and experiments indicate that the dipolar moment of lipids is oriented almost perpendicular to the normal axis of the monolayer ($\approx 85°$) [9, 18–20], *i.e.* practically in the plane of the monolayer. These results are against one of the main assumptions of some studies [3, 9, 11]. And secondly, the line tension λ is considered to be isotropic. Nevertheless, in interfaces with orientational order, an anisotropic λ is expected [21].

Therefore, whether these domains are stable or not remains unclear. Likewise, we believe that it is important to examine the relevance of anisotropic line tensions, as well as the orientation of the dipole moment of lipids, for the stabilisation of LC domains in lipid monolayers [3, 9, 11, 17]. In this chapter we will present detailed MD simulations of single-lipid monolayers at an air-water interface. The total areas per lipid explored will span the region of $LC - LE$ coexistence. To this end we will use the CHARMM36 atomistic model of a DPPC lipid molecule [22, 23] in combination with the four-point OPC model for a water molecule [24]. This combination provides excellent agreement with isothermal compression-expansion experiments in the temperature range $298 - 310\ K$ [25]. Our study is a state-of-the-art simulation of DPPC lipid monolayer due to different reasons: On the one hand, these simulations are the largest (in terms of system size) presented so far in

the literature for this system. This ensures the observation of large LC and LE domains. On the other hand, we propose a novel analysis technique, alternative to previous Voronoi methods [26], to distinguish between lipids that belong to LC and LE domains. Our method is based on a local crystalline order parameter. In Sect. 3.2 we will characterise the structural properties of lipids in different domains (LC and LE), *e.g.* head and tail angle distributions and their relative angle distribution. By doing so, we will show some relevant features of DPPC lipids, not discussed up to now in the literature, on the relative orientation of the head group of lipids. In Sect. 3.2.1, we will show interesting and contrary findings to previous experimental reports regarding the hydration of the head group of lipids [19, 27]. Finally, in Sect. 3.3, we will also characterise some structural properties of the LC and LE domains.

3.1 Atomistic Simulations of DPPC Monolayers at Air-Water Interfaces

As we have already mentioned in the introduction to this chapter, it is of vital importance to elucidate whether the line tension is anisotropic and also to determine the orientation of the dipole moment. These two questions might be relevant in connection with the theoretical models for the shape of domains that have been presented in the literature [3, 9, 11]. Consequently, detailed MD simulations are fundamental in this respect.

We have used a web-based graphical user interface for CHARMM [28] to build up DPPC monolayers in the $x-y$ plane with a mean area per lipid $\bar{a} \equiv \frac{A}{N} = 58,\ 61,\ 63,\ 65,\ 68$ and $71\ \text{Å}^2$ (with A the area of a monolayer and N the number of lipids in a monolayer). In this manner, we almost cover the whole region of $LC-LE$ coexistence [1, 25]. The number of lipids employed is 1152, distributed in two monolayers (576 per monolayer) that are separated by a water film containing 93312 water molecules (see Fig. 3.1). These parameters give systems that are a factor ≈ 1.4 larger (in lateral size) than previous systems used by Javanainen *et al.* [25].

Simulations for these first systems (one simulation per value of $\bar{a}$) were performed using NVT MD simulations with the open-source package GROMACS 2018.3 [29, 30]. In these simulations we employed a leap-frog algorithm to integrate the equations of motion using a time step $\Delta t = 0.002\ ps$. Electrostatic interactions were fully treated by means of the Particle Mesh Ewald (PME) method [31]. Note that, since a PME method is used, the length of the simulation box along the z axis, L_z, cannot be extended to infinite since a

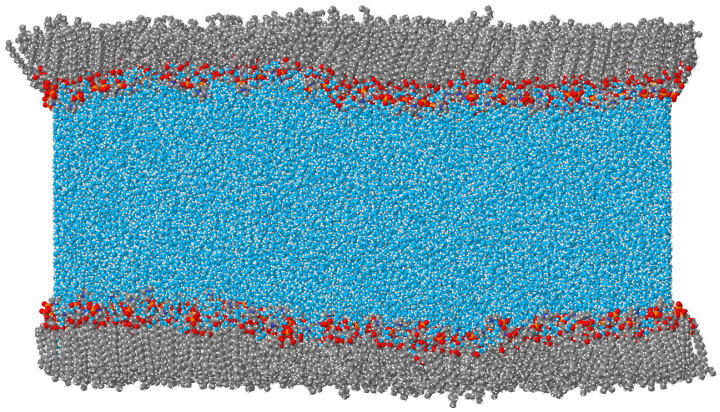

Figure 3.1: Representation of typical systems employed for studying lipid monolayers (in red and green) in an air-water interface (water in blue) contained in the $x-y$ plane. To improve statistics two monolayers are simulated at the same time. Simulations are performed using periodic boundary conditions (PBC).

larger length in z involves a more expensive calculation of the long-range contribution of electrostatics. Hence, the box length along z was set to a finite and small value, $L_z = 22\ nm$, in order to minimise the computational cost, while avoiding as much as possible finite size effects. Unfortunately, a direct consequence of using small values of L_z is that the average number of water molecules in the air (vapour) phase is close to zero[1]. Nevertheless we do not believe that the vapour phase may have any significant effect on our final results.

Furthermore, we truncated the LJ interactions at a cut-off distance $r_c = 1.2\ nm$, and smoothly shifted them from 1.0 nm to the cut-off distance, so that the interactions goes to zero at r_c smoothly. This procedure is used to avoid any spurious artefact. To minimise the effects of truncated interactions, we applied corrections to the pressure and the energy. These systems were simulated for 50 ns at temperature $T = 298\ K$ using a Berendsen thermostat [32] in the equilibration period. After this initial period, the simulations were run during 250 ns using a Nosé-Hoover thermostat [33] coupled to a thermal reservoir with a coupling constant $\tau = 1.0\ ps$. These runs were used for production purposes. Therefore each system was simulated for a total of 300 ns (which is equivalent to about 21 days of real on 288 CPU cores). The long span of the simulation allows for a complete phase separation between the LC and LE phases.

[1] In the ideal gas approximation, the equation of state of the vapour phase is $PV = Nk_BT$, so the number of water molecules in the vapour phase can be estimated by using the experimental values of the vapour pressure of water at 298 K and the volume of the simulation domains minus the volume occupied by water and DPPC molecules. With the parameters used in our simulations, the average number of water molecules is $\approx 0.5-0.8$

Finally, in addition to the setup presented above (called A in Table 3.1), we performed extra NVT MD simulations in order to estimate how system size effects influence our results. To this aim, we use three additional setups: in a second setup (B), we decreased the lateral size of the simulating box by a factor ≈ 1.5 (*i.e.* similar system size of Ref. [25]). Conversely, in a third setup (C), we increased the value of L_z from 22 to 65 nm, and additionally remove one of the monolayers to avoid interactions between lipids via both periodic images and hydrodynamic (water-mediated) interactions. Lastly, in a fourth setup (D), we used the original configuration but with a subtle difference: electrostatic interactions are now solved by means of the Reaction Field (RF) method, using an effective dielectric constant equal to that of water at 298 K and 1 atm *i.e.* $\epsilon_{RF} = 78.4$. We are aware that this method is not recommended for inhomogeneous systems, but previous simulations published [34, 35] show that the RF method reproduces correct bilayer properties (area per lipid, water density, deuterium order parameter, and so on). In the last setup we further explore the limits of RF methods.

Table 3.1: Parameters employed for MD simulations of DPPC lipid monolayers at an air-water interface: temperature T is given in Kelvin $[K]$. The electrostatic methods used are PME and RF. N_p and N_w stands for the number of DPPC and water molecules respectively, and L_z is the simulating box lengthen in the z direction in nanometers $[nm]$. All simulations use PBC.

Setup	T	Electrostatics	N_p	N_w	L_z
A	298	PME	1152	93312	22.0
B	298	PME	512	41994	22.0
C	298	PME	576	93312	65.0
D	298	RF	1152	93312	22.0

3.2 Characterisation of Lipids of Condensed and Expanded Domains

Within the present force fields, it is not known whether structural properties of lipids, such as head group orientation, belonging to different domains (LC and LE) are different. *A priori* it seems reasonable to think that these properties may not be the same. To avoid misleading interpretations about structural properties of lipids, we find useful to characterise separately lipids of different coexisting phases (LC and LE). However, finding

a criterion to clearly distinguish lipids in LC or LE domains is not an easy task. For instance, from the definition of phase coexistence, the distribution of area per lipid in LE domains is expected to be different from the corresponding distribution in LC domains. But these distributions widely overlap, which prevents a clear discrimination between domains.

Here we propose an accurate criterion based on a local crystalline order parameter. First, we distinguish between both monolayers, which we refer to as up and down monolayers depending on their z coordinate ($z_{\text{up}} > z_{\text{down}}$). This is crucial since our classification algorithm depends on the instantaneous configuration of isolated lipid monolayers. Of course results from both monolayers are averaged to improve statistics. Second, we establish that the i-th lipid belongs to a LC domain if its local crystalline order parameter $\Psi_i > 0.5$, while it belongs to a LE domain otherwise. Ψ_i is defined as:

$$\Psi_i = \frac{1}{6N} \left| \sum_{j=1}^{N} \sum_{k=1}^{6} \exp\left(\mathrm{i}\boldsymbol{G}_k \cdot (\boldsymbol{q}_i - \boldsymbol{q}_j)\right) \right|, \tag{3.1}$$

with $\boldsymbol{q}_i - \boldsymbol{q}_j$ the 2D relative position vector ($z_i = 0$ and $z_j = 0$) between the centre of mass of the lipid carbonyl groups[2] (one carbonyl group per acyl chain, two acyl chains per lipid) of the i-th lipid and its j-th first neighbour (N in total), and $\boldsymbol{G}_k$ is the set of 6 vectors of the first-shell of reciprocal lattice vectors of a stretched triangular lattice. This criterion has been established from the observation that the projection in the plane $z = 0$ of the centre of mass of the carbonyl groups in a tilted configuration form a stretched triangular lattice, with a stretching factor of ≈ 2.5 in the direction along which the acyl chains are projected[3].

To calculate Ψ_i, we need to know in advance the reciprocal vectors $\boldsymbol{G}_k$. To obtain these vectors it is necessary to know the local orientation of the lattice with respect a tagged lipid i. The local orientation of the lattice is obtained from the projection in the plane $z = 0$ of the eigenvector associated with the largest eigenvalue of the orientational order parameter tensor

$$\boldsymbol{Q} = \frac{1}{2N} \sum_{k=1}^{2N} \frac{1}{2} \left(3\hat{\boldsymbol{t}}_k \otimes \hat{\boldsymbol{t}}_k - \boldsymbol{I}\right), \tag{3.2}$$

[2] The carbonyl groups (C=O) of lipids separate the head and tail groups of lipids, so we employ this group as the mid-plane of the lipid.

[3] The projection in the plane $z = 0$ of tilted acyl chains of lipids looks like a prolate ellipsoid of aspect ratio ≈ 2.5.

where $\otimes$ is the dyadic product, $\boldsymbol{I}$ the unit matrix, and $\hat{\boldsymbol{t}}_k$ the orientation of the acyl chains (two per lipid) of the j-th first neighbour of the tagged i lipid. The orientation $\hat{\boldsymbol{t}}_k$ of an acyl chain k is calculated from the eigenvector associated with the largest eigenvalue of the gyration tensor

$$\boldsymbol{R} = \frac{1}{M}\sum_{l=1}^{M} \boldsymbol{q}_l^{(k)} \otimes \boldsymbol{q}_l^{(k)}, \tag{3.3}$$

with M the number of carbon atoms of the acyl chain k and $\boldsymbol{q}_l^{(k)}$ their position vectors with respect to their centre of mass *i.e.* $\sum_{l=1}^{M} \boldsymbol{q}_l^{(k)} = 0$.

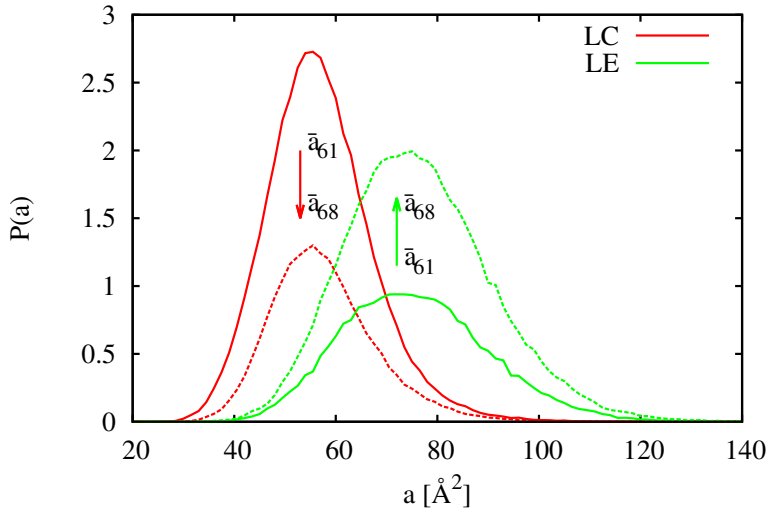

Figure 3.2: Distribution of area per lipid for *LC* (red lines) and *LE* (green lines) domains. For this analysis we have made use of two monolayer systems, one with mean area per lipid $\bar{a}$ = 0.61 Å^2 (solid lines) and another with $\bar{a}$ = 0.68 Å^2 (dashed lines).

Subsequently, as a test of our criterion for the classification of lipids, we start analysing the area per lipid for *LC* and *LE* domains. Here, though, we present the analysis of a couple of selective cases, $\bar{a}$ = 61 and 68 Å^2, which were simulated with the parameters of setup A in Table 3.1. Once the lipids are classified according to the type of domain they belong to, we estimate the area per lipid by means of Voronoi algorithms. As a result, we present in Fig. 3.2 the resulting normalised (with respect to the total number of lipids) area per lipid distributions. The *LC* phase has an average area per lipid of $\approx$ 55 Å^2, whereas the *LE* phase has $\approx$ 74.5 Å^2. These results are essentially independent of the value of $\bar{a}$, as expected for the coexistence region of a first-order phase transition. Our results are in excellent agreement with the coexistence values reported in Refs. [25, 36, 37], so providing

support to this new criterion.

On the occasion of one of the main goals of this chapter, we study the orientation of the dipole moment as well as the orientation of the tail groups separately for *LC* and *LE* domains. To this end, we define an unit vector $\hat{\boldsymbol{h}}$, which we call head vector, as a vector pointing from the position of the Phosphorous (P) atom to that of the Nitrogen (N) atom. This vector can be taken as a measure of the dipole-moment orientation. Also, we use our previously defined unit vector $\hat{\boldsymbol{t}}$, which we call tail vector (two per lipid). In addition we define the vector normal to the monolayer as always pointing toward the water phase ($\hat{\boldsymbol{n}}$). Then, Fig. 3.3 shows the distributions of the head and tail angles with respect to the normal, obtained by averaging over the last 100 *ns* of our simulations (distributions are seen to converge in that time span) form monolayers with $\bar{a}$ = 61, 63, 65 and 68 Å^2. The parameters used were those of setup A in Table 3.1.

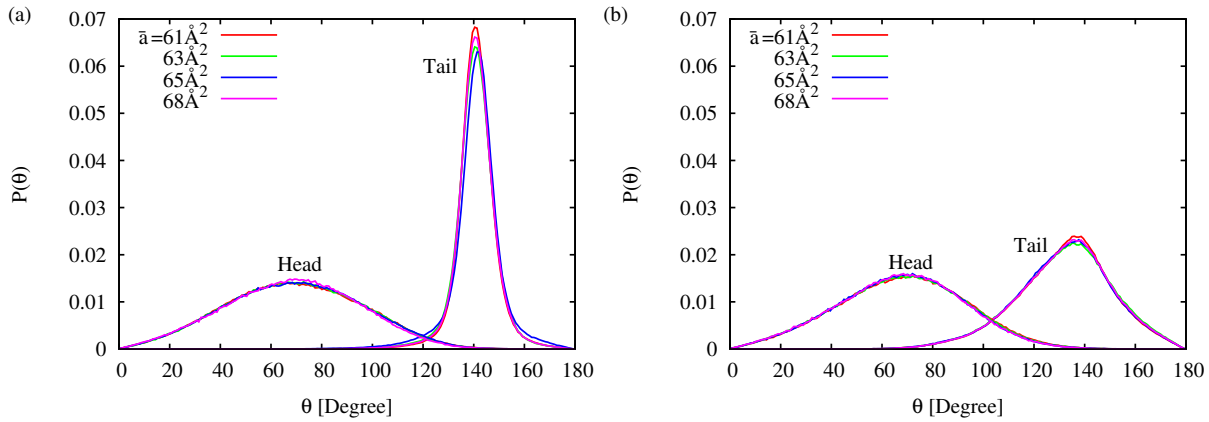

Figure 3.3: (a) Head and tail angle distributions of lipids within a *LC* domain. (b) Head and tail angle distributions of lipids within a *LE* domain. These distributions have been calculated for mean area per lipid $\bar{a}$ = 61, 63, 65 and 68 Å^2.

As expected, the tail distribution of lipids within a *LC* domain (panel (a)) is sharper than the tail distribution of lipids within a *LE* domain (panel (b)), indicating that lipids within a *LC* domain are in a tilted configuration. From the tail distribution of lipids within a *LC* we obtain a mean tilt angle of ≈ 141°, which is similar to previously reported values of the tilt angle (≈ 155°) [9, 19, 27]. It must be noted, however, that the CHARMM36+OPC force fields slightly underestimate the tilt angle of the lipids chains. On the other hand, it is surprising to find that the head angle distribution in *LC* and *LE* domains are almost identical, since we were expecting that different hydrations of the head group in different kind of domains would affect them [19, 27]. The mean head angle obtained from the distributions is ≈ 72.5° for both *LC* and *LE*, somewhat smaller than previously reported values

($\approx 85°$) [9, 18–20]. Therefore, the CHARMM36+OPC force fields not only underestimate the mean head angle of lipids, but also seem to exhibit some deficiencies when determining their hydration level.

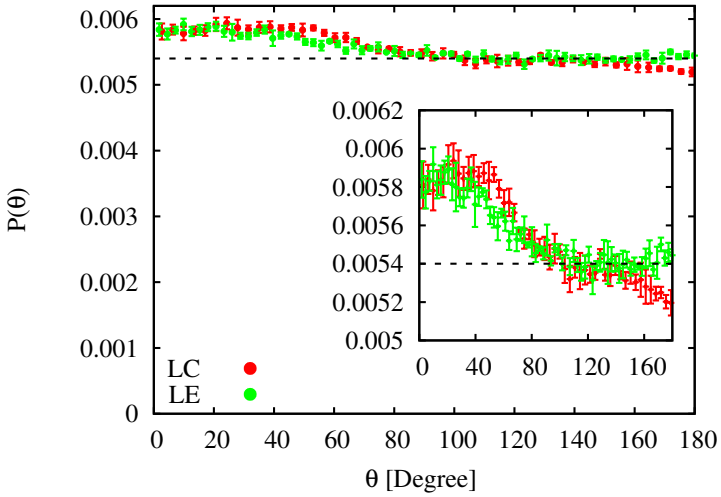

Figure 3.4: Two-dimensional head-tail angle distribution in *LC* (red) and *LE* (green) domains. Symbols and error bars are obtained from the average and the standard error of the mean of systems with $\bar{a} = 61,\ 63,\ 65$ and 68 Å^2, and the dashed line is arbitrarily drawn at $P(\theta) = 0.0054$ as a visual guide. For clarity, we show a zoom of $P(\theta)$ in the inset.

Clarifying this issue is fundamental since all conclusions about the relevance of the in-plane component of the dipole moment of lipids are inferred from the head angle distribution. In Section 3.2.1 we will further explore the predictive capability of the CHARMM36+OPC force fields concerning the hydration level of the head groups. Meanwhile, to complement the previous study about the head angle distribution in *LC* and *LE* domains, we study the 2D head angle distribution, which is also important to elucidate whether the in-plane component of the dipole moment of lipids is relevant for theoretical models. To carry out this study, in Fig. 3.4 we show the 2D head-tail angle distribution $\hat{\boldsymbol{h}}_{2D} \cdot \hat{\boldsymbol{t}}_{2D}$ (obtained by projecting the head and tail vectors $\hat{\boldsymbol{h}}$ and $\hat{\boldsymbol{t}}$ in the monolayer plane) averaged over the last 100 *ns* of our simulations. It is worth to comment that because the 2D head-tail angle distribution is quite noisy, we have also averaged over $\bar{a} = 61,\ 63,\ 65$ and 68 Å^2, assigning error bars to the resulting distribution from the standard error of the mean. Unexpectedly, we find that this distribution is almost uniform, which suggests that dipole vectors within *LC* and *LE* are randomly oriented in the monolayer plane. Our first indications point out that the in-plane component of the dipole moment can be neglected leaving the normal component as the only one relevant, which would give theoretical support to one of the

main assumption used in theoretical models for domain shapes [3, 9, 11]. Notice though, that this aspect of lipids has never been discussed, neither computationally nor experimentally (or at least we are not aware of such a discussion). Thus, we cannot discard that our result may be spurious considering that the CHARMM36+OPC force fields may suffer from some deficiencies.

Finally, in order to evaluate possible finite size effects in the distributions we recalculated them using the same initial configurations of monolayers with $\bar{a}$ = 61, 63, 65 and 68 Å^2, and simulating with parameters of setups B, C and D in Table 3.1. For setups B and C we do not appreciate any significant difference with respect to the results presented above. By contrast, setup D shows a subtle difference. Namely, the $\hat{\boldsymbol{h}}_{2D}$ vector is preferentially antiparallel to the $\hat{\boldsymbol{t}}_{2D}$ vector (15% more likely), but in any case, we arrive at the same conclusion as above: the in-plane component of the dipole moment can be neglected. This last result has to be taken with care though, since RF methods may lead to misleading results when applied to inhomogeneous systems.

3.2.1 Hydration of the Head Group

Experimentally, it has been reported that lipids within *LC* and *LE* domains exhibit different hydration levels, yielding different structures of the head groups [19, 27]. However, in our simulations we have not found any evidence of this. In fact, we have just seen that the angular distributions in *LC* and *LE* domains are similar. However, we recall that there exists the possibility that the force fields we are using are not accurate in reproducing the angular distributions. We propose an additional analysis in which we directly measure the hydration of the head groups.

We study how lipids of *LC* and *LE* domains distribute at the air-water interface. To this aim, we take as a reference point the centre of mass of the carbonyl groups of lipids, and calculate their distribution along the normal axis of the monolayer. As it can be seen from Fig. 3.5 (a), the (mean) z positions of lipids in both domains (*LC* and *LE*) are different (for clarity we only show results from one of the monolayers). To be precise, we find a separation along z axis of about 0.5 nm between lipids in *LC* and *LE* domains. However, this cannot be interpreted as a confirmation that lipids of one of the domains (*LC* in this case) penetrate deeper in the water phase, since we still do not know the position of the air-water interface relative to the lipids of each domain. In other words, the difference in height between lipids may be because: (1) lipids of the *LC* domains penetrate deeper in the water phase than lipids of *LE* domains, which would be contrary to experimental observations

[19, 27]; (2) lipids of *LC* domains displace the air-water interface while at the same time keeping the same penetration in the water phase as lipids of *LE* domains; and (3), lipids of *LC* domains displace the air-water interface and at the same time they penetrate deeper in the water phase than lipids of *LE* domains, which would also be contrary to experimental observations [19, 27].

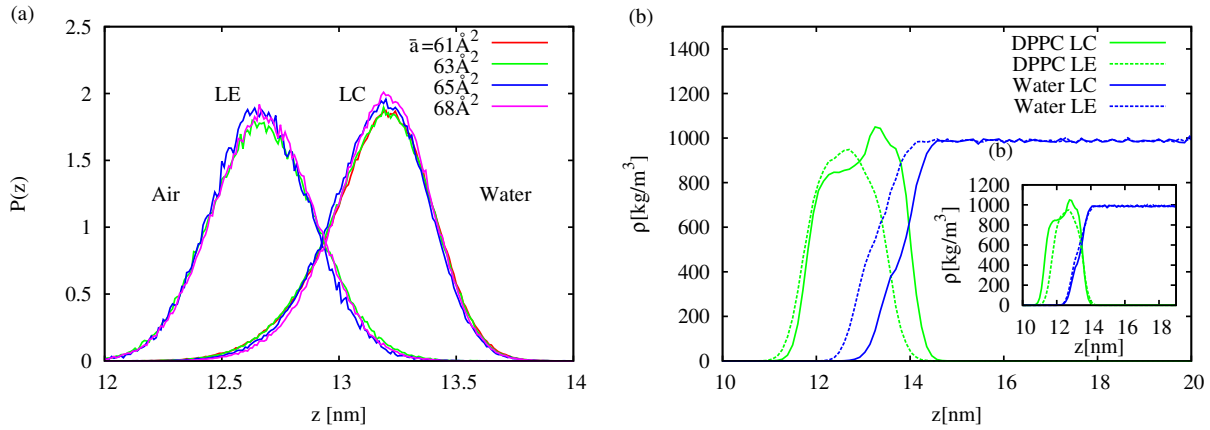

Figure 3.5: (a) z distribution in *LC* and *LE* domains for monolayers with $\bar{a}$ = 61, 63, 65 and 68 Å^2 and simulated with parameters of setup A in Table 3.1. (b) Density profiles (3.4) of lipids and water molecules of a monolayer with $\bar{a}$ = 0.65 Å^2 and simulated with parameters of setup A in Table 3.1. Solid lines are the density profiles over the regions where a *LC* domain is located, while dashed lines are the density profiles over *LE* domains. In the inset the z axis of the *LC* density profile has been displaced by −0.5 *nm i.e.* $\rho_{LC}(z-0.5)$.

To elucidate whether lipids of *LC* domains penetrate deeper in the water phase or not, we have also examined the density profile of the whole DPPC lipids and also of the water molecules over the two kinds of domains along the normal axis. In other words, we average the density profile over the areas Ω_{LC} and Ω_{LE} corresponding to the *LC* and *LE* domains:

$$\rho_{LC}(z) = \int_{\Omega_{LC}} \rho(x,y,z)\,dxdy, \tag{3.4a}$$

$$\rho_{LE}(z) = \int_{\Omega_{LE}} \rho(x,y,z)\,dxdy. \tag{3.4b}$$

As it is shown in Fig. 3.5 (b) lipids of *LC* domains (solid green line) displace the air-water interface (solid blue line). We believe that this effect is due to the more efficient packing associated with the tilt of the acyl chains, which makes a lipid of a *LC* domain to have, on average, a larger size along the axis normal to the monolayer. Because of the mismatch

between the length of lipids in LC and LE domains, the system finds more convenient to disturb the air-water interface by aligning acyl chains near the vapour phase and creating a gap (in height) between the head groups in both domains.

Even more surprisingly, if we displace the z axis of the LC density profiles by $-0.5\ nm$ (equal to the mean difference in height between lipids in the two domains), *i.e.* $\rho_{LC}(z-0.5)$ (solid blue and solid green lines), as shown in the inset of Fig. 3.5 (b), we can finally conclude that, with the present force fields, the hydration of the head groups of lipids in LC domains is the same as that in LE domains. This result strongly suggest that the CHARMM36+OPC force fields may be inaccurate when reproducing the properties of the head groups of lipids [19, 27], which could explain why the angular distributions of the head groups in LC and LE domains are similar. Therefore, we feel that this issue should be further investigated in future studies, since this is of crucial relevance for theoretical modelling [3, 9, 11].

3.3 Structural Properties of Domains

In addition to the characterisation of individual lipids in different domains, we can also tackle their collective arrangement and properties. As a first step, we analyse the final configuration of monolayers with $\bar{a} = 58,\ 61,\ 63,\ 65,\ 68$ and $71\ \text{Å}^2$, simulated with parameters of setup A in Table 3.1.

Since the z dimension of domains is highly constrained, we characterise most of their properties only from their projection on the plane $z = 0$. For simplicity, we display lipids as 2D ellipses of aspect ratio 2.5 and oriented along their $\hat{\boldsymbol{t}}_{2D}$ vectors. Furthermore, ellipses are coloured according to their local crystalline order parameter (3.1). As shown in Fig. 3.6, it is intriguing that LC domains prefer to adopt elongated rather than circular shapes, as would be expected in isotropic systems, which is considered a signature of an anisotropic line tension. Another direct signature of an anisotropic line tension is the specific angle between the acyl chains of the lipids that belong to a LC domain ($\Psi > 0.5$) and the $LC-LE$ interface, which is $\approx 20°$. Nevertheless, within the present model and the length scales explored in the simulations, it is difficult to further assess both the morphology of LC domains and the line tension of the $LC-LE$ interface. Not to mention the stabilisation of multiple LC domains (if it actually occurs in the experiments).

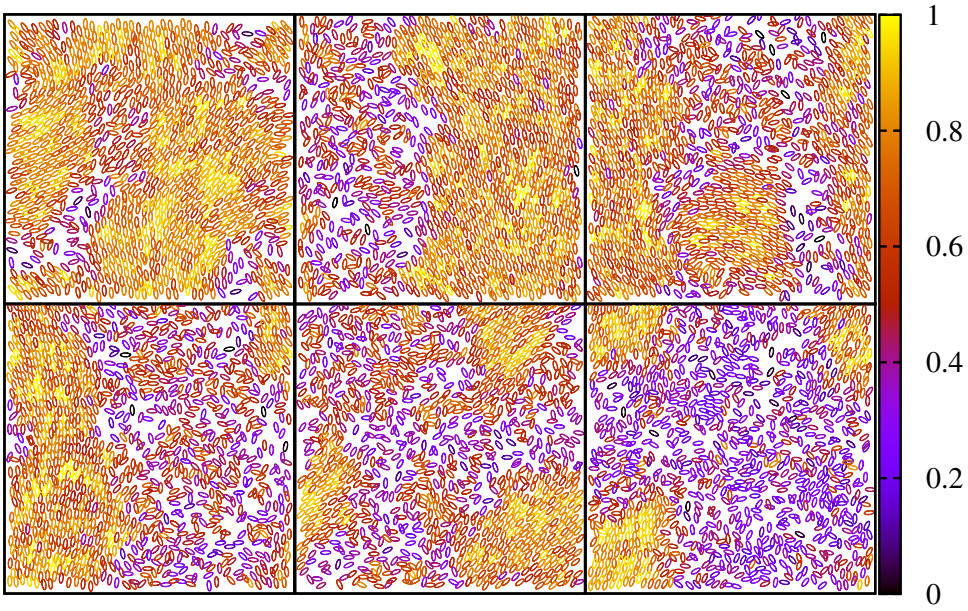

Figure 3.6: Local crystalline order parameter (colour box) of lipids (2D ellipses of aspect ratio 2.5) in one of the monolayers with $\bar{a} = 58,\ 61,\ 63,\ 65,\ 68$ and $71\ \text{Å}^2$ (85%, 70%, 59%, 48%, 33% and 17% of LC phase, from left to right and from top to bottom).

On the other hand, from Fig. 3.6, it is more than obvious that LC domains present a high orientational order while LE domains do not at all. To strictly quantify such an order, we calculate the correlation of the $\hat{\boldsymbol{h}}_{2D}$ and $\hat{\boldsymbol{t}}_{2D}$ vectors of lipids that belong to LC and LE domains. To be specific, we examine their polar and nematic correlation functions versus the relative distance between lipids. These two functions are complementary to describe the orientational order of the domains. Mathematically, we define the polar and the nematic correlation functions, respectively, as

$$\langle \cos\theta \rangle (\boldsymbol{r}) = \langle \hat{\boldsymbol{e}}_i \cdot \hat{\boldsymbol{e}}_j \delta (\boldsymbol{r} - \boldsymbol{r}_{ij}) \rangle , \tag{3.5a}$$

$$\langle \cos 2\theta \rangle (\boldsymbol{r}) = \left\langle \left[2 (\hat{\boldsymbol{e}}_i \cdot \hat{\boldsymbol{e}}_j)^2 - 1 \right] \delta (\boldsymbol{r} - \boldsymbol{r}_{ij}) \right\rangle , \tag{3.5b}$$

where $\boldsymbol{r}_{ij}$ is the 2D relative position vector ($z = 0$) between the centre of mass of the carbonyl groups, $\delta (\boldsymbol{r} - \boldsymbol{r}_{ij})$ is the delta function and, $\hat{\boldsymbol{e}}_i$ and $\hat{\boldsymbol{e}}_j$ are 2D unit vectors that are defined either by the $\hat{\boldsymbol{h}}_{2D}$ or the $\hat{\boldsymbol{t}}_{2D}$ vectors depending on whether we are calculating the head or the tail correlation function.

After averaging over molecules and over the last 100 ns of monolayers at $\bar{a} = 61,\ 63,\ 65$ and $68\ \text{Å}^2$, we can see in Fig. 3.7 that the polar (top) and nematic (bottom) correlations between the $\hat{\boldsymbol{t}}_{2D}$ vectors in LC domains (labelled as "Tail(LC)" in the figure) are quite

high. Consequently, we can conclude that *LC* domains are characterised by a high 2D order that is originated by the 3D order of acyl chains. This 2D order is polar (acyl chains pointing in the same direction). This kind of order resembles the kind of order found in liquid crystals, which is characterised by quasi-long-range order (correlations follow an algebraic decay) [38]. Unfortunately, we cannot accurately quantify how slow (or fast) these correlations decay, since they may be highly affected by finite size effects. Namely, in our calculations we are assuming translational invariance of the correlation functions with respect to the position in the domain. But this is not true, since lipids that are at the centre of a domain present correlations that are very different from those of lipids at the boundary (correlations are disturbed at the boundary of the domain). As a result, correlations in a small *LC* domain ($\bar{a}$ = 68 Å^2) differ from the correlations in larger *LC* domain ($\bar{a}$ = 61, 63 and 65 Å^2) at large distances.

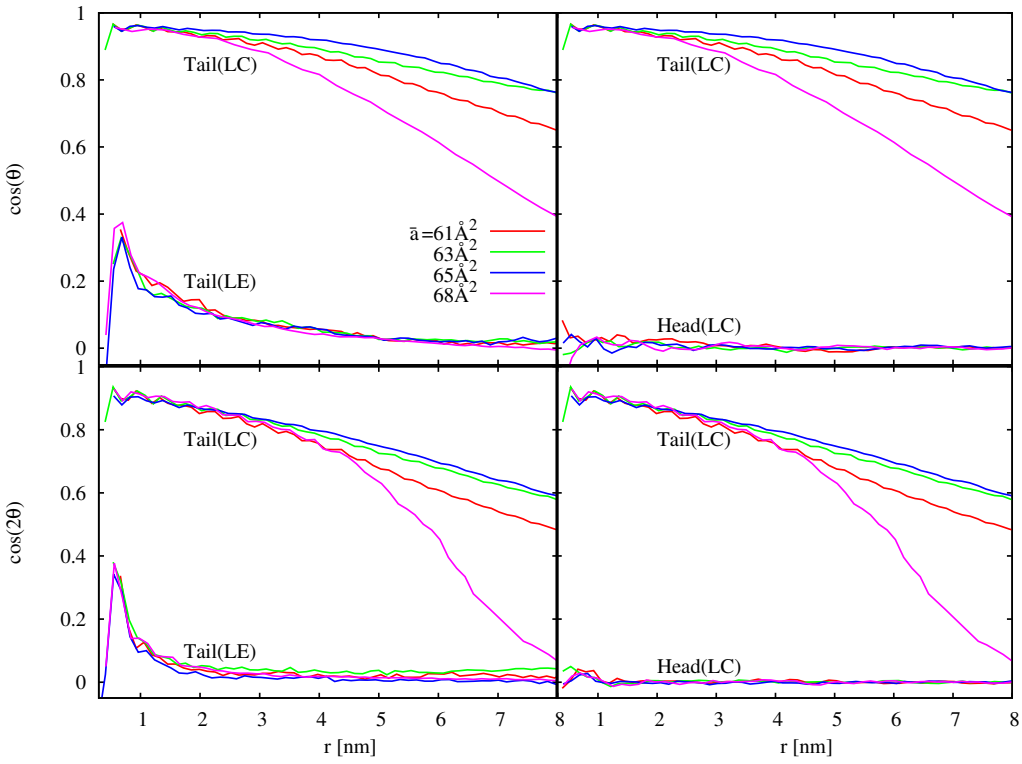

Figure 3.7: Polar (top) and nematic (bottom) correlation functions of $\hat{\boldsymbol{h}}_{2D}$ and $\hat{\boldsymbol{t}}_{2D}$ vectors versus relative distance between lipids in systems with $\bar{a}$ = 61, 63, 65 and 68 Å^2. Curves labelled "Tail(*LC*)" and "Tail(*LE*)" correspond to correlations of $\hat{\boldsymbol{t}}_{2D}$ vectors of lipids in *LC* and *LE* domains, respectively. Curves labelled "Head(*LC*)" correspond to correlations of $\hat{\boldsymbol{h}}_{2D}$ vectors of lipids in *LC* domains.

On the other hand, the correlation functions of the $\hat{\boldsymbol{t}}_{2D}$ vectors of lipids in *LE* do-

mains ("Tail(LE)") show some short-ranged polar order only, and decay within very short distances. Therefore LE domains are characterised by 2D disorder (as we can also see visually in Fig. 3.6) that is originated by the 3D disorder of acyl chains. Lastly, the correlation functions of the $\hat{\boldsymbol{h}}_{2D}$ vectors of lipids in a LC ("Head(LC)") and LE ("Head(LE)") domains show no order at all (for clarity we only present in Fig. 3.7 the "Head(LC)" correlations). Thus, once again, this result indicates that the in-plane component of the dipole moment of lipids is irrelevant for theoretical modelling [3, 9, 11], although it is also true that the predictive capabilities of the force fields concerning the lipid head groups may be an issue.

Bibliography

[1] E. Parra and J. Pérez-Gil, *Composition, structure and mechanical properties define performance of pulmonary surfactant membranes and films*, Chemistry and Physics of Lipids **185**, 153 (2015).

[2] J. Pérez-Gil, K. Nag, S. Taneva, and K. Keough, *Pulmonary surfactant protein sp-c causes packing rearrangements of dipalmitoylphosphatidylcholine in spread monolayers*, Biophysical Journal **63**, 197 (1992).

[3] C. W. McConlogue and T. K. Vanderlick, *A close look at domain formation in dppc monolayers*, Langmuir **13**, 7158 (1997).

[4] K. Y. C. Lee and H. M. McConnell, *Quantized symmetry of liquid monolayer domains*, The Journal of Physical Chemistry **97**, 9532 (1993).

[5] K. Klopfer and T. Vanderlick, *Isotherms of dipalmitoylphosphatidylcholine (dppc) monolayers: Features revealed and features obscured*, Journal of Colloid and Interface Science **182**, 220 (1996).

[6] K. Ekelund, E. Sparr, J. Engblom, H. Wennerström, and S. Engström, *An afm study of lipid monolayers. 1. pressure-induced phase behavior of single and mixed fatty acids*, Langmuir **15**, 6946 (1999).

[7] P. Dhar, E. Eck, J. N. Israelachvili, D. W. Lee, Y. Min, A. Ramachandran, A. J. Waring, and J. A. Zasadzinski, *Lipid-protein interactions alter line tensions and domain size distributions in lung surfactant monolayers*, Biophys. J. **102**, 56 (2012).

[8] A. K. Sachan and J. A. Zasadzinski, *Interfacial curvature effects on the monolayer morphology and dynamics of a clinical lung surfactant*, Proceedings of the National

Academy of Sciences **115**, E134 (2018).

[9] H. Mohwald, *Phospholipid and phospholipid-protein monolayers at the air/water interface*, Annual Review of Physical Chemistry **41**, 441 (1990).

[10] M. Seul and D. Andelman, *Domain shapes and patterns: The phenomenology of modulated phases*, Science **267**, 476 (1995).

[11] F. Campelo, A. Cruz, J. Pérez-Gil, L. Vázquez, and A. Hernández-Machado, *Phase-field model for the morphology of monolayer lipid domains*, The European Physical Journal E **35**, 49 (2012).

[12] J. H. Ipsen, O. G. Mouritsen, and M. J. Zuckermann, *Decoupling of crystalline and conformational degrees of freedom in lipid monolayers*, The Journal of Chemical Physics **91**, 1855 (1989).

[13] R. Almog and D. S. Berns, *The role of polar groups in the interaction of dipalmitoyl phosphatidylcholine with chlorophyll a in monolayers*, Journal of Colloid and Interface Science **81**, 332 (1981).

[14] F. MacRitchie and P. Fletcher, *Chemistry at interfaces: Academic press, san diego, ca, 1990.* (1990).

[15] J. Israelachvili, *Self-assembly in two dimensions: Surface micelles and domain formation in monolayers*, Langmuir **10**, 3774 (1994).

[16] C. M. Rosetti, A. Mangiarotti, and N. Wilke, *Sizes of lipid domains: What do we know from artificial lipid membranes? what are the possible shared features with membrane rafts in cells?*, Biochimica et Biophysica Acta (BBA) - Biomembranes **1859**, 789 (2017).

[17] H. M. McConnell and V. T. Moy, *Shapes of finite two-dimensional lipid domains*, The Journal of Physical Chemistry **92**, 4520 (1988).

[18] H. Dominguez, A. M. Smondyrev, and M. L. Berkowitz, *Computer simulations of phosphatidylcholine monolayers at air/water and ccl4/water interfaces*, The Journal of Physical Chemistry B **103**, 9582 (1999).

[19] G. Ma and H. C. Allen, *Dppc langmuir monolayer at the airwater interface: probing the tail and head groups by vibrational sum frequency generation spectroscopy*, Langmuir **22**, 5341 (2006).

[20] H. Hauser, I. Pascher, R. Pearson, and S. Sundell, *Preferred conformation and molecular*

packing of phosphatidylethanolamine and phosphatidylcholine, Biochimica et Biophysica Acta (BBA) - Reviews on Biomembranes **650**, 21 (1981).

[21] F. Bresme, *Theoretical approaches to investigate anisotropic particles at fluid interfaces* (Elsevier, Amsterdam, 2018), pp. 233 – 260,

[22] J. Huang and A. D. MacKerell Jr, *Charmm36 all-atom additive protein force field: Validation based on comparison to nmr data*, Journal of Computational Chemistry **34**, 2135 (2013).

[23] J. B. Klauda, R. M. Venable, J. A. Freites, J. W. O'Connor, D. J. Tobias, C. Mondragon-Ramirez, I. Vorobyov, A. D. MacKerell, and R. W. Pastor, *Update of the charmm all-atom additive force field for lipids: Validation on six lipid types*, The Journal of Physical Chemistry B **114**, 7830 (2010).

[24] S. Izadi, R. Anandakrishnan, and A. V. Onufriev, *Building water models: A different approach*, The Journal of Physical Chemistry Letters **5**, 3863 (2014).

[25] M. Javanainen, A. Lamberg, L. Cwiklik, I. Vattulainen, and O. H. S. Ollila, *Atomistic model for nearly quantitative simulations of langmuir monolayers*, Langmuir **34**, 2565 (2018).

[26] S. Baoukina, E. Mendez-Villuendas, and D. P. Tieleman, *Molecular view of phase coexistence in lipid monolayers*, Journal of the American Chemical Society **134**, 17543 (2012).

[27] J. Miñones, J. R. Patino, O. Conde, C. Carrera, and R. Seoane, *The effect of polar groups on structural characteristics of phospholipid monolayers spread at the air–water interface*, Colloids and Surfaces A: Physicochemical and Engineering Aspects **203**, 273 (2002).

[28] S. Jo, T. Kim, V. G. Iyer, and W. Im, *Charmm-gui: A web-based graphical user interface for charmm*, Journal of Computational Chemistry **29**, 1859 (2008).

[29] S. Pronk, S. Páll, R. Schulz, P. Larsson, P. Bjelkmar, R. Apostolov, M. R. Shirts, J. C. Smith, P. M. Kasson, D. van der Spoel, et al., *Gromacs 4.5: a high-throughput and highly parallel open source molecular simulation toolkit*, Bioinformatics **29**, 845 (2013).

[30] GROMACS, *reference manual*.

[31] M. Deserno and C. Holm, *How to mesh up ewald sums. i. a theoretical and numerical comparison of various particle mesh routines*, The Journal of Chemical Physics **109**, 7678 (1998).

[32] H. J. C. Berendsen, J. P. M. Postma, W. F. van Gunsteren, A. DiNola, and J. R. Haak, *Molecular dynamics with coupling to an external bath*, The Journal of Chemical Physics **81**, 3684 (1984).

[33] D. J. Evans and B. L. Holian, *The Nose–Hoover thermostat*, The Journal of Chemical Physics **83**, 4069 (1985).

[34] D. H. de Jong, S. Baoukina, H. I. Ingólfsson, and S. J. Marrink, *Martini straight: Boosting performance using a shorter cutoff and gpus*, Computer Physics Communications **199**, 1 (2016).

[35] D. Poger and A. E. Mark, *Lipid bilayers: The effect of force field on ordering and dynamics*, Journal of Chemical Theory and Computation **8**, 4807 (2012).

[36] J. M. Crane, G. Putz, and S. B. Hall, *Persistence of phase coexistence in disaturated phosphatidylcholine monolayers at high surface pressures*, Biophysical Journal **77**, 3134 (1999).

[37] H. M. Mansour and G. Zografi, *Relationships between equilibrium spreading pressure and phase equilibria of phospholipid bilayers and monolayers at the airwater interface*, Langmuir **23**, 3809 (2007).

[38] A. Ranjkesh, M. Ambrožič, T. J. Sluckin, and S. Kralj, *Domain patterns in homogeneous and random perturbed nematic liquid crystals: A simulation study*, Molecular Crystals and Liquid Crystals **615**, 26 (2015).

Part II.

Diffusion in Lipid Membranes

4

Fluctuating Hydrodynamics in Quasi-Two-Dimensional Diffusion

In the second part of this thesis, we will study a phenomenon that is traditionally set in colloidal particle systems at liquid-liquid and air-liquid interfaces. This phenomenon leads to exotic properties concerning the collective and the individual motion of particles, which we believe may explain recent questions about the diffusion of membrane lipids [1–4], essential to understand the dynamic processes within the pulmonary surfactant system [5].

In recent years, colloidal science has become a popular interdisciplinary field with branches in physics, chemistry, nanotechnology and material science [6–9]. A science plenty of revolutionary applications, among which, we would like to remark the building of new materials, the developing of biological sensors and the controlling of rheological properties [10–12]. Due to the close relation between rheological properties and interfaces, the colloidal science has also had a great impact on the study of colloidal suspensions systems in liquid-liquid and air-liquid interfaces [13], also known as quasi-two-dimensional (Q2D) systems. Experimentally, colloids can be trapped in liquid interfaces by means of ultrasound forces (acoustophoresis) [14–16] or optical tweezers [17], or simply using two walls [18, 19]. By contrast, other instances show that the natural positioning of colloidal particles is in liquid interfaces *e.g.* Asphaltenes in water-oil mixtures [20] or surfactants in polar fluids [21].

Advances in the field of colloidal suspensions has prompted a new understanding of the dynamic properties of Q2D systems. Specifically, a 1995 experiment of a diblock copolymer (polystyrene-b-polymethilmethacrylate) supported in an air-water interface unveiled that particles/molecules in Q2D systems behave anomalously [22]. In this experiment, authors made use of evanescent light scattering techniques (lightning the interface from the air phase) to study the *collective diffusion* coefficient $D_c(k)$[1] of polymers. And as a result, they arrived to the conclusion that the collective diffusion coefficient diverges inversely proportional to the wavenumber k of the system ($D_c \propto 1/k$) [22] due to an ill-defined self-diffusion coefficient [23]. Thereby, the real merit of this study was to discover the pathological behaviour of the dynamic properties of Q2D systems since the real cause was not well tackled.

Then, posterior discoveries about the anomalous onset of collective diffusion coefficients in Q2D systems was made by Bleibel *et al.* in 2014 [24], and successively verified by means of different points of views [25, 26]. In their original work, they correctly pointed out that the assumption of incompressible fluid can not generally be guaranteed in the plane of motion of particles (interface) due to the fact that part of the fluid is expelled into the normal direction (out of the interface), so that the fluid is apparently compressible ($\nabla_{\parallel} \cdot \boldsymbol{\mathcal{M}} = -\partial_z \boldsymbol{\mathcal{M}} \neq \mathbf{0}$). As a consequence, in the reciprocal linearised diffusion equation appears an extra term, $\hat{\boldsymbol{k}} \cdot \int \exp(-\mathrm{i}\boldsymbol{k}\cdot\boldsymbol{r})\, \boldsymbol{\mathcal{M}}(\boldsymbol{r}, z=0)\, d\boldsymbol{r} \cdot \hat{\boldsymbol{k}}$, which leads to a divergent collective diffusion coefficient. Physically, this divergent coefficient is also inferred from an effective pair-wise force between particles that emerges from the apparent compressibility of the fluid ($\boldsymbol{f} \propto \nabla_{\parallel} \cdot \boldsymbol{\mathcal{M}}$), being this force long-ranged and repulsive $\boldsymbol{f} \propto 1/r^2$ (Coulomb like) [26]. In this way, it is elucidated that the anomaly in the collective transport coefficient, although of hydrodynamic origin, was not due to an ill-defined self-diffusion coefficient. Eventually, it is stated that anomalous collective diffusion coefficients ($D_c(k) \propto 1/k$) is a general characteristic of Q2D systems *i.e.* it does not depended on the (short-range) interacting nature of particles, although the exponent differs close to walls [24–27]. Albeit, this effect, and its consequences, has not been treated in complex systems yet, for example a lipid membrane.

Therefore, to the end of elucidating whether membrane lipids behave as particles of Q2D systems, let us start in the present chapter, and continue in the next, providing some insight on this new phenomenon. Thus, during the present chapter, we will review the diffusion properties of particles within strict 2D liquid-liquid interfaces by means of

[1] The collective diffusion coefficient is referred to a diffusion coefficient of an entity that is composed of many particles/molecules.

a FDDFT-HI formalism. For that, in Sect. 4.2, we will study the ensemble average of a density of particles. Formally, it has been established that the ensemble average of the density of particles in systems without hydrodynamic interactions (uncorrelated walkers) [28, 29], and the ensemble average of the density of particles in incompressible fluids [30, 31] are governed by a diffusion equation (Fick's law). Notwithstanding, we will show that in Q2D systems this law is not valid any more, bringing with it the anomalous character of the collective diffusion coefficient. Then, in contrast to prior works [26], in Sect. 4.3 we will also study fluctuations around the ensemble average. So far it is known that, because of the hydrodynamic interactions, the ensemble average of the fluctuations in incompressible fluids is radically different with respect to the one of uncorrelated walkers [30, 31]; under specific circumstances hydrodynamic interactions lead to the so-called *giant fluctuations* [32, 33] and *colossal fluctuations* [34]. However, this phenomenon has not been addressed in Q2D hydrodynamic systems yet. As we will show, Q2D hydrodynamics leads to what we know as *quasi-giant fluctuations*.

Moreover, understanding fluctuations is meaningful for the next reasons: the first and more obvious reason is because what one can really observe/measure in experiments (*e.g.* by using fluorescence techniques) are the actual trajectories of particles and not their ensemble average[2]. Second, fluctuations contain key information about the microscopic mechanisms for the diffusion of particles *e.g.* the signature of hydrodynamics. And third, as we will show in Sect. 4.2 and 4.3, the generalisation of the Q2D theory to account for species density fluctuations appeals to be a natural extension that is suitable for direct comparison with fluorescence experiments.

4.1 Theory for Strict Quasi-Two-Dimensional Diffusion

To introduce the Q2D theory for the diffusion of particles in liquid interfaces, let us start considering N ideal (tracer) Brownian particles that are strictly confined in a 2D interface (interface width $\delta \to 0$), and surrounded by two incompressible fluids (one above and one below) of equal characteristics (density, viscosity, temperature, etc.).

We know that for a 3D particle systems, the Ito equations of motion associated with the Fokker-Planck equation for the probability density $P(\boldsymbol{Q}, t)$ ($\boldsymbol{Q} = \{\boldsymbol{q}_1, \cdots, \boldsymbol{q}_N\}$) of (cor-

[2]One may think that tracking many trajectories is equivalent to track the ensemble average, but this is not always true [32–34].

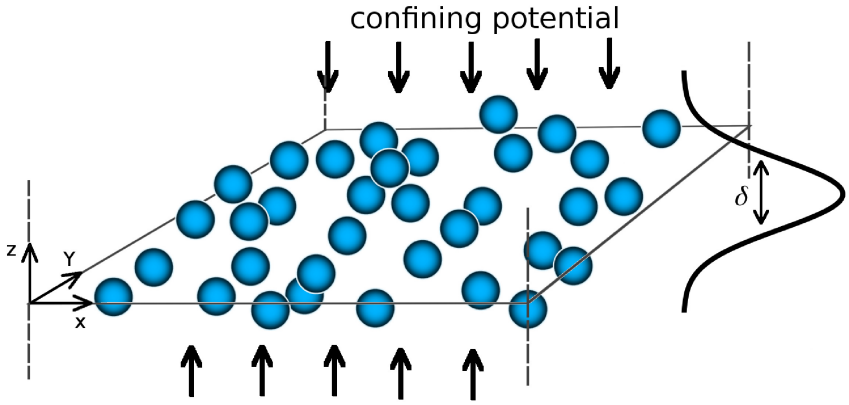

Figure 4.1: Schematic representation of a particle systems that is confined to a liquid-liquid interface of width δ by means of an external potential.

related) Brownian particles are given by Eqs. (2.19), which in the particular case of Q2D, may be split up as

$$d\boldsymbol{q}_i^{\parallel} = \boldsymbol{\mathcal{M}}^{\parallel}\boldsymbol{F}_i^{\parallel}dt + \left(2k_BT\boldsymbol{\mathcal{M}}^{\parallel}\right)^{\frac{1}{2}}\boldsymbol{\xi}_i^{\parallel}dt + k_BT\left(\nabla_{\boldsymbol{q}_i^{\parallel}}\cdot\boldsymbol{\mathcal{M}}^{\parallel}\right)dt, \quad i = 1\ldots N, \tag{4.1a}$$

$$d\boldsymbol{q}_i^{\perp} = \boldsymbol{\mathcal{M}}^{\perp}\boldsymbol{F}_i^{\perp}dt + \left(2k_BT\boldsymbol{\mathcal{M}}^{\perp}\right)^{\frac{1}{2}}\boldsymbol{\xi}_i^{\perp}dt + k_BT\left(\nabla_{\boldsymbol{q}_i^{\perp}}\cdot\boldsymbol{\mathcal{M}}^{\perp}\right)dt, \quad i = 1\ldots N, \tag{4.1b}$$

with the first set of equations associated with the motion of particles along the interface $(x-y)$ plane and the second with the motion of particles along the normal direction (z axis).

This decomposition is always true whenever one can diagonalize the mobility tensor by blocks,

$$\boldsymbol{\mathcal{M}} = \begin{bmatrix} \boldsymbol{\mathcal{M}}^{\parallel\parallel} & \boldsymbol{\mathcal{M}}^{\parallel\perp} \\ \boldsymbol{\mathcal{M}}^{\perp\parallel} & \boldsymbol{\mathcal{M}}^{\perp\perp} \end{bmatrix} = \begin{bmatrix} \boldsymbol{\mathcal{M}}^{\parallel} & \\ & \boldsymbol{\mathcal{M}}^{\perp} \end{bmatrix}, \tag{4.2}$$

which is in fact the case of symmetric positive semi-definite mobility tensors in Q2D systems: due to the symmetry of the confining forces (see Fig. 4.1) these cannot induce motion in the $(x-y)$ plane, in the same way that forces that are parallel to the interface cannot induce motion along the z axis. Thus, one could simply ignore the motion of particles in normal direction and focus on the in-plane direction (Eqs. (4.1a)).

Since in this chapter (and the subsequent) we will solely address incompressible fluids, at this point it is crucial to comment on the main difference between Eqs. (4.1a) and

Eqs. (2.19) when $\nabla \cdot \boldsymbol{\mathcal{M}} = 0$. This is that the last term in Eqs. (4.1a) ($k_B T \left(\nabla_{\boldsymbol{q}^{\parallel}} \cdot \boldsymbol{\mathcal{M}}^{\parallel}\right)$) remain non-zero, unlike it occurs in Eqs. (2.19) (2D and 3D systems). This fact may be understood as if fluids in Q2D systems were compressible in the plane of motion of particles [26]. To put into context this unusual term, let us consider the following academic derivation; the velocity of a particle i, $\boldsymbol{v}_i^{\parallel}$, due to the drag created by a particle j is $\boldsymbol{v}_i^{\parallel} = \int P_{\perp}(z_j) \boldsymbol{\mathcal{M}}_{ij}^{\parallel\perp}(\boldsymbol{q}_i, \boldsymbol{q}_j) \boldsymbol{F}_j^{\perp}(z_j) dz_j$, where $\boldsymbol{F}_j^{\perp} = -\nabla V(z_j)$ is an external force that constrains the particle j to move in the $x-y$ plane. Since particles are assumed to be strictly confined (infinitely large confining forces), their motion in the z axis is expected to be infinitely fast. In this way, we can consider that particles are in a steady state along the z axis, and so the probability distribution $P(\boldsymbol{Q}, t)$ factorises,

$$P(\boldsymbol{Q}, t) \approx P_{\parallel}(\boldsymbol{Q}_{\parallel}, t) \prod_{i=1}^{N} P_{\perp}(z_i), \tag{4.3}$$

with $P_{\perp}(z)$ the probability distributions of particles along the z axis, which becomes a Dirac delta under strict confinement, and $P_{\parallel} = 1$ (ideal gas approximation) the probability distribution of particles along the $x-y$ axes. Thus, if we rewrite the velocity $\boldsymbol{v}_i^{\parallel}$ using $\boldsymbol{F}^{\perp}(z_j) P(z_j) = k_B T \partial_{z_j} P_{\perp}(z_j)$, then integrating by parts we find that $\boldsymbol{v}_i^{\parallel} = \int \boldsymbol{\mathcal{M}}_{ij}^{\parallel\perp}(\boldsymbol{q}_i, \boldsymbol{q}_j) \partial_{z_j} P_{\perp}(z_j) dz_j = -k_B T \int P_{\perp}(z_j) \partial_{z_j} \boldsymbol{\mathcal{M}}_{ij}^{\parallel\perp}(\boldsymbol{q}_i, \boldsymbol{q}_j) dz_j$. Again, using the strict confinement limit and the fact that $\nabla_{\boldsymbol{q}_i^{\parallel}} \cdot \boldsymbol{\mathcal{M}}_{ij}^{\parallel\parallel} + \partial_{z_j} \boldsymbol{\mathcal{M}}_{ij}^{\parallel\perp} = 0$ we get $\boldsymbol{v}_i^{\parallel\parallel} = -k_B T \nabla_{\boldsymbol{q}_2^{\parallel}} \cdot \boldsymbol{\mathcal{M}}_{ij}^{\parallel\parallel}\left(\boldsymbol{q}_i^{\parallel}, \boldsymbol{q}_j^{\parallel}\right) = k_B T \nabla_{\boldsymbol{q}_i^{\parallel}} \cdot \boldsymbol{\mathcal{M}}_{ij}^{\parallel\parallel}\left(\boldsymbol{q}_i^{\parallel}, \boldsymbol{q}_j^{\parallel}\right)$. Eventually, using the Rotne-Prager-Yamakawa (RPY) approximation for the mobility (see Appx. A for more details on its derivation), we arrive at the conclusion that the unusual drift term $k_B T \left(\nabla_{\boldsymbol{q}^{\parallel}} \cdot \boldsymbol{\mathcal{M}}^{\parallel}\right)$ in Eq. (4.1a) can be interpreted as a long-ranged repulsive force $\boldsymbol{f} \propto \nabla_{\boldsymbol{q}^{\parallel}} \cdot \boldsymbol{\mathcal{M}}^{\parallel} \propto 1/r^2$ [26], induced by the confining forces.

Then, as introduced in Sect. 2.3.2, and explained in detail in Refs. [30, 31], applying Ito's rule in Eq. (4.1a) yields a closed non-linear Ito stochastic advection-diffusion equation for the microscopic density $\hat{\rho}$

$$\begin{aligned} \frac{\partial \hat{\rho}(\boldsymbol{r}, t)}{\partial t} = &- \nabla \cdot \left(\boldsymbol{\omega}(\boldsymbol{r}, t) \hat{\rho}(\boldsymbol{r}, t)\right) + D_s \nabla^2 \hat{\rho}(\boldsymbol{r}, t) \\ &+ (k_B T) \nabla \cdot \left(\hat{\rho}(\boldsymbol{r}, t) \int \boldsymbol{\mathcal{M}}(\boldsymbol{r} - \boldsymbol{r}') \nabla' \hat{\rho}(\boldsymbol{r}', t) \, d\boldsymbol{r}'\right), \end{aligned} \tag{4.4}$$

where D_s is the self-diffusion coefficient and $\boldsymbol{\omega}$ a random fluid velocity field which emerges from the thermal fluctuations of the background fluid. Notice that the non-linear (and non-local) term in (4.4) can be rewritten as $-(k_B T) \nabla \cdot (\hat{\rho}(\boldsymbol{r}, t) \int \nabla' \cdot \boldsymbol{\mathcal{M}}(\boldsymbol{r} - \boldsymbol{r}') \hat{\rho}(\boldsymbol{r}', t) \, d\boldsymbol{r}')$, which vanishes for 2D and 3D incompressible fluids, where $\nabla \cdot \boldsymbol{\mathcal{M}} = 0$. In Q2D, however, it

does not.

Equation (4.4) can trivially be solved by a linear approximation ($\hat{\rho}(\boldsymbol{r},t) \approx \rho_0 + \delta\rho(\boldsymbol{r},t)$, with $\delta\rho(\boldsymbol{r},t) \ll \rho_0$) in Fourier space if we neglect the random advection term (we further explore this approximation in Sect. 4.2). So we find that the linearised microscopic density evolves according to

$$\tilde{\delta\rho}(\boldsymbol{k},t) = \tilde{\delta\rho}(\boldsymbol{k},0)\exp\left(-k^2 D_c(k)t\right), \tag{4.5}$$

where the tilde denotes the Fourier transform, $\boldsymbol{k}$ the wavenumber vector and $D_c(k)$ the collective diffusion coefficient[3],

$$D_c(k) = D_s + (k_B T\rho_0)\left(\hat{\boldsymbol{k}}\cdot\tilde{\boldsymbol{\mathcal{M}}}_{\boldsymbol{k}}\cdot\hat{\boldsymbol{k}}\right). \tag{4.6}$$

Since the mobility $\boldsymbol{\mathcal{M}}$ (and thus its Fourier transform $\tilde{\boldsymbol{\mathcal{M}}}_{\boldsymbol{k}}$) is a symmetric positive semi-definite tensor, $\hat{\boldsymbol{k}}\cdot\tilde{\boldsymbol{\mathcal{M}}}_{\boldsymbol{k}}\cdot\hat{\boldsymbol{k}} \geq 0$, hydrodynamics always speeds up the collective dynamics of Q2D systems, and it does proportionally with the density ρ_0. To quantify how much the collective dynamics (in particular the collective diffusion) is enhanced we approximate the mobility tensor $\boldsymbol{\mathcal{M}}$ in the far field ($ka \ll 1$) by the Oseen tensor, for which $\hat{\boldsymbol{k}}\cdot\tilde{\boldsymbol{\mathcal{M}}}_{\boldsymbol{k}}\cdot\hat{\boldsymbol{k}} \approx \frac{1}{4\eta k}$ (see Ref. [25] and Appx B). Thus, Eq. (4.6) results in a collective diffusion coefficient that diverges inversely with the wavenumber, *i.e.* the larger a set of particles is, the faster it collectively diffuses,

$$D_c(k) = D_s\left(1 + \frac{1}{L_h k}\right), \tag{4.7}$$

with $L_h = 4\eta D_s/(k_B T\rho_0) = \left(\frac{2}{3\phi}\right)a$ a hydrodynamic length above which the collective diffusion behaves anomalously and $\phi = \rho_0\pi a^2$ the 2D density fraction. Remarkably, we reproduce results predicted by Bleibel *et al.* [24, 25] for the anomalous behaviour of the collective diffusion ($D_c \propto 1/k$). However, as we will later show, this is not the only anomaly of Q2D systems.

[3] In this chapter we will not distinguish between the short and long-time collective diffusion coefficient so that we will generically refer to $D_c(k)$.

4.2 Ensemble Average in Two-Dimensional Systems

Another of the implications of the drift term $k_BT\left(\nabla_{\parallel}\cdot\boldsymbol{\mathcal{M}}^{\parallel}\right)$ in Eq. (4.1a) is that the Q2D ensemble average density is not governed by a diffusion equation, as in 2D and 3D systems. Hence, to further evaluate this fact, in the following sections we will study the time evolution of the ensemble average of the density of particles and the ensemble average of the density of labelled species (mixtures). To this end, we will consider two main systems to which we will refer as setup A and setup B.

Table 4.1: Typical parameters used for the majority of the simulations throughout this chapter. All simulations use square simulating domains of length L with PBC. Depending on the setup proposed, we use different density fractions ϕ, domain length and grid cells N_{FFT} while the radius of the particles a, thermal energy k_BT, fluid density ρ_f and fluid dynamic viscosity η remain intact (units are arbitrary).

Setup	k_BT, ρ_f, η and a	ϕ	N	$L_x \times L_y$	N^2_{FFT}
A	1.0	0.5	10^5	800.0×800.0	1152^2
B	1.0	1.0	10^5	560.5×560.5	864^2

4.2.1 Ensemble Average for Density

To obtain the ensemble average of Eq. (4.4) we first need to average over the noise ($\boldsymbol{\omega}$) realisations [30, 35]. For ideal but hydrodynamic interacting particles the ensemble average equation is

$$\frac{\partial\rho\left(\boldsymbol{r},t\right)}{\partial t} = \nabla\cdot\left(D_s\nabla\rho\left(\boldsymbol{r},t\right)\right) + \left(k_BT\right)\nabla\cdot\left(\int\boldsymbol{\mathcal{M}}\left(\boldsymbol{r},\boldsymbol{r'}\right)\nabla'\rho^{(2)}\left(\boldsymbol{r},\boldsymbol{r'},t\right)\,d\boldsymbol{r'}\right), \quad (4.8)$$

a non-linear non-local integro-differential equation that is not closed *i.e.* Eq. (4.8) depends on the unknown two-point correlation function $\rho^{(2)}$. For an ideal gas, though, a standard closure equation is

$$\rho^{(2)}\left(\boldsymbol{r},\boldsymbol{r'},t\right) \approx \rho\left(\boldsymbol{r},t\right)\rho\left(\boldsymbol{r'},t\right), \quad (4.9)$$

which yields so a closed non-lineal non-local integro-differential equation

$$\frac{\partial \rho(\boldsymbol{r},t)}{\partial t} = \nabla \cdot \left(D_s \nabla \rho(\boldsymbol{r},t) + (k_B T)\, \rho(\boldsymbol{r},t) \int \boldsymbol{\mathcal{M}}(\boldsymbol{r},\boldsymbol{r}')\, \nabla' \rho(\boldsymbol{r}',t)\, d\boldsymbol{r}' \right). \tag{4.10}$$

Comparing Eq. (4.4) with (4.10) we see that the main between difference (roughly speaking) is essentially the stochastic term $-\nabla \cdot (\boldsymbol{\omega}(\boldsymbol{r},t)\, \hat{\rho}(\boldsymbol{r},t))$. So we understand that using the approximation (4.9) is equivalent to neglecting fluctuations. It is also important to note that Eq. (4.10) does not represent a diffusive process, but instead an advective-diffusive process. Thus, the term $\boldsymbol{v}\rho = (k_B T)\, \nabla \cdot \int \boldsymbol{\mathcal{M}}(\boldsymbol{r},\boldsymbol{r}')\, \nabla \rho(\boldsymbol{r}',t)\, d\boldsymbol{r}' \rho(\boldsymbol{r},t)$ acts as an advection, induced by the confining forces. This is radically different from 2D and 3D hydrodynamics, where Eq. (4.10) reduces to a diffusion equation ($\frac{\partial \rho(\boldsymbol{r},t)}{\partial t} = D_s \nabla^2 \rho(\boldsymbol{r},t)$).

Then, to test how good an approach (4.9) is, we compare the numerical solution of Eq. (4.10) with simulations of Eq. (4.1a) for which, we propose an efficient algorithm for Q2D Brownian dynamics with hydrodynamic interactions (BDHI) simulations [36], which is implemented as part of the solver FLUAM [37–40] (see Appx. B for more details about Q2D BDHI algorithms). In this numerical experiment, we use parameters of setup A in Tab. 4.1 and we average the numerical results over one thousand simulations. In the initial configuration, we randomly distribute 9×10^4 particles in a square simulation box of $L_x \times L_y = 800 \times 800\ au$. Then, we create an over-density in the stripe $-L_y/6 \leq y \leq L_y/6$ using 1×10^4 extra particles.

In particular, in the left panel of Fig. 4.2 we compare results for $\rho(y,t)\, \frac{1}{L} \int_{-L_x/6}^{L_x/6} \rho(x,y,t)\, dx$ from Q2D BDHI simulations (Algo. 1 in Appx. B) and the numerical solution of Eq. (4.10) assuming that D_s is equal to the shot-time self-diffusion coefficient ($D_s = D_0$), given by the Stokes-Einstein relation[4]. After a time $t = 2100\ au$ we can see that both solutions agree remarkably well. This suggests that neglecting the stochastic term in (4.10), or equivalently, neglecting fluctuations is a reasonable approach in this respect. On the other hand, to evaluate the effect of the non-linear term of Eq. (4.10) in the ensemble average of the density, we compare the Q2D BDHI simulations with simulations of Eq. (4.1a) in absence of hydrodynamic interactions (BD simulations). In this way we demonstrate that the initially imposed over-densities in BD and BDHI are homogenised differently. Therefore, because of the extra term $(k_B T)\, \rho(\boldsymbol{r},t) \int \boldsymbol{\mathcal{M}}(\boldsymbol{r},\boldsymbol{r}')\, \nabla' \rho(\boldsymbol{r}',t)\, d\boldsymbol{r}'$, the evolution of density perturbations in Q2D system are very different from the ones in 2D and 3D systems.

[4] $D_0 = k_B T/(6\pi\eta a)$, with η the fluid dynamic viscosity and a the particle radius.

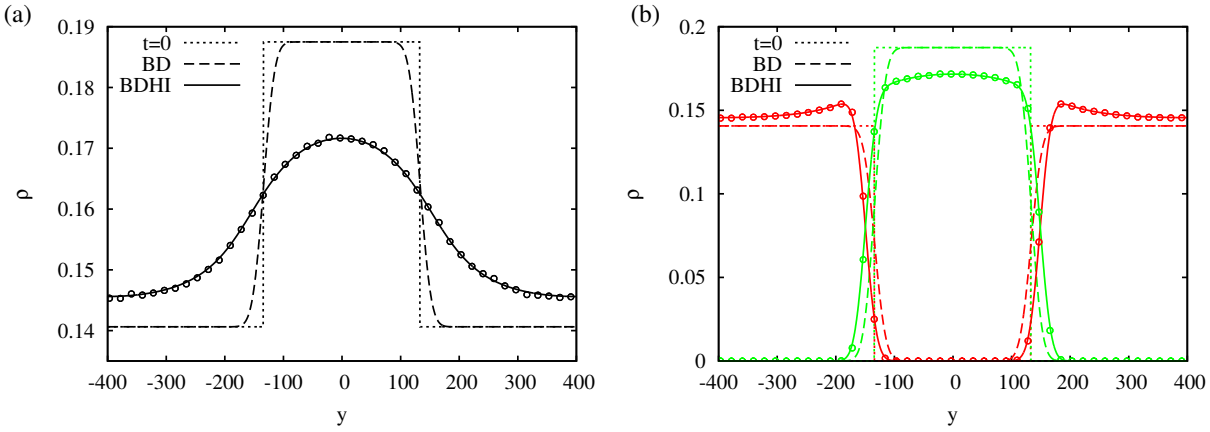

Figure 4.2: Ensemble averaged of the one dimensional density profiles at time $t = 0$ (dotted lines) and at time $t = 2100$ *au* using the numerical solution of Eq. (4.10) (solid lines), Q2D BDHI simulations (circles) and BD simulations (dashed lines). On the left we illustrate the evolution of the over-density relative to the homogeneous density background. On the right we show the evolution of the density in the three thirds of the L_y domain. We tag as "green" particles to those particles that initially started in the second third and "red" to the others.

4.2.2 Ensemble Average for Mixtures

To complement the previous result for the ensemble average density, we study in this section how density perturbations are homogenised in term of spatial distributions. It is very well known that in 2D and 3D hydrodynamics density perturbations decay showing the so-called *Gaussian tails*, however, in previous works it has been shown that in Q2D hydrodynamics density perturbations decay rather differently [24, 26], showing $1/r^3$ power-law tails. So far, the precise manner in which Q2D hydrodynamics develop these power-law tails remains unknown, which leads to the following questions: *Do some/all/few particles quickly displace very far, so as to create a power-law tail for $t > 0$?* Or, *do particles still displace by small diffusive displacements, but a power-law tail arises in the average due to correlations?*.

Hence, to answer these questions, we will use an extension of the standard Q2D theory for diffusion to account for labelled species. The extension of Eq. (4.10) is straightforward to write down by simply considering that the total density is now a sum of n species densities $\rho = \rho_1 + \rho_2 + \ldots \rho_n$ (ideal approximation). Then, by substituting this total density ρ into Eq. (4.10) we find a set of n coupled non-linear non-local differential equations.

Here, for practical reasons, we will consider the case of binary mixtures[5], for which we

[5]Fluorescence experiments usually deal with two species: labelled and unlabelled particles.

only have two coupled non-linear non-local differential equations

$$\begin{aligned}\frac{\partial \rho_R(\boldsymbol{r},t)}{\partial t} &= \nabla\cdot\left(D_s\nabla\rho_R(\boldsymbol{r},t) + (k_BT)\,\rho_R(\boldsymbol{r},t)\int \boldsymbol{\mathcal{M}}(\boldsymbol{r},\boldsymbol{r}')\,\nabla'\rho(\boldsymbol{r}',t)\,d\boldsymbol{r}'\right), \\ \frac{\partial \rho_G(\boldsymbol{r},t)}{\partial t} &= \nabla\cdot\left(D_s\nabla\rho_G(\boldsymbol{r},t) + (k_BT)\,\rho_G(\boldsymbol{r},t)\int \boldsymbol{\mathcal{M}}(\boldsymbol{r},\boldsymbol{r}')\,\nabla'\rho(\boldsymbol{r}',t)\,d\boldsymbol{r}'\right),\end{aligned} \tag{4.11}$$

one for the first species, let us say red (R), and another for the second specie, let us say green (G), with $\rho = \rho_R + \rho_G$.

Then, we use an initial configuration as the one used in the left panel of Fig. 4.2, and we label all the particles in the central stripe $-L_y/6 \leq y \leq L_y/6$ as green, and the remaining particles as red. In this way, we manage to track the density evolution in the central stripe and the remaining domain independently. Eventually, in the right panel of Fig. 4.2 we compare results for $\rho_G(y,t)$ and $\rho_R(y,t)$ from Q2D BDHI simulations (Algo. 1 in Appx. B), BD simulations and the numerical solution of Eq. (4.11) assuming that $D_s = D_0$. After a time $t = 2100\ au$, while in absence of hydrodynamic interactions we get the typical Gaussian tails (as expected), in Q2D hydrodynamics we observe the excess of green particles in the middle stripe gives rise an effective unbalanced repulsion among particles in the direction of minus the total density (ρ) gradient that drags both red and green particles. As a consequence, the density of red particles shows a power-law tail $1/y^3$ whereas the density of green particles shows a rapidly decaying Gaussian tail. This can be further investigated by means of the computation of the second moment

$$\left\langle y^2\right\rangle_G(t) = \frac{\left\langle \int \rho_G(y,t)\,y^2 dy\right\rangle}{\left\langle \int \rho_G(y,t)\,dy\right\rangle}. \tag{4.12}$$

In the left panel of Fig. 4.3 we appreciate that the Q2D hydrodynamics leads to a notably non-linear trend at short-times, which eventually vanishes to lead a fast but normal diffusion, as always occurs in the absence of hydrodynamics. This suggests that, at long-times, systems tend to exhibit Gaussian tails. In other words, if we repeat the previous calculations with $\rho_G = \rho_R$ =const. we would find that the power-law tails disappear since the repulsion among particles are now balanced on average, *i.e.* particles are not dragged on average. In fact, this is predicted by Eqs. (4.11), where in such case the non-linear term disappears and one obtains a pair of uncoupled diffusion equations.

To verify this claim, we perform additional Q2D BDHI simulations using parameters of setup B in Tab. 4.1 and we average the numerical results over one hundred simulations and over time intervals of $2\times10^3\ au$. In the initial configuration, we randomly distribute

1×10^5 particles in a square simulation box of $L_x \times L_y = 560.5 \times 560.5\ au$, and we label all the particles in the central stripe $-L_y/6 \leq y \leq L_y/6$ as green, and the remaining particles as red. Then, we study the one dimensional ensemble average of the density of green particles. From the right panel of Fig. 4.3, we can demonstrate that the density of green particles exhibits Gaussian tails, which supports our conjecture, although simulations only agree with numerical solution of Eq. (4.11) when the self-diffusion coefficient is $D_s = 0.85 D_0$ (dashed lines), rather than $D_s = D_0$ (solid lines).

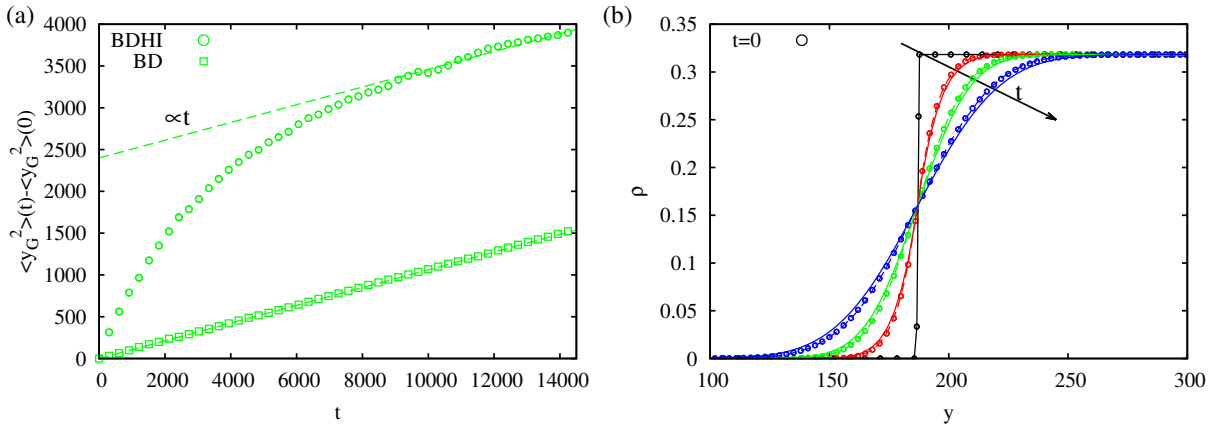

Figure 4.3: (a) Mean squared displacement $\langle y^2 \rangle_G (t) - \langle y^2 \rangle_G (0)$ along the y axis for the green particles with hydrodynamic interactions (circles), and without hydrodynamics interactions (squares). (b) Time evolution of the one dimensional ensemble average density of green particles starting from $\rho_G = \rho_R = 0.318$. The density is averaged over time intervals $0 < t \leq 2 \times 10^3$ (red lines), $2 \times 10^3 < t \leq 4 \times 10^3$ (green lines) and $4 \times 10^3 < t \leq 6 \times 10^3$ (blue lines). Theoretical results are based on Eq. (4.11) assuming $D_s = D_0$ (solid lines) and $D_s = 0.85 D_0$ (dashed lines). Q2D BDHI simulations are represented with circles.

This last result suggests that, even if particles are tracers, the self-diffusion coefficients D_s at short and long-times are different ($D_0 \neq D_s^{(l)}$). To show this unexpected feature of the Q2D hydrodynamics we study the self-diffusion coefficient of a tracer particle from the slope of the mean squared displacement (MSD). For that, we calculate the average square displacement of tracer particles over the x axis (eq.). The self-diffusion coefficient can also be computed using a non-equilibrium method. This is done by pulling a single and isolated particle with a force $\boldsymbol{F} = F\hat{\boldsymbol{x}} = 1\hat{\boldsymbol{x}}$. Then, in linear response theory, the non-equilibrium

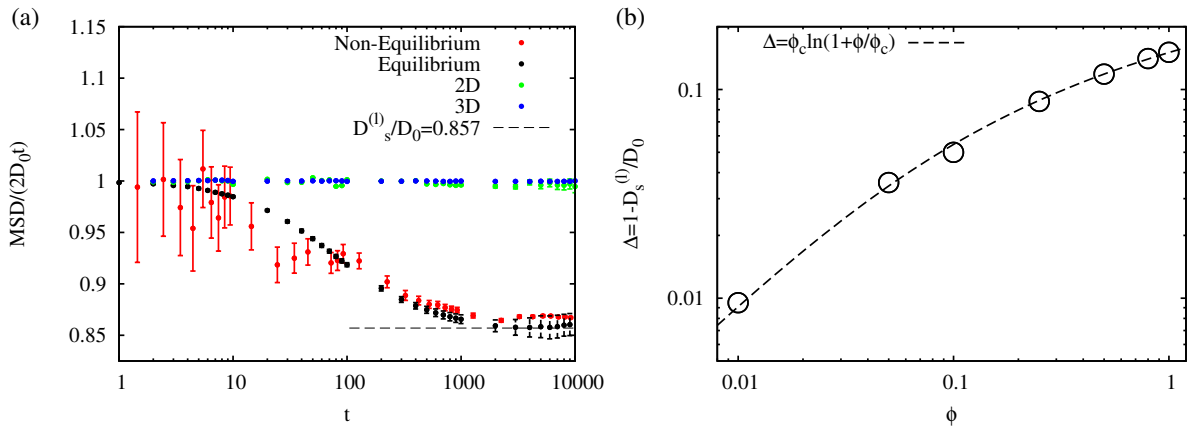

Figure 4.4: (a) Scaled self-diffusion coefficient of Q2D ideal particles computed from the slope of the equilibrium MSD (black circles) and non-equilibrium MSD (red circles) MSD at density fraction $\phi = 1$. Note that the statistical error bars at short-time for non-equilibrium calculations are quite large (even after averaging over 5000 independent simulations) due to the fact that only a single particle is pulled. For comparison, we include the scaled self-diffusion coefficient of 2D (green circles) and 3D (blue circles) ideal particles. (b) Relative decreases Δ in the self-diffusion coefficient of Q2D ideal particles versus the concentration of particles.

MSD (n.eq.) can be related with the equilibrium one [41, 42] as follows

$$\mathrm{MSD}_{\mathrm{n.eq.}}(t) = -\frac{F}{k_B T}\int_0^t \langle x(0)\dot{x}(t-t')\rangle \, \mathrm{d}t' = \frac{F}{2k_B T}\mathrm{MSD}_{\mathrm{eq.}}(t), \tag{4.13a}$$

$$\mathrm{MSD}_{\mathrm{eq.}}(t) = \left\langle (x(t)-x(0))^2 \right\rangle. \tag{4.13b}$$

As we illustrate in the left panel of Fig. 4.4, the self-diffusion coefficient is not constant in time but exhibits a transient regime that differentiates between its short and long-time character. Thus, for the particular case of density packing $\phi = 1.0$ we find that the long-time self-diffusion coefficient $D_s^{(l)} \approx 0.85 D_0$. This means that the value of $D_s = 0.85 D_0$ (dashed lines) used in the right panel of Fig 4.3 corresponds to $D_s^{(l)}$. The same operations were systematically done for smaller density fractions, yielding long-time self-diffusion coefficients $D_s^{(l)}(\phi = 1) \leq D_s^{(l)}(\phi) \leq D_0$. As we show in the right panel of Fig. 4.4, the difference between the short and long-time self-diffusion coefficients progressively vanishes as $\phi \to 0$, following the empirical law $\Delta \approx \phi_c \ln(1 + \phi/\phi_c)$, with $\phi_c \approx 0.0493$. This basically means that if we reduce ϕ the self-diffusion coefficient tends to behave as that of 2D and 3D hydrodynamics *i.e.* ideally. Therefore, although particles do repeal each other equally on average, occasionally, thermal fluctuations lead to local unbalanced repulsions that eventually leads to a time-dependent self-diffusion coefficient. Thereby, the

approximation (4.9) leads to average densities equations ((4.11) and (4.10)) that are not exact, *i.e.* fluctuations play a non-negligible role. However, because the non-linear term in Eqs. (4.10) and (4.11) dominates, differences in the panels of Fig. 4.2 are unnoticeable.

4.3 Fluctuations in Two-Dimensional Systems

In the previous section we have just seen that the thermal fluctuations are important in Q2D hydrodynamics; we have just seen that density fluctuations (due to the thermal agitation) renormalise the self-diffusion coefficient of ideal (tracer) particles at long times (times larger than the typical time needed by a particle to diffuse a distance larger than its diameter). Thus, it seems natural to wonder, *are thermal fluctuations in Q2D hydrodynamics giant or colossal?*.

To answer this question, in the subsequent sections we will investigate the density fluctuations in systems at equilibrium and out of equilibrium. More precisely, we will study the ensemble averaged spectrum of the fluctuations

$$S(\boldsymbol{k}) = \left\langle \tilde{\delta\rho}(\boldsymbol{k},t)\left(\tilde{\delta\rho}(\boldsymbol{k},t)\right)^{\star}\right\rangle, \tag{4.14}$$

also known as the *static structure factor*, and the ensemble averaged spectrum of the fluctuations at a given time t

$$F_c(\boldsymbol{k},t) = \left\langle \tilde{\delta\rho}(\boldsymbol{k},t)\left(\tilde{\delta\rho}(\boldsymbol{k},0)\right)^{\star}\right\rangle, \tag{4.15}$$

also known as the *collective intermediate scattering function*.

4.3.1 Equilibrium Fluctuations

4.3.1.1 Density Fluctuations

Obtaining a linearised fluctuating hydrodynamics (FHD) equation from Eq. (4.4) is far from trivial [30, 31], however, this can be essentially guessed from the fluctuation-dissipation balance and from the fact that uncorrelated particles at thermodynamic equilibrium must present a radial distribution function $g(r) = 1$ and $S(k) = \rho_0$. Thereby, one finds that the

linearised FHD version of Eq. (4.4) is written as follows

$$\begin{aligned}\frac{\partial \delta\rho(\boldsymbol{r},t)}{\partial t} &= D_s\nabla^2\delta\rho(\boldsymbol{r},t) + \sqrt{2\rho_0 D_s}\,\nabla\cdot\boldsymbol{\xi}\,(\boldsymbol{r},t) \\ &\quad + \rho_0\,(k_BT)\,\nabla\cdot\left(\int \boldsymbol{\mathcal{M}}(\boldsymbol{r}-\boldsymbol{r}')\nabla'\delta\rho(\boldsymbol{r}',t)\,d\boldsymbol{r}'\right) - \rho_0\,(\nabla\cdot\boldsymbol{\omega})\,,\end{aligned} \tag{4.16}$$

where $\sqrt{2\rho_0 D_s}\,\nabla\cdot\boldsymbol{\xi}\,(\boldsymbol{r},t)$ is a random term that is included for the fluctuation-dissipation balance of the term $D_s\nabla^2\delta\rho(\boldsymbol{r},t)$, with $\boldsymbol{\xi}\,(\boldsymbol{r},t)$ a white noise Gaussian vector [31]. Notice also that the term $\rho_0\,(\nabla\cdot\boldsymbol{\omega})$ comes from the random advection field

$$\nabla\cdot(\boldsymbol{\omega}\,(\boldsymbol{r},t)\,\rho_0\,(\boldsymbol{r},t)) = \rho_0\,(\boldsymbol{r},t)\,\nabla\cdot\boldsymbol{\omega}\,(\boldsymbol{r},t) + \boldsymbol{\omega}\,(\boldsymbol{r},t)\cdot\nabla\rho_0\,(\boldsymbol{r},t)\,, \tag{4.17}$$

in Eq. (4.4), which upon linearisation at equilibrium results in a null $\boldsymbol{\omega}\cdot\nabla\rho_0$ term.

In Fourier space Eq. (4.16) reads

$$\frac{\partial\tilde{\delta\rho}(\boldsymbol{k},t)}{\partial t} = -\left(D_sk^2 + k_BT\rho_0\left(\boldsymbol{k}\cdot\tilde{\boldsymbol{\mathcal{M}}}_{\boldsymbol{k}}\cdot\boldsymbol{k}\right)\right)\tilde{\delta\rho}(\boldsymbol{k},t) + \sqrt{2\rho_0 D_s}\,\left(\mathrm{i}k\tilde{\xi}_{\boldsymbol{k}}\right) - \rho_0\,(\mathrm{i}\boldsymbol{k}\cdot\tilde{\boldsymbol{\omega}})\,, \tag{4.18}$$

with $\tilde{\xi}_{\boldsymbol{k}}$ white noises (one per wavenumber) that are associated with $\boldsymbol{\xi}\,(\boldsymbol{r},t)$. Using the fact that Eq. (4.18) represents an Ornstein-Uhlenbeck process ($dx = -axdt + \sigma d\xi$), $\left\langle\tilde{\boldsymbol{\omega}}_{\boldsymbol{k}}\tilde{\boldsymbol{\omega}}^{\star}_{\boldsymbol{k}}\right\rangle = 2\,(k_BT)\,\tilde{\boldsymbol{\mathcal{M}}}_{\boldsymbol{k}}$ and $\tilde{\boldsymbol{\omega}}_{\boldsymbol{k}}$ and $\tilde{\xi}_{\boldsymbol{k}}$ are uncorrelated, we find the equilibrium spectrum

$$S(\boldsymbol{k}) = S_0 = \left\langle\left|\tilde{\delta\rho}\right|^2\right\rangle = \frac{\rho_0 D_sk^2 + \rho_0^2\,(k_BT)\left(\boldsymbol{k}\cdot\tilde{\boldsymbol{\mathcal{M}}}_{\boldsymbol{k}}\cdot\boldsymbol{k}\right)}{D_sk^2 + \rho_0\,(k_BT)\left(\boldsymbol{k}\cdot\tilde{\boldsymbol{\mathcal{M}}}_{\boldsymbol{k}}\cdot\boldsymbol{k}\right)} = \rho_0, \tag{4.19}$$

which corresponds to the value for an ideal gas at equilibrium.

Finally, the collective intermediate scattering function is

$$F_c(\boldsymbol{k},t) = \boldsymbol{S}_0\exp\left(-k^2D_c(k)t\right), \tag{4.20}$$

with $D_c(k) = D_s + \left(\frac{k_BT\rho_0}{\eta k}\right)c_1(ak)$ given by Eqs. (4.6) and (B.7). We validate this result by comparing the numerical values of the collective intermediate scattering function and the collective diffusion coefficient with their theoretical predictions. For that, we use the parameter of setup B in Tab. 4.1. Then, we see in the right panel of Fig. 4.5 an excellent agreement for the collective diffusion coefficient. Likewise, we see in the left panel of Fig. 4.5 that the collective intermediate scattering function decay agrees with the theoretical

mono-exponential decay (4.20) [24, 25]. However, it is not clear yet how a time-dependent self-diffusion coefficient may affect these quantities (F_c and D_c). Thus, to better face this issue we will present additional results in the next section and in Chap. 5.

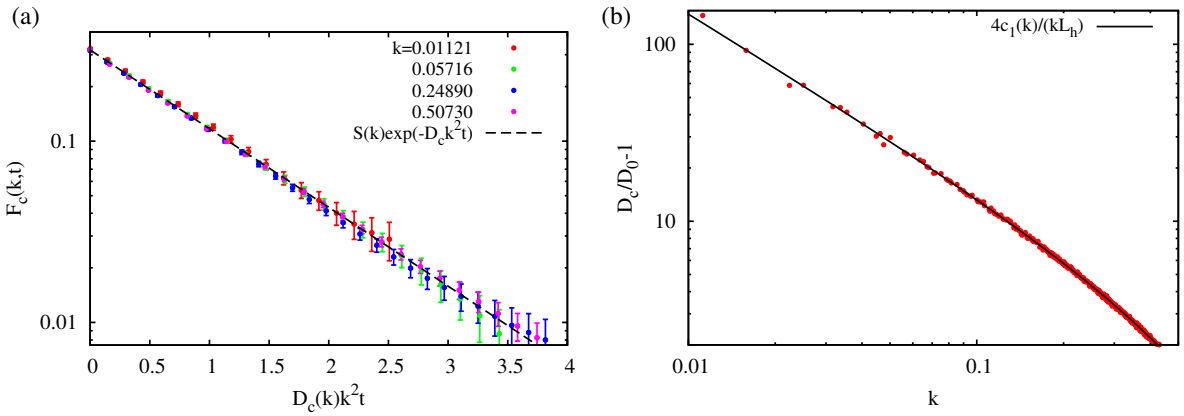

Figure 4.5: (a) Collective intermediate scattering functions obtained from the average of 1000 Q2D BDHI simulations (circles) and compared with their theoretical predictions (dashed line). (b) Collective diffusion coefficient relative to the short-time self-diffusion coefficient as a function of the wavenumber. Red circles stand for $D_c(k)/D_0 - 1$ values estimated from the fitting of $F_c(k,t)$ to a mono-exponential with time rate $\tau^{-1} = D_c(k)k^2$. The solid line represents the theoretical prediction.

4.3.1.2 Density Fluctuations in Binary Mixtures

Following the same philosophy as the previous section, we infer from Eqs. (4.11) and (4.16) the linearised FHD Eqs.

$$\begin{aligned}
\frac{\partial \delta\rho_R(\boldsymbol{r},t)}{\partial t} &= D_s\nabla^2\delta\rho_R(\boldsymbol{r},t) + \sqrt{2\rho_{R_0}D_s}\,\nabla\cdot\boldsymbol{\xi}_R(\boldsymbol{r},t) \\
&\quad + \rho_{R_0}(k_BT)\,\nabla\cdot\left(\int \boldsymbol{\mathcal{M}}(\boldsymbol{r}-\boldsymbol{r}')\nabla'\delta\rho_G(\boldsymbol{r}',t)\,d\boldsymbol{r}'\right) - \rho_{R_0}(\nabla\cdot\boldsymbol{\omega}), \\
\frac{\partial \delta\rho_G(\boldsymbol{r},t)}{\partial t} &= D_s\nabla^2\delta\rho_G(\boldsymbol{r},t) + \sqrt{2\rho_{G_0}D_s}\,\nabla\cdot\boldsymbol{\xi}_G(\boldsymbol{r},t) \\
&\quad + \rho_{G_0}(k_BT)\,\nabla\cdot\left(\int \boldsymbol{\mathcal{M}}(\boldsymbol{r}-\boldsymbol{r}')\nabla'\delta\rho_G(\boldsymbol{r}',t)\,d\boldsymbol{r}'\right) - \rho_{G_0}(\nabla\cdot\boldsymbol{\omega}).
\end{aligned} \tag{4.21}$$

In Fourier space, Eqs. (4.21) read

$$\partial_t \begin{bmatrix} \tilde{\delta\rho}_R \\ \tilde{\delta\rho}_G \end{bmatrix} = -k^2 \begin{bmatrix} D_s + \Delta_R D_c^{(s)} & \Delta_R D_c^{(s)} \\ \Delta_G D_c^{(s)} & D_s + \Delta_G D_c^{(s)} \end{bmatrix} \begin{bmatrix} \tilde{\delta\rho}_R \\ \tilde{\delta\rho}_G \end{bmatrix} + \text{Stochastic Forcing} =$$
$$= -k^2 \boldsymbol{M} \begin{bmatrix} \tilde{\delta\rho}_R \\ \tilde{\delta\rho}_G \end{bmatrix} + \text{Stochastic Forcing}, \tag{4.22}$$

where we have introduced the collective diffusion enhancement for the specie x

$$\Delta_x D_c^{(s)}(k) = D_0 \left(\frac{4c_1(ka)}{kL_{h,x}} \right) \approx \frac{k_B T}{4\eta k} \rho_{x_0}, \tag{4.23}$$

with $L_{h,x} = \left(\frac{2}{3\phi_{x_0}}\right) a$ a hydrodynamic length-scale above which the collective diffusion of the species x behaves anomalously. Then, for a binary mixture the structure factor is given by a 2×2 matrix

$$\boldsymbol{S}(\boldsymbol{k}) = \begin{bmatrix} \left\langle \tilde{\delta\rho}_R(\boldsymbol{k},t) \left(\tilde{\delta\rho}_R(\boldsymbol{k},t)\right)^\star \right\rangle & \left\langle \tilde{\delta\rho}_R(\boldsymbol{k},t) \left(\tilde{\delta\rho}_G(\boldsymbol{k},t)\right)^\star \right\rangle \\ \left\langle \tilde{\delta\rho}_G(\boldsymbol{k},t) \left(\tilde{\delta\rho}_R(\boldsymbol{k},t)\right)^\star \right\rangle & \left\langle \tilde{\delta\rho}_G(\boldsymbol{k},t) \left(\tilde{\delta\rho}_G(\boldsymbol{k},t)\right)^\star \right\rangle \end{bmatrix} = \begin{bmatrix} S_{RR} & S_{RG} \\ S_{GR} & S_{GG} \end{bmatrix}. \tag{4.24}$$

Using the fact that Eqs. (4.21) represent a system of Ornstein-Uhlenbeck equations it is trivial to show that for equilibrium conditions the structure factor is

$$\boldsymbol{S}(\boldsymbol{k}) = \boldsymbol{S}_0 = \begin{bmatrix} \rho_{R_0} & 0 \\ 0 & \rho_{G_0} \end{bmatrix}, \tag{4.25}$$

which is logical since ideal and uniform mixtures are characterised by uncoupled species diffusion equations (see Eqs. (4.11)).

Finally, the collective intermediate scattering function for a binary mixture is

$$\boldsymbol{F}_c(\boldsymbol{k},t) = S_0 \exp\left(-\boldsymbol{M} k^2 t\right), \tag{4.26}$$

where $\exp\left(-\boldsymbol{M} k^2 t\right)$ has to be interpreted as a Taylor series of the exponential function *i.e.* $\exp[-\boldsymbol{M} k^2 t] = \sum_{n=0}^{\infty} \frac{(-k^2 t)^n}{n!} \boldsymbol{M}^n$.

In the case of an equimolar mixture ($\rho_{R_0} = \rho_{G_0} = \rho_0/2$) Eq. (4.26) yields

$$\begin{aligned} F_{c_{RR}}(\boldsymbol{k},t) = F_{c_{GG}}(\boldsymbol{k},t) &= \frac{\rho_0}{4}\left(\exp\left(-D_c k^2 t\right) + \exp\left(-D_s k^2 t\right)\right), \\ F_{c_{RG}}(\boldsymbol{k},t) = F_{c_{GR}}(\boldsymbol{k},t) &= \frac{\rho_0}{4}\left(\exp\left(-D_c k^2 t\right) - \exp\left(-D_s k^2 t\right)\right), \end{aligned} \tag{4.27}$$

which turns out to be a sum of two modes, one associated with the self-diffusion coefficient D_s and another associated with the collective diffusion coefficient D_c.

Very interestingly, for binary mixtures in which one of the species is in a much lower proportion, let us say the red species ($\rho_{R_0} \ll \rho_{G_0} \approx \rho_0$), we get that its collective intermediate scattering function is given as

$$F_{c_{RR}}(\boldsymbol{k},t) \approx \rho_{R_0} \exp\left(-D_s k^2 t\right), \tag{4.28}$$

which is very convenient to study the behaviour of the collective intermediate scattering function exclusively as a function of the self-diffusion coefficient D_s. To this end, we perform Q2D BDHI simulations using parameters of setup B in Tab. 4.1. In the initial configuration, we randomly distribute 1×10^5 particles in a square simulation box of $L_x \times L_y = 560.5 \times 560.5\ au$, and we randomly label 1/16 of the particles as red. In this way, we finally obtain a $F_{c_{RR}}$ that exhibits two exponential regimes, one associated with the short-time self-diffusion coefficient (solid lines in Fig. 4.6) and another associated with the long-time self-diffusion coefficient (dashed lines in Fig. 4.6). This means that fluctuations not only renormalise the self-diffusion coefficient of particles but also play a role in the collective dynamics of particles. In particular, the renormalisation of the self-diffusion coefficient may also lead to a renormalisation of the collective diffusion coefficient. So far, though, we have not found any trace of a renormalised collective diffusion coefficient, and neither do other authors [25].

It must be said that, for ideal particles, the renormalisation of D_s is so small that any effect of it on D_c may be hidden by the numerical uncertainty. To elucidate this issue, we will further explore in Chap. 5 the possible renormalisation of D_c at long-times by means of BDHI simulations. Alternatively, one might prove this issue from a Q2D theory for the diffusion that includes memory effects, although this theory is beyond the scope of this thesis.

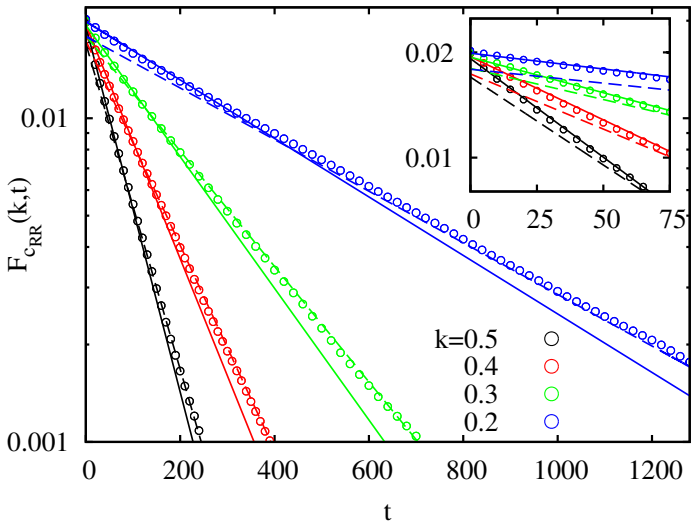

Figure 4.6: Collective intermediate scattering function for red particles in a binary mixture with $\rho_{R_0}/\rho_{G_0} \sim 1/16$ and $\phi = 1$. In solid lines we show the theoretical prediction (4.3) with $D_s = D_0$ and in dashed lines $D_s = D_s^{(l)} = 0.85D_0$. In the inset, we zoom in on $F_{c_{RR}}$ in the region $t \in [0, 75]$.

4.3.2 Non-Equilibrium Fluctuations

We are aware that this is not the first time it is reported that thermal fluctuations renormalise the dynamics of particle systems [31–34]; theoretically, linearised FHD equations have predicted that non-equilibrium fluctuations in 2D and 3D hydrodynamics alter the dynamics of mixing *i.e.* the non-equilibrium fluctuations are strongly enhanced (colossal and giant fluctuations are shown) and long-ranged ($S(k) \propto 1/k^4$) compared to the equilibrium fluctuations.

Non-equilibrium fluctuations have not been measured in Q2D hydrodynamics yet. Thus, the idea of this section is to elucidate whether non-equilibrium fluctuation in Q2D hydrodynamics may be giant or colossal. To this end, we will study the non-equilibrium density fluctuations by imposing an initial density gradient [43]. And we will investigate the magnitude and the dynamics of the non-equilibrium density fluctuations from the static structure factor. To make things as simple as possible, from the theoretical point of view, we will assume that the gradients are smooth in space and constant in time, although during simulations these vary both in space and time.

4.3.2.1 Density Gradient

To get the non-equilibrium spectrum of fluctuations, let us consider in this section Q2D systems with a constant and weak density gradient $\nabla\rho_0 = g\hat{\boldsymbol{y}}$. Since the non-equilibrium FHD equation is unknown, we propose Eq. (4.16) as the best guess of its linearised version *i.e.* we are assuming that the ensemble average of the non-equilibrium FHD equation is the same as the approximated Eq. (4.10) (linear response approximation). By doing so we obtain that the linearised non-equilibrium FHD equation is

$$\begin{aligned}\frac{\partial\delta\rho(\boldsymbol{r},t)}{\partial t} &= D_s\nabla^2\delta\rho(\boldsymbol{r},t) + \sqrt{2\rho_0 D_s}\,\nabla\cdot\boldsymbol{\xi}\,(\boldsymbol{r},t)\\ &\quad + \rho_0\,(k_BT)\,\nabla\cdot\left(\int \boldsymbol{\mathcal{M}}(\boldsymbol{r}-\boldsymbol{r}')\nabla'\delta\rho(\boldsymbol{r}',t)\,d\boldsymbol{r}'\right) - \rho_0\,(\nabla\cdot\boldsymbol{\omega}) - \boldsymbol{\omega}\cdot\nabla\rho_0,\end{aligned} \tag{4.29}$$

where now, in contrast to the previous sections, there is also an extra term involved ($\boldsymbol{\omega}\cdot\nabla c_0$) that comes from the stochastic advection term (4.17).

Taking the Fourier transform of the expression (4.29) and considering that the wavenumber $\boldsymbol{k}$ points in the direction perpendicular to the density gradient $\nabla\rho_0$ ($\boldsymbol{k}\perp\hat{\boldsymbol{y}}$), Eq. (4.29) yields

$$\begin{aligned}\frac{\partial\tilde{\delta\rho}\,(\boldsymbol{k},t)}{\partial t} &= -\left(D_sk^2 + \rho_0\left(\frac{k_BT}{\eta}\right)kc_1(ka)\right)\tilde{\delta\rho} + \sqrt{2\rho_0D_s}\,\left(\mathrm{i}k\tilde{\xi}_{\boldsymbol{k}}\right)\\ &\quad - \mathrm{i}\rho_0\sqrt{\frac{2\,(k_BT)\,kc_1\,(ka)}{\eta}}\,\tilde{\xi}^{(1)}_{\boldsymbol{k}} - g\sqrt{\frac{2\,(k_BT)\,c_2\,(ka)}{\eta k}}\,\tilde{\xi}^{(2)}_{\boldsymbol{k}},\end{aligned} \tag{4.30}$$

where $\tilde{\xi}_{\boldsymbol{k}}$ are white noises associated with $\boldsymbol{\xi}\,(\boldsymbol{r},t)$, and $\tilde{\xi}^{(1)}_{\boldsymbol{k}}$ and $\tilde{\xi}^{(2)}_{\boldsymbol{k}}$ are independent white noises associated with $\boldsymbol{\omega}$. Eventually, solving the Ornstein-Uhlenbeck Eq. (4.30) we obtain that

$$S(k) = \left\langle\left|\tilde{\delta\rho}\right|^2\right\rangle = S_0 + \Delta S = \rho_0 + g^2\frac{\pi a^2c_2\,(ka)}{k^2\,(a/6k + c_1\,(ka)\,\phi)}. \tag{4.31}$$

So, the structure factor (4.31) is given by the equilibrium ($S_0 = \rho_0$) and the non-equilibrium (ΔS) contributions of the fluctuations. Then, to estimate the relevance of the non-equilibrium contribution, we evaluate the relative structure factor increment at small wavenumbers ($ka \ll 1$) and compare it against that of 2D hydrodynamic systems,

$$\frac{\Delta S}{S_0}\,(ka\ll 1) \approx g^2\begin{cases}\frac{2}{\rho_0^2}\cdot\frac{1}{k^2}, & \text{for Q2D,}\\ \frac{4\pi}{\rho_0\,\ln\left(\frac{L}{3.71a}\right)}\cdot\frac{1}{k^4}, & \text{for 2D.}\end{cases} \tag{4.32}$$

As we already knew, non-equilibrium fluctuations of the density in 2D hydrodynamics are long-ranged ($S(k) \propto 1/k^4$) and colossal. Conversely, non-equilibrium fluctuations of the density in Q2D hydrodynamics seems to be much weaker ($S(k) \propto 1/k^2$). To get an insight into the magnitude of these fluctuations we assume that the density gradient is imposed over a length scale L ($g = \rho_0/L$). Thus, for wavenumber associated with the length of the domain $k = 2\pi/L$ we estimate

$$\max \frac{\Delta S}{S_0} \approx \begin{cases} \frac{1}{2\pi^2} \ll 1, & \text{for Q2D,} \\ \frac{(\frac{L}{a})^2 \phi}{4\pi^4 \ln(N_L/3.71)} \gg 1, & \text{for 2D.} \end{cases} \tag{4.33}$$

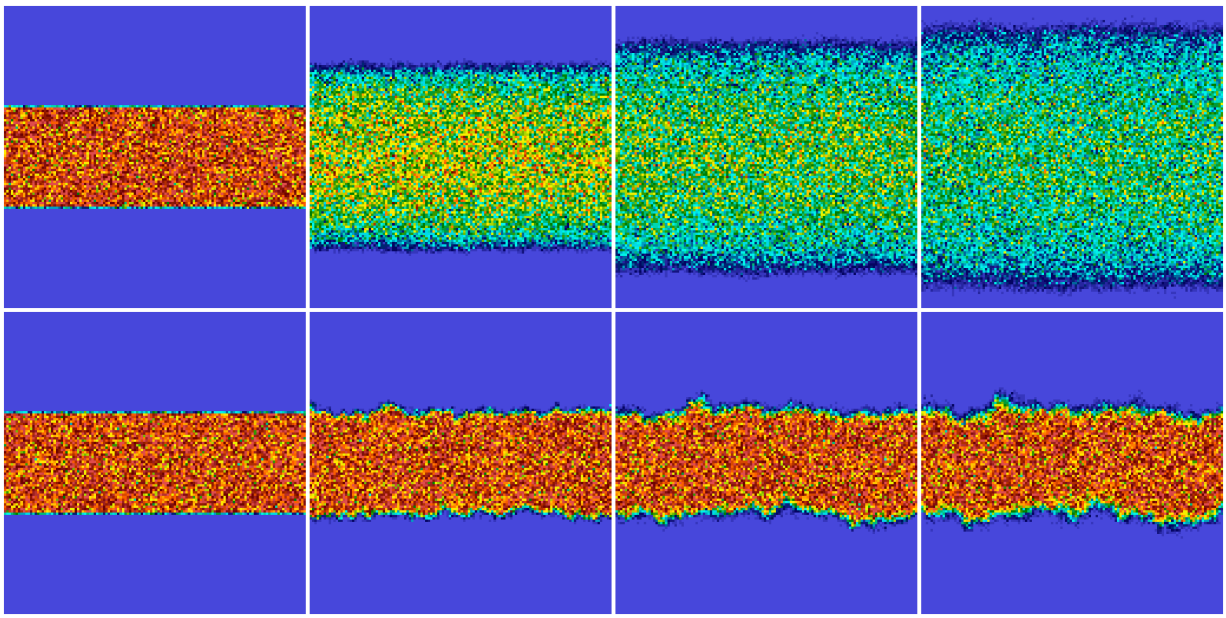

Figure 4.7: Time evolution (from left to right) of a density stripe that is initially localised in the $-L_y/6 \leq y \leq L_y/6$ domain. Images show the number density for Q2D (top) and 2D (bottom) simulations. We represent in colour the number density from 0 (blue) to 0.4 (red).

From Eq. (4.33) we demonstrate that the non-equilibrium fluctuations are much smaller than the equilibrium fluctuations, so that we believe the non-equilibrium fluctuations are hardly measurable. In any case, to ratify this fact, we performed Q2D BDHI simulations of non-equilibrium densities. Additionally, for completeness, we performed 2D BDHI simulations, for which we made use of the solver FLUAM [37–40]. In the initial configuration, we randomly distributed 1.333×10^5 in the middle stripe $-L_y/6 \leq y \leq L_y/6$ of a square simulation domain of $L_x \times L_y = 1121 \times 1121$ au with 128^2 N_{FFT}^2, *i.e.* the initial density

fraction in the middle stripe is $\phi = 1$, and we used the rest of the parameters of setup B in Tab. 4.1. By simple visual inspection of Fig. 4.7 we can appreciate large-scale structure of the density fluctuations for 2D (as we expected). By contrast, these are imperceptible in Q2D. Likewise, we were unable to measure them (within statistical accuracy) from the spectrum of the fluctuations. Consequently, we conclude that non-equilibrium fluctuations in Q2D are neither giant nor colossal. We finally note that, because of the additional effective repulsions among particles in Q2D, the central stripe in Q2D (top panels) evolves much faster than in 2D (bottom panels)[6].

4.3.2.2 Density Gradient in Binary Mixtures

We believe that, at the same time as the collective repulsions among particles enhance their collective motion in Q2D, these (long-ranged) repulsions may also be responsible for suppressing non-equilibrium fluctuations in Q2D. For instance, it is known that gravity suppresses fluctuations in 3D hydrodynamics [32, 33]. Thus, to elucidate this issue, in this section we consider non-equilibrium density fluctuations in the presence of a constant and weak gradient in the density of the species without a gradient in the total density *i.e.* $\nabla\rho_{R_0} = -\nabla\rho_{G_0} = g\hat{\boldsymbol{y}}$ (the second term in Eqs. (4.11) vanishes). Analogously to the previous section, since the non-equilibrium FHD equations for the species of a binary mixture are unknown, we propose Eqs. (4.21) as the best guess for their linearised versions. Taking the Fourier transform of these equations and considering that the wavenumber $\boldsymbol{k}$ points in the direction perpendicular to the density gradients $\nabla\rho_{R_0} = -\nabla\rho_{G_0}$ ($\boldsymbol{k} \perp \hat{\boldsymbol{y}}$) we arrive at

$$\begin{aligned}\partial_t \begin{bmatrix} \tilde{\delta\rho}_R \\ \tilde{\delta\rho}_G \end{bmatrix} &= -\left(D_s k^2 \boldsymbol{I} + \left(\frac{k_B T}{\eta}\right) k c_1(ak) \begin{bmatrix} \rho_{R_0} & \rho_{R_0} \\ \rho_{G_0} & \rho_{G_0} \end{bmatrix} \right) \begin{bmatrix} \tilde{\delta\rho}_R \\ \tilde{\delta\rho}_G \end{bmatrix} + \mathrm{i}k \begin{bmatrix} \sqrt{2D_s\rho_{R_0}}\,\tilde{\xi}_{\boldsymbol{k},R} \\ \sqrt{2D_s\rho_{G_0}}\,\tilde{\xi}_{\boldsymbol{k},G} \end{bmatrix} \\ &\quad - \mathrm{i}\sqrt{\frac{2\left(k_B T\right) k c_1\left(ka\right)}{\eta}} \begin{bmatrix} \rho_{R_0} \\ \rho_{G_0} \end{bmatrix} \tilde{\boldsymbol{\xi}}^{(1)}_{\boldsymbol{k}} - \sqrt{\frac{2\left(k_B T\right) c_2\left(ka\right)}{\eta k}} \begin{bmatrix} g \\ -g \end{bmatrix} \tilde{\boldsymbol{\xi}}^{(2)}_{\boldsymbol{k}}, \end{aligned} \tag{4.34}$$

where $\tilde{\xi}_{\boldsymbol{k},R}$ and $\tilde{\xi}_{\boldsymbol{k},G}$ are independent white noises associated with $\boldsymbol{\xi}_R(\boldsymbol{r},t)$ and $\boldsymbol{\xi}_G(\boldsymbol{r},t)$ respectively and $\tilde{\boldsymbol{\xi}}^{(1)}_{\boldsymbol{k}}$ and $\tilde{\boldsymbol{\xi}}^{(2)}_{\boldsymbol{k}}$ are independent vectorial white noises associated with $\boldsymbol{\omega}$.

[6] The Q2D BDHI simulation lasted a total time $t_{q2D} = 6775\ au$ while the 2D BDHI simulation lasted a total time $t_{2D} = 791\ au$. In this way we ensured that at the final time of the simulations the diffusive mixing is the same *i.e.* $D_{q2D}t_{q2D} = D_{2D}t_{2D}$.

Eventually, solving the linear Ornstein-Uhlenbeck Eqs. (4.34) we obtain

$$\boldsymbol{S}(k) = \boldsymbol{S}_0 + \Delta\boldsymbol{S} = \begin{bmatrix} \rho_{R_0} & 0 \\ 0 & \rho_{G_0} \end{bmatrix} + g^2 \frac{6\pi a\, c_2(ka)}{k^3} \begin{bmatrix} 1 & -1 \\ -1 & 1 \end{bmatrix}. \tag{4.35}$$

Therefore, the structure factor (4.35) is given by the equilibrium ($\boldsymbol{S}_0$) and the non-equilibrium ($\Delta\boldsymbol{S}$) contributions of the fluctuations. Again, to estimate how relevant the non-equilibrium contribution is, we evaluate the relative structure factor increment of one of the species, let us say green, at small wavenumbers ($ka \ll 1$) and compare it with the results from 2D hydrodynamic systems[7],

$$\frac{\Delta S_{GG}}{S_{0GG}}(ka \ll 1) \approx g^2 \begin{cases} \frac{3\pi a}{\rho_{G_0} k^3}, & \text{for Q2D,} \\ \frac{4\pi}{\rho_{G_0} \ln\left(\frac{L}{3.71a}\right)} \cdot \frac{1}{k^4}, & \text{for 2D.} \end{cases} \tag{4.36}$$

Although the non-equilibrium fluctuations of the density of the species in Q2D systems are still weaker than those of 2D, in this case, they seem to be larger than the non-equilibrium fluctuations of the total density. In fact, for equimolar mixtures ($\rho_{R_0} = \rho_{G_0} = \rho_0$), $\phi = 0.5$, $L/a = 560.5$, $k = 2\pi/L$ and $g \sim \rho_0/L$ we demonstrate that

$$\max \frac{\Delta S_{GG}}{S_{0GG}} \approx \begin{cases} \frac{3\phi L}{8\pi^3 a} \sim 5, & \text{for Q2D,} \\ \frac{\left(\frac{L}{a}\right)^2 \phi}{4\pi^4 \ln\left(\frac{L}{a}/3.71\right)} \sim 150, & \text{for 2D.} \end{cases} \tag{4.37}$$

This means that Q2D hydrodynamics exhibit large non-equilibrium fluctuations in binary mixture systems, which may be now measurable in simulations (and/or experiments). To achieve this goal, we performed new Q2D BDHI simulations using parameters of setup B in Tab. 4.1. And we performed BD simulations for comparison purposes[8]. In the initial configuration, we randomly distributed 1×10^5 particles in a square simulation box of $L_x \times L_y = 560.5 \times 560.5$ au, and we labelled all the particles in the central stripe $-L_y/6 \leq y \leq L_y/6$ as green, and the remaining particles as red. Although the differences between BD and Q2D were very subtle, by simple visual inspection of Fig. 4.7 we appreciate

[7] We recall that in 2D hydrodynamics particles are purely tracers, *i.e.* they do not interact via effective repulsive forces, therefore the structure factor in systems with a total density gradient ($\nabla\rho_0 = g\hat{\boldsymbol{y}}$) and a specie density gradient ($\nabla\rho_{R_0} = -\nabla\rho_{G_0} = g\hat{\boldsymbol{y}}$) are the same.

[8] Similarly to the previous section we fixed $D_{BD}t_{BD} = D_{q2D}t_{q2D} = D_{2D}t_{2D}$ in order to guarantee that at the final time of the simulation the diffusive mixing was the same.

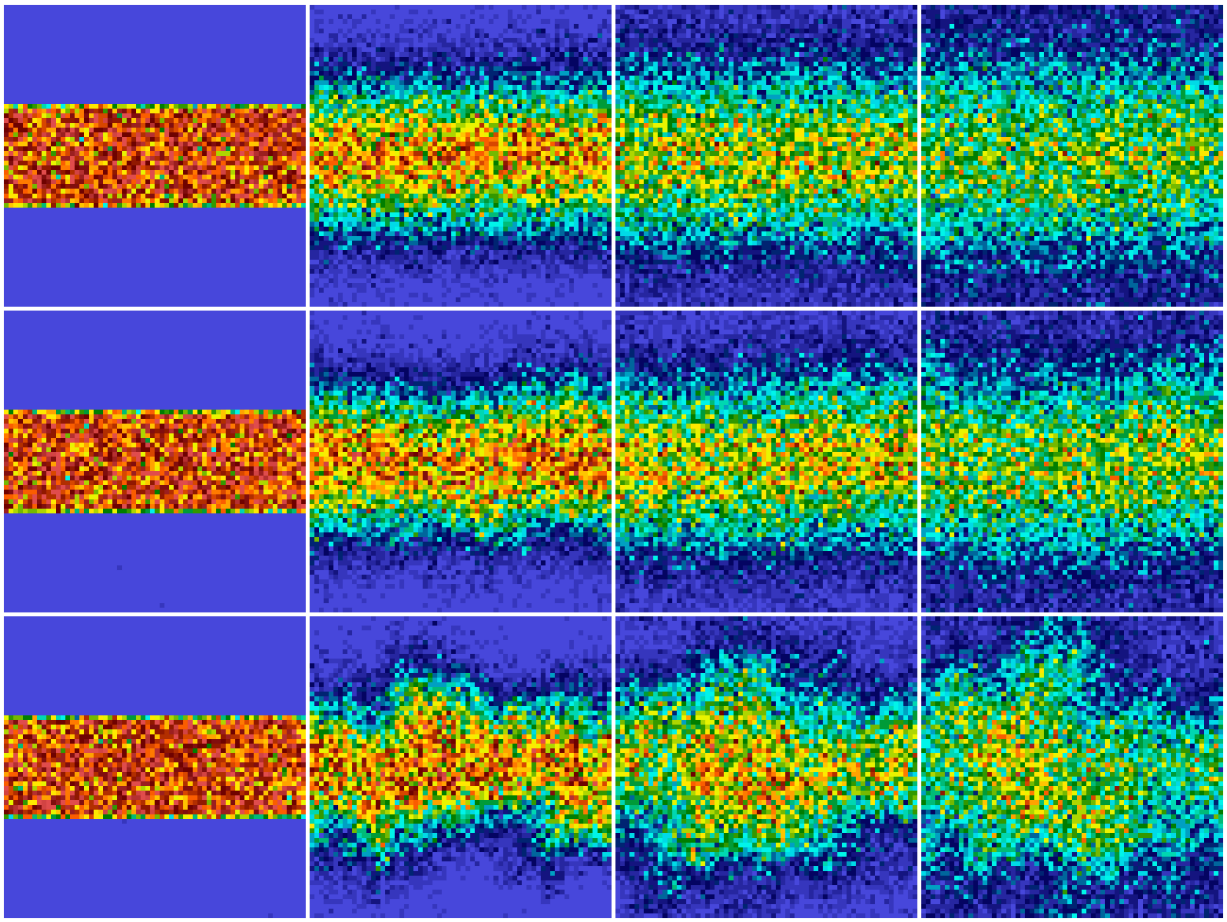

Figure 4.8: Time evolution (from left to right) of the density of green particles in a binary mixture (red particles not shown). Images show the number density for BD (top), Q2D BDHI (middle) and 2D (bottom) simulations. We represent in colour the number density from 0 (blue) to 0.4 (red).

that Q2D hydrodynamics in binary mixtures does exhibit large fluctuations, to which we refer to as *quasi-giant fluctuations* from now on. More evidently, there is no doubt that 2D hydrodynamics exhibits colossal fluctuations.

Interestingly, however, even if we use the linearised FHD equations we are able to predict colossal and quasi-giant fluctuations. Basically, in Q2D and 2D hydrodynamics, fluctuations are of the order of the mean, so that in principle one would expect that the linearised version of the FHD equations is not accurate in this respect. For a more quantitative study, we analysed the structure factor $S_{RG}(\boldsymbol{k})$ ($S_{RG}(k) = \Delta S_{RG}$) of Q2D and 2D hydrodynamic systems versus wavenumbers that are perpendicular to the gradients $\rho_{R_0} = -\rho_{G_0}$. Then, the $S_{RG}(\boldsymbol{k})$ spectrum is averaged over the first half (time $0 < t \leq T/2$) and second half (time $T/2 < t \leq T$) of the total simulation. With this we try to show the time evolution

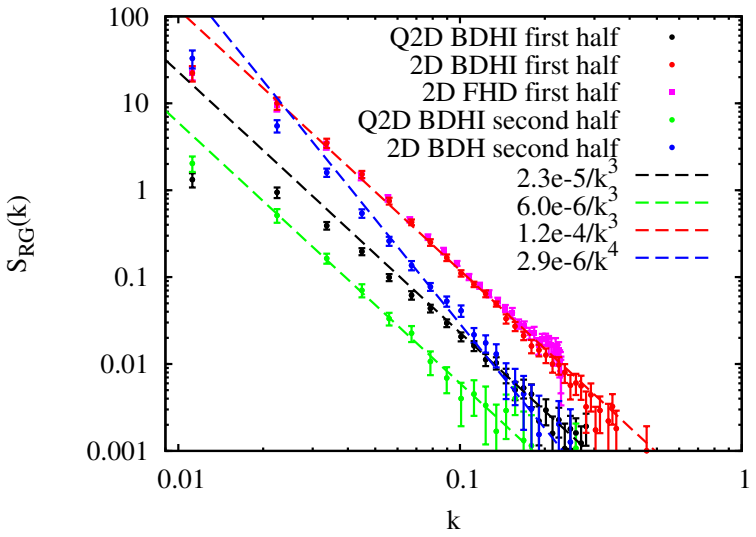

Figure 4.9: Red-green structure factor in a binary mixture with a gradient in the density of the species $\nabla\rho_{R_0} = -\nabla\rho_{G_0}$ without a gradient in the total density $\nabla\rho_0 = 0$. The structure factor has been averaged over the two halves of the simulations (circle) during a mixing process in Q2D and 2D hydrodynamics. The empirical power laws $S_{RG} \sim -k^{-3}$ and $S_{RG} \sim -k^{-4}$ (dashed lines) were fitted over a broad range of wavenumbers. The numerical solution of the full 2D FHD equation [44] is indicated with squared symbols.

of the spectrum in its evolution toward its asymptotic power-law behaviour. Thus, see in Fig. 4.9 that the first and second halves of the Q2D BDHI simulation (black and green circles) show static structure factors ($S(k) \propto 1/k^3$) that are predicted by the linearised FHD theory (dash lines). Conversely, the 2D BDHI simulation (red and blue circles) shows different behaviours during its first ($S(k) \propto 1/k^3$) and second halves ($S(k) \propto 1/k^4$), where only the behaviour of the second half was predicted by the linearised FHD theory. Most probably, this may happened because at the beginning of the simulations non-linear effects are stronger (gradients are larger there). To prove this statement, we numerically resolved the (full) 2D FHD equation $\partial_t\hat{\rho} = -\epsilon^{\frac{1}{2}}\boldsymbol{\omega}\cdot\nabla\hat{\rho} + D\nabla^2\hat{\rho}$ [44] (squares in Fig. 4.9). Notice that the excellent agreement between the 2D FHD results and the first half of the 2D BDHI simulation supports our claim. Therefore, we conclude that in 2D hydrodynamics non-linearities are essential, while in Q2D hydrodynamics non-linearities play a small role.

Bibliography

[1] J.-F. Tocanne, L. Dupou-Cézanne, and A. Lopez, *Lateral diffusion of lipids in model and natural membranes*, Progress in Lipid Research **33**, 203 (1994).

[2] W. Vaz and P. Almeida, *Microscopic versus macroscopic diffusion in one-component fluid phase lipid bilayer membranes*, Biophysical Journal **60**, 1553 (1991).

[3] K. Jacobson, *Lateral diffusion in membranes*, Cell Motility **3**, 367 (1983).

[4] P. F. F. Almeida, W. L. C. Vaz, and T. E. Thompson, *Lateral diffusion in the liquid phases of dimyristoylphosphatidylcholine/cholesterol lipid bilayers: a free volume analysis*, Biochemistry **31**, 6739 (1992).

[5] E. Parra and J. Pérez-Gil, *Composition, structure and mechanical properties define performance of pulmonary surfactant membranes and films*, Chemistry and Physics of Lipids **185**, 153 (2015).

[6] J. Alexander, *The practical applications of colloidal chemistry.*, Journal of Industrial & Engineering Chemistry **12**, 434 (1920).

[7] P. J. Lu and D. A. Weitz, *Colloidal particles: Crystals, glasses, and gels*, Annual Review of Condensed Matter Physics **4**, 217 (2013).

[8] S. E. Lohse and C. J. Murphy, *Applications of colloidal inorganic nanoparticles: From medicine to energy*, Journal of the American Chemical Society **134**, 15607 (2012).

[9] Z. Jian and H. M. C., *Assembly and electronic applications of colloidal nanomaterials*, Advanced Materials **29**, 1603895 (2017).

[10] M. J. Solomon, *Reconfigurable colloids*, Nature **464**, 496 EP (2010).

[11] A. Hess, M. Pretzl, L. Heymann, A. Fery, and N. Aksel, *Systematic modification of the rheological properties of colloidal suspensions with polyelectrolyte multilayers*, Phys. Rev. E **84**, 031407 (2011).

[12] W. J. Parak, D. Gerion, T. Pellegrino, D. Zanchet, C. Micheel, S. C. Williams, R. Boudreau, M. A. L. Gros, C. A. Larabell, and A. P. Alivisatos, *Biological applications of colloidal nanocrystals*, Nanotechnology **14**, R15 (2003).

[13] B. P. Binks and T. S. Horozov, *Colloidal particles at liquid interfaces* (Cambridge University Press, 2006).

[14] G. Whitworth and W. T. Coakley, *Particle column formation in a stationary ultrasonic field*, The Journal of the Acoustical Society of America **91**, 79 (1992).

[15] H. Bruus, J. Dual, J. Hawkes, M. Hill, T. Laurell, J. Nilsson, S. Radel, S. Sadhal, and M. Wiklund, *Forthcoming lab on a chip tutorial series on acoustofluidics: Acoustofluidics—exploiting ultrasonic standing wave forces and acoustic streaming in microfluidic systems for cell and particle manipulation*, Lab Chip **11**, 3579 (2011).

[16] M. Settnes and H. Bruus, *Forces acting on a small particle in an acoustical field in a viscous fluid*, Phys. Rev. E **85**, 016327 (2012).

[17] X. Ding, J. Shi, S.-C. S. Lin, S. Yazdi, B. Kiraly, and T. J. Huang, *Tunable patterning of microparticles and cells using standing surface acoustic waves*, Lab Chip **12**, 2491 (2012).

[18] H. Acuña Campa, M. D. Carbajal-Tinoco, J. L. Arauz-Lara, and M. Medina-Noyola, *Collective dynamics in quasibidimensional colloidal suspensions*, Phys. Rev. Lett. **80**, 5802 (1998).

[19] B. Lin, J. Yu, and S. A. Rice, *Direct measurements of constrained brownian motion of an isolated sphere between two walls*, Phys. Rev. E **62**, 3909 (2000).

[20] J. P. Rane, V. Pauchard, A. Couzis, and S. Banerjee, *Interfacial rheology of asphaltenes at oil–water interfaces and interpretation of the equation of state*, Langmuir **29**, 4750 (2013).

[21] J. Pérez-Gil, *Structure of pulmonary surfactant membranes and films: The role of proteins and lipid–protein interactions*, Biochimica et Biophysica Acta (BBA) - Biomembranes **1778**, 1676 (2008).

[22] B. Lin, S. A. Rice, and D. A. Weitz, *Experimental evidence for the divergence of a transport coefficient in a quasi-two-dimensional fluid*, Phys. Rev. E **51**, 423 (1995).

[23] B. J. Alder and T. E. Wainwright, *Decay of the velocity autocorrelation function*, Phys. Rev. A **1**, 18 (1970).

[24] J. Bleibel, A. Dominguez, F. Gunther, J. Harting, and M. Oettel, *Hydrodynamic interactions induce anomalous diffusion under partial confinement*, Soft Matter **10**, 2945 (2014).

[25] J. Bleibel, A. Domínguez, and M. Oettel, *3d hydrodynamic interactions lead to divergences in 2d diffusion*, Journal of Physics: Condensed Matter **27**, 194113 (2015).

[26] J. Bleibel, A. Domínguez, and M. Oettel, *A dynamic dft approach to generalized diffusion*

equations in a system with long-ranged and hydrodynamic interactions, Journal of Physics: Condensed Matter **28**, 244021 (2016).

[27] B. Lin, X. Xu, R. Zangi, H. Diamant, and S. A. Rice, *Divergence of the long-wavelength collective diffusion coefficient in quasi-one- and quasi-two-dimensional colloidal suspensions*, Phys. Rev. E **89**, 022303 (2014).

[28] D. S. Dean, *Langevin equation for the density of a system of interacting langevin processes*, Journal of Physics A: Mathematical and General **29**, L613 (1996).

[29] U. M. B. Marconi and P. Tarazona, *Dynamic density functional theory of fluids*, The Journal of Chemical Physics **110**, 8032 (1999).

[30] A. Donev and E. Vanden-Eijnden, *Dynamic density functional theory with hydrodynamic interactions and fluctuations*, The Journal of Chemical Physics **140**, 234115 (2014).

[31] A. Donev, T. G. Fai, and E. Vanden-Eijnden, *A reversible mesoscopic model of diffusion in liquids: from giant fluctuations to fick's law*, Journal of Statistical Mechanics: Theory and Experiment **2014**, P04004 (2014).

[32] R. Cerbino, Y. Sun, A. Donev, and A. Vailati, *Dynamic scaling for the growth of non-equilibrium fluctuations during thermophoretic diffusion in microgravity*, Scientific Reports **5**, 14486 EP (2015).

[33] A. Vailati, R. Cerbino, S. Mazzoni, C. J. Takacs, D. S. Cannell, and M. Giglio, *Fractal fronts of diffusion in microgravity*, Nat. Commun. **2**, 290 (2011).

[34] D. Brogioli and A. Vailati, *Nonequilibrium fluctuations during diffusion in liquid layers*, Phys. Rev. E **96**, 012136 (2017).

[35] M. Rex and H. Löwen, *Dynamical density functional theory for colloidal dispersions including hydrodynamic interactions*, The European Physical Journal E **28**, 139 (2009).

[36] R. P. Peláez, F. B. Usabiaga, S. Panzuela, Q. Xiao, R. Delgado-Buscalioni, and A. Donev, *Hydrodynamic fluctuations in quasi-two dimensional diffusion*, Journal of Statistical Mechanics: Theory and Experiment **2018**, 063207 (2018).

[37] F. BalboaUsabiaga, J. Bell, R. Delgado-Buscalioni, A. Donev, T. Fai, B. Griffith, and C. Peskin, *Staggered schemes for fluctuating hydrodynamics*, Multiscale Modeling & Simulation **10**, 1369 (2012).

[38] S. Delong, F. B. Usabiaga, R. Delgado-Buscalioni, B. E. Griffith, and A. Donev, *Brownian*

dynamics without green's functions, The Journal of Chemical Physics **140**, 134110 (2014).

[39] F. B. Usabiaga, R. Delgado-Buscalioni, B. E. Griffith, and A. Donev, *Inertial coupling method for particles in an incompressible fluctuating fluid*, Computer Methods in Applied Mechanics and Engineering **269**, 139 (2014).

[40] FLUAM, *fluid and matter*.

[41] M. S. Green, *Markoff random processes and the statistical mechanics of time-dependent phenomena. ii. irreversible processes in fluids*, The Journal of Chemical Physics **22**, 398 (1954).

[42] R. Kubo, *Statistical-mechanical theory of irreversible processes. i. general theory and simple applications to magnetic and conduction problems*, Journal of the Physical Society of Japan **12**, 570 (1957).

[43] J. M. O. de Zárate and J. V. Sengers, *Hydrodynamic Fluctuations in Fluids and Fluid Mixtures* (Elsevier, Amsterdam, 2006),

[44] S. Delong, Y. Sun, B. E. Griffith, E. Vanden-Eijnden, and A. Donev, *Multiscale temporal integrators for fluctuating hydrodynamics*, Phys. Rev. E **90**, 063312 (2014).

5

Collective Diffusion Under Soft Confinement I

So far, we have presented the basis of the Q2D theory for diffusion assuming that particles are strongly confined in a liquid-liquid interface. Starting from the Ito equations for the BDHI, and using the FDDFT-HI formalism, we consolidated prior studies in which the collective diffusion coefficient is enhanced by a factor inversely proportional to the wavenumber k [1–3]. As we have reiterated in Chap. 4, the physical origin of this new phenomenon is a long-ranged repulsive force between pair of particles, which arises from an apparent compressibility of the embedding fluid in the particle plane of motion. Additionally, we have formulated a more generalised Q2D theory for diffusion that accounts for the distinction of species. Although its primary use is for the study of power-law tails ($1/r^3$) in the decay of density perturbations [2] of the (density) ensemble average, we also propose its use for direct comparison with fluorescence experiments. Finally, we have proved that fluctuations in Q2D hydrodynamics are not negligible at all. On the one hand, equilibrium fluctuations renormalise the self-diffusion coefficient of particles over the time, while on the other hand, non-equilibrium fluctuations lead to quasi-giant fluctuations in binary mixtures.

Hereunder, we will discuss further subjects that have not been considered previously. As the main contribution of this chapter, we will show that the anomalous behaviour of the collective diffusion coefficient ($D_c(k) \propto 1/k$) progressively dissolves as the confinement is weakened, which eventually gives rise to the collective diffusion coefficient of 3D systems (normal). For this, we will follow a theoretical route that is totally different from the ones taken in Chap. 4 and Refs. [3]; the Q2D theory for the diffusion using a FDDFT-HI framework and including general confinements is so complicated (it includes differential geometry calculus) [4–7] that we will have to renounce it. The proposed Q2D theory for the diffusion is now devoted to short-time regimes as well as to the explicit control of the confinement [8–13]. For this reason, we will first validate the Q2D theory for the diffusion at short-times. Concerning the confinements, we will show that the most convenient way to deal with soft confinements is by applying a harmonic external force $f = k_s\,(z - z_0)$ on each particle. In this manner, we will easily control the confining plane of particles (z_0) and the confining/interface width δ (zero for strong confinement and infinite for null confinement) as a function of a confining constant k_s (see Fig. 4.1). On the other hand, because we will address Q2D systems under soft confinements, we will be forced to use a standard 3D BDHI algorithm when performing simulations[1], which is more computationally demanding.

Another pertinent topic that we will treat in this chapter is the effect of interparticle interactions on the Q2D theory for diffusion. It has been reported that long-ranged interactions, *e.g.* capillary forces, dramatically modify the behaviour of the collective diffusion coefficient [3] while short-ranged interactions do not [3, 14]. However, the latter conclusion has only been inferred and not directly measured. As we will show in Sect. 5.2, 3D BDHI simulations of strongly confined interacting particles confirm that the behaviour of D_c remains intact at large distances, while it is strongly modified at very short distances (up to two or three particle diameters). Using also interacting particles we will complete previous studies on the long-time regime of the collective diffusion coefficient. Interestingly, we will demonstrate that the short and the long-time collective diffusion coefficients differ.

At the end of this chapter, we will explore the limits of the Q2D theory for the diffusion. One of the assumptions of this theory is that the fluid in which particles are embedded adapts to its environment adiabatically (Reynolds number $Re \ll 1$), *i.e.* any local perturbation exerted on the fluid is instantaneously propagated across the system, which is usually a reasonable approximation for colloidal systems in standard fluids. Nevertheless, this time-scale separation between the fluid dynamics and the particle dynamics is not always true

[1] We recall that in our Q2D BDHI algorithm the confinement is introduced through a holomonic constrain and $\delta = 0$.

in Q2D systems [15]. As we will show in Sect. 5.4, the violation of this assumption leads to a regime in which the Q2D theory is not valid anymore.

5.1 Theory for Quasi-Two-Dimensional Diffusion Under Soft Confinements

We already saw in Chap. 4 that the collective intermediate scattering function F_c is a useful quantity to describe the collective response of Q2D systems. In particular, we saw that F_c is directly related to the collective diffusion coefficient $D_c(k)$, which is in turn related to the hydrodynamics of the system. Empirically, F_c can be directly measured from light scattering experiments *e.g.* neutron spin echo, quasi-elastic neutron scattering, inelastic neutron scattering, etc. Analytically, the collective intermediate scattering function can be obtained as the time correlation function

$$F_c(\boldsymbol{k},t) = \langle \tilde{\hat{\rho}}(\boldsymbol{k},t)\left(\tilde{\hat{\rho}}(\boldsymbol{k},0)\right)^{\star}\rangle, \tag{5.1}$$

with

$$\tilde{\hat{\rho}}(\boldsymbol{k},t) = \int \hat{\rho}\left(\boldsymbol{r},t\right)\exp\left(-\mathrm{i}\boldsymbol{k}\cdot\boldsymbol{r}\right)d\boldsymbol{r}, \tag{5.2}$$

the Fourier transform of the microscopic density (2.12), which depends on the particles position coordinates $\boldsymbol{q}_1,...\boldsymbol{q}_N$ at a time t [16].

One way to arrive at an explicit dependence of $F_c(\boldsymbol{k},t)$ on the hydrodynamics of a Q2D system consists in combining the continuity equation for the ensemble average of the density of particles $\rho\left(\boldsymbol{r},t\right) \equiv \langle\hat{\rho}\left(\boldsymbol{r},t\right)\rangle$, and the time-independent Navier-Stokes equations for the fluid momentum (Stokes flow) [14]. This route accesses long-time regimes, but one has to linearise the density versus the fluctuations ($\delta\rho \ll \rho_0$), which is known to lead to inexact equations (see Sect. 4.2.2). To avoid this issue, we will deploy another strategy[2]. To this end, we combine the continuity equation $\rho\left(\boldsymbol{r},t\right) = -\nabla\cdot\boldsymbol{J}\left(\boldsymbol{r},t\right)$, where the density current $\boldsymbol{J}(\boldsymbol{r},t) = -\int\int D_s(\boldsymbol{r}-\boldsymbol{r}',t-t')\nabla\rho(\boldsymbol{r}',t')d\boldsymbol{r}'dt'$ is given by the time and spatial convolution of the self-diffusion coefficient D_s with a density gradient $\nabla\rho$, and the time evolution equation for the N-particle probability distribution [16]. Assuming that memory

[2]In principle, this route may access to long-time regimes too, however, the theoretical formalism rapidly gets hard to work with *i.e.* one has to handle memory kernels.

effects are negligible (Stokes flow approximation), we have

$$D_s\left(\boldsymbol{r}-\boldsymbol{r}',t-t'\right)=D_s\left(\boldsymbol{r}-\boldsymbol{r}',t\right)\delta\left(t-t'\right), \tag{5.3}$$

that is, the time dependence of $D_s\left(\boldsymbol{r}-\boldsymbol{r}',t-t'\right)$ is exclusively due to the temporal evolution of the density field, consequently $\boldsymbol{J}(\boldsymbol{r},t)=-\int D_s(\boldsymbol{r}-\boldsymbol{r}',t)\nabla\rho(\boldsymbol{r}',t)d\boldsymbol{r}'$. In Fourier space, the continuity equation for the density reads

$$\frac{\partial\tilde{\rho}(\boldsymbol{k},t)}{\partial t}=-k^2D_s(\boldsymbol{k},t)\tilde{\rho}(\boldsymbol{k},t), \tag{5.4}$$

whose solution in rotationally invariant systems (spherical particles) is just

$$\tilde{\rho}(k,t)=\tilde{\rho}(k,0)\exp\left[-k^2D_c(k,t)t\right], \tag{5.5}$$

with $D_c(k,t)=\frac{1}{t}\int_0^t D_s(k,t')dt'$ being the collective diffusion coefficient[3]. On the other hand, it can be demonstrated that the time correlation of the macroscopic density Eq. (5.5) is related to Eq. (5.1) as

$$\frac{F_c(k,t)}{S(k)}=\frac{\left\langle\tilde{\hat{\rho}}\left(k,t\right)\tilde{\hat{\rho}}^{\star}\left(k,0\right)\right\rangle}{\left\langle\tilde{\hat{\rho}}\left(k,0\right)\tilde{\hat{\rho}}^{\star}\left(k,0\right)\right\rangle}=\exp\left[-k^2D_c(k,t)t\right], \tag{5.6}$$

where $S(k)=\left\langle\tilde{\hat{\rho}}\left(k,0\right)\tilde{\hat{\rho}}^{\star}\left(k,0\right)\right\rangle$ is the static structure factor [16]. Lastly, to connect $F_c(k,t)$ and the hydrodynamics of the system, we make use of the microscopic description of $F_c(k,t)$. To this end, let us first introduce the Fokker-Planck equation for the time-dependent conditional probability distribution $P(\boldsymbol{Q},t|\boldsymbol{Q}_0,t_0)$ of correlated Brownian particles with positions $\boldsymbol{Q}=\{\boldsymbol{q}_1,\cdots,\boldsymbol{q}_N\}$ (probability of having a configuration $\boldsymbol{Q}$ at time t starting from $\boldsymbol{Q}_0$ at $t_0=0$),

$$\frac{\partial P(\boldsymbol{Q},t|\boldsymbol{Q}_0,t_0)}{\partial t}=\hat{\mathcal{L}}_{\mathcal{S}}P(\boldsymbol{Q},t|\boldsymbol{Q}_0,t_0) \tag{5.7}$$

[3]Here, in contrast to Chap. 4, we will distinguish between short and long-time collective diffusion coefficients.

where $\hat{\mathcal{L}}_{\mathcal{S}}$ is the so-called Smoluchovsky operator

$$\hat{\mathcal{L}}_S = \nabla_{\boldsymbol{Q}} \cdot \{\boldsymbol{\mathcal{M}}(\boldsymbol{Q}) \left[\nabla_{\boldsymbol{Q}} \Phi\left(\boldsymbol{Q}\right) + k_B T \nabla_{\boldsymbol{Q}}\right]\}, \tag{5.8}$$

with $\boldsymbol{\mathcal{M}}(\boldsymbol{Q})$ the mobility tensor (which depends on $\boldsymbol{Q}$ in general) and $\Phi(\boldsymbol{Q})$ the particle potential. Formally, the solution to the Fokker-Planck equation (5.7) with initial condition $\delta(\boldsymbol{Q}-\boldsymbol{Q}_0)$ is just $P(\boldsymbol{Q},t|\boldsymbol{Q}_0,t_0) = \exp[\hat{\mathcal{L}}_S(t-t_0)]\delta(\boldsymbol{Q}-\boldsymbol{Q}_0)$, where the exponential operator $\exp[\hat{\mathcal{L}}_S\left(t-t_0\right)]$ has to be interpreted as a Taylor series of the exponential function, *i.e.* $\exp[\hat{\mathcal{L}}_S\left(t-t_0\right)] = \sum_{n=0}^{\infty} \frac{(t-t_0)^n}{n!} \hat{\mathcal{L}}_S^n$. Therefore, we can write Eq. (5.1) as

$$F_c(k,t) = \left\langle \tilde{\hat{\rho}}\left(k,t\right) \tilde{\hat{\rho}}^{\star}\left(k,0\right)\right\rangle = \int \tilde{\hat{\rho}}(k,t) \exp[\hat{\mathcal{L}}_S t][\tilde{\hat{\rho}}^*(\boldsymbol{k},0) P(\boldsymbol{Q})] d\boldsymbol{Q}, \tag{5.9}$$

with $P(\boldsymbol{Q})$ standing for the probability distribution. In the same way as in Sect. 4.1, we assume that the probability distribution function of particles that are confined in a liquid-liquid interface factorises as $P(\boldsymbol{Q}) \approx \mathcal{Z}^{-1} \exp[-\beta\Psi\left(\boldsymbol{Q}_{\parallel}\right)] \exp[-\beta V(\boldsymbol{Z})]$, with $\beta \equiv 1/k_B T$ (inverse of the thermal energy), $\mathcal{Z} = \int \exp[-\beta\Psi\left(\boldsymbol{Q}_{\parallel}\right)] \exp[-\beta V(\boldsymbol{Z})] d\boldsymbol{Q}_{\parallel} d\boldsymbol{Z}$ a normalisation constant, $\Psi(\boldsymbol{Q}_{\parallel})$ an interparticle potential and $V(\boldsymbol{Z})$ a confining potential that is applied on each particle. Integrating Eq. (5.9) by parts we get

$$F_c(k,t) = \langle \tilde{\hat{\rho}}^*(k,0) e^{\hat{\mathcal{L}}_S^{\dagger} t} \tilde{\hat{\rho}}(k,0)\rangle, \tag{5.10}$$

with

$$\hat{\mathcal{L}}_S^{\dagger} = \left(k_B T \nabla_{\boldsymbol{Q}} - \nabla_{\boldsymbol{Q}} \Phi(\boldsymbol{Q})\right) \{\boldsymbol{\mathcal{M}}(\boldsymbol{Q}) \nabla_{\boldsymbol{Q}}\}, \tag{5.11}$$

the Hermitian conjugate of the operator $\hat{\mathcal{L}}_S$. If we Taylor expand to the first order in time the exponential operator $\exp[\hat{\mathcal{L}}_S^* t] = 1 + \mathcal{L}_S^{\dagger} t + \mathcal{O}(t^2)$ in Eq. (5.10) we obtain $F_c(k,t) = S(k) - \langle \nabla_{\boldsymbol{Q}} \tilde{\hat{\rho}}^*(k,0) \boldsymbol{\mathcal{M}}(\boldsymbol{Q}) \nabla_{\boldsymbol{Q}} \tilde{\hat{\rho}}(k,0)\rangle t + \mathcal{O}(t^2)$[4]. Finally, introducing this result into Eq. (5.6) and expanding in time the right side of Eq. (5.6) ($\exp[-k^2 D_c\left(k,t\right) t] = 1 - k^2 D_c^{(s)} t + \mathcal{O}(t^2)$), we find that

$$D_c^{(s)}(k) = D_0 \frac{H(k)}{S(k)}, \tag{5.12}$$

with D_0 the short-time self-diffusion coefficient (given by the Stokes-Einstein relation), k

[4]For any two functions $a(\boldsymbol{Q})$ and $b(\boldsymbol{Q})$ we have $\langle a(\boldsymbol{Q}) \hat{\mathcal{L}}_S^{\dagger} b(\boldsymbol{Q})\rangle = -\langle \nabla_{\boldsymbol{Q}} a(\boldsymbol{Q}) \boldsymbol{\mathcal{M}}(\boldsymbol{Q}) \nabla_{\boldsymbol{Q}} b(\boldsymbol{Q})\rangle$.

an in-plane wavenumber ($\boldsymbol{k} \cdot \hat{\boldsymbol{z}} = 0$) and

$$H(k) = \frac{k_B T}{N} \sum_i \sum_j \left\langle \hat{\boldsymbol{k}} \cdot \frac{\boldsymbol{\mathcal{M}}_{ij}(\boldsymbol{q}_i - \boldsymbol{q}_j)}{D_0} \cdot \hat{\boldsymbol{k}} \exp\left[-\mathrm{i}\boldsymbol{k} \cdot (\boldsymbol{q}_i - \boldsymbol{q}_j)\right] \right\rangle, \tag{5.13}$$

a function that codifies the hydrodynamic properties of the system. Specifically, the hydrodynamic function $H(k)$ involves the mobility tensor $\boldsymbol{\mathcal{M}}(\boldsymbol{Q})$ which, to first order, we approximate as a pair-wise (two-body) mobility ($\boldsymbol{\mathcal{M}}(\boldsymbol{r} = \boldsymbol{q}_i - \boldsymbol{q}_j)$). Without loss of generality, we can decompose the hydrodynamic function

$$H(k) = H_s + H_c(k), \tag{5.14}$$

where the first term on the right side (H_s) stands for the self-contribution of $H(k)$, which comes from the diagonal of the mobility tensor and does not depend on k, and where the second term on the right side ($H_c(k)$) stands for the cross contribution of $H(k)$, which comes from the off-diagonal elements of the mobility tensor and does depend on k. Notice that in the absence of hydrodynamic interactions ($H = 1$) Eq. (5.12) leads to a normal short-time collective diffusion coefficient, $D_c^{(s)}(k) = D_0/S(k)$. More interesting however is the case of hydrodynamically interacting particles ($H_c(k) \neq 0$). Consistently with Eq. (5.3), we impose that the mobility tensor is given by the Oseen tensor (see Appx. A for more details on its derivation),

$$\boldsymbol{\mathcal{M}}_{ij}(\boldsymbol{r}) = \frac{1}{8\pi\eta r} \left(\boldsymbol{I} + \hat{\boldsymbol{r}} \otimes \hat{\boldsymbol{r}}\right), \tag{5.15}$$

with η is the dynamic viscosity. Then, using the additivity of $\boldsymbol{\mathcal{M}}_{ij}$ we are able to write down the cross contribution of $H(k)$ as

$$H_c(k) \approx N\,(k_B T) \int P_2(\boldsymbol{q}_1, \boldsymbol{q}_2) \hat{\boldsymbol{k}} \cdot \frac{\boldsymbol{\mathcal{M}}_{12}(\boldsymbol{r})}{D_0} \cdot \hat{\boldsymbol{k}} \exp[-\mathrm{i}\boldsymbol{k} \cdot \boldsymbol{r}] d\boldsymbol{q}_1 d\boldsymbol{q}_2, \tag{5.16}$$

with $P_2(\boldsymbol{q}_1, \boldsymbol{q}_2)$ the reduced two-particle probability distribution. Equation (5.16) can analytically be solved for ideal particles ($\Psi(\boldsymbol{Q}_\parallel) = 0$) that are confined by means of a harmonic potential $V(\boldsymbol{Z}) = \frac{1}{2} k_s \left[(z_1 - z_0)^2 + \cdots + (z_N - z_0)^2\right]$, with z_0 the confining plane and k_s the

confining force. Thus, it can be demonstrated (see Appx. C) that expression (5.16) yields

$$H_c(k) = 3\phi\frac{\delta}{a}\left\{\left[\frac{1}{2}(k\delta)^{-1} + (k\delta)\right]e^{(k\delta)^2}\mathrm{erfc}(k\delta) - \frac{1}{\sqrt{\pi}}\right\}, \tag{5.17}$$

with ϕ the density fraction of particles, a the particle radius and δ the confining width, which gives rise to two main regimes: (anomalous) Q2D diffusion and (normal) 3D diffusion. This will be extensively discussed in the subsequent sections and ratified by results obtained from the simulation of three main setups: A, B and C. It is also worth mentioning that this derivation is in agreement with parallel studies [17].

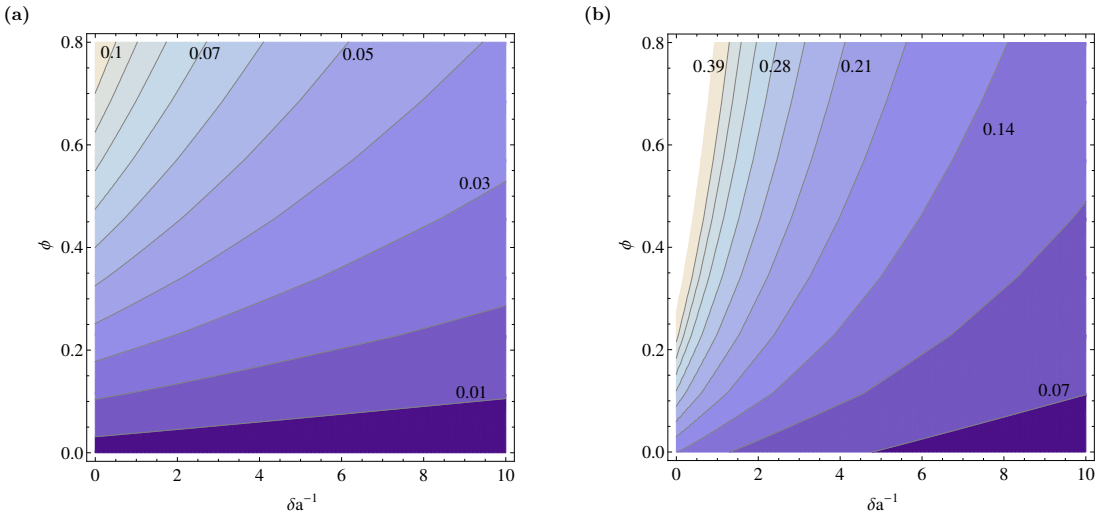

Figure 5.1: Iso-contour plots of the wavenumber ka at which the cross contribution of $H(k)$ fulfills the following constrains: (a) $H_c(k) = 10$ and (b) $H_c(k) = 1$.

Interestingly, Eq. (5.17) can be used to predict the minimum wavenumber required for the collective diffusion coefficient to become significantly enhanced. This can be done by solving the transcendental equation $k = k(H_c, \phi, \delta)$. For instance, using as a reference the parameters of Fig. 3 in Ref. [1], for polymer molecules of radius $a \approx 120\ nm$ in an air-water interface at the density fraction $\phi \approx 0.12$ (dilute regime *i.e.* $H_s \approx 1$), and assuming that the typical experimental techniques are able to handle a confinement width of about the particle radius ($\delta \approx a$) [10, 18, 19], Fig. 5.1 (b) predicts that the collective diffusion coefficient is enhanced to about double its value at $ka \approx 0.175$ ($k \approx 0.15 \times 10^5\ cm^{-1}$). This result is very near the wavenumber ($k \approx 0.2{\times}10^5\ cm^{-1}$) for which the experimental collective diffusion coefficient is enhanced by a factor of two [1]. Following the same reasoning we find from Fig. 5.1 (a) that the collective diffusion coefficient is enhanced about ten-fold at the wavenumber $k \approx 0.01 \times 10^5\ cm^{-1}$. Unfortunately, we do not have any experimental data

to compare against.

Table 5.1: Parameters used for performing simulations in this chapter. Depending on the setup proposed we use different fluid dynamic viscosities η, confinement widths δ, domain lengths $L_x \times L_y \times L_z$ and grid cells N_{FFT} along the x, y and z axes respectively. On the other hand, we keep constant the thermal energy k_BT, fluid density ρ_f and particles radius a (The units are arbitrary). In all simulations we apply PBC.

Setup	k_BT and ρ_f	a	η	ϕ	δ	N_{FFT} and $L_x \times L_y \times L_z$
A	1.0	0.91	1.0	$[0.04, 0.54]$	≈ 0.10	$64 \times 64 \times 16$
B	1.0	0.91	1.0	0.50	$[0.14, 3.16]$	$128 \times 128 \times 100$
C	1.0	0.91	$[0.5, 7.0]$	0.50	≈ 0.10	$128 \times 128 \times 100$

5.2 Strong Confinement

5.2.1 Ideal Particles

It is straightforward to demonstrate from Eq. (5.17) that, in the limit of strong confinement ($\delta \to 0$), we recover the anomalous enhancement of the collective diffusion coefficient at small wavenumbers [2, 17]. Equivalently, wavelengths much larger than the confining width ($k\delta \ll 1$) fulfill $D_c^{(s)}(k) \propto 1/k$, that is

$$\lim_{k\delta \ll 1} H_c(k) = \frac{1}{L_h k}, \tag{5.18}$$

with L_h a hydrodynamic length,

$$L_h = \left(\frac{2}{3\phi}\right) a, \tag{5.19}$$

above which the collective diffusion coefficient behaves anomalously. Therefore, for ideal particles (S(k)=1 and $H_s = 1$) we get

$$D_c^{(s)} = D_0 \left(1 + \frac{1}{L_h k}\right) = D_0 \left(1 + \frac{3\phi}{2ka}\right). \tag{5.20}$$

In contrast to Refs. [2, 3, 14], where the collective diffusion coefficient is derived for long times, the validity of expression (5.20) is restricted to short times. For this reason, we start with an unavoidable test of the Q2D theory for the diffusion at short times. Hence,

we perform 3D BDHI simulations of strongly confined ideal (tracer) particles using the solver FLUAM [20–23]. The confining potential is harmonic and the confining constant $k_s = 100$. In these numerical experiments, we use the parameters of setup A in Tab. 5.1 and we average the numerical results over the equilibrium configurations. For the initial configurations, we randomly distribute particles in the plane $z = 0$ of a simulation domain of $L_x \times L_y \times L_z = 64 \times 64 \times 16$ au at several density fractions $\phi \in [0.04, 0.54]$ ($L_h \in [1, 15]$). Finally, we estimate $D_c^{(s)}(k)$ from the fitting of the numerical $F_c(k,t)$ to the theoretical prediction (5.6).

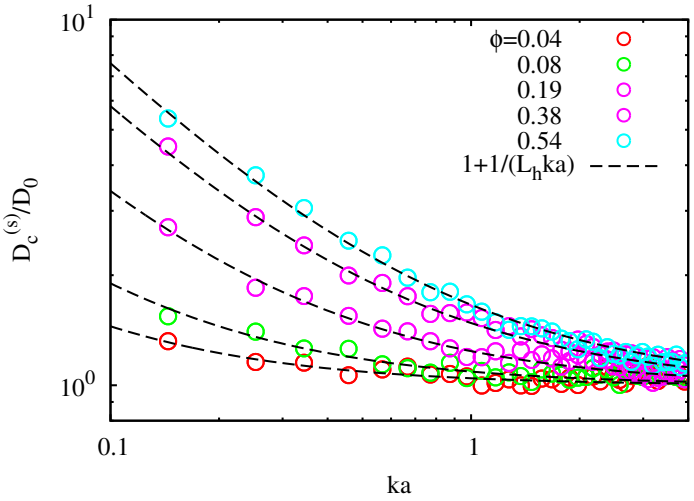

Figure 5.2: Short-time collective diffusion coefficient of strongly confined ideal particles. Circles stand for $D_c^{(s)}(k)/D_0 - 1$ values estimated from the fitting of $F_c(k,t)$ to Eq. (5.6) for several density fractions ϕ. Dashed lines represent the theoretical predictions (5.20).

Notably, we can observe in Fig. 5.2 the excellent agreement between the estimated $D_c^{(s)}(k)$ (circles) and the theory (dashed lines) for all density fractions. As it is also predicted by the theory, notice that increasing the density, or equivalently the density fraction, magnifies the collective diffusion coefficient, which is logical since the number of effective repulsions among particles is increased too.

5.2.2 Short-Range Interactions

Solving analytically Eq. (5.16) taking into account short-ranged interparticle interactions rapidly becomes an arduous task. However, we can still measure $H(k)$ by means of computer simulations. To do this, we repeat the simulations presented in the previous section, but now using particles that interact via a WCA potential. Then, we estimate $H(k)$

through the relation (5.12), where $D_c^{(s)}$ is obtained from the fitting of the numerical $F_c(k,t)$ to the theoretical prediction (5.6), and $S(k)$ from its definition. As we can see in Fig. 5.3 (a), independently of the density fraction chosen the hydrodynamic function tends to behave anomalously in the far field ($H(k \to 0) \propto 1/(L_h k)$), and so does the short-time collective diffusion coefficient. However, because of the interparticle interactions, the collective diffusion coefficient is renormalised in the far field by the structure factor ($D_c^{(s)}(k) = D_0 \frac{H(k)}{S(k)} \sim D_0 \frac{1+1/(L_h k)}{s_0}$, with $s_0 = S(k \to 0)$). In contrast, in the near field $H(k)$ is strongly altered by the interparticle interactions, which also leads to a modification of the short-time collective diffusion coefficient in the near field (up to three times the particle diameter). Interestingly, Fig. 5.3 (a) suggests that we may reasonably approach diluted systems by $D_c^{(s)}(k) = D_0 \left[1 + \frac{1}{L_h k}\right]/S(k)$ over a wide range of wavenumers. Finally, we can arrive at similar results using LJ particles, so we believe short-ranged interactions may generally present similar features.

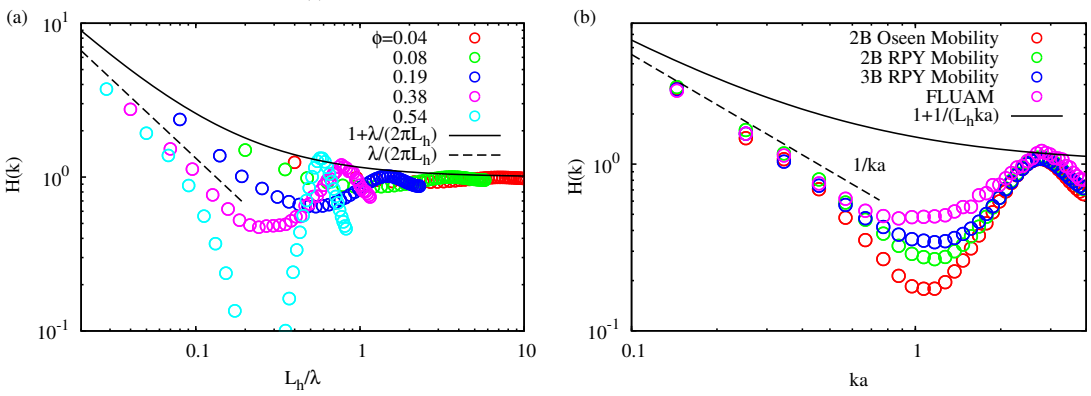

Figure 5.3: (a) Hydrodynamic function $H(k)$ of WCA particles at several surface fractions (circles) versus the ratio L_h/λ, with λ being a density disturbance length equal to $2\pi/k$. Dashed line shows the asymptotic behaviour of $H(k)$. (b) Hydrodynamic function $H(k)$ at surface fraction $\phi = 0.38$ for different mobility tensors. Calculations were done by averaging Eq. (5.13) over equilibrium configurations. Dashed line indicates the asymptotic behaviour $H(k)$.

This must indicate that the near-field contribution of the hydrodynamic function $H(k)$ depends strongly on the approximations applied to the mobility $\boldsymbol{\mathcal{M}}(\boldsymbol{Q})$. During our 3D BDHI simulations we make use of a mobility tensor that is pair-wise (two-body) and high-order in distance, to which we refer as FLUAM mobility. Unfortunately, this mobility tensor does not take into account the particle rigidity (stresslet), and consequently it does not include three-body effects. To include them, the boundary conditions would need to be modified for the hydrodynamic model (Eq. (2.26)) or alternatively, several particles would have to be joined to form the so-called multiblob [24, 25]. Then, to further explore

the effect of different mobility tensors on the hydrodynamic function $H(k)$ we compare the FLUAM approximation for the mobility tensor [21] with a pair-wise (2B) and three-body (3B) mobility tensors. More precisely, we insert in Eq. (5.13) the formulae for the two and three-body contributions to the hard sphere mobility at the level of the Oseen and RPY approximations [16], and we average over equilibrium configurations that are obtained from simulations. Then, as reflected in Fig. 5.3 (b), high-order mobilities increase the hydrodynamic function of particles at distances slightly larger than their diameter (about three times). Hence, the FLUAM mobility[5] is the one that results in the largest values of the hydrodynamic function in the near field. Albeit in any case, we remark that independently of the mobility used, we always recover the same asymptotic behaviour of the hydrodynamic function (without any renormalisation). This means that the Oseen approximation for the mobility is good enough to characterise the anomalous behaviour of the collective diffusion coefficient for both interacting and noninteracting particles.

5.2.2.1 Long-Time Collective Diffusion Coefficient

It has been demonstrated in Chap. 4 that thermal fluctuations in Q2D systems give rise to a renormalisation of the self-diffusion coefficient of particles at long times (even if particles are ideal). Likewise, the collective intermediate scattering function of labelled particles at low concentrations is renormalised at long-times. Nevertheless, whether the collective diffusion coefficient is renormalised at long-times or not remains elusive. This is because within the systems studied (ideal particles), the renormalisation of the self-diffusion coefficient is so small that any effect of it on D_c may be hidden by numerical errors.

Therefore, to avoid this issue we investigate the collective diffusion coefficient of WCA particles (as they present much more differentiated short and long-time regimes). Thus, we perform new simulations of WCA particles exploring large length scales and long time scales, for which we will use our Q2D BDHI algorithm, and we average the numerical results over ten simulations. For the initial configuration, we randomly distribute particles in a simulation domain of $L_x \times L_y = 560.5 \times 560.5\ au$ with 864^2 N_{FFT}, and we use the rest of the parameters of setup A in Tab. 5.1. Although the present theory does not tackle the long-time regime of the collective diffusion coefficient, from prior studies we know that

[5] As we have done previously, we estimate the FLUAM $H(k)$ through simulations *i.e.* $H(k) = D_c(k)S(k)/D_0$, where $D_c(k)$ is obtained from the fitting of the numerical $F_c(k,t)$ to the theoretical prediction (5.6) and $S(k)$ is obtained from its definition.

$F_c(k,t) = \exp\left[-D_c(k,t)k^2t\right] \approx \exp\left[-D_s^{(l)}(k)\frac{H(k)}{S(k)}k^2t\right]$, with $D_c^{(l)}$ and $D_s^{(l)}$ the long-time collective and self-diffusion coefficients respectively [14]. Therefore, we can estimate the short and the long-time collective diffusion coefficient of WCA particles from the numerical $F_c(k,t)$. We recall that in the study aforementioned (Ref. [14]) authors simulated the dynamics of tracer particles, and no deviation from a mono-exponential trend was found in F_c.

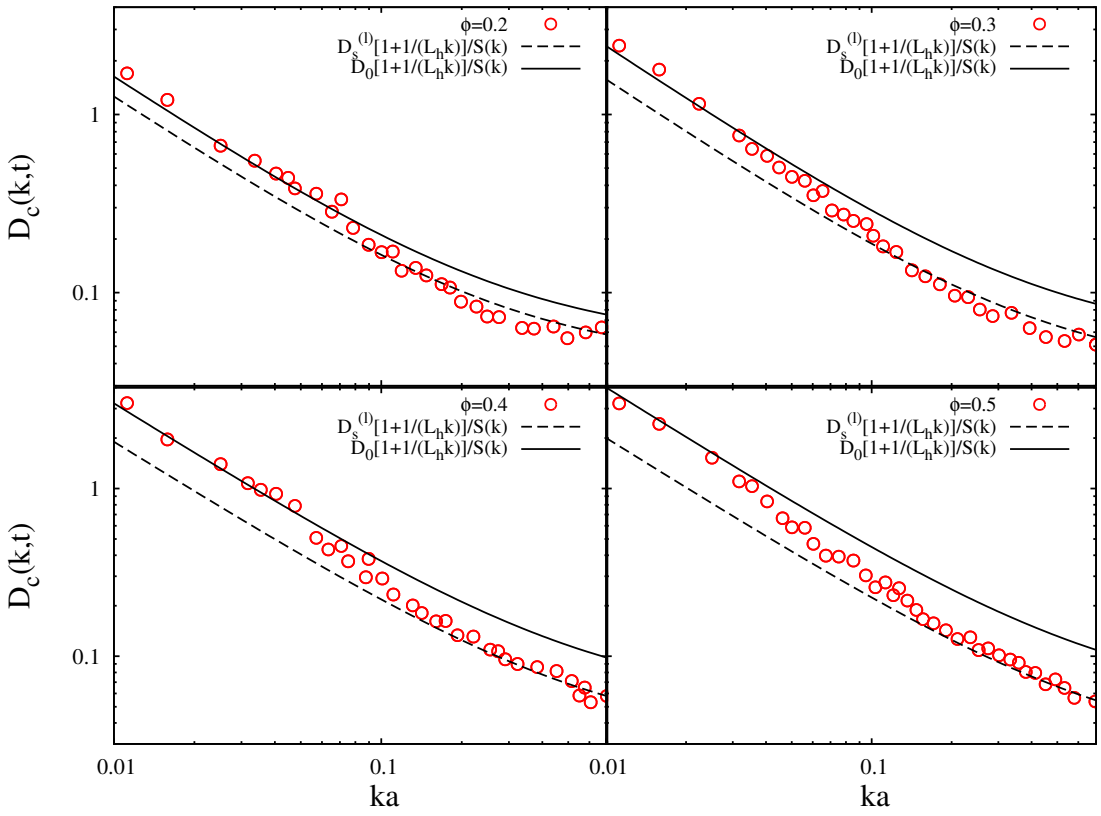

Figure 5.4: Collective diffusion coefficient of WCA particle in Q2D systems at several density fraction ϕ. In circles we show the collective diffusion coefficient obtained from a single exponential fit to Eq. (5.6). Solid and dashed lines represent the asymptotic limits of $D_c(k)$ at short and long-times respectively.

From the visual inspection of the numerical $F_c(k,t)$ of our simulations, we do not appreciate any deviation from the mono-exponential behaviour either, so that we fit F_c to a single exponential. Nevertheless, we find that the estimated $D_c(k,t)$ at large wavenumbers deviates from the theoretical asymptotic limit $\frac{D_0}{S(k)}\left[1+1/(L_hk)\right]$ (solid lines in Fig. 5.4). Precisely, in Fig. 5.4 we demonstrate that $D_c(k,t)$ at large wavenumbers agrees with the Q2D theory for the diffusion at long-times *i.e.* $D_c(k,t) \approx \frac{D_s^{(l)}}{S(k)}\left[1+\frac{1}{L_hk}\right]$ (dashed lines in

Fig. 5.4), with $D_s^{(l)}$ estimated from the long-time regime of the MSD. On the other hand we demonstrate that $D_c(k,t)$ at small wavenumbers agrees with the Q2D theory for the diffusion at short-times *i.e.* $D_c(k,t) \approx \frac{D_0}{S(k)}\left[1+\frac{1}{L_h k}\right]$. It unveils that, indeed, both short and long-time collective diffusion coefficients diverge [2, 26], although they do so with different slopes, which are D_0 and $D_s^{(l)}$ respectively. On the other hand, Fig. 5.4 also indicates that smaller wavenumbers take longer collective times $\tau_{D_c(k)}$ to enter the long-time regime ($\tau_{D_c(k)} \propto k^{-1}$), but they are faster than those of standard diffusion ($\tau_{D_c(k)} \propto k^{-2}$).

5.3 Transition to Three-Dimensional Diffusion

In the opposite limit to the strict confinement, particles are not confined at all ($\delta \to \infty$), and then the collective diffusion coefficient recovers its normal behaviour. Equivalently, this limit is given by wavelengths much smaller than the confining width ($k\delta \gg 1$), for which we have

$$\lim_{k\delta \gg 1} H_c(k) = 0. \tag{5.21}$$

To corroborate this analytic prediction, we performed 3D BDHI simulations of ideal particles at density fraction $\phi = 0.6$ and varying the confinement width $\delta \in [0.04, 0.54]$. To control δ, we apply an external harmonic potential on each particle in such a way we can easily manipulate $\delta\left(\sim\sqrt{\langle z^2\rangle} = \sqrt{\frac{k_B T}{k_s}}\right)$ and the confining plane z_0. In these simulations we use parameters of setup B in Tab. 5.1, where large simulating domains along the z axis ($L_z = 100\ au$) are introduced in order to avoid finite size effects due to the confinement as much as possible. For the initial configurations, we randomly distributed particles in the plane $z_0 = 0$, and to improve the statistics, we averaged the numerical results over equilibrium configurations of long runs. Then, results shown in Fig. 5.5 confirm an excellent agreement between the theoretical prediction (5.16) and simulations, confirming also that $H_c(\delta k \gg 1) = 0$. Moreover, it reveals that there exists a smooth and gradual transition between the anomalous Q2D dynamics ($\delta k \ll 1$) and the normal 3D dynamics ($k\delta \gg 1$), with the transition taking place at about $\delta k \sim 1$.

This gradual transition is better understood by studying the average hydrodynamic force exerted by an infinite column of particles on another. Specifically, we assume that the columns are disposed along the z direction and are separated from each other by an in-plane distance $|\boldsymbol{s}|$ *i.e.* $\boldsymbol{r} = \boldsymbol{s} + z\hat{\boldsymbol{z}}$. Then, we first define the average hydrodynamic force on a tagged particle "i" due to another particle "j" as $\mu_0 \boldsymbol{v}_i = \boldsymbol{\mathcal{M}}_{ij}\boldsymbol{F}_j$, with $\mu_0 = \frac{1}{6\pi\eta a}$ the

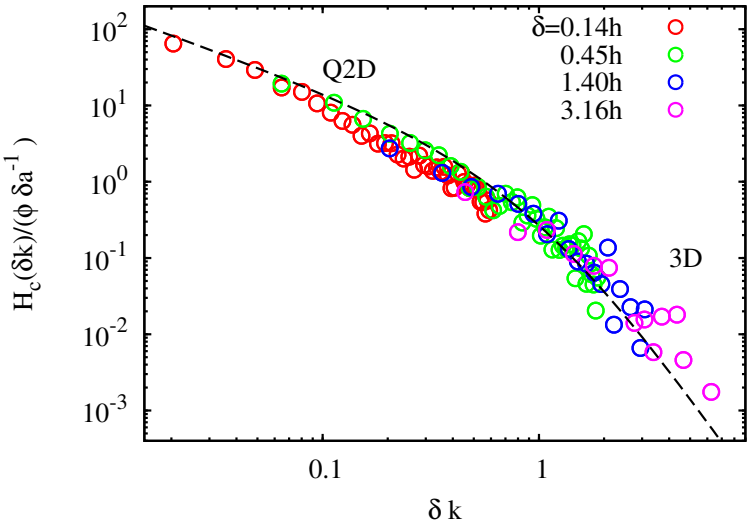

Figure 5.5: Cross hydrodynamic function $H_c(k)$ versus the confining parameter δk at surface fraction $\phi = 0.6$. Circles correspond to values estimated from 3D BDHI simulations at several confining widths δ whereas the dashed line corresponds to the analytic master curve $H_c(\delta k)/(\phi\delta a^{-1})$.

.

bare mobility of a particle and $\boldsymbol{F}_j = -k_s z_j \hat{\boldsymbol{z}}$ a harmonic confining force that acts on the particle j. Thus, the total force exerted by one column of particles on another is obtained by integrating over the hydrodynamic force on each particle of one column due to the particles of the other column,

$$\boldsymbol{f}(s) = \mu_0^{-1} \int \int P_2(\boldsymbol{q}_i, \boldsymbol{q}_j) \boldsymbol{\mathcal{M}}_{ij}(\boldsymbol{q}_j - \boldsymbol{q}_i) \boldsymbol{F}_j(\boldsymbol{q}_j) dz_i dz_j. \tag{5.22}$$

Then, rewriting Eq. (5.22) in the two-body coordinate system $Z = (z_i + z_j)/2$ and $z = (z_i - z_j)$, and integrating the Z coordinate, one gets

$$\boldsymbol{f}(\tilde{s}) = -\frac{3k_s a}{8\sqrt{\pi}} \int_{-\infty}^{\infty} \exp\left[-\frac{\tilde{z}^2}{4}\right] \frac{\tilde{z}^2}{(\tilde{s}^2 + \tilde{z}^2)^{3/2}} \tilde{s} d\tilde{z}, \tag{5.23}$$

where $\tilde{\boldsymbol{s}} = (s/\delta)\hat{\boldsymbol{s}}$ and $\tilde{z} = z/\delta$ are the δ scaled distances z and s. This integral can also be evaluated analytically, leading to

$$\boldsymbol{f}(\tilde{s}) = k_s a g(\tilde{s})\, \hat{\boldsymbol{s}}, \tag{5.24a}$$

$$g(\tilde{s}) = \frac{3\tilde{s}}{32\sqrt{\pi}} \exp\left[\tilde{s}^2/8\right] \left[\left(\tilde{s}^2 + 4\right) K_0\left(\frac{\tilde{s}^2}{8}\right) - \tilde{s}^2 K_1\left(\frac{\tilde{s}^2}{8}\right) \right], \tag{5.24b}$$

with K_0 and K_1 the modified Bessel functions of second kind and $\hat{\boldsymbol{s}}$ an in-plane unitary vector. We highlight that, as usual, the average hydrodynamic force (5.24a) is basically long-ranged ($1/s^2$) and repulsive in the far field (see Fig. 5.6 (a)), and proportional to the confining constant k_s, meaning that the collective diffusion coefficient of the column becomes normal as the confinement is made softer. Equivalently, it is interesting to note that at small distances with respect to the confinement width δ (soft confinement), the average hydrodynamic force gradually dies out for $s/\delta \to 0$ as $f \sim -s\log(s/\delta)/\delta$, reaching the 3D limit at $s = 0$ ($f = 0$) and the transition to the Q2D limit at $s/\delta \simeq 0.667$ (maximum in Fig. 5.6 (a)). This means that the gradual transition observed in Fig. 5.5 is caused by the gradual demise/emergence of the Q2D repulsive forces ($\boldsymbol{f} \propto \nabla_{\parallel} \cdot \boldsymbol{\mathcal{M}}$) among particles. To

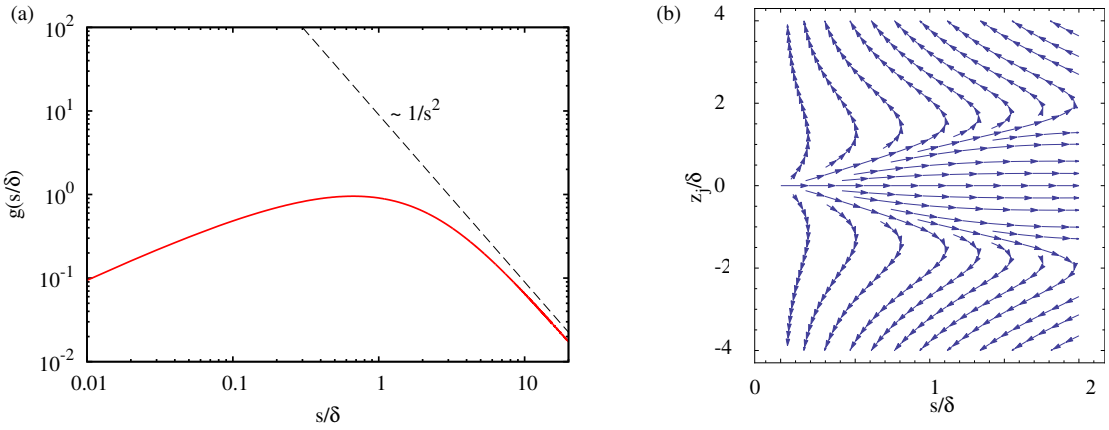

Figure 5.6: (a) Average hydrodynamic force between two infinite columns of particles versus their relative in-plane distance. The maximum of the force is at $s/\delta \sim 0.667$. (b) Average hydrodynamic force field exerted by a column of particles on a single particle j that is placed at the scaled distance z_j/δ with respect to the confining plane $z = 0$. The in-plane distance between the particle and the column is s/δ.

the same end, we also analyse the average hydrodynamic force field exerted by an infinite column of particles on a particle j that is at height z_j (softly confined) with respect to a confining plane (let us say $z = 0$), and at relative in-plane distance $|\boldsymbol{s}|$ with respect to the column. Following the same reasoning, the parallel (along the $\hat{\boldsymbol{s}}$ direction) and perpendicular (along the $\hat{\boldsymbol{z}}$ direction) components of the force $\boldsymbol{f}$ are

$$\boldsymbol{f}\cdot\hat{\boldsymbol{s}} = -\frac{3k_s a}{4\sqrt{2\pi}}\int_{-\infty}^{\infty}\frac{\exp\left[-(\tilde{z}_j+\tilde{z})^2/2\right]\,\tilde{s}\tilde{z}(\tilde{z}_j+\tilde{z})}{\left(\tilde{s}^2+\tilde{z}^2\right)^{3/2}}d\tilde{z}, \tag{5.25}$$

$$\boldsymbol{f}\cdot\hat{\boldsymbol{z}} = -\frac{3k_s a}{4\sqrt{2\pi}}\int_{-\infty}^{\infty}\frac{\exp\left[-(\tilde{z}_j+\tilde{z})^2/2\right]}{\left(\tilde{s}^2+\tilde{z}^2\right)^{1/2}}\left[1+\frac{\tilde{z}^2}{\left(\tilde{s}^2+\tilde{z}^2\right)}\right](\tilde{z}_j+\tilde{z})d\tilde{z}. \tag{5.26}$$

Very interestingly, from Fig. 5.6 (b) we find that poorly confined particles ($|z_j| > \delta$) feel an attractive hydrodynamic force that points towards the column. This attraction (counter-flow) is a clear signature of the 3D Oseen tensor, and it is the origin for the gradual dying out of the Q2D repulsive forces among particles.

5.4 Cross-Over to the Inertial Regime

Usually, the dynamics of colloidal suspensions are depicted in the Stokes flow regime [27], where the typical time taken for fluid momentum to propagate ($\tau_\nu(k) = (\nu k^2)^{-1}$, being $\nu = \frac{\eta}{\rho_f}$ the fluid kinematic viscosity) is assumed to be much smaller than the typical time taken for a colloidal particle to diffuse ($\tau_D(k) = (D_s k^2)^{-1}$, with D_s representing a self-diffusion coefficient), $\tau_\nu(k) \ll \tau_D(k)$, *i.e.* in the system of reference of a colloidal particle the fluid momentum propagates instantaneously. Mathematically, this means that the fluid momentum equation of a fluid (Eq. (2.31b)) can be approximated as time-independent, and thus, fluid inertial terms vanish. However, as indicated by Domínguez *et al.* [15], this assumption is not always valid in Q2D systems. In particular, because of the anomalous feature of the collective diffusion coefficient ($D_c(k) \propto 1/k$), we can find a critical wavenumber k_c from which the typical time taken for colloidal particles to diffuse collectively $\tau_D(k) = (D_c(k)k^2)^{-1} \lesssim \tau_\nu(k)$. There, the flow vorticity (inertia) is not negligible, and causes damped oscillatory density fields (rather than exponential). Reflecting this transition, the collective intermediate scattering function is stated as

$$F_c(k,t) = S(k)\left\{\frac{4}{3}e^{-\frac{\omega}{2}t}\cos\left(\frac{\sqrt{3}}{2}\omega t\right) - \frac{1}{\pi}\int_0^\infty dx \frac{\sqrt{\pi}}{x^3+1}e^{-\omega t x}\right\}, \tag{5.27a}$$

$$\omega = \left(\frac{4\rho_f \eta}{(k_b T)^2 \rho_{2D}^2}\right)^{-\frac{1}{3}} k^{4/3}, \tag{5.27b}$$

with ω the frequency of the oscillatory density field, which depends algebraically as $k^{4/3}$ due to the advection of the ambient flow. Specifically, this is expected to happen at

$$k_c \sim \frac{3}{2a\mathrm{Sc}}\phi, \tag{5.28}$$

with $\mathrm{Sc} = \frac{\eta}{\rho_f D_0} = \frac{6\pi\eta^2 R_h}{\rho_f k_B T}$ the so-called *Schmidt number*[6]. Thus, a typical Schmidt number in colloidal suspension ($\mathrm{Sc} \sim 10^4$) yields $k_c \sim 3.5 \times 10^{-4}\ m^{-1}$. This implies that the cross-

[6] Sc represents the ratio between the fluid momentum diffusivity (η/ρ_f) and the mass diffusion (D_s).

over to the inertial regime takes place around macroscopic length-scales (about hundred of microns).

Thus, with the aim of completing early investigations about the limits of the Q2D theory, we perform new Q2D hydrodynamic simulations of strongly confined ideal particles using the time-dependent scheme of FLUAM[7] [20]. For this, we use parameters of setup C in Tab. 5.1 and we average the numerical results over the equilibrium configurations. In order to access the inertial regime we use unrealistically low values of $\mathrm{Sc} \in [5, 900]$ ($\eta \in [0.5, 7.0]$), which lead to reachable critical wavenumbers $k_c \in [0.001, 0.18]$. For the initial configurations, we randomly distribute particles in the plane $z = 0$ of a simulation domain of $L_x \times L_y \times L_z = 128 \times 128 \times 100\ au$ at several density fractions $\phi = 0.5$.

Then, comparing the collective intermediate scattering function at wavenumbers above and below the critical wavenumber k_c, we can rapidly detect the differences between them. Precisely, in Fig. 5.7 (a) and (b) we illustrate that for $k > k_c$, simulations (red circles) present an overdamped dynamics, and consistently with the Stokes flow approximation, they agree with expression (5.6), while for $k < k_c$, simulations (blue circles) present an oscillatory damped dynamics, and they agree with expression in Eq. (5.27a). Analogously, if we repeat the same procedure for $k \lesssim k_c$ and we fit the numerical $F_c(k,t)$ to the theoretical expression (5.27), we find the agreement with the theory (relative error within a 3%) is remarkably good for the smaller wavenumber (see Fig. 5.7 (c)). Larger wavenumbers instead deviate considerable from the theory (relative error within a 25%), although they are expected. Notice in Fig. 5.7 (d) that as soon as wavenumbers get closer to k_c, the minimum (negative) of the density correlation F_c progressively vanishes until the dynamics is fully overdamped, which explains the progressive deviations in Fig. 5.7 (c) with the wavenumber. Therefore, this confirms that the Stokes flow approximation does not apply at wavenumbers below k_c (Eq. (5.28)) [15], and neither does the Q2D theory for the diffusion.

[7] In the time-dependent scheme of FLUAM the Navier-Stokes equations are fully solved *i.e.* we keep all inertial terms in the equations of motion.

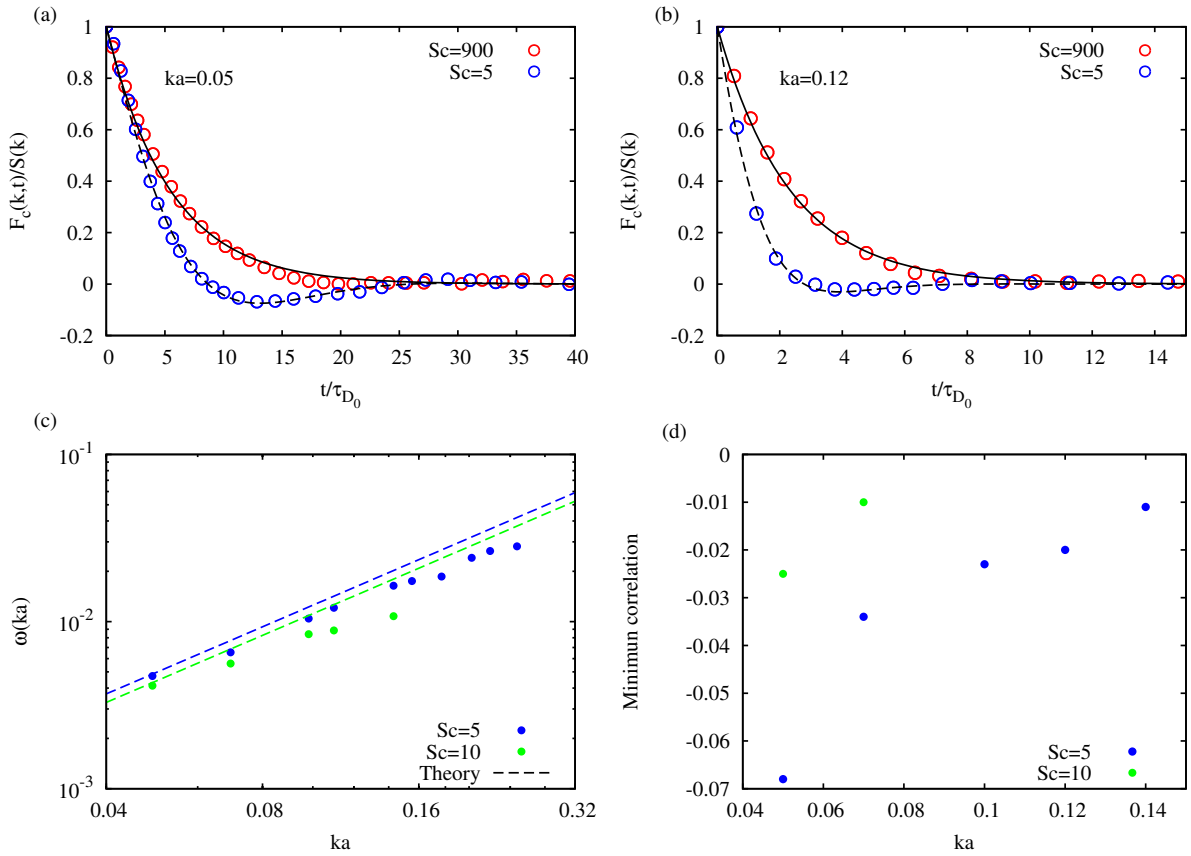

Figure 5.7: Normalised collective intermediate scattering function of ideal particles at surface fraction $\phi = 0.5$, wavenumbers (a) $ka = 0.05$ and (b) $ka = 0.12$, and Schmidt numbers Sc = 900 and 5, versus the scaled time $t/\tau_{D_0} = \frac{ta^2}{D_0(\mathrm{Sc})}$ (the diffusion coefficient D_0 is assigned as a function of Sc [28]). Circles stands for $F_c(k,t)/S(k)$ obtained from simulations while dashed and solid lines are the theoretical predictions (5.27a) and (5.6) respectively. (c) Values of the frequency ω of the oscillatory density field obtained from the fit of our simulations to Eq. (5.27a) (circles) and from the theoretical Eq. (5.27b) (dashed lines) for Sc = 5 and 10. (d) First minimum of the normalised collective intermediate scattering function $F_c(k,t)/S(k)$ versus ka for Sc = at 5 and 10. The values of the critical wavenumber $k_c a$ are 0.18, 0.09 and 0.001 corresponding to Sc at values 5, 10 and 900 respectively.

Bibliography

[1] B. Lin, S. A. Rice, and D. A. Weitz, *Experimental evidence for the divergence of a transport coefficient in a quasi-two-dimensional fluid*, Phys. Rev. E **51**, 423 (1995).

[2] J. Bleibel, A. Dominguez, F. Gunther, J. Harting, and M. Oettel, *Hydrodynamic interactions induce anomalous diffusion under partial confinement*, Soft Matter **10**, 2945

(2014).

[3] J. Bleibel, A. Domínguez, and M. Oettel, *A dynamic dft approach to generalized diffusion equations in a system with long-ranged and hydrodynamic interactions*, Journal of Physics: Condensed Matter **28**, 244021 (2016).

[4] D. C. Morse, *Theory of Constrained Brownian Motion* (Wiley-Blackwell, 2004), chap. 2, pp. 65–189, .

[5] G. Ciccotti, T. Lelièvre, and E. Vanden-Eijnden, *Projection of diffusions on submanifolds: Application to mean force computation*, Communications on Pure and Applied Mathematics **61**, 371 (2007).

[6] I. Fatkullin, G. Kovacic, and E. Vanden-Eijnden, *Reduced dynamics of stochastically perturbed gradient flows*, Commun. Math. Sci. **8**, 439 (2010).

[7] H. C. Öttinger, *Preservation of thermodynamic structure in model reduction*, Phys. Rev. E **91**, 032147 (2015).

[8] G. Whitworth and W. T. Coakley, *Particle column formation in a stationary ultrasonic field*, The Journal of the Acoustical Society of America **91**, 79 (1992).

[9] H. Bruus, J. Dual, J. Hawkes, M. Hill, T. Laurell, J. Nilsson, S. Radel, S. Sadhal, and M. Wiklund, *Forthcoming lab on a chip tutorial series on acoustofluidics: Acoustofluidics—exploiting ultrasonic standing wave forces and acoustic streaming in microfluidic systems for cell and particle manipulation*, Lab Chip **11**, 3579 (2011).

[10] M. Settnes and H. Bruus, *Forces acting on a small particle in an acoustical field in a viscous fluid*, Phys. Rev. E **85**, 016327 (2012).

[11] X. Ding, J. Shi, S.-C. S. Lin, S. Yazdi, B. Kiraly, and T. J. Huang, *Tunable patterning of microparticles and cells using standing surface acoustic waves*, Lab Chip **12**, 2491 (2012).

[12] H. Acuña Campa, M. D. Carbajal-Tinoco, J. L. Arauz-Lara, and M. Medina-Noyola, *Collective dynamics in quasibidimensional colloidal suspensions*, Phys. Rev. Lett. **80**, 5802 (1998).

[13] B. Lin, J. Yu, and S. A. Rice, *Direct measurements of constrained brownian motion of an isolated sphere between two walls*, Phys. Rev. E **62**, 3909 (2000).

[14] J. Bleibel, A. Domínguez, and M. Oettel, *3d hydrodynamic interactions lead to divergences in 2d diffusion*, Journal of Physics: Condensed Matter **27**, 194113 (2015).

[15] A. Domínguez, *Signature of time-dependent hydrodynamic interactions on collective diffusion in colloidal monolayers*, Phys. Rev. E **90**, 062314 (2014).

[16] J. Dhont, *An introduction to dynamic of colloids*, vol. 2 (Elsevier, 1996).

[17] J. Bleibel, A. Domínguez, and M. Oettel, *Onset of anomalous diffusion in colloids confined to quasimonolayers*, Phys. Rev. E **95**, 032604 (2017).

[18] F. B. Usabiaga, I. Pagonabarraga, and R. Delgado-Buscalioni, *Inertial coupling for point particle fluctuating hydrodynamics*, Journal of Computational Physics **235**, 701 (2013).

[19] F. Balboa Usabiaga and R. Delgado-Buscalioni, *Minimal model for acoustic forces on brownian particles*, Phys. Rev. E **88**, 063304 (2013).

[20] F. BalboaUsabiaga, J. Bell, R. Delgado-Buscalioni, A. Donev, T. Fai, B. Griffith, and C. Peskin, *Staggered schemes for fluctuating hydrodynamics*, Multiscale Modeling & Simulation **10**, 1369 (2012).

[21] S. Delong, F. B. Usabiaga, R. Delgado-Buscalioni, B. E. Griffith, and A. Donev, *Brownian dynamics without green's functions*, The Journal of Chemical Physics **140**, 134110 (2014).

[22] F. B. Usabiaga, R. Delgado-Buscalioni, B. E. Griffith, and A. Donev, *Inertial coupling method for particles in an incompressible fluctuating fluid*, Computer Methods in Applied Mechanics and Engineering **269**, 139 (2014).

[23] FLUAM, *fluid and matter*.

[24] F. Balboa Usabiaga, B. Kallemov, B. Delmotte, A. Bhalla, B. Griffith, and A. Donev, *Hydrodynamics of suspensions of passive and active rigid particles: A rigid multiblob approach*, Communications in Applied Mathematics and Computational Science **11** (2016).

[25] A. Vázquez-Quesada, F. Balboa Usabiaga, and R. Delgado-Buscalioni, *A multiblob approach to colloidal hydrodynamics with inherent lubrication*, The Journal of Chemical Physics **141**, 204102 (2014).

[26] S. Panzuela, R. P. Peláez, and R. Delgado-Buscalioni, *Collective colloid diffusion under soft two-dimensional confinement*, Phys. Rev. E **95**, 012602 (2017).

[27] I. Proudman and J. R. A. Pearson, *Expansions at small reynolds numbers for the flow past a sphere and a circular cylinder*, Journal of Fluid Mechanics **2**, 237–262 (1957).

[28] F. Balboa Usabiaga, X. Xie, R. Delgado-Buscalioni, and A. Donev, *The stokes-einstein*

relation at moderate schmidt number, The Journal of Chemical Physics **139**, 214113 (2013).

6

Collective Diffusion Under Soft Confinement II: Lipid Membranes

After Chap. 5 it is clear that a hydrodynamically interacting particle in Q2D systems exhibits an anomalous collective diffusion coefficient that diverges inversely proportional to the wavenumber ($D_c \propto 1/k$). Specifically, we have just proved that particles that additionally interact via short-ranged interparticle interactions lead to an anomalous collective diffusion coefficient, just as occurs with ideal (tracer) particles. The only difference between both sorts of particles is that short-ranged interactions may strongly alter (depending on the concentration of particles) the collective diffusion coefficient at large wavenumbers (distances about three times the particle diameter)[1]. Not only that, we have demonstrated that the anomalous behaviour of the collective diffusion coefficient is not only present in strict Q2D systems, but is also present in softly confined Q2D systems, progressively disappearing as the confinement is weakened (3D normal diffusion). Namely, indeed, weakening the confinement results in less intense Q2D repulsive forces among particles ($\boldsymbol{f} \propto \nabla_{\parallel} \cdot \boldsymbol{\mathcal{M}}$), yielding a smooth transition from Q2D dynamics to 3D dynamics. To prove these re-

[1] We recall long-ranged interactions do dramatically alter the collective diffusion coefficient [1].

sults we have followed an alternative theoretical route [2] to the one in Chap. 4 and Ref. [1] that allows for studying finite confinements ($\delta \neq 0$). Very interestingly too, we have numerically unveiled that short-time collective diffusion coefficients as well as long-time collective diffusion coefficients are anomalous, although they diverge with different slopes, *i.e.* $D_c^{(l)}(k) \neq D_c^{(s)}(k)$. Finally, we have studied the limits of the Q2D theory the diffusion. As it was mathematically predicted [3], we have shown that the violation of the Stokes flow approximation leads to the breakdown of the Q2D theory for the diffusion. This has been estimated to take place a wavenumbers of about $k \lesssim k_c \sim \frac{3a}{2a\mathrm{Sc}}\phi$.

Then, in analogy to typical particle systems at liquid-liquid and air-liquid interfaces, one may think of membrane lipids as a particular case of "particles" that are (softly) constrained to move in a liquid-liquid interface (membrane surface). Therefore, it seems reasonable to wonder, *Does the Q2D theory for diffusion apply to membrane lipids?*. To prove this, we will mainly focus on the features of the short and long-time collective diffusion coefficient of membranes lipids. These analyses will be obtained from computer simulations of lipid membranes immersed in water. For comparison, we will use different models of lipid membranes (MARTINI and Cooke-Deserno models), and we will also use different approaches to hydrodynamic interactions (BD, BDHI and MD simulations). Then, as main contribution of this chapter, in Sect. 6.2.1 we will demonstrate that the short-time collective diffusion coefficient of hydrodynamically interacting lipids diverges inversely proportional to the wavenumber ($D_c^{(s)}(k) \propto 1/k$), just as the Q2D theory for diffusion forecasts. Strikingly, in Sect. 6.2.2 we will show that the long-time collective diffusion coefficient of hydrodynamically interacting lipids of one of the models (Cooke-Deserno) does not diverge. In fact, we will show that this diffusion coefficient is equal to the long-time self-diffusion coefficient ($D_c^{(l)} = D_s^{(l)}$) of lipids. By contrast, we will show non-conclusive and puzzling results for the long-time collective diffusion coefficient of hydrodynamically interacting lipids of the remaining model (MARTINI).

Beyond the mere check of the Q2D theory for the diffusion in lipid membranes, at the end of this chapter we will briefly make use of this theory to address open questions with regard to phenomenology about coherent motion of lipids at short times [4–8]. As we will comment in Sect. 6.3, preliminary evidence strongly suggest that Q2D hydrodynamic interactions induce lipid-lipid velocity correlations, which are compatible with the correlations found in previous studies [4–8]. Additionally, we will show that velocities generated by hydrodynamic simulations are compatible with the ones reported experimentally [5, 6], which supports the hydrodynamic origin of these correlations. Finally, we will try to connect the effective repulsion of Q2D systems with the origin of these correlations. For this latter point, we will compare the full width at half mean (FWHM) of dynamic structure factors

measured in experiments with the one predicted by the Q2D theory for diffusion.

6.1 Preliminary Considerations

As we have indicated in the prelude to this chapter, one of the goals of this study is to discern whether the Q2D theory for diffusion is suitable for membrane lipids or not. We believe the most straightforward manner to reach a conclusion in this respect is through the analysis of the collective diffusion coefficient of membrane lipids, for which we will perform computer simulations of lipid membranes that are immersed in water. In principle, this effect is independent of the lipid specie chosen, yet, for consistency within this thesis, we will address DPPC lipids membranes. On the other hand, so far, all simulations employed to illustrate the anomalous behaviour of the collective diffusion coefficient in the previous two chapters have been accomplished via BDHI algorithms. However, to further test the Q2D theory for diffusion, in this chapter we will consider MD simulations in addition to BDHI simulations. Notice then that momentum propagation will be treated in totally different ways. This is, in BDHI simulations, momentum conservation comes from lipid-lipid collisions and the transferring of lipid forces to the fluid momentum (and vice versa) [9–11]. By contrast, in MD simulations, momentum conservation comes exclusively from interparticle collisions (lipid-water, water-water and lipid-lipid collisions). Hence, because momentum propagation will be treated differently in MD and BDHI simulations, we will be forced to use different approaches to membranes lipids. The main reason for this is that, in order to perform BDHI simulations, one requires lipid models that stabilise amphipathic structures without the presence of explicit water molecules (dry membranes) [12, 13]. While, conversely, to perform MD simulations one requires lipid models that stabilise amphipathic structures (dry membranes) with the presence of explicit water molecules (see Figs. 6.3 (b) and (c) for illustrative purposes).

Therefore, to perform MD simulations of lipid membranes, we will combine the GROMACS 2018.3 MD algorithm [14, 15] with the MARTINI model of a DPPC lipid (martini-v2.0 and martini-v2.0-lipids) [16]. As commented earlier in Sect. 2.5.1, the MARTINI force field, and in particular its version for lipid membranes, is widely known to provide a high reliability versus atomistic simulations and experiments of lipid membranes, while at the same time it improves statistical sampling with respect to atomistic simulations [16–19]. Thus, in these simulations we will employ the leap-frog integration algorithm with a time-step $\Delta t = 0.04\ ps$ and we will use parameters of setup A in Tab. 6.1. We recall that within

the MARTINI force field, interactions are truncated and shifted; Coulomb interactions are softly modified from distance $r = 0$ to $1.2\ nm$ while LJ interactions are only modified from distance $r = 0.9$ to $1.2\ nm$. Thus, we will run simulations in the NPT ensemble for $200\ ns$ using a Berendsen thermostat and barostat [20] (equilibration purposes). And we will proceed with a NVT ensemble simulation during $2.5\ \mu s$ using a Nosé-Hoover thermostat (production purposes) [21], which is weakly coupled (coupling constant $\tau = 15.0\ ps$) to a thermal reservoir in order to minimise the possible thermostat disturbance on the momentum conservation (this will be further treated in Sect. 6.1.3). Hence, each system will be run for $2.7\ \mu s$ in total ($\sim$ 12 days with 4 GTX 1080 GPU). It is important to mention that, to strictly conserve local as well as total momentum in GROMACS, one should perform very expensive double precision NVE simulations [22]. However, it would prevent us from exploring large length-scales and reasonable time-scales, so that we had to renounce this route. We do not discard ratifying our results with future NVE simulations, though.

With regard to BDHI simulations, we will combine the 3D BDHI algorithm of FLUAM [9–11, 23] with the Cooke-Deserno model [13]. This lipid model has been chosen since, with respect to other (dry) models [24–28], it provides a fast, versatile and accurate approach of the main features of a lipid membrane [13, 29–32]. Thus, in these hydrodynamic simulations we will use a time step $\Delta t = 0.01$ and we will make use of the parameters of setup B in Tab. 6.1. These simulations will last up to times $t = 10100$ ($\sim$ 20 days with 1 Tesla K40 GPU), discarding the first 100 times for equilibration purposes. It is worth mentioning that the Cooke-Deserno model does not specify lipid species, but it treats lipids as a general entity [13]. For this, in the preceding section we will explain the election of a "DPPC" Cooke-Deserno lipid.

Lastly, for comparison purposes, we will perform BD simulations using DPPC Cooke-Deserno lipids again. Notice that in these simulations momentum is not conserved at all (particles move randomly), consequently, the collective diffusion coefficient is expected to be normal. For this, we will use the BD algorithm of GROMACS and parameters of setup C in Tab. 6.1. Then, simulations will be performed using a time step of $\Delta t = 0.001\ ps$ over $1.1\ \mu s$ ($\sim$ 7 days with 12 CPUs), discarding the first $100\ ns$ (for equilibration purposes).

Table 6.1: Parameters used during hydrodynamic simulations (A), Brownian dynamics simulations (B) and Molecular dynamics simulations (C): Temperature T, fluid dynamic density ρ_f, surface tension γ, number of lipids N_p, number of waters N_w, lipid radius a, excess mass m_e, fluid viscosity η, domain lengths $L_x \times L_y \times L_z$ and grid cells N_{FFT} along the x, y and z axes respectively. The basic units are arbitrary for BDHI simulations and nm, ps, K, electron charge (e) and atomic mass unit (u) for BD and MD simulations. In all simulations we apply PBC.

	T	ρ_f	γ	N_p	N_w	a	m_e	η	N_{FFT}	$L_x \times L_y \times L_z$
A	1	1	0	18432	–	0.40	0	5	220^3	$88.07 \times 88.07 \times 88.07$
B	310	–	0	18432	–	0.40	–	–	–	$88.07 \times 88.07 \times 88.07$
C	310	–	0	25088	5210240	0.235	–	–	–	$85.55 \times 85.55 \times 85.55$

6.1.1 Lateral Structures of Lipid Membranes

Since the collective diffusion coefficient of lipids depend non-trivially on the lateral properties of lipid membranes ($D_c(k) \propto 1/S(k)$), we consider convenient (for comparison reasons) to look for a Cooke-Deserno lipid membrane that, to the extent possible, best reproduces relevant (from the collective diffusion perspective) lateral properties of a MARTINI DPPC lipid membrane. Thus, we find that tuning the energetic ratio between the LJ interacting energy of lipids and the thermal temperature $\epsilon/k_BT = 1.35$, the lipid long-range cut-off $\omega_c = 1.2\sigma$ and the lipid diameter $\sigma = 0.8\ nm$ (see Sect. 2.5.3 for more details on the Cooke-Deserno interactions), we roughly reproduce the predominant contribution of the in-plane radial radial distribution function of MARTINI membrane lipids (see Fig. 6.1 (a)).

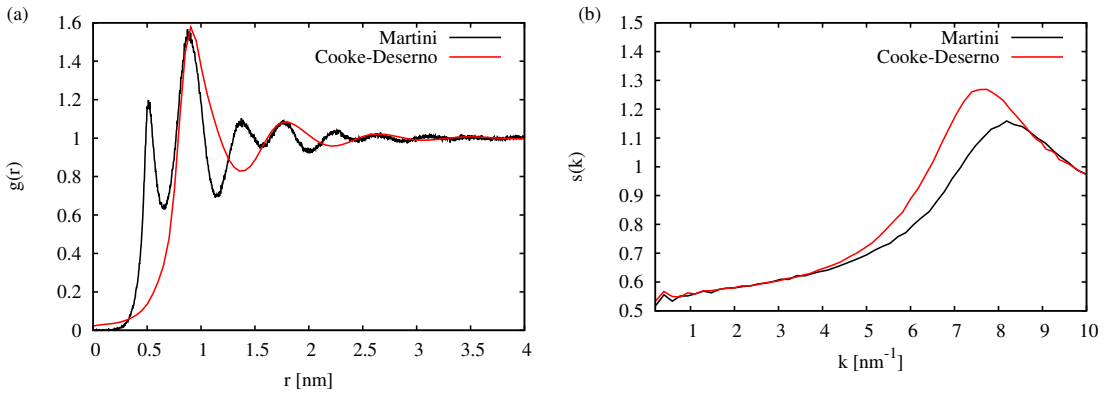

Figure 6.1: (a) In-plane radial distribution function of the head group of lipids versus de in-plane distance r, and (b) the associated static structure factor versus the wavenumber k (with $\boldsymbol{k} \cdot \hat{\boldsymbol{z}} = 0$). For this, each leaflet of the membrane has been analysed independently.

Notice that because of the poor level of resolution of Cooke-Deserno lipids, we cannot tune better radial distribution functions either. Even so, as we can see from Fig. 6.1 (b), the static structure factors of both models agree remarkably well, especially in the far field ($S(k \to 0) \simeq 0.5$).

6.1.2 Self-Diffusion Coefficient of Lipids

The collective diffusion coefficient of lipids also depends on their self-diffusion coefficient D_s. Specifically, we know it provides essential information about the time regime of the collective diffusion coefficient ($D_c(k,t) \propto D_s(t)$). Therefore, the great relevance of studying the time evolution of the self-diffusion coefficient of lipids is more than obvious. To that end, we calculate the self-diffusion coefficient of lipids from the slope of their in-plane MSD, $D_s = \mathrm{MSD}(t)/4t = \langle[\boldsymbol{q}_\parallel(t) - \boldsymbol{q}_\parallel(0)]^2\rangle/4t$.

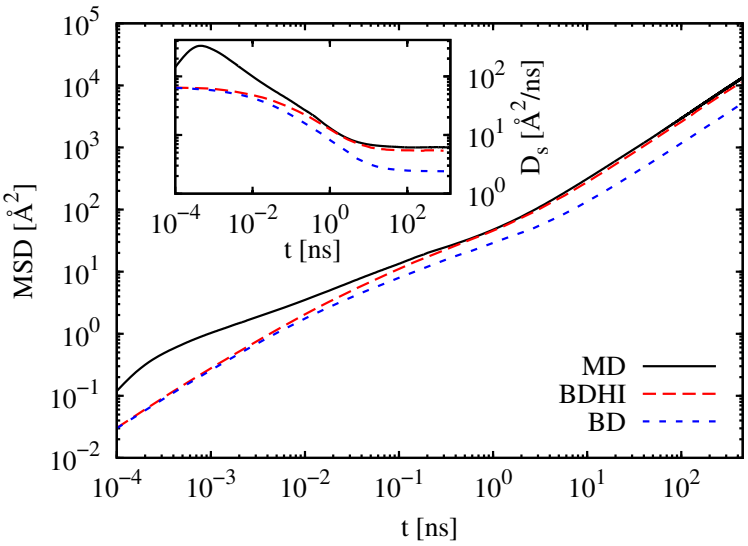

Figure 6.2: Mean square displacement of lipids obtained from MD, BD and BDHI simulations. Units are in the international system. With that goal, the Cooke-Deserno model is scaled to match the Stokes diffusion time σ^2/D_0, with $D_0 = k_BT/(6\pi\eta a)$ the Stokes-Einstein self-diffusion coefficient, which is calculated by using the viscosity of the MARTINI water model [33] and using a temperature $T = 310\ K$. In the inset we show the self-diffusion coefficient $D_s = \mathrm{MSD}(t)/(4t)$.

Then, from Fig. 6.2 we can highlight different regimes. At short times, BD as well as BDHI simulations lead to a short-time self-diffusion regime, while MD simulations lead a ballistic regime. In both cases these regimes were expected by construction of the simulations. Then, at intermediate times (approximately from 0.01 to 10 ns), all models enter a

sub-diffusive regime that is characterised by MSD $\propto t^{\alpha}$ with $\alpha \in [0.45, 0.55]$ [34]. It should be noted that the MD model passes from a ballistic regime to a sub-diffusive regime through an instantaneous diffusive regime (maximum in inset of Fig. 6.2), to which we relate to the short-time self-diffusion coefficient ($D_0 = 400$ Å$^2/ns$) [35–38]. Finally, at long-times (typical time needed by a lipid to diffuse a distance that is larger than its diameter), all models reach a long-time self-diffusion regime with $D_s^{(l)} = 7.8$ Å$^2/ns$ (MD), 6.4 Å$^2/ns$ (BDHI) and 6.0 Å$^2/ns$ (BD). In contrast to quasi-elastic neutron scattering experiments ($D_s^{(l)} = 1.4$ Å$^2/ns$ at $T = 300$ K) [39], our results yield long-time self-diffusion coefficients that are about 4 times larger, although it has extensively been reported that the MARTINI model gives rise to a four-fold speed-up of the dynamics [17].

6.1.3 Averaged Relative Displacement Field

We have extensively demonstrated in Chap. 4 and 5 that the Q2D theory for diffusion is based on the momentum conservation law, so its total violation leads to the breakdown of the Q2D theory for diffusion, as we have seen by means of BD simulations. Therefore, since in our MD simulations we make use of a Nosé-Hoover thermostat, we find it compulsory to estimate in advance how disrupting the momentum conservation affects the Q2D hydrodynamics, even if this thermostat is weakly coupled to a thermal reservoir.

Qualitatively, we can estimate this alteration by means of the computation of the in-plane mobility tensor of MD simulations and its posterior comparison with that of BDHI simulations. To this end, we assume the mobility tensor is related to velocity correlations between lipids (Stokes flow approximation)[2], or equivalently displacement correlations,

$$\left\langle \delta \boldsymbol{q}_{j\parallel}(t_1) \otimes \hat{\delta} \boldsymbol{q}_{i\parallel}(t_1) \right\rangle = 2k_B T \boldsymbol{\mathcal{M}}(\boldsymbol{s} = \boldsymbol{q}_{j\parallel}(t_0) - \boldsymbol{q}_{i\parallel}(t_0), 0) \Delta t. \tag{6.1}$$

Here, we meticulously explain the procedure to obtain the mobility tensor $\boldsymbol{\mathcal{M}}$ from the in-plane displacements $\delta \boldsymbol{q}_{j\parallel}(t_1)$ and $\hat{\delta} \boldsymbol{q}_{i\parallel}(t_1)$ associated to the lag-time Δt. For that purpose, let us assume we have a central tagged particle (lipid) "i" at t_0, and we want to know its local displacement field after a lag time $\Delta t = t_1 - t_0$. Thus, we look for the "j"-th particle displacement at the given relative distance $\boldsymbol{s} = \boldsymbol{q}_{j\parallel}(t_0) - \boldsymbol{q}_{i\parallel}(t_0)$ in the system of coordinates of the i-th particle displacement. We define the average displacement of particles i and j after a time t_1 such as $\delta \boldsymbol{q}_{i\parallel}(t_1) = (\boldsymbol{q}_{i\parallel}(t_1) - \boldsymbol{q}_{i\parallel}(t_0))$ and $\delta \boldsymbol{q}_{j\parallel}(t_1) = (\boldsymbol{q}_{j\parallel}(t_1) - \boldsymbol{q}_{j\parallel}(t_0))$. And

[2] Notice that, strictly speaking, the velocity of lipids is not well defined in Brownian dynamics, but they still provide an insight about correlations (see discussion at the end of Sect 2.2).

we calculate the dyadic product $\delta\boldsymbol{q}_{j\parallel}(t_1)\otimes\hat{\delta}\boldsymbol{q}_{i\parallel}(t_1)$, with $\hat{\delta}\boldsymbol{q}_{i\parallel}(t_1)$ a normalised displacement vector $([\delta\boldsymbol{q}_{i\parallel}(t_1)-\hat{\delta}\boldsymbol{q}_{i\parallel}(t_0)]/|\delta\boldsymbol{q}_{i\parallel}(t_1)-\hat{\delta}\boldsymbol{q}_{i\parallel}(t_0)|)$ that points in the direction $\hat{e}_\parallel=\delta\boldsymbol{q}_{i\parallel}/|\delta\boldsymbol{q}_{i\parallel}|$ of the system of coordinates $\{\hat{e}_\parallel,\hat{e}_\perp\}$, with $\hat{e}_\perp=\hat{e}_\parallel\times\hat{\boldsymbol{z}}$ (i.e. $\hat{e}_\parallel\cdot\hat{e}_\perp=0$).

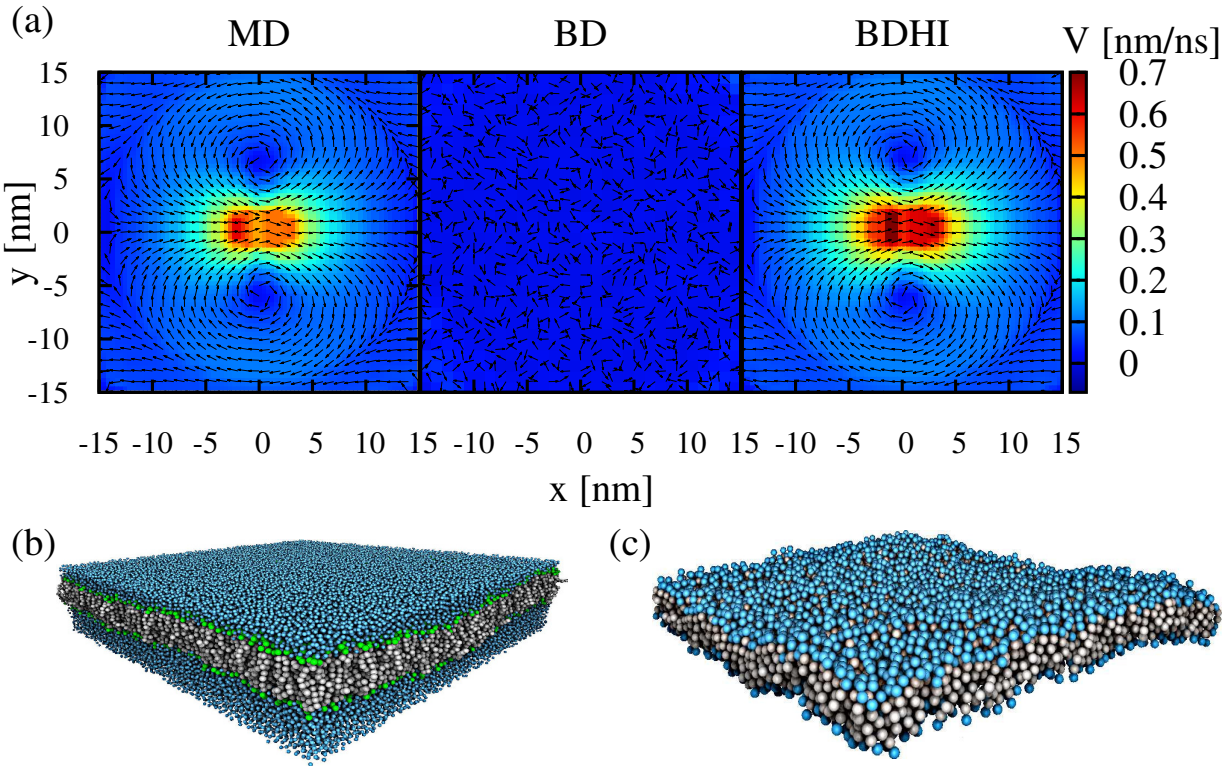

Figure 6.3: (a) Averaged velocity field (black arrows) of membrane lipids evaluated from the displacement correlations (6.1) of a central tagged lipid at $\Delta t = 400\ ps$. We represent in colour the intensity (magnitude) of the field. The three cases presented have been obtained from MD, BD and BDHI simulations, and each leaflet of the membranes has been analysed independently. (b) and (c) are (in that order) snapshots of typical configurations of a MARTINI and Cooke-Deserno lipid membrane.

Thus, in Fig. 6.3 (a) we show the typical vortical correlations obtained from MD, BD and BDHI simulations using a time-lag $\Delta t = 400\ ps$. As expected, BD simulations show no trace of correlations at all. So, we absolutely expect that systems with this kind of correlations lead to a normal Q2D collective diffusion coefficient. This contrasts dramatically with results found for MD and BDHI simulations. Notably, despite of the differences between them, they present very similar vortical patterns. Even more interesting, these correlations seem to be very similar to those correlations found in prior dissipative particle dynamics (DPD) simulations of lipid membranes [8]. Thus, we believe it could be possible that, within the time scales and length scales explored in our MD simulations, even if local momentum is

altered, it only occurs weakly, in such a way that the dynamics are very well approximated. Albeit, there exist also the possibility that these correlations are not the most appropriate quantities to evaluate adverse effects due to thermostats. In either case, hereunder we will present quantitative differences between the collective diffusion coefficients of the different models used in this chapter.

6.2 Collective Intermediate Scattering Function

In much the same spirit as Chap. 5, we study the collective intermediate scattering function $F_c(k,t)$ of lipids with the purpose of estimating their collective diffusion coefficient. Unlike fits made in previous chapters ($\frac{F_c(k,t)}{S(k)} = \exp[-D_c(k,t)k^2t]$), we find that $F_c(k,t)$ can be fitted using an *ad hoc* two-exponential model,

$$\frac{F_c(k,t)}{S(k)} \approx A_1(k)\exp[-D_c^{(1)}(k)k^2t] + [1 - A_1(k)]\exp[-D_c^{(2)}(k)k^2t], \tag{6.2}$$

with $A_1(k), D_c^{(1)}(k)$ and $D_c^{(2)}(k)$ our fitting parameters now. As proof, we show in Figs. 6.4 (a) and (c) that the two-exponential model (dashed lines) is in excellent agreement with the decay of the $F_c(k,t)$ obtained from MD and BDHI simulations (circles). Additionally, in inset of Figs. 6.4 (a) and (c) we show the region of wavenumbers in which the two-exponential model works reasonably well. Empirically, this has been found for values of the fitting parameters $A_1(k)$ and $A_2(k)$ included in the range $[0.2, 0.8]$. This model is also in agreement with the decay of the $F_c(k,t)$ obtained from BD simulations, although it is not shown in Fig. 6.4 (a) for the sake of clarity.

As we will show later, these two relaxation times, $\tau^{(1)} = 1/(D_c^{(1)}(k)k^2)$ at short-times and $\tau^{(2)} = 1/(D_c^{(2)}(k)k^2)$ at long-times, are related to the short and long-time character of the self-diffusion coefficient D_s. Although it can already be inferred from the comparison of the self-diffusion coefficients of lipids and WCA and ideal particles that are confined in a liquid-liquid interface. It should be noted that the differences between the short and long-time self-diffusion coefficients of membrane lipids are much larger that the ones found for ideal and WCA particles. These are about one order of magnitude for the Cooke-Deserno model, and around two orders of magnitude for the MARTINI model. That is probably why, unlike previous analyses about the time dependence of the collective diffusion coefficient, we are now able to identify from the visual inspection of $F_c(k,t)$ both relaxations times.

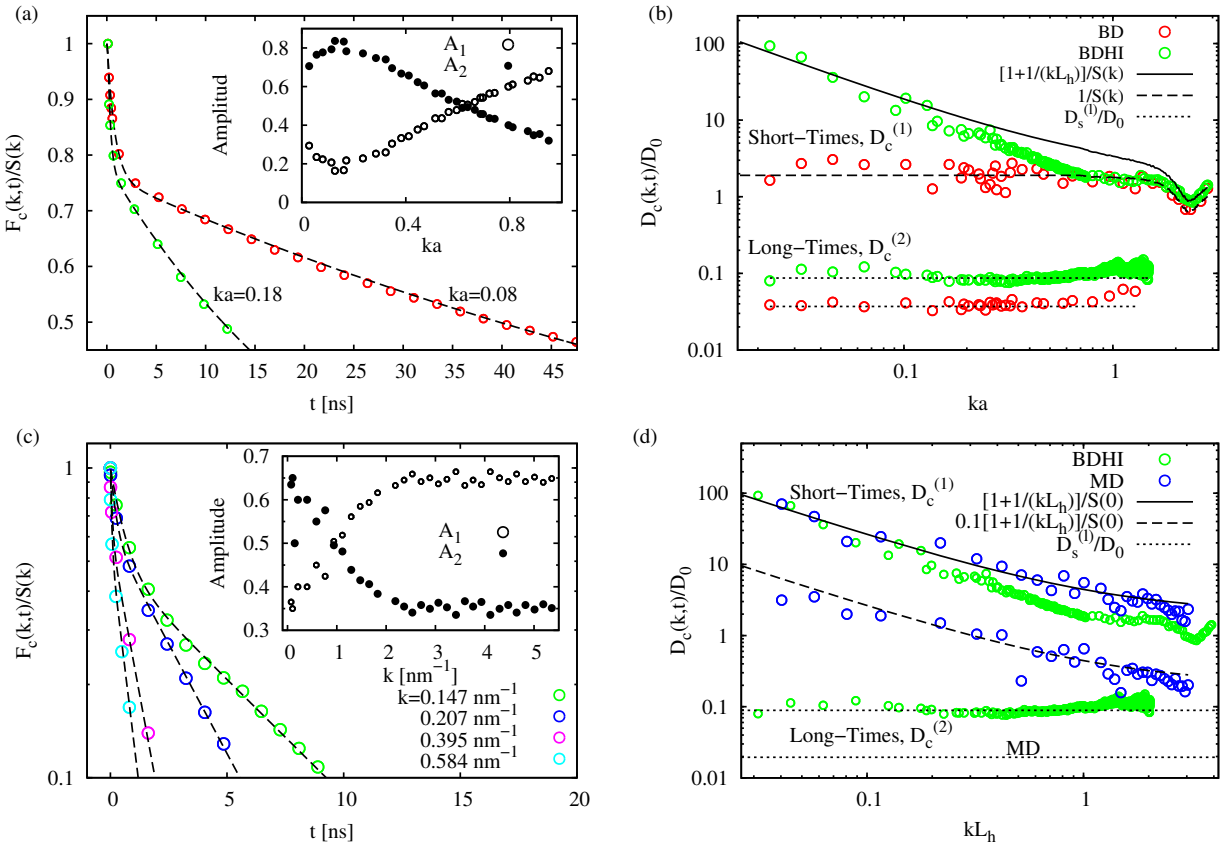

Figure 6.4: (a) Time dependence of the normalised collective intermediate scattering function obtained from BDHI and (c) MD simulations (circles). Each leaflet of the membranes has been analysed independently. Dashed lines stand for a fit to Eq. (6.2), whose amplitudes A_1 and $(1-A_1)$ are shown in insets. (b) Normalised collective diffusion coefficients at short-times ($D_c^{(1)}(k)$) and long-times ($D_c^{(2)}(k)$) obtained from BD and BDHI simulations, and from (d) BDHI and MD simulations. $D_c^{(1)}(k)$ and $D_c^{(2)}(k)$ are extracted from the fit of $F_c(k,t)$ to Eq. (6.2). Solid and dashed lines in (b) are theoretical predictions for the asymptotic behaviour of the short-time collective diffusion coefficient of BDHI and BD simulations respectively. Dotted lines in (b) stand for the long-time self-diffusion coefficient. The solid line in (d) is the theoretical prediction for the asymptotic behaviour of the short-time collective diffusion coefficient of BDHI and MD simulations and the dashed line is the theoretical prediction for the asymptotic behaviour of the short-time collective diffusion coefficient multiplied by a factor 0.1. The dotted line in (d) stands for the long-time self-diffusion coefficient for BDHI and MD simulations.

6.2.1 Short-Time Collective Diffusion Coefficient

With the aim of studying the first relaxation mode in Eq. (6.2) ($D_c^{(1)}(k)$), we start by analysing the results for the Cooke-Deserno model. We illustrate in Fig. 6.4 (b) the values of $D_c^{(1)}(k)/D_0$ estimated from the fit of the numerical $F_c(k,t)$ (BD and BDHI) to Eq. (6.2). Thus, as we already advanced, $D_c^{(1)}(k)$ is found to be related to the short-time self-diffusion coefficient. And in addition, we discover that $D_c^{(1)}(k)$ is anomalous for hydrodynamically interacting membrane lipids (BDHI). Conversely (as expected), $D_c^{(1)}(k)$ is normal for Brownian membrane lipids (BD). To demonstrate these results we show in Fig. 6.4 (b) the theoretical predictions of the Q2D theory for diffusion for BD, $D_c(k,t) = D_c^{(1)}(k) = D_0/S(k)$, and BDHI, $D_c(k,t) = D_c^{(1)}(k) = D_0\left[1 + 1/(L_h k)\right]/S(k)$, with $L_h = \left(\frac{2}{3\phi}\right)a = 0.44$ the hydrodynamic length (assuming that the projection of a lipid in the plane $z = 0$ is a circle of radius a) and $\phi \approx 0.6$ the density fraction of the leaflets of the membrane. See that the agreement between the asymptotic behaviour of the theory and simulations is quite good. For $ka > 0.1$ the agreement is not that good, although we should remind the reader that the collective diffusion coefficient of molecularly interacting particles is expected to deviate from the theory at distances from one to three times the particle diameter (see Sect. 5.2.2).

Then, we repeat the same procedure for the MARTINI model. Again, as we demonstrate in Fig 6.4 (d), the short-time collective diffusion coefficient of MARTINI lipids (MD) matches the asymptotic behaviour of the Q2D diffusion theory at short times, *i.e.* $D_c(k,t) = D_c^{(1)}(k) = D_0\left[1 + 1/(L_h k)\right]/S(0)$[3], with $L_h = 0.53$ and $\phi \approx 0.3$ the density fraction of the leaflets of the membrane. Very interestingly, we find that even if we are making use of a Nosé-Hoover thermostat, we recover a remarkably good match with the theoretical prediction of the Q2D theory for diffusion. This reinforces our previous argument concerning the conservation of momentum *i.e.* we believe that, despite the fact that the Nosé-Hoover thermostat does perturb the local momentum conservation, it does so only weakly, otherwise, we would have got similar behaviour to the one of BD simulations in Fig. 6.4 (b).

Therefore, it seems plausible to use of the following analogy in order to interpret the origin of the anomalous behaviour of the collective diffusion coefficient of membrane lipids: lipid membranes, by contrast to particles systems confined in liquid-liquid and air-liquid

[3] To compare collective diffusion coefficients obtained from MD and BDHI simulations versus an unique master curve we have used S(k=0). This is done because their S(k) differ at large wavenumbers while their asymptotic value, which is what really matters, coincide (see Fig. 6.1).

interfaces, do not need external forces to be confined, but they self-confine. Thus, we believe that forces that arise from intermolecular interactions in the normal direction to the membrane surface (amphipathic and elastic forces) are the original culprits of the anomalous behaviour of the Q2D dynamics of lipids.

6.2.2 Long-Time Collective Diffusion Coefficient

To study the second relaxation mode in Eq. (6.2) ($D_c^{(2)}(k)$) we follow the same procedure as in the previous section. Thus, we start by analysing the results for the Cooke-Deserno model. A very disconcerting observation, shown in Fig. 6.4 (b), is that the long-time collective diffusion coefficient $D_c(k,t) = D_c^{(2)}(k)/D_0$ of hydrodynamically interacting lipids (BDHI) does not diverge at all, contrary to the results found in Sect. 5.2.2.1 (collective diffusion coefficient of WCA particles diverge at short and long times). Moreover, we find that, just like in BD simulations, $D_c^{(2)}(k) = D_s^{(l)}$ *i.e.* lipids diffuse totally uncorrelatedly.

One hypothesis for the unexpected violation of the Q2D theory for diffusion at long-times is that the theoretical predictions were based on a lipid mobility that is described by the Oseen tensor, which could result in a very rough approximation. It is broadly accepted that the mobility tensor that governs the dynamics of lipids and proteins in lipid membranes at long times is given by the Saffman-Delbrück mobility [40–46]. This mobility tensor leads to hydrodynamic interactions among lipids very similar to those of a 3D fluid for distances $r \gg L_{SD}$ (Oseen-like), and similar to those of 2D fluids for distances $r \ll L_{SD}$ (logarithmic like), with the crossover length being the so-called Saffman-Delbrück length $L_{SD} = \frac{\eta_m}{2\eta_f}$, with η_f the fluid dynamic viscosity and η_m the (unknown for the Cooke-Deserno model) membrane dynamic viscosity [47]. Thus, it may be possible that within the system size studied the mobility tensor is given by the one for 2D fluids ($r \ll L_{SD}$) [47], making the divergence of the collective diffusion coefficient vanish (somehow). To rigorously prove this, we would have to derive some Q2D theory for diffusion using the Saffman-Delbrück mobility, which is beyond the scope of this thesis.

A further very interesting discovery involves the behaviour of the collective diffusion coefficient $D_c^{(2)}$ of MARTINI lipids (MD) which is very different to the ones in BDHI and BD simulations. Specifically, see in Fig. 6.4 (d) that $D_c(k,t) = D_c^{(2)}(k)/D_0$ diverges. Yet, it does so unconventionally, *i.e.* we reveal $D_c^{(2)} \approx 0.1 D_c^{(s)}$ instead of $D_c^{(2)} = D_s^{(l)}\left[1 + 1/(L_h k)\right]/S(k)$. Unfortunately, we do not find any plausible explanation for $D_c^{(2)}$, so , its meaning remains elusive. It evinces, though, that our MD simulations are not long enough to reach the long-

time behaviour (dotted line), so we believe the results found here for $D_c^{(2)}$ have nothing to do with prior lucubrations about the mobility of lipids. Therefore, this issue should also be further investigated in future studies.

6.3 Connection with Experiments

Neutron scattering techniques have demonstrated the existence of coherent motion of lipids at short times [4–6]. Specifically, analyses of the FWHM of the dynamic structure factor (temporal Fourier transform of the collective intermediate scattering function) of lipid membranes show a long-ranged (involving several lipid) flow-like diffusion of lipids (FWHM $\propto k$, with k a wavenumber in the plane of the membrane *i.e.* $\boldsymbol{k} \cdot \hat{\boldsymbol{z}} = 0$) [5, 6] with characteristic velocity $v \in [0.3, 1.1]$ nm/ns. Consistently, computer simulations of lipid membranes have also discovered similar flow-like diffusion of lipids [7, 8, 48]. However, we still lack an explanation for this behaviour of lipids [8].

Then, we present here two indications that may shed some light on the relevance of the Q2D hydrodynamics for the flow-like diffusion of lipids. First of all and most straightforward, we infer from the comparison of the three panels of Fig. 6.3 (a) that hydrodynamically interacting lipids yields flow-like correlations that are consistent with previous studies [4–8]. Although authors in Ref. [8], based on the strict violation of the local momentum conservation, rejected the implication of the Q2D hydrodynamics on the origin these flow-like correlations, we stress that, most probably, slight alterations of the local momentum conservation still yield these correlations. Additionally, we find that the MARTINI lipids (the most realistic model of the two treated here) coherently propagate with a characteristic velocity $v = 0.7$ nm/ns (see Fig. 6.3 (a)), which is included in the range of velocities reported experimentally for flow-like diffusion of lipids [5, 6]. Secondly, the Q2D theory for diffusion also predicts flow-like diffusion of lipids *i.e.* FWHM $\propto k$. To demonstrate this, let us accept that the collective intermediate scattering function can be approximated as Eq. (6.2). Thus, the dynamic structure factor

$$\begin{aligned} S(k,\omega) &= \int_{-\infty}^{\infty} F_c(k,t) \exp\left[-\mathrm{i}\omega t\right] dt \\ &= \frac{S(k)}{\pi} \left[A_1 \frac{D_c^{(s)} k^2}{\left(D_c^{(s)} k^2\right)^2 + \left(\frac{\omega}{2\pi}\right)^2} + (1 - A_1) \frac{D_c^{(l)} k^2}{\left(D_c^{(l)} k^2\right)^2 + \left(\frac{\omega}{2\pi}\right)^2} \right], \end{aligned} \tag{6.3}$$

is given by the sum of two Lorentzians, one coming from the short-time contribution and

with FWMH = $2D_c^{(s)}k^2$, and another coming from the long-time contribution and with FWMH = $2D_c^{(l)}k^2$. At short times, the asymptotic regime of the Q2D theory for diffusion ($D_c^{(s)} \propto 1/k$) yields FWHM $\propto k$, which is in agreement with experimental measurements of the FWHM. That is, repulsions among lipids due to the Q2D hydrodynamics may cause short-time and local coherent motion. Nevertheless, because it is very hard to simultaneously access fast time scales and large length scales experimentally[4], and the model of lipid may shift the hydrodynamic length L_h, we find the direct comparison between theory and experiment very complicated. So this last indication should be further revisited in future studies.

Bibliography

[1] J. Bleibel, A. Domínguez, and M. Oettel, *A dynamic dft approach to generalized diffusion equations in a system with long-ranged and hydrodynamic interactions*, Journal of Physics: Condensed Matter **28**, 244021 (2016).

[2] J. Dhont, *An introduction to dynamic of colloids*, vol. 2 (Elsevier, 1996).

[3] A. Domínguez, *Signature of time-dependent hydrodynamic interactions on collective diffusion in colloidal monolayers*, Phys. Rev. E **90**, 062314 (2014).

[4] M. C. Rheinstädter, J. Das, E. J. Flenner, B. Brüning, T. Seydel, and I. Kosztin, *Motional coherence in fluid phospholipid membranes*, Phys. Rev. Lett. **101**, 248106 (2008).

[5] C. L. Armstrong, M. Trapp, J. Peters, T. Seydel, and M. C. Rheinstadter, *Short range ballistic motion in fluid lipid bilayers studied by quasi-elastic neutron scattering*, Soft Matter **7**, 8358 (2011).

[6] S. Busch, C. Smuda, L. C. Pardo, and T. Unruh, *Molecular mechanism of long-range diffusion in phospholipid membranes studied by quasielastic neutron scattering*, Journal of the American Chemical Society **132**, 3232 (2010).

[7] E. Falck, T. Róg, M. Karttunen, and I. Vattulainen, *Lateral diffusion in lipid membranes through collective flows*, Journal of the American Chemical Society **130**, 44 (2008).

[8] T. Apajalahti, P. Niemelä, P. N. Govindan, M. S. Miettinen, E. Salonen, S.-J. Marrink, and

[4] Optical microscopy provides spatial resolutions about $10^5 - 10^3$ Å and temporal resolutions about $10^7 - 10^5$ *ps* while neutron scattering techniques access spatial scales of about $10^2 - 1$ Å and temporal scales of about $10^5 - 10^2$ *ps*.

I. Vattulainen, *Concerted diffusion of lipids in raft-like membranes*, Faraday Discuss. **144**, 411 (2010).

[9] F. BalboaUsabiaga, J. Bell, R. Delgado-Buscalioni, A. Donev, T. Fai, B. Griffith, and C. Peskin, *Staggered schemes for fluctuating hydrodynamics*, Multiscale Modeling & Simulation **10**, 1369 (2012).

[10] S. Delong, F. B. Usabiaga, R. Delgado-Buscalioni, B. E. Griffith, and A. Donev, *Brownian dynamics without green's functions*, The Journal of Chemical Physics **140**, 134110 (2014).

[11] F. B. Usabiaga, R. Delgado-Buscalioni, B. E. Griffith, and A. Donev, *Inertial coupling method for particles in an incompressible fluctuating fluid*, Computer Methods in Applied Mechanics and Engineering **269**, 139 (2014).

[12] C. Arnarez, J. J. Uusitalo, M. F. Masman, H. I. Ingólfsson, D. H. de Jong, M. N. Melo, X. Periole, A. H. de Vries, and S. J. Marrink, *Dry martini, a coarse-grained force field for lipid membrane simulations with implicit solvent*, Journal of Chemical Theory and Computation **11**, 260 (2015).

[13] I. R. Cooke and M. Deserno, *Solvent-free model for self-assembling fluid bilayer membranes: Stabilization of the fluid phase based on broad attractive tail potentials*, The Journal of Chemical Physics **123**, 224710 (2005).

[14] S. Pronk, S. Páll, R. Schulz, P. Larsson, P. Bjelkmar, R. Apostolov, M. R. Shirts, J. C. Smith, P. M. Kasson, D. van der Spoel, et al., *Gromacs 4.5: a high-throughput and highly parallel open source molecular simulation toolkit*, Bioinformatics **29**, 845 (2013).

[15] GROMACS, *reference manual*.

[16] S. J. Marrink, H. J. Risselada, S. Yefimov, D. P. Tieleman, and A. H. de Vries, *The martini force field: coarse grained model for biomolecular simulations*, The Journal of Physical Chemistry B **111**, 7812 (2007).

[17] S. J. Marrink, A. H. de Vries, and A. E. Mark, *Coarse grained model for semiquantitative lipid simulations*, The Journal of Physical Chemistry B **108**, 750 (2004).

[18] S. Baoukina, L. Monticelli, H. J. Risselada, S. J. Marrink, and D. P. Tieleman, *The molecular mechanism of lipid monolayer collapse*, Proceedings of the National Academy of Sciences **105**, 10803 (2008).

[19] W. D. Bennett and D. P. Tieleman, *Computer simulations of lipid membrane domains*, Biochimica et Biophysica Acta (BBA) - Biomembranes **1828**, 1765 (2013).

[20] H. J. C. Berendsen, J. P. M. Postma, W. F. van Gunsteren, A. DiNola, and J. R. Haak, *Molecular dynamics with coupling to an external bath*, The Journal of Chemical Physics **81**, 3684 (1984).

[21] D. J. Evans and B. L. Holian, *The Nose–Hoover thermostat*, The Journal of Chemical Physics **83**, 4069 (1985).

[22] M. Winger, D. Trzesniak, R. Baron, and W. F. van Gunsteren, *On using a too large integration time step in molecular dynamics simulations of coarse-grained molecular models*, Phys. Chem. Chem. Phys. **11**, 1934 (2009).

[23] FLUAM, *fluid and matter*.

[24] J. Drouffe, A. Maggs, and S. Leibler, *Computer simulations of self-assembled membranes*, Science **254**, 1353 (1991).

[25] T. Sintes and A. Baumgärtner, *Protein attraction in membranes induced by lipid fluctuations*, Biophysical Journal **73**, 2251 (1997).

[26] H. Noguchi and M. Takasu, *Self-assembly of amphiphiles into vesicles: A brownian dynamics simulation*, Phys. Rev. E **64**, 041913 (2001).

[27] G. Brannigan, L. C.-L. Lin, and F. L. H. Brown, *Implicit solvent simulation models for biomembranes*, European Biophysics Journal **35**, 104 (2006).

[28] O. Farago, *"water-free" computer model for fluid bilayer membranes*, The Journal of Chemical Physics **119**, 596 (2003).

[29] V. A. Harmandaris and M. Deserno, *A novel method for measuring the bending rigidity of model lipid membranes by simulating tethers*, The Journal of Chemical Physics **125**, 204905 (2006).

[30] J. M. Gardner, M. Deserno, and C. F. Abrams, *Effect of intrinsic curvature and edge tension on the stability of binary mixed-membrane three-junctions*, The Journal of Chemical Physics **145**, 074901 (2016).

[31] B. J. Reynwar, G. Illya, V. A. Harmandaris, M. M. Müller, K. Kremer, and M. Deserno, *Aggregation and vesiculation of membrane proteins by curvature-mediated interactions*, Nature **447**, 461 EP (2007).

[32] M. Hu, J. J. Briguglio, and M. Deserno, *Determining the gaussian curvature modulus of lipid membranes in simulations*, Biophysical Journal **102**, 1403 (2012).

[33] W. den Otter and S. Shkulipa, *Intermonolayer friction and surface shear viscosity of lipid bilayer membranes*, Biophysical Journal **93**, 423 (2007).

[34] R. Metzler, J.-H. Jeon, and A. Cherstvy, *Non-brownian diffusion in lipid membranes: Experiments and simulations*, Biochimica et Biophysica Acta (BBA) - Biomembranes **1858**, 2451 (2016).

[35] J.-F. Tocanne, L. Dupou-Cézanne, and A. Lopez, *Lateral diffusion of lipids in model and natural membranes*, Progress in Lipid Research **33**, 203 (1994).

[36] W. Vaz and P. Almeida, *Microscopic versus macroscopic diffusion in one-component fluid phase lipid bilayer membranes*, Biophysical Journal **60**, 1553 (1991).

[37] K. Jacobson, *Lateral diffusion in membranes*, Cell Motility **3**, 367 (1983).

[38] P. F. F. Almeida, W. L. C. Vaz, and T. E. Thompson, *Lateral diffusion in the liquid phases of dimyristoylphosphatidylcholine/cholesterol lipid bilayers: a free volume analysis*, Biochemistry **31**, 6739 (1992).

[39] J. Tabony and B. Perly, *Quasielastic neutron scattering measurements of fast local translational diffusion of lipid molecules in phospholipid bilayers*, Biochimica et Biophysica Acta (BBA) - Biomembranes **1063**, 67 (1991)

[40] P. G. Saffman and M. Delbrück, *Brownian motion in biological membranes*, Proceedings of the National Academy of Sciences **72**, 3111 (1975).

[41] M. Vögele, J. Köfinger, and G. Hummer, *Hydrodynamics of diffusion in lipid membrane simulations*, Phys. Rev. Lett. **120**, 268104 (2018).

[42] M. Vögele and G. Hummer, *Divergent diffusion coefficients in simulations of fluids and lipid membranes*, The Journal of Physical Chemistry B **120**, 8722 (2016).

[43] B. A. Camley, M. G. Lerner, R. W. Pastor, and F. L. H. Brown, *Strong influence of periodic boundary conditions on lateral diffusion in lipid bilayer membranes*, The Journal of Chemical Physics **143**, 243113 (2015).

[44] B. A. Camley and F. L. H. Brown, *Diffusion of complex objects embedded in free and supported lipid bilayer membranes: role of shape anisotropy and leaflet structure*, Soft Matter **9**, 4767 (2013).

[45] P. Cicuta, S. L. Keller, and S. L. Veatch, *Diffusion of liquid domains in lipid bilayer membranes*, The Journal of Physical Chemistry B **111**, 3328 (2007).

[46] E. P. Petrov and P. Schwille, *Translational diffusion in lipid membranes beyond the saffman-delbrück approximation*, Biophysical Journal **94**, L41 (2008).

[47] N. Oppenheimer and H. Diamant, *Correlated diffusion of membrane proteins and their effect on membrane viscosity*, Biophysical Journal **96**, 3041 (2009).

[48] G. S. Ayton and G. A. Voth, *Mesoscopic lateral diffusion in lipid bilayers*, Biophysical Journal **87**, 3299 (2004).

Part III.

Epilogue

7 General Conclusions

– Very interesting, Mr. Faraday, but what is the practical value of electricity?
– One day, sir, you may tax it.

— **Michael Faraday**, 1850.

7.1 English

Throughout this thesis we have faced different matters of interest in lateral properties of amphipathic complexes of the pulmonary surfactant system. In chapter 3 we have started analysing lipid domains present in DPPC monolayers. Along this study, we have characterised structural properties of lipids that belong to different domains, as well as the properties of domains. Conversely, chapter 6 has been devoted to the study of the collective motion of lipids within membranes. To this end, we have previously developed a fundamental theory on collective diffusion, which is presented and tested through chapters 4 and 5. In this final chapter, we will summarise the general conclusion of this thesis, discussing also the remaining open questions and the possible prospects of different lines of inquery.

7.1.1 Lateral Properties of Lipid Monolayers

As discussed in the general introduction of this thesis (chapter 1), the stabilisation of multiple condensed lipid domains (LC) that coexist with an expanded lipid domain (LE)

is a controversial topic [1–9]. To shed some light in this respect, in chapter 3 of this thesis we have faced general questions regarding the stabilisation of condensed domains, using a very detailed computational model (CHARMM36+OPC) of a lipid monolayer that is located in a water-vapour interface [10]. In contrast to earlier studies [11], here we study these domains independently. To this end, we have developed an accurate methodology based on the local crystalline properties of domains. As it has been demonstrated, this methodology almost perfectly predicts the region of coexistence of condense and expanded phases (LC and LE) which provides support for it use. Applying this method, we have obtained an average orientation of the tail groups of lipids qualitatively in agreement with the value already reported previously, although it seems to indicate the force field gives rise to a slight underestimation of the orientation ($\sim 5-10^{\circ}$). On the other hand, we have encountered that the average orientation of the head group of lipids as well as its level of hydration are the same independently of whether a lipid belongs to a LC or LE domain, which is totally in disagreement with experimental results [12, 13]. This result, together with other results with regard to the angle distributions of lipids (the head group of lipids is randomly oriented in the monolayer plane), suggest that the CHARMM36+OPC force field may be incorrect when reproducing the properties of the head group of lipids. Because of this setback, we cannot conclude whether the perpendicular component (with respect to the normal vector of the monolayer) of the dipolar moment of lipids plays any role in the stabilisation of condensed domains [6–9]. Although this defect of the force field is very subtle, we believe it could affect other properties of lipids such as the tilt orientation of the tail group of lipids and interfacial properties (surface tension, water hydration layer and so on), so that we recommend future lines of research in this direction. Thus, one of the most important questions to solve is whether the failure in the predictive capabilities of the force field is exclusively due to the CHARMM36 force field or, on the contrary, it is caused by the combination of the CHARMM36 and OPC force fields.

With regard to the properties of domains, we have proposed a new way of representing them simplifying their visualisation and characterisation. As we already explained, it consists on representing lipids that composed the domains as 2D prolate ellipses of aspect ratio 2.5 in the membrane plane. From these analyses we have found condensed domains present elongated/rectangular shapes rather than circular, which seems to indicate the presence of an anisotropic line tension at the border of domains. On the other hand, we have seen condensed domains exhibit a high dipolar order, as a result of the strong (parallel) orientation of the acyl chains of lipids. Furthermore, we have noticed the average orientation of condensed domains, and equivalently, the orientation of acyl chains of lipids with respect to the interface of the condensed-expanded phases is about 10°. Again, this indicates the

presence of an anisotropic line tension at the boundary of condensed domains, however, models for the stabilisation of domains do not address this fact [6–9]. To contrast the relevance of an anisotropic line tension, it would be interesting to incorporate this property of condensed domains in future theoretical work for the stabilisation of domains [6–9].

Notwithstanding, the enormous progress made, there are still many other unanswered questions concerning the stabilisation of condensed domains. Due to obvious reasons, atomistic simulations are extremely inefficient for these studies. Instead, simplified (coarse-grained) models, may be useful in this respect. We think one could take advantage of the in-plane properties of lipids (aspect ratio, angle distributions and correlations) to translate the study of the features of domains *e.g.* morphology and orientation, and their presumable stabilisation, to a 2D effective problem. Within this view, we would restrict to exclusively address the properties of condensed and expanded domains (individual features of lipids would not be relevant anymore), but with the colossal gain of computer efficiency in simulating techniques such as MD. Along the same line, one could also take advantage of this view of a lipid to study, quantitatively, line tension and curvature properties of expanded and condensed domains as a function of the dipolar orientation of a lipid.

7.1.2 Diffusion in Lipid Membranes

Another of the most fascinating properties of lipids that we have treated in the second part of this thesis, but seldom regarded in the field of biomembranes, is its collective dynamics. Chapters 4-6 of this thesis have been devoted to the development of a theoretical framework for studying the collective motion of membrane lipids. In chapter 4 we have started with the development of FDDFT-HI, with which we have studied the collective response of particles that are strictly confined to liquid-liquid interfaces (Q2D). And we have developed an ultra-fast GPU algorithm (which scales linearly with the number of particles) to simulate strict Q2D systems. Applying this theory, to which we refer to as the Q2D theory for diffusion, we have demonstrated that confinement forces induce long-ranged repulsive solvent-mediated forces among particles, which eventually lead to anomalous properties in the dynamics of particles, some of them already known [14–17]. Formally, we have shown this is equivalent to affirm that the surrounding fluid, while being incompressible (in 3D), is apparently compressible in the particle plane of motion. As a result, the dynamics of the macroscopic density of particles is not governed by a standard diffusion equation but an advection-diffusion equation. It leads to density perturbations in the macroscopic density (ensemble average) decay showing the so-called $1/r^3$ power-law tails [15–17]. In addition

to these theoretical predictions, we have demonstrated by means of Q2D simulations that equilibrium thermal fluctuations yield a renormalisation of the self-diffusion coefficient of particles at long-times, even if the particles are ideal (tracer; non-interacting via interparticle potentials) *i.e.* equilibrium thermal fluctuations are not negligible. It has also been proved that, because of the repulsions among particles, the collective diffusion coefficient diverges at large distances (small wavenumber). Paradoxically, this implies that the collective response of large set of particles is faster than the collective response of small sets of particles. On the other hand, we have shown that non-equilibrium fluctuations in binary mixtures are considerable (quasi-giant). Despite being as big as those of 2D fluids and microgravity experiments [18–20], we expect they may be measurable in experiments. Finally, it is worth highlighting that, the general framework of the Q2D theory for diffusion is straightforward applicable to experiments.

In chapter 5 we have derived an alternative formalism for the Q2D theory for the diffusion that allows considering non-ideal scenarios *i.e.* particles can fluctuate around the confinement plane and interact via short-ranged interparticle potentials. This formalism, in contrast to others used in theories for the Q2D diffusion [15–17, 21], is devoted to the analysis of the short-time collective diffusion coefficient. Nevertheless, it can be extended to long-times. In preliminary studies, we have ratified this new formalism by previous results obtained, and we have completed partial studies about short-ranged interacting particles [17]. In both cases, as expected, the collective diffusion coefficient diverges. Interestingly, we have discovered that the anomalous properties of confined particles disappear as the confinement is removed, up to the 3D limit (normal diffusion). The main reason for this effect is that repulsive forces among particles vanish as the confinement is removed. This progressive transition between Q2D and 3D dynamics has simultaneously been predicted by Bleibel *et al.* [21]. Moreover, we have proved for the first time that, indeed, the short and long-time collective diffusion coefficient diverge, notwithstanding they do with different slopes, which are associated to the short and long time self-diffusion coefficients (respectively) of particles. Although this divergence has only been predicted for WCA interacting particles, we do not expect any deviation for any short-ranged interacting potential. Last, we have explored by means of computer simulations the theoretical limits of applicability of the Q2D theory for diffusion [22]. Indeed, as the theory already predicted, we have found that for very small wavenumbers (smaller than the critical wavenumber k_c), the collective diffusion coefficient propagates so fast that the Stokes flow approximation does not hold anymore, and neither does the Q2D theory for the diffusion.

Lastly, in chapter 6 we have applied the Q2D theory for the diffusion to membrane lipids. To prove its validity, we have performed MD simulations of the MARTINI model

of a DPPC lipid membrane in water, and we have performed BDHI simulations of the Cooke-Deserno model of a lipid membrane. For both cases we have shown that the short-time collective diffusion coefficient of lipids diverges in the same way as that of particles in liquid-liquid interfaces. Even if in our MD simulations we have employed a Nosé-Hoover thermostat (weakly coupled to a thermal reservoir), it does not preclude the anomalous behaviour of the collective diffusion coefficient. Based on the excellent agreement between MD, BDHI and the Q2D theory for the diffusion, we guess that, even if the Nosé-Hoover thermostat is violating the lineal momentum conservation, this fact weakly affects the collective diffusion coefficient (particle correlations). This hypothesis should be checked in future work by addressing, for instance, how different thermostats and coupling affect the collective diffusion coefficient. As we have already demonstrated, Brownian dynamics definitively violates the Q2D theory for diffusion. It would also be convenient, not to say compulsory, to compare this behaviour with constant energy simulations (NVE).

At long times, results on the collective diffusion coefficient are more controversial. On the one hand, we have observed that the MARTINI model leads to an anomalous collective diffusion coefficient, although this coefficient does not coincide with the one at long times. The complexity of the model makes its interpretation hard so that at present we do not have any explanation in this respect. It is clear, though, that the long-time regime is not reached. This is known from the slope of the collective diffusion coefficient, which is associated to an intermediate regime. To conclude in these respect, it would be necessary to discuss several aspects. First of all, it would be very convenient to simulate longer times in order to reach the long-time regime. Furthermore, BD simulations of the MARTINI model could be very helpful for comparison purposes. Alternatively, BDHI simulations of the dry MARTINI model (without the presence of explicit water molecules) could be very handy to ensure the approach of the long-time regime while testing complex models of membrane lipids.

On the other hand, we have discovered by means of BDHI simulations of the Cook-Deserno model that the long-time collective diffusion coefficient of lipids does not diverge. What is more, this diffusion coefficient is equal to that of BD simulations. This is the first evidence of the breakdown of the Q2D theory for the diffusion applied to membrane lipids. A plausible explanation of this effect could be an incorrect approximation to the mobility of a lipid. Namely, the standard Q2D theory for the diffusion assumes that the mobility tensor of lipids is Oseen-like. However, it has extensively been proved that, at long-times, the mobility tensor of lipids is intimately related to the Saffman-Delbrück mobility [23, 24]. Thus, we suppose the Saffman-Delbrück mobility must, somehow, make the collective diffusion coefficient of membrane lipids normal. Strictly, to elucidate this

issue, one would need the development of a Q2D theory for diffusion devoted to long times and using the Saffman-Delbrück mobility tensor.

At the end of chapter 6 we have tried to demonstrate the relation between the coherent motion of lipids at short-times [25–29] and Q2D hydrodynamics. By means of MD and BDHI simulations we have reproduced similar coherent motion of lipids and their velocities. Additionally, from the comparison of the theoretical FWHM of the dynamic structure factor of a lipid membrane with the experimental one, we have been able to detect that their mechanisms for diffusing are the same (flow-like) [27]. Nevertheless, we are not sure yet whether the length scales at which these phenomena take place overlap. In this sense, prospective experimental studies may be relevant to reach a conclusion.

Despite the fact that the Q2D theory for the diffusion has only been applied (in biological systems) to lipid bilayers, this theory can be potentially applied to a wider number of systems (we recall this effect is generic *i.e.* it does not depend on the short-ranged nature of particles but this is a general feature/signature of the Q2D hydrodynamics). To name a few applications, this theory may be valuable to explain the collective dynamics of proteins embedded in a lipid bilayer or monolayers, which are known to be essentially relevant for fundamental processes such as membrane fusion and pore opening/closing. This theory would also be very useful for other hot topics in the field of biomembranes: dynamics of lipid rafts and mixture of species within lipid membranes and monolayers.

7.2 Español

A lo largo de esta tesis hemos tratado diferentes asuntos de interés en las propiedades laterales de complejos anfifáticos del sistema surfactante pulmonar. En el capítulo 3 hemos comenzado analizando dominios lipídicos presentes en monocapas de DPPC. Durante este estudio hemos caracterizado las propiedades estructurales de los lípidos que conforman los diferentes dominios, así como las propiedades de los dominios. Por otro lado, el capítulo 6 ha sido dedicado al estudio de movimientos colectivos de lípidos en membranas de DPPC. Con este fin, hemos desarrollado previamente una teoría elemental sobre la difusión colectiva, la cual es presentada y verificada a lo largo de los capítulos 4 y 5. En este último capítulo, resumiremos las conclusiones generales de esta tesis, debatiendo las preguntas que permanecen sin resolver y las posible futuras líneas de trabajo.

7.2.1 Propiedades Laterales de Monocapas Lipídicas

Como hemos debatido en la introducción general de esta tesis (capítulo 1), la estabilización de múltiples dominios lipídicos condensados (LC) que coexisten con un dominio lipídico expandidos (LE) es un tema controvertido [1–9]. Para aportar aclaraciones en este asunto, en el capítulo 3 hemos abordado preguntas generales que conciernen a la estabilización de dominios condensados, usando simulaciones de modelos computaciones muy precisos (CHARMM36+OPC) de una monocapa lipídica que se encuentra ubicada en una interfaz agua-vapor [10]. Con diferencia a estudios previos [11], en esta tesis hemos estudiado los dominios de forma independiente. Para ello, hemos desarrollado una metodología muy precisa basada en las propiedades cristalinas de los dominios. Como hemos demostrado, esta metodología predice casi a la perfección la región de coexistencia de las fases condensadas y expandidas (LC y LE), lo que da credibilidad para su uso. Aplicando esta técnica, hemos obtenido que la orientación promedio de los grupos cola de los lípidos son cualitativamente iguales a las ya reportadas previamente, aunque parecen indicar que el campo de fuereza da lugar a una leve subestimación de las orientaciones ($\sim 5-10°$). Por otro lado, hemos encontrado que tanto la orientación promedio de los grupos cabeza de los lípidos como su nivel de hidratación son los mismos independientemente de a qué dominio (LC/LE) pertenezca un lípido, siendo esto contrario a experimentos [12, 13]. Este resultado, junto con otros resultados sobre la distribución de ángulos de los lípidos (el grupo cabeza de

los lípidos se encuentra orientado aleatoriamente en el plano de la monocapa) sugieren que el campo de fuerza CHARMM36+OPC podría ser incorrecto a la hora de reproducir las propiedades del grupo cabeza de los lípidos. A consecuencia de este inconveniente, no podemos concluir si la componente perpendicular (respecto a la normal de la monocapa) del momento dipolar de los lípidos juega algún papel para la estabilización de dominios condensados [6–9]. Aunque este defecto del modelo computacional sea muy sutil, pensamos que pudiese afectar otras propiedades de los lípidos tales como la orientación del grupo cola y las propiedades interfaciales (tensión superficial, capa de hidratación de agua, etc.), por lo que recomendamos futuras líneas de investigación en esta dirección. Así, una de las principales preguntas a resolver es si el fallo de predicción del modelo computacional se debe exclusivamente al campo de fuerza CHARMM36, o por lo contrario, se debe a la combinación de los campos de fuerzas CHARMM36 y OPC.

En cuanto a las propiedades de los dominios, hemos propuesto una nueva forma de representarlos, simplificando su visualización y caracterización. Como ya explicamos, esto consiste en representar en el plano de la monocapa los lípidos que componen los dominios como elipses de relación de aspecto 2.5. A partir de estos análisis nos hemos dado cuenta de que los dominios condensados tienden a presentar formas elongadas/rectangulares, en lugar de circulares, lo que parece indicar la presencia de una tensión de linea anisotrópica en la frontera de los dominios. Por otro lado, hemos visto que los dominios condensados presentan un gran orden dipolar, siendo este orden consecuencia directa de la fuerte orientación (paralela) de las cadenas acílicas de los lípidos. Además, hemos notado que la orientación promedio de los dominios condensados (y por tanto de las cadenas acílicas de los lípidos) respecto a la interfaz de las fases expandida y condensada es alrededor de 10°. Esto apunta de nuevo a la presencia de una tensión de linea anisotrópica en la frontera de los dominios, hecho que no ha sido aún considerado teóricamente [6–9]. Para comprobar la relevancia de esta tensión de línea, sería interesante la incorporación de esta propiedad de los dominios condensados en futuras teorías de la estabilización de dominios.

No obstante, a pesar del progreso realizado, todavía quedan muchas preguntas por resolver en cuanto a las estabilización de dominios. Por razones obvias, las simulaciones atomísticas son extremadamente ineficientes para estos estudios. En cambio, modelos simplificados (grano grueso) podrían ser útiles en este aspecto. Pensamos que se podrían aprovechar de las propiedades 2D de los lípidos (relación de aspecto, distribución de ángulos y correlaciones) para trasladar el estudio de las propiedades de los dominios *e.g.* morfología y orientación, y el estudio de su presunta estabilización, a un problema efectivo en 2D. Dentro de esta visión, uno se restringiría al estudio exclusivo de las propiedades de los dominios condensados y expandidos (las propiedades de los lípidos no serían relevantes),

aunque con una gran ganancia de eficiencia computacional en técnicas de simulación tales como dinámica molecular (MD). En la misma dirección, uno también podría aprovechar esta particular visión de un lípido para estudiar, cuantitativamente, propiedades de tensión de línea y curvatura de dominios lipídicos en función de la orientación dipolar de un lípido.

7.2.2 Difusión en Membranas Lipídicas

Otra propiedad fascinante de los lípidos que hemos tratado en la segunda parte de esta tesis, aunque mucho menos considerada en el campo de la membranas biológicas, es su movimiento colectivo. Los capítulos 4-6 de esta tesis han sido dedicados al desarrollo de un marco teórico para estudiar los movimientos colectivos de lípidos en membranas. En el capítulo 4 hemos comenzado con el desarrollo de una teoría del funcional de la densidad dinámica con interacciones hidrodinámicas y fluctuaciones (FDDFT-HI), con la cual hemos estudiado la respuesta colectiva de partículas que se encuentra estrictamente confinadas en una interfaz líquido-líquido (Q2D). Y con el desarrollo de un algoritmo ultra rápido en GPU (escala linealmente con el número de partículas) para simular sistemas Q2D estrictos. Aplicando esta teoría, a la cual nos referimos como la teoría Q2D de la difusión, hemos demostrado que las fuerzas confinantes inducen a través del fluido fuerzas repulsivas de largo alcance entre las partículas, lo que finalmente da lugar a propiedades anómalas en la dinámica de las partículas, alguna de ellas ya conocidas [14–17]. Formalmente, hemos explicado que esto es equivalente a afirmar que un fluido, a pesar de ser incompresible (en 3D), de forma efectiva, en el plano de las partículas se comporta como un fluido compresible. Como resultado, la dinámica de la densidad macroscópica de partículas no está regida por una ecuación de difusión, sino por una ecuación de advección-difusión. Esto da lugar a que una perturbación de la densidad macroscópica (colectivo promedio) decaiga mostrando las llamadas $1/r^3$ colas largas [15–17]. Además de estas predicciones teóricas, hemos demostrado a partir de simulaciones Q2D que las fluctuaciones de equilibrio conllevan a tiempos largos a una renormalización del coeficiente de difusión propio de las partículas, incluso si estas son ideales (trazadoras; no interactuantes a partir de potenciales entre particular) *i.e.* la fluctuaciones de equilibrio no son despreciables. También ha sido probado que a consecuencia de la repulsiones entre partículas, el coeficiente de difusión colectivo de ellas diverge a largas distancias (pequeños números de onda). Paradójicamente, esto implica que la respuesta colectiva de un gran número de partículas sea más rápida que la respuesta colectiva de un pequeño número de partículas. Por otro lado, hemos demostrado que las fluctuaciones de no equilibrio en mezclas binarias son considerables

(casi gigantes). Aunque estas no sean tan grandes como las presentes en fluidos 2D y en experimentos en microgravedad [18–20], esperamos que sean medibles en experimentos. Cabe destacar que tal cual es derivado el marco teórico de esta teoría Q2D de la difusión, la aplicación de esta teoría en experimentos es fácil.

En el capítulo 5 hemos derivado un formalismo alternativo para la teoría Q2D de la difusión, lo que permite el estudio de situaciones no ideales *i.e.* las partículas pueden fluctuar respecto al plano de confinamiento e interactuar mediante potenciales entre partículas de corto alcance. Este formalismo, a diferencia de otros usados para la teoría Q2D de la difusión [15–17, 21], es dedicado a el análisis del coeficiente de difusión colectivo a cortos tiempos, aunque puede ser extendido a largos tiempos. En estudios preliminares, hemos ratificado con este nuevo formalismo los resultados previos obtenidos y completado estudios parciales sobre interacciones de corto alcance entre partículas [17]. En ambos casos, como se esperaba, el coeficiente de difusión colectivo diverge. Interesantemente, hemos descubierto que las propiedades anómalas de partículas confinadas desaparecen de manera progresiva a medida que el confinamiento es disminuido, hasta alcanzar el límite 3D (difusión normal). La principal razón para esto es que las fuerzas repulsivas entre partículas desaparecen a medida que el confinamiento es eliminado. Esta transición progresiva entre la dinámica Q2D y 3D ha sido predicha al mismo tiempo por Bleibel *et al.* [21]. Además, hemos probado por primera vez que, efectivamente, el coeficiente de difusión colectivo a cortos y largos tiempos diverge. No obstante, lo hacen con diferentes pendientes, las cuales se encuentran asociadas a los coeficientes de difusión propios de las partículas a cortos y largos tiempos (respectivamente). Aunque esto ha sido solamente probado para partículas interactuantes WCA, no esperamos ninguna desviación en cualquier otro potencial de corto alcance entre partículas. Por último, hemos explorado a partir de simulaciones los límites de aplicación de la teoría Q2D de la difusión [22]. En efecto, como la teoría ya predijo, hemos encontrado que para números de onda muy pequeños (más pequeños que el número de onda crítico k_c) el coeficiente de difusión colectivo se propaga tan rápido que la aproximación de flujo de Stokes no es válida, así como tampoco la teoría Q2D para la difusión.

Finalmente, en el capítulo 6 hemos aplicado la teoría Q2D para la difusión a membranas lipídicas. Para comprobar su validez, hemos realizado simulaciones MD del modelo computacional MARTINI de una membrana lipídica de DPPC en agua, y simulaciones Brownianas con interacciones hidrodinámicas (BDHI) del modelo computacional Cooke-Deserno de una membrana lipídica. En ambos casos hemos demostrado que el coeficiente de difusión colectivo de los lípidos diverge a cortos tiempos, de la misma forma en que lo haría el de partículas en una interfaz líquido-líquido. Incluso si en nuestras simulaciones

MD hemos usado un termostato de Nosé Hoover (débilmente acoplado a un reservorio térmico), esto no evita el comportamiento anómalo del coeficiente de difusión colectivo. En base al excelente acuerdo entre simulaciones de MD, BDHI y la teoría Q2D de la difusión, conjeturamos que, incluso si el termostato de Nosé Hoover viola la conservación del momento lineal, esto solo afecta débilmente a el coeficiente de difusión colectivo (correlaciones entre partículas). Esta hipótesis tendría que ser comprobada en futuras lineas de investigación abordando, por ejemplo, los efectos de los diferentes termostatos y sus acoplamientos en el coeficiente de difusión colectivo. Para el caso de dinámica Browniana, ya hemos demostrado que viola la teoría Q2D para la difusión. Por razones obvias, sería también conveniente, por no decir obligatorio, la comparación con simulaciones de energía constante (NVE).

A largos tiempos, los resultados sobre el coeficiente de difusión colectivo son más controvertidos. Por un lado, hemos observado que el modelo MARTINI da lugar a un coeficiente de difusión colectivo anómalo, aunque este coeficiente de difusión no coincide con el de tiempos largos. La complejidad del modelo computacional hace que su interpretación sea ardua, por lo que a tiempo presente no tenemos ninguna explicación en este asunto. Sin embargo, está claro que el régimen de largos tiempos no ha sido alcanzado. Esto es sabido a partir de la pendiente del coeficiente de difusión colectivo, siendo asociado a un régimen intermedio. Para concluir en este sentido sería necesario discutir distintos aspectos. Antes de nada, sería muy conveniente realizar simulaciones más largas para así alcanzar el régimen de largos tiempos. Además, simulaciones de BD del modelo MARTINI podrían ser muy útiles para contrastar opiniones. Alternativamente, simulaciones de BDHI del modelo computacional MARTINI seco (sin moléculas de aguas explicitas) podrían ser muy útiles para asegurar el alcance del régimen de largos tiempos con modelos computaciones complejos de membranas lipídicas.

Por otro lado, hemos descubierto a partir de simulaciones BDHI que el coeficiente de difusión colectivo a largos tiempos del modelo computacional Cooke-Deserno no diverge. Es más, este es igual al de simulaciones BD. Esta es la primera evidencia que tenemos de la violación de la teoría Q2D de la difusión aplicada a membranas lipídicas. Una explicación plausible a este hecho podría ser que estuviésemos asumiendo una aproximación incorrecta de la movilidad de un lípido. En concreto, la teoría Q2D de la difusión asume que el tensor de movilidad de un lípido está dado por el tensor de Oseen. Sin embargo, es sabido que a tiempos largos el coeficiente de difusión propio de un lípido está íntimamente relacionado a la movilidad de Saffman-Delbrück [23, 24]. Por tanto, creemos que la movilidad de Saffman-Delbrück hace que, de alguna forma, el coeficiente de difusión colectivo no diverja. De forma estricta, para resolver este tema, uno tendría que desarrollar una teoría Q2D de la difusión

a largos tiempos y usando la movilidad de Saffman-Delbrück.

A final del capítulo 6 hemos intentado demostrar la relación entre el movimiento coordinado de lípidos a cortos tiempos [25–29] y la hidrodinámica Q2D. A partir de simulaciones MD y BDHI hemos reproducido similares movimientos coherentes de lípidos y sus velocidades. Además, a partir de la comparación entre la anchura máxima a mitad de altura (FWHM) teórica del factor de estructura dinámico de una membrana lipídica, y la correspondiente de experimentos, hemos detectado que los lípidos usan el mismo mecanismo para difundir (en forma de flujo) [27]. No obstante, no estamos seguros aún de si las escalas donde ocurren estos fenómenos coinciden. Para ello, serían necesarios nuevo experimentos.

A pesar de que la teoría Q2D de la difusión ha sido solo aplicada (en sistemas biológicos) a membranas lipídicas, esta teoría tiene un rango de aplicación potencialmente más amplio (recordamos que este efecto es genérico *i.e.* no depende de la naturaleza -de corto alcance- de las partículas sino de las propiedades generales de la hidrodinámica Q2D). Por nombrar algunas aplicaciones, esta teoría podría ser muy valiosa para explicar el movimiento colectivo de proteínas embebidas en bicapas o monocapas lipídicas, lo que es sabido ser esencial para procesos tales como la fusión de membranas o apertura y cierre de poros. También sería muy útil para otro temas de actualidad en el campo de las biomembranas: dinámica de balsas lipídicas y mezclas de especies dentro de membranas y monocapas.

Bibliography

[1] F. MacRitchie and P. Fletcher, *Chemistry at interfaces: Academic press, san diego, ca, 1990.* (1990).

[2] J. H. Ipsen, O. G. Mouritsen, and M. J. Zuckermann, *Decoupling of crystalline and conformational degrees of freedom in lipid monolayers*, The Journal of Chemical Physics **91**, 1855 (1989).

[3] J. Israelachvili, *Self-assembly in two dimensions: Surface micelles and domain formation in monolayers*, Langmuir **10**, 3774 (1994).

[4] K. Ekelund, E. Sparr, J. Engblom, H. Wennerström, and S. Engström, *An afm study of lipid monolayers. 1. pressure-induced phase behavior of single and mixed fatty acids*, Langmuir **15**, 6946 (1999).

[5] C. M. Rosetti, A. Mangiarotti, and N. Wilke, *Sizes of lipid domains: What do we know from artificial lipid membranes? what are the possible shared features with membrane rafts*

in cells?, Biochimica et Biophysica Acta (BBA) - Biomembranes **1859**, 789 (2017).

[6] F. Campelo, A. Cruz, J. Pérez-Gil, L. Vázquez, and A. Hernández-Machado, *Phase-field model for the morphology of monolayer lipid domains*, The European Physical Journal E **35**, 49 (2012).

[7] H. Mohwald, *Phospholipid and phospholipid-protein monolayers at the air/water interface*, Annual Review of Physical Chemistry **41**, 441 (1990).

[8] C. W. McConlogue and T. K. Vanderlick, *A close look at domain formation in dppc monolayers*, Langmuir **13**, 7158 (1997).

[9] H. M. McConnell and V. T. Moy, *Shapes of finite two-dimensional lipid domains*, The Journal of Physical Chemistry **92**, 4520 (1988).

[10] M. Javanainen, A. Lamberg, L. Cwiklik, I. Vattulainen, and O. H. S. Ollila, *Atomistic model for nearly quantitative simulations of langmuir monolayers*, Langmuir **34**, 2565 (2018).

[11] H. Dominguez, A. M. Smondyrev, and M. L. Berkowitz, *Computer simulations of phosphatidylcholine monolayers at air/water and ccl4/water interfaces*, The Journal of Physical Chemistry B **103**, 9582 (1999).

[12] G. Ma and H. C. Allen, *Dppc langmuir monolayer at the airwater interface: probing the tail and head groups by vibrational sum frequency generation spectroscopy*, Langmuir **22**, 5341 (2006).

[13] J. Miñones, J. R. Patino, O. Conde, C. Carrera, and R. Seoane, *The effect of polar groups on structural characteristics of phospholipid monolayers spread at the air–water interface*, Colloids and Surfaces A: Physicochemical and Engineering Aspects **203**, 273 (2002).

[14] B. Lin, S. A. Rice, and D. A. Weitz, *Experimental evidence for the divergence of a transport coefficient in a quasi-two-dimensional fluid*, Phys. Rev. E **51**, 423 (1995).

[15] J. Bleibel, A. Dominguez, F. Gunther, J. Harting, and M. Oettel, *Hydrodynamic interactions induce anomalous diffusion under partial confinement*, Soft Matter **10**, 2945 (2014).

[16] J. Bleibel, A. Domínguez, and M. Oettel, *3d hydrodynamic interactions lead to divergences in 2d diffusion*, Journal of Physics: Condensed Matter **27**, 194113 (2015).

[17] J. Bleibel, A. Domínguez, and M. Oettel, *A dynamic dft approach to generalized diffusion equations in a system with long-ranged and hydrodynamic interactions*, Journal of Physics:

Condensed Matter **28**, 244021 (2016).

[18] D. Brogioli and A. Vailati, *Nonequilibrium fluctuations during diffusion in liquid layers*, Phys. Rev. E **96**, 012136 (2017).

[19] R. Cerbino, Y. Sun, A. Donev, and A. Vailati, *Dynamic scaling for the growth of non-equilibrium fluctuations during thermophoretic diffusion in microgravity*, Scientific Reports **5**, 14486 EP (2015).

[20] A. Vailati, R. Cerbino, S. Mazzoni, C. J. Takacs, D. S. Cannell, and M. Giglio, *Fractal fronts of diffusion in microgravity*, Nat. Commun. **2**, 290 (2011).

[21] J. Bleibel, A. Domínguez, and M. Oettel, *Onset of anomalous diffusion in colloids confined to quasimonolayers*, Phys. Rev. E **95**, 032604 (2017).

[22] A. Domínguez, *Signature of time-dependent hydrodynamic interactions on collective diffusion in colloidal monolayers*, Phys. Rev. E **90**, 062314 (2014).

[23] P. G. Saffman and M. Delbrück, *Brownian motion in biological membranes*, Proceedings of the National Academy of Sciences **72**, 3111 (1975).

[24] B. A. Camley and F. L. H. Brown, *Diffusion of complex objects embedded in free and supported lipid bilayer membranes: role of shape anisotropy and leaflet structure*, Soft Matter **9**, 4767 (2013).

[25] M. C. Rheinstädter, J. Das, E. J. Flenner, B. Brüning, T. Seydel, and I. Kosztin, *Motional coherence in fluid phospholipid membranes*, Phys. Rev. Lett. **101**, 248106 (2008).

[26] C. L. Armstrong, M. Trapp, J. Peters, T. Seydel, and M. C. Rheinstadter, *Short range ballistic motion in fluid lipid bilayers studied by quasi-elastic neutron scattering*, Soft Matter **7**, 8358 (2011).

[27] S. Busch, C. Smuda, L. C. Pardo, and T. Unruh, *Molecular mechanism of long-range diffusion in phospholipid membranes studied by quasielastic neutron scattering*, Journal of the American Chemical Society **132**, 3232 (2010).

[28] E. Falck, T. Róg, M. Karttunen, and I. Vattulainen, *Lateral diffusion in lipid membranes through collective flows*, Journal of the American Chemical Society **130**, 44 (2008).

[29] T. Apajalahti, P. Niemelä, P. N. Govindan, M. S. Miettinen, E. Salonen, S.-J. Marrink, and I. Vattulainen, *Concerted diffusion of lipids in raft-like membranes*, Faraday Discuss. **144**, 411 (2010).

Appendix

A

Incompressible Stokes Flow

In this appendix we present common approximations that can greatly reduce the level of complexity of the inertial coupling equations of particles that are immersed in a fluid (solvent),

$$\partial_t \rho + \nabla \cdot (\rho \boldsymbol{u}) = 0, \tag{A.1a}$$

$$\partial_t (\rho \boldsymbol{u}) + \nabla \cdot (\rho \boldsymbol{u}\boldsymbol{u}) = -\nabla p + \nabla \cdot \boldsymbol{\sigma} - \boldsymbol{S}\boldsymbol{\lambda}, \tag{A.1b}$$

$$m_e \frac{d\boldsymbol{v}}{dt} = \boldsymbol{F} + \boldsymbol{\lambda}, \tag{A.1c}$$

$$\frac{d\boldsymbol{q}}{dt} = \boldsymbol{v} = \boldsymbol{J}\boldsymbol{u}. \tag{A.1d}$$

Generally, relaxation times of the fluid are known to be very fast compared to the relaxation times of the particles. Thus, in the particle frame of reference one can assume that all inertial terms in the momentum equation of the fluid (Eq. (A.1b)) are negligible. Additionally, unless the density of the particles is colossally high compare to the density of the fluid, at diffusive time-scales the momentum of these particles is assumed to be in equilibrium, *i.e.* inertial terms in the momentum equation of the particles (Eq. (A.1c)) are negligible too. Hence, these two approximations give place to the so-called Stokes flow, which is characterised by a fluid flow with a small *Reynolds number Re* (ratio of inertial forces to viscous forces). Another usual approach is to consider a fluid as incompressible ($\rho \approx$ const.), for which one gets incompressible flows ($\nabla \cdot \boldsymbol{u} = 0$).

Putting all these approximations together, Eqs. (A.1) simplify to

$$\nabla \cdot \boldsymbol{u} = 0. \tag{A.2a}$$

$$\eta \nabla^2 \boldsymbol{u} - \nabla p + \boldsymbol{SF} = 0, \tag{A.2b}$$

$$\frac{d\boldsymbol{q}}{dt} = \boldsymbol{v} = \boldsymbol{J}\boldsymbol{u}. \tag{A.2c}$$

Formally, incompressible Stokes flow equations ((A.2a) and (A.2b)) can be solved analytically assuming that the exerted forces on the fluid are point-forces (forcing term $\boldsymbol{SF} = \boldsymbol{f} \cdot \delta(\boldsymbol{r})$) and boundary conditions for the pressure and the velocity $|\boldsymbol{u}|, p \to 0$ as $r \to \infty$. This yields

$$\boldsymbol{u}(\boldsymbol{r}) = \boldsymbol{\mathcal{M}}(\boldsymbol{r}) \cdot \boldsymbol{SF}, \qquad p(\boldsymbol{r}) = \frac{\hat{\boldsymbol{r}} \cdot \boldsymbol{SF}}{4\pi r^2}, \tag{A.3}$$

where $\boldsymbol{\mathcal{M}}$ is Green's function (impulse response of the inhomogeneous lineal equation $Lu(x) = f(x)$ *i.e.* $u(x) = \int \mathcal{G}(s-x) f(x) ds$, with $L\mathcal{G}(s-x) = \hat{\delta}(s-x)$, $\hat{\delta}$ the Dirac function, L a lineal differential operator and $\mathcal{G}$ the Green function) of the linear Eqs. (A.2a) and (A.2b), also known as the Oseen mobility tensor,

$$\boldsymbol{\mathcal{M}}(\boldsymbol{r}) = \frac{1}{8\pi\eta r}\left(\boldsymbol{I} + \hat{\boldsymbol{r}} \otimes \hat{\boldsymbol{r}}\right). \tag{A.4}$$

The Oseen tensor perfectly recovers the long-range character of the hydrodynamic interactions of particles in the far field ($r \gg 1$), albeit, it yields a poor hydrodynamic description of finite-sized particles in the near field ($r \sim 1$). This issue can be solved by integrating the Oseen tensor over a spherical surface of radius a [J. Fluid Mech. **731**, R3 (2013)], yielding the RPY mobility tensor

$$\boldsymbol{\mathcal{M}}(\boldsymbol{r}) = \frac{1}{6\pi\eta r}\begin{cases} \frac{3}{4}\left[\boldsymbol{I} + \hat{\boldsymbol{r}} \otimes \hat{\boldsymbol{r}}\right] + \frac{a^2}{2r^2}\left[\boldsymbol{I} - 3\hat{\boldsymbol{r}} \otimes \hat{\boldsymbol{r}}\right], & r < 2a, \\ \frac{r}{a}\boldsymbol{I} - \left[\frac{9r^2}{64a^2}\boldsymbol{I} - \frac{3r^2}{64a^2}\hat{\boldsymbol{r}} \otimes \hat{\boldsymbol{r}}\right], & r \geq 2a. \end{cases} \tag{A.5a}$$

Thus, the RPY mobility tensor takes into account the finite size of (spherical) particles, improving their near-field hydrodynamics.

B

Brownian Dynamics with Hydrodynamic Interactions in Quasi-Two-Dimensions

In this appendix we present a novel and efficient algorithm (linear in the number of particles) to perform BDHI simulations in Q2D systems. Unlike prior works, in which the algorithms used are fully 3D (particles are constrained to a plane by means of a harmonic potential), our algorithm is based on the FDDFT-HI Eq. (4.4). The main idea is to solve a much cheaper 2D equation for the evolution of particles (completely eliminating the third dimension) in exchange for adding a non-zero divergent flow. This new algorithm combines the fluctuating force-coupling method and the immersed boundary method.

From Eqs. (A7) and (A10) of Ref. [J. Stat. Mech. Theory Exp. **2014**, P04004 (2014)] it is straightforward to demonstrate that Eqs. (4.1) can be written as

$$\frac{d\boldsymbol{q}_i}{dt} = \boldsymbol{\omega}\left(\boldsymbol{q}_i, t\right) + \int \delta_a\left(\boldsymbol{q}_i - \boldsymbol{r}'\right) \sum_j \mathcal{G}\left(\boldsymbol{r}', \boldsymbol{r}''\right) \left[\boldsymbol{F}_j \delta_a\left(\boldsymbol{q}_j - \boldsymbol{r}''\right) + \left(k_B T\right) \nabla \delta_a\left(\boldsymbol{q}_j - \boldsymbol{r}''\right)\right] d\boldsymbol{r}' d\boldsymbol{r}'', \tag{B.1}$$

where we have used the general properties of a translational invariant and isotropic mobility tensor

$$\boldsymbol{\mathcal{M}}\left(\boldsymbol{q}_i, \boldsymbol{q}_j\right) = \boldsymbol{\mathcal{M}}\left(\boldsymbol{q}_i - \boldsymbol{q}_j\right) = \int \delta_a\left(\boldsymbol{q}_i - \boldsymbol{r}'\right) \mathcal{G}\left(\boldsymbol{r}' - \boldsymbol{r}''\right) \delta_a\left(\boldsymbol{q}_j - \boldsymbol{r}''\right) d\boldsymbol{r}' d\boldsymbol{r}'', \tag{B.2}$$

with $\mathcal{G}$ the Green function of a 3D incompressible flow and δ_a some regularising kernel of width a [Acta Numerica **11**, P479 (2002)]. For convenience of the Q2D algorithm, we employ Gaussian regularising kernels[1] because: (1) they are the ones that yield numerical accuracy without the need for near-field corrections, (2) these kernels avoid grid artefacts and (3) they simplify analytical computations. We must point out the gradient of the kernel $\nabla\delta_a$ in Q2D simulations should be taken in the particle plane of motion.

B.1 Force-Coupling Method in Quasi-Two-Dimensions

In Q2D, the Fourier transform of the force-coupling kernel (Eq. (B.2)) can be estimated from the integration of the Fourier transform of the Oseen tensor along the z axis, this is

$$\tilde{\boldsymbol{\mathcal{M}}}_{\boldsymbol{k}} = \frac{1}{2\pi\eta}\int_{k_z=-\infty}^{\infty}\frac{dk_z}{(k^2+k_z^2)}\exp\left(-\frac{a^2\,(k^2+k_z^2)}{\pi}\right)\left(\boldsymbol{I}-\frac{(\boldsymbol{k},k_z)\otimes(\boldsymbol{k},k_z)}{(k^2+k_z^2)}\right), \tag{B.3}$$

where $\exp\left(-\frac{a^2(k^2+k_z^2)}{\pi}\right)$ comes from the square of the kernels δ_a. Performing the integral we find that the resulting mobility has the isotropic form

$$\tilde{\boldsymbol{\mathcal{M}}}_{\boldsymbol{k}} = \frac{1}{\eta k}\left(c_2\,(ka)\;\hat{\boldsymbol{k}}_\perp\otimes\hat{\boldsymbol{k}}_\perp + c_1\,(ka)\;\hat{\boldsymbol{k}}\otimes\hat{\boldsymbol{k}}\right), \tag{B.4}$$

where we have used $\boldsymbol{k}=(k_x,k_y)$, $\boldsymbol{k}_\perp=\boldsymbol{k}\times\hat{\boldsymbol{z}}=(-k_y,k_x)$ and

$$c_1\,(K) = \frac{1}{2\pi}\left[-K\,\exp\left(-\frac{K^2}{\pi}\right)-\left(K^2+\frac{\pi}{2}\right)\left(\operatorname{erf}\left(\frac{K}{\sqrt{\pi}}\right)-1\right)\right], \tag{B.5a}$$

$$c_2\,(K) = \frac{1}{2}\left[1-\operatorname{erf}\left(\frac{K}{\sqrt{\pi}}\right)\right]. \tag{B.5b}$$

which totally differ from the ones for a 2D system

$$c_1\,(K) = 0, \tag{B.6a}$$

$$c_2\,(K) = \frac{a}{K}\,\exp\left(-\frac{K^2}{\pi}\right). \tag{B.6b}$$

[1] Notice that the kernels δ_a are still three dimensional objects in Q2D.

It is worth pointing out that this Q2D kernel is a minimal mobility model that captures the anomalous behaviour of the collective diffusion coefficient in the far field

$$\hat{\boldsymbol{k}} \cdot \tilde{\boldsymbol{\mathcal{M}}}_{\boldsymbol{k}} \cdot \hat{\boldsymbol{k}} = \left(\frac{1}{\eta k}\right) c_1(ak) \approx \frac{1}{4\eta k}. \tag{B.7}$$

Another important note on this Q2D mobility is that it decays exponentially in Fourier space, $\exp(-a^2k^2)$, which is crucial as well as characteristic of force-coupling methods. Finally, in real space the Q2D mobility tensor yields

$$\boldsymbol{\mathcal{M}}(\boldsymbol{q}_i, \boldsymbol{q}_j) = \boldsymbol{\mathcal{M}}(\boldsymbol{r} = \boldsymbol{q}_i - \boldsymbol{q}_j) = f(r)\boldsymbol{I} + g(r)\hat{\boldsymbol{r}} \otimes \hat{\boldsymbol{r}}, \tag{B.8}$$

where

$$f(r) = \frac{1}{8\pi\eta\, r}\left[\left(1 + 2\,\frac{a^2}{\pi\, r^2}\right)\operatorname{erf}\left(\frac{r\sqrt{\pi}}{2a}\right) - 2\frac{a}{\pi\, r}\exp\left(-\frac{\pi\, r^2}{4a^2}\right)\right], \tag{B.9a}$$

$$g(r) = \frac{1}{8\pi\eta\, r}\left[\left(1 - 6\,\frac{a^2}{\pi\, r^2}\right)\operatorname{erf}\left(\frac{r\sqrt{\pi}}{2a}\right) + 6\frac{a}{\pi\, r}\exp\left(-\frac{\pi\, r^2}{4a^2}\right)\right]. \tag{B.9b}$$

From the expressions (B.9) we can obtain system size corrections Δ_{D_0} of the short-time self-diffusion coefficient

$$D_0 = (k_B T)\, f(r = 0) = \frac{k_B T}{\eta}\Delta_{D_0}, \tag{B.10}$$

with

$$\Delta_{D_0} = \frac{1}{6\pi a} \cdot \frac{1}{1 + 4.41a/L}, \qquad \text{for Quasi2D,} \tag{B.11a}$$

$$\Delta_{D_0} = \frac{1}{4\pi}\ln\left(\frac{L}{3.71a}\right), \qquad \text{for 2D,} \tag{B.11b}$$

with L being the length of a square simulating domain. In stark contrast to the 2D case, the Q2D hydrodynamics gives rise to finite-size corrections that display an inverse proportionality to the system length.

B.2 Efficient Two-Dimensional Brownian Dynamics

Equation (B.1) is the base of our Q2D BDHI algorithm. The key to this algorithm consists in spreading the force density term $\boldsymbol{F}_j\delta_a + k_BT\nabla\delta_a$ to a grid localised around a particle j, and then performing the spatial convolution in (B.1) using the fast Fourier transform. For this last step, we require the Fourier transform of the Green function $\mathcal{G}_{\boldsymbol{k}}$. As we explained in the previous section, the Q2D mobility was derived from the integration of the Fourier transform of Eq. (B.2) over the z axis, thus including the regularisation kernels within the mobility. Here, in contrast, we implicitly include the in-plane contribution of the regularisation kernels in the force densities term $\boldsymbol{F}_j\delta_a + k_BT\nabla\delta_a$ by its calculation on a $x-y$ grid. Consequently, the force coupling kernel of our Q2D algorithm is given by

$$\begin{aligned}\tilde{\mathcal{G}}_{\boldsymbol{k}} &= \frac{1}{2\pi\eta}\int_{k_z=-\infty}^{\infty}\frac{dk_z}{(k^2+k_z^2)}\exp\left(-\frac{a^2k_z^2}{\pi}\right)\left(\boldsymbol{I}-\frac{(\boldsymbol{k},k_z)\otimes(\boldsymbol{k},k_z)}{(k^2+k_z^2)}\right)\\ &= \frac{1}{\eta k}\left(c_2'(ka)\,\boldsymbol{k}_\perp\otimes\boldsymbol{k}_\perp + c_1'(ka)\,\boldsymbol{k}\otimes\boldsymbol{k}\right),\end{aligned} \tag{B.12}$$

with

$$c_1'(K) = \frac{1}{2\pi}\left[-K-\exp\left(\frac{K^2}{\pi}\right)\left(K^2+\frac{\pi}{2}\right)\left(\operatorname{erf}\left(\frac{K}{\sqrt{\pi}}\right)-1\right)\right], \tag{B.13a}$$

$$c_2'(K) = \frac{1}{2}\left[1-\operatorname{erf}\left(\frac{K}{\sqrt{\pi}}\right)\right]\exp\left(\frac{K^2}{\pi}\right). \tag{B.13b}$$

On the other hand, the random advection term $\boldsymbol{\omega}(\boldsymbol{q},t)$ in Eq. (B.1) is directly generated in Fourier space by means of its reciprocal representation

$$\tilde{\boldsymbol{\omega}}_{\boldsymbol{k}} = \sqrt{\frac{2k_BT}{\eta k}}\left(\sqrt{c_2'(ka)}\,\hat{\boldsymbol{k}}_\perp\tilde{\xi}_{\boldsymbol{k}}^{(2)} + \sqrt{c_1'(ka)}\,\hat{\boldsymbol{k}}\tilde{\xi}_{\boldsymbol{k}}^{(1)}\right), \tag{B.14}$$

where $\tilde{\xi}_{\boldsymbol{k}}^{(1)}(t)$ and $\tilde{\xi}_{\boldsymbol{k}}^{(2)}(t)$ are scalar white noise processes, uncorrelated of each other in time and wavenumbers, and with symmetry properties to ensure that the resulting velocity field $\boldsymbol{\omega}(\boldsymbol{q},t) = \frac{1}{(2\pi)^2}\int\tilde{\boldsymbol{\omega}}_{\boldsymbol{k}}(t)\,e^{i\boldsymbol{k}\cdot\boldsymbol{q}}d\boldsymbol{k}$ is real-valued.

Algorithm 1 Summary of the n-th time step of a Q2D BDHI algorithm.

1. Compute the particle forces $\boldsymbol{F}_i(t)$.

2. Evaluate the force density term

$$\boldsymbol{f}(\boldsymbol{r}) = \sum_i \boldsymbol{F}_i(t)\delta_a(\boldsymbol{q}_i(t) - \boldsymbol{r}) + (k_B T)\sum_i (\nabla\delta_a)(\boldsymbol{q}_i(t) - \boldsymbol{r}) + \boldsymbol{f}_{\text{ext}}(\boldsymbol{r}),$$

   on a staggered grid with PBC and use the fast Fourier transform to convert $\boldsymbol{f}$ to Fourier space ($\tilde{\boldsymbol{f}}_{\boldsymbol{k}}$). The extra term $\boldsymbol{f}_{ext}(\boldsymbol{r})$ represents a possible external force *e.g.* gravity.

3. Compute the total fluid velocity in Fourier space,

$$\tilde{\boldsymbol{u}}_k = \tilde{\boldsymbol{u}}_k^{\text{det}} + \tilde{\boldsymbol{u}}_k^{\text{stoch}},$$

   with the deterministic part of the velocity $\tilde{\boldsymbol{u}}_k^{\text{det}} = \tilde{\mathcal{G}}_{\boldsymbol{k}}\tilde{\boldsymbol{f}}_{\boldsymbol{k}}$ and the stochastic part $\tilde{\boldsymbol{u}}_k^{\text{stoch}} = \sqrt{\frac{2k_BT}{\eta k\Delta t}}\left(\sqrt{c_2'(ka)}\,\hat{\boldsymbol{k}}_\perp\tilde{\xi}_{\boldsymbol{k}}^{(2)} + \sqrt{c_1'(ka)}\,\hat{\boldsymbol{k}}\tilde{\xi}_{\boldsymbol{k}}^{(1)}\right)$.

4. Use the fast Fourier transform to convert the velocity to real space.

5. Convolve $\boldsymbol{u}(\boldsymbol{r})$ with a Gaussian in real space to compute the velocities of the particles

$$\boldsymbol{v}_i(t) = \int \delta_a(\boldsymbol{q}_i(t) - \boldsymbol{r})\,\boldsymbol{u}(\boldsymbol{r})\,d\boldsymbol{r}.$$

6. Advance the particle positions

$$\boldsymbol{q}_i(t + \Delta t) = \boldsymbol{q}_i(t) + \boldsymbol{v}_i(t)\Delta t.$$

From preliminary simulations, we have inferred that the grid spacing h should be about $h \lesssim 0.8a$ in order to guarantee a relative error smaller than 10^{-4} in the short-time self-diffusion coefficient D_0. It implies a simulation box of 800×800 a.u (arbitrary units) requires at least of 1000×1000 grid cells. For efficiency of the fast Fourier transform, we look for a number of grid cells that can be factorised into small prime numbers. Thus, a simulation box of 800×800 a.u would require 1152×1152 grid cells. Another important factor concerning the computation time is the interpolating Gaussian kernel δ_a. This kernel is forced to be cut off after 4 neighbour cells. This yields a numerical accuracy of about 10^{-4} in the relative error while keeping the numerical efficiency. Although in Algo. 1 we present (for pedagogical reasons) a temporal discretisation based on a first order forward (Euler) algorithm, in

practice, we use a mid-point temporal discretisation. The election of the time step Δt is made such that the equilibrium radial distribution function $g(r)$ and the structure factor $S(k)$ are well behaved; for an ideal gas, the theoretical radial distribution function equals $g(r) = 1$. However, the spatial discretisation may artificially promote large errors at small distances $r \ll 1$. The reason for this fact is obscure to us but it has empirically been observed that this error tends to zero for small time steps.

C

Derivation of the Cross Hydrodynamic Function

In this appendix we present an explicit derivation of the cross hydrodynamic function

$$H_c(k) = N\,(k_BT)\int P_2(\boldsymbol{q}_1,\boldsymbol{q}_2)\hat{\boldsymbol{k}}\cdot\frac{\boldsymbol{\mathcal{M}}_{12}(\boldsymbol{q}_2-\boldsymbol{q}_1)}{D_0}\cdot\hat{\boldsymbol{k}}\exp[-\mathrm{i}\boldsymbol{k}\cdot(\boldsymbol{q}_2-\boldsymbol{q}_1)]d\boldsymbol{q}_1d\boldsymbol{q}_2, \tag{C.1}$$

for ideal particles that are constrained to move in a confining plane ($z_0 = 0$) by means of a harmonic external potential ($V = \frac{1}{2}k_s(z_1 - z_0)^2 + \frac{1}{2}k_s(z_2 - z_0)^2$). Assuming that the two-particle probability distribution P_2 is given by the Gibbs-Boltzmann distribution we arrive at

$$P_2(\boldsymbol{R},\boldsymbol{r}) = \frac{1}{\mathcal{Z}_2}\exp[-\beta V(\boldsymbol{q}_1,\boldsymbol{q}_2)] = \frac{1}{\mathcal{Z}_2}\exp\left\{\frac{k_s}{2}\left[2Z^2+\frac{1}{2}z^2\right]\right\} \equiv \frac{1}{\mathcal{Z}_2}P_R(Z)P_r(z). \tag{C.2}$$

where we have made use of the two-body coordinates $\boldsymbol{R} = (\boldsymbol{q}_1+\boldsymbol{q}_2)/2 = \boldsymbol{S}+Z\hat{\boldsymbol{Z}}$, $\boldsymbol{r} = \boldsymbol{q}_2-\boldsymbol{q}_1 = \boldsymbol{s}+z\hat{\boldsymbol{z}}$, which are split up into the in-plane coordinates, $\boldsymbol{S}$, $\boldsymbol{s}$ and into the perpendicular coordinates $\boldsymbol{Z}$, $\boldsymbol{z}$. Notice the confining force employed is not unique, *e.g.* for an exponential trap, $V(z_1,z_2) = \exp(-az_1)+\exp(-az_2)$, $V(Z+z) = 2\exp(-aZ)\cosh(az/2)$, however, we find this one to ease the calculation of the cross hydrodynamic function.

Then, substituting Eq. (C.2) in Eq. (C.1) we write

$$H_c(k) = B\,(k_B T)\int e^{-\beta V_r(z)}\hat{\boldsymbol{k}}\cdot\frac{\boldsymbol{\mathcal{M}}_{12}(\boldsymbol{r})}{D_0}\cdot\hat{\boldsymbol{k}}\exp\{-\mathrm{i}\boldsymbol{k}\cdot\boldsymbol{r}\}\,d\boldsymbol{r}, \tag{C.3}$$

with $\boldsymbol{k}$ a two-dimensional vector over the confining plane, *i.e.* $\boldsymbol{k}\cdot\hat{\boldsymbol{z}}=0$, and

$$B \equiv \frac{N\int e^{-\beta V_R(Z)}d\boldsymbol{R}}{\mathcal{Z}_2} = \frac{N}{\int\exp[-\beta V_r(z)]d\boldsymbol{r}} = \frac{\rho_{2D}\sqrt{\beta k_s}}{2\sqrt{\pi}}. \tag{C.4}$$

Accepting that the mobility matrix $\boldsymbol{\mathcal{M}}_{12}(\boldsymbol{r})$ is given by the (3D) Oseen tensor

$$\frac{\boldsymbol{\mathcal{M}}_{12}(\boldsymbol{r})}{D_0} = \frac{1}{(2\pi)^3 D_0}\int e^{\mathrm{i}\boldsymbol{k}'\cdot\boldsymbol{r}}\frac{1}{\eta k'^2}\left[\boldsymbol{I}-\frac{\boldsymbol{k}'\boldsymbol{k}'}{k'^2}\right]d\boldsymbol{k}', \tag{C.5}$$

we have

$$H_c(k) = \frac{6\pi a B}{(2\pi)^3}\int e^{-\beta k_s\frac{z^2}{4}}\hat{\boldsymbol{k}}\cdot\int d^3k'\frac{1}{k'^2}\left[\boldsymbol{I}-\frac{\boldsymbol{k}'\boldsymbol{k}'}{k'^2}\right]e^{\mathrm{i}k'_z z}\cdot\hat{\boldsymbol{k}}\int e^{-\mathrm{i}\boldsymbol{k}\cdot\boldsymbol{s}}e^{-\mathrm{i}\boldsymbol{k}'_\parallel\cdot\boldsymbol{s}}d\boldsymbol{s}d\boldsymbol{k}'dz, \tag{C.6}$$

which can be simplified using $\hat{\boldsymbol{k}}\cdot\frac{1}{k'^2}\left[\boldsymbol{I}-\frac{\boldsymbol{k}'\boldsymbol{k}'}{k'^2}\right]\cdot\hat{\boldsymbol{k}} = \frac{k'^2_\parallel+k'^2_z-(\hat{\boldsymbol{k}}\cdot\boldsymbol{k}')^2}{(k'^2_\parallel+k'^2_z)^2}$ and $\int\exp\left\{-\mathrm{i}\boldsymbol{s}\cdot(\boldsymbol{k}-\boldsymbol{k}'_\parallel)\right\}d\boldsymbol{s} = (2\pi)^2\hat{\delta}^2(\boldsymbol{k}-\boldsymbol{k}'_\parallel)$ (where $\hat{\delta}$ is the Dirac delta function). Thereby, we obtain

$$H_c(k) = \frac{6\pi a B}{(2\pi)}\int_{-\infty}^{\infty}\frac{k'^2_z}{\left(k'^2_z+k^2\right)^2}\mathcal{V}(k'_z)dk'_z. \tag{C.7}$$

where we have denoted by $\mathcal{V}(k'_z)$ in Eq. (C.7) the 1D Fourier transform of the Boltzmann factor associated to the confining potential,

$$\mathcal{V}(k'_z) \equiv \int_{-\infty}^{\infty} e^{-\beta V_r(z)}e^{ik'_z z}dz. \tag{C.8}$$

From Eq. (C.7) we clearly see the effect of the confining potential: for strict confinements $P_2(R,r)\to\hat{\delta}(z)\hat{\delta}(Z)$ and $\mathcal{V}(k'_z)\to 1$, therefore recovering the expression derived in previous works [Soft Matter **10**, 2945 (2014)]. Under soft confinement, $\mathcal{V}(k'_z) = 2\sqrt{\pi}\delta\exp[-(k'_z\delta)^2]$ *i.e.* the confining potential acts as a wavenumber filter, damping out wavenumber contri-

butions that fulfil $k_z'\delta > 1$,

$$H_c(k) = \frac{6\pi aB\delta}{\sqrt{\pi}} \int_{-\infty}^{\infty} \frac{{k_z'}^2}{\left({k_z'}^2 + k^2\right)^2} e^{-(k_z'\delta)^2} dk_z'. \tag{C.9}$$

Finally, integrating Eq. (C.9) we arrive at the final expression

$$H_c(k) = 3\phi\frac{\delta}{a}\left\{\left[\frac{1}{2}(k\delta)^{-1} + (k\delta)\right] e^{(k\delta)^2}\mathrm{erfc}(k\delta) - \frac{1}{\sqrt{\pi}}\right\}. \tag{C.10}$$

List of Tables

List of Figures

List of Publications

Contributions related to the content of this Thesis

[1] S. Panzuela, P. Tieleman, L. Mederos and E. Velasco, *Molecular ordering in lipid monolayers: an atomistic simulation*, (in preparation).

[2] S. Panzuela and R. Delgado-Buscalioni, *Solvent hydrodynamics enhances the collective diffusion of membrane lipids*, Phys. Rev. Lett. **121**, 047702 (2018).

[3] R. P. Peláez, F. B. Usabiaga, S. Panzuela, Q. Xiao, R. Delgado-Buscalioni and A. Donev, *Hydrodynamic fluctuations in quasi-two dimensional diffusion*, J. Stat. Mech. Theory Exp. **2018**, 063207 (2018).

[4] S. Panzuela, R. P. Peláez and R. Delgado-Buscalioni, *Collective colloid diffusion under soft two-dimensional confinement*, Phys. Rev. E **95**, 012602 (2017).

Other Contributions

[1] S. Panzuela, M. Bernabei, E. Velasco, R. Delgado-Buscalioni and P. Tarazona, *A novel technique to predict the solubility of planar molecules*, Energy & Fuels **30**, 10747 (2016).